

1

²A SEARCH FOR LONG-LIVED, CHARGED, SUPERSYMMETRIC PARTICLES
³USING IONIZATION WITH THE ATLAS DETECTOR

4

BRADLEY AXEN

5

September 2016 – Version 0.56

6



⁸ Bradley Axen: *A Search for Long-Lived, Charged, Supersymmetric Particles using*
⁹ *Ionization with the ATLAS Detector*, Subtitle, © September 2016

10

Usually a quotation.

11

Dedicated to.

₁₂ ABSTRACT

₁₃ How to write a good abstract:

₁₄ <https://plg.uwaterloo.ca/~migod/research/beck00PSLA.html>

₁₅ PUBLICATIONS

₁₆ Some ideas and figures have appeared previously in the following publications:

₁₇

₁₈ Put your publications from the thesis here. The packages `multibib` or `bibtopic`
₁₉ etc. can be used to handle multiple different bibliographies in your document.

²¹ ACKNOWLEDGEMENTS

²² Put your acknowledgements here.

²³

²⁴ And potentially a second round.

²⁵

26 CONTENTS

27	I	INTRODUCTION	1
28	1	INTRODUCTION	3
29	II	THEORETICAL CONTEXT	5
30	2	STANDARD MODEL	7
31	2.1	Action and the Lagrangian	7
32	2.2	Gauge Invariance and Forces	8
33	2.2.1	$SU(2) \times U(1)$ and the Electroweak Force	10
34	2.2.2	$SU(3)$ and the Strong Force	10
35	2.3	Noether's Theorem, Charges, and Matter	10
36	2.3.1	Quarks	11
37	2.3.2	Leptons	12
38	2.3.3	Chirality	12
39	2.4	Higgs Mechanism and Mass	13
40	2.5	Phenomenology	14
41	2.5.1	Electroweak Physics	14
42	2.5.2	Strong Physics	15
43	2.5.3	Proton-Proton Collisions	15
44	2.6	Limitations	16
45	2.6.1	Theoretical Concerns	16
46	2.6.2	Cosmological Observations	18
47	3	SUPERSYMMETRY	21
48	3.1	Structure and the MSSM	21
49	3.2	Motivation	22
50	4	LONG-LIVED PARTICLES	23
51	4.1	Mechanisms	23
52	4.1.1	Examples in Supersymmetry	23
53	4.2	Phenomenology	23
54	4.2.1	Disimilarities to Prompt Decays	23
55	4.2.2	Characteristic Signatures	23
56	III	EXPERIMENTAL STRUCTURE AND RECONSTRUCTION	25
57	5	THE LARGE HADRON COLLIDER	27
58	5.1	Injection Chain	28
59	5.2	Design	29
60	5.2.1	Layout	29
61	5.2.2	Magnets	30
62	5.2.3	RF Cavities	31
63	5.2.4	Beam	33
64	5.3	Luminosity Parameters	33
65	5.4	Delivered Luminosity	34

66	6	THE ATLAS DETECTOR	37
67	6.1	Coordinate System	39
68	6.2	Magnetic Field	40
69	6.3	Inner Detector	42
70	6.3.1	Pixel Detector	45
71	6.3.2	Semiconductor Tracker	47
72	6.3.3	Transition Radiation Tracker	50
73	6.4	Calorimetry	51
74	6.4.1	Electromagnetic Calorimeter	52
75	6.4.2	Hadronic Calorimeters	53
76	6.5	Muon Spectrometer	55
77	6.5.1	Monitored Drift Tube	57
78	6.5.2	Resistive Plate Chamber	58
79	6.5.3	Cathode Strip Chamber	58
80	6.5.4	Thin Gap Chamber	59
81	6.6	Trigger	60
82	7	EVENT RECONSTRUCTION	65
83	7.1	Charged Particles	65
84	7.1.1	Pixel Neural Network	67
85	7.1.2	Pixel dE/dx	68
86	7.1.3	Vertex Reconstruction	69
87	7.2	Electrons and Photons	69
88	7.2.1	Photon Identification	71
89	7.2.2	Electron Identification	71
90	7.3	Muons	71
91	7.3.1	Muon Identification	72
92	7.4	Jets	72
93	7.4.1	Topological Clustering	72
94	7.4.2	Jet Algorithms	74
95	7.4.3	Jet Energy Scale	74
96	7.5	Missing Transverse Energy	75
97	IV	CALORIMETER RESPONSE	79
98	8	RESPONSE MEASUREMENT WITH SINGLE HADRONS	81
99	8.1	Dataset and Simulation	82
100	8.1.1	Data Samples	82
101	8.1.2	Simulated Samples	82
102	8.1.3	Event Selection	82
103	8.2	Inclusive Hadron Response	83
104	8.2.1	E/p Distribution	83
105	8.2.2	Zero Fraction	84
106	8.2.3	Neutral Background Subtraction	85
107	8.2.4	Corrected Response	87
108	8.2.5	Additional Studies	89
109	8.3	Identified Particle Response	92
110	8.3.1	Decay Reconstruction	92

111	8.3.2	Identified Response	93
112	8.3.3	Additional Species in Simulation	95
113	8.4	Summary	96
114	9	JET ENERGY RESPONSE AND UNCERTAINTY	99
115	9.1	Motivation	99
116	9.2	Uncertainty Estimate	99
117	9.3	Summary	102
118	V	SEARCH FOR LONG-LIVED PARTICLES	105
119	10	LONG-LIVED PARTICLES IN ATLAS	107
120	10.1	Event Topology	107
121	10.1.1	Detector Interactions	108
122	10.1.2	Lifetime Dependence	109
123	10.2	Simulation	112
124	11	EVENT SELECTION	115
125	11.1	Trigger	116
126	11.2	Kinematics and Isolation	117
127	11.3	Particle Species Rejection	121
128	11.4	Ionization	124
129	11.4.1	Mass Estimation	125
130	11.5	Efficiency	126
131	12	BACKGROUND ESTIMATION	129
132	12.1	Background Sources	129
133	12.2	Prediction Method	130
134	12.3	Validation	131
135	12.3.1	Closure in Simulation	131
136	12.3.2	Validation Region in Data	132
137	13	SYSTEMATIC UNCERTAINTIES AND RESULTS	135
138	13.1	Systematic Uncertainties	135
139	13.1.1	Background Estimate	135
140	13.1.2	Signal Yield	136
141	13.2	Final Yields	142
142	13.3	Cross Sectional Limits	143
143	13.4	Mass Limits	145
144	13.5	Context for Long-Lived Searches	147
145	VI	CONCLUSIONS	151
146	14	SUMMARY AND OUTLOOK	153
147	14.1	Summary	153
148	14.2	Outlook	153
149	VII	APPENDIX	155
150	A	INELASTIC CROSS SECTION	157
151	B	EXPANDED R-HADRON YIELDS AND LIMITS	159
152		BIBLIOGRAPHY	165

153 LIST OF FIGURES

154	Figure 1	A Feynman diagram representing the interaction of the A field with a generic fermion, f	10
155			
156	Figure 2	The particle content of the Standard Model (SM)	12
157	Figure 3		
158			
159			
160			
161	Figure 4	The Feynman diagrams representing the decays of the W and Z bosons to fermions. Here f indicates a generic fermion, \bar{f} its antiparticle, and f' the partner of that fermion in the same generation.	15
162			
163			
164			
165			
166	Figure 5	The parton distribution functions (PDFs) for proton-proton collisions at $Q^2 = 10 \text{ GeV}^2$ and $Q^2 = 10^4 \text{ GeV}^2$. Each shows the fraction of particles which carry a fraction x of the total proton energy at the specified scale [1].	16
167			
168	Figure 6	An approximation of the running of the coupling constants in the SM up to the Planck scale [unification_plot].	17
169			
170			
171			
172	Figure 7	The distribution of velocities of stars as a function of the radius from the center of the galaxy. The contributions to the velocity from the various components of matter in the galaxy are shown [2].	18
173			
174			
175			
176	Figure 8	The four collision points and corresponding experiments of the Large Hadron Collider (LHC). The image includes the location of the nearby city of Geneva as well as the border of France and Switzerland.	28
177			
178			
179			
180			
181	Figure 9	The cumulative luminosity over time delivered to the A Toroidal LHC ApparatuS (ATLAS) experiment from high energy proton-proton collisions since 2011. The energies of the collisions are listed for each of the data-taking periods.	29
182			
183			
184			
185	Figure 10	The accelerator complex that builds up to the full design energies at the LHC . The protons are passed in order to Linac 2, the PSB , the PS , the SPS and then the LHC	30
186			
187			
188			
189	Figure 11	A schematic of the layout of the LHC , not to scale. The arched and straight sections are illustrated at the bottom of the schematic, and all four crossing sites are indicated with their respective experiments.	31
190			
191			
192			
193			
194			
		A cross section of the the cryodipole magnets which bend the flight path of protons around the circumference of the LHC . The diagram includes both the superconducting coils which produce the magnetic field and the structural elements which keep the magnets precisely aligned.	32

195	Figure 12	The arrangement of four radiofrequency (RF) cavities within a cryomodule.	32
196			
197	Figure 13	The cumulative luminosity versus time delivered to ATLAS (green), recorded by ATLAS (yellow), and certified to be good quality data (blue) during stable beams for pp collisions at 13 TeV in 2015.	35
198			
199			
200			
201	Figure 14	The luminosity-weighted distribution of the mean number of interactions per crossing for the 2015 pp collision data at 13 TeV.	36
202			
203			
204	Figure 15	A cut-away schematic of the layout of the ATLAS detector. Each of the major subsystems is indicated.	38
205			
206	Figure 16	A cross-sectional slice of the ATLAS experiment which illustrates how the various SM particles interact with the detector systems.	38
207			
208			
209	Figure 17	The layout of the four superconducting magnets in the ATLAS detector.	41
210			
211	Figure 18	The arrangement of the subdetectors of the ATLAS inner detector. Each of the subdetectors is labeled in the cut-away view of the system.	43
212			
213			
214	Figure 19	A quarter section of the ATLAS inner detector which shows the layout of each of the subdetectors in detail. The lower panel shows an enlarged view of the pixel detector. Example trajectories for a particle with $\eta = 1.0, 1.5, 2.0, 2.5$ are shown. The Insertible B-Layer (IBL), which was added after the original detector commissioning, is not shown.	43
215			
216			
217			
218			
219			
220			
221	Figure 20	A computer generated three-dimensional view of the inner detector along the line of the beam axis. The subdetectors and their positions are labeled.	44
222			
223			
224	Figure 21	An alternative computer generated three-dimensional view of the inner detector transverse to the beam axis. The subdetectors and their positions are labeled.	44
225			
226			
227	Figure 22	The integrated radiation lengths traversed by a straight track at the exit of the ID envelope, including the services and thermal enclosures. The distribution is shown as a function of $ \eta $ and averaged over ϕ . The breakdown indicates the contributions of individual subdetectors, including services in their active volume.	45
228			
229			
230			
231			
232			
233	Figure 23	A cut away image of the outer three layers of the pixel detector.	48
234			
235	Figure 24	An image of the insertion of the IBL into the current pixel detector.	48
236			
237	Figure 25	A three-dimensional computer-generated image of the geometry of the IBL with a view (a) mostly transverse to the beam pipe (b) mostly parallel to the beam pipe.	49
238			
239			

240	Figure 26	An expanded view of the geometry of the silicon microstrip (<a>SCT) double layers in the barrel region.	50
241		51
242	Figure 27	The depth of (a) the electromagnetic barrel calorimeter in radiation lengths and (b) all calorimeters in interaction lengths as a function of pseudorapidity.	52
243	Figure 28	
244		
245		
246	Figure 29	A schematic of the liquid argon (<a>LAr) calorimeter in the barrel region, highlighting the accordion structure.	53
247		
248	Figure 30	A schematic of a hadronic tile module which shows the alternating layers of steel and plastic scintillator.	54
249		
250	Figure 31	The segmentation in depth and η of the tile-calorimeter modules in the central (left) and extended (right) barrels.	55
251		
252	Figure 32	A cut-away diagram of the muon systems on <a>ATLAS	56
253	Figure 33	
254		
255		
256		
257		
258	Figure 34	A quarter view of the muon spectrometer which highlights the layout of each of the detecting elements. The BOL, BML, BIL, EOL, EML, and EIL are all Monitored Drift Tube (<a>MDT) elements, where the acronyms encode their positions.	56
259		
260	Figure 35	A schematic of the cross-section of the muon spectrometer in the barrel region.	57
261		
262		
263	Figure 36	A schematic of the Cathode Strip Chamber (<a>CSC) end-cap, showing the overlapping arrangement of the eight large and eight small chambers.	59
264		
265		
266	Figure 37	A schematic of the Thin Gap Chamber (<a>TGC) doublet and triplet layers.	60
267		
268	Figure 38	The L1 Trigger rate broken down into the types of triggers as a function of the luminosity block for the 2015 data collection period.	62
269		
270		
271	Figure 39	The HLT Trigger rate broken down into the types of triggers as a function of the luminosity block for the 2015 data collection period.	63
272		
273		
274	Figure 40	An illustration of the perigee representation of track parameters for an example track. The charge is not directly shown, but is indicated by the direction of curvature of the track [15].	66
275		
276		
277		
278	Figure 41	The x and y locations of the hits generated in a simulated $t\bar{t}$ event in the inner detector. The hits which belong to tracks formed using the inside-out algorithm are highlighted in red, while the hits which belong to tracks formed using the outside-in algorithm are circled in black.	67
279		
280		
281		
282		
283		

284	Figure 42	Examples of the clusters formed in a single layer of the pixel detector for (a) a single isolated particle, (b) two nearly-overlapping particles, and (c) a particle which emits a δ -ray [16].	68
285			
286			
287			
288	Figure 43	The total, fractional jet energy scale (JES) uncertainties estimated for 2015 data as a function of jet p_T	76
289			
290	Figure 44	An illustration (a) of the E/p variable used throughout this paper. The red energy deposits come from the charged particle targeted for measurement, while the blue energy deposits are from nearby neutral particles and must be subtracted. The same diagram (b) for the neutral-background selection, described in Section 8.2.3.	84
291			
292			
293			
294			
295			
296	Figure 45	The E/p distribution and ratio of simulation to data for isolated tracks with (a) $ \eta < 0.6$ and $1.2 < p/\text{GeV} < 1.8$ and (b) $ \eta < 0.6$ and $2.2 < p/\text{GeV} < 2.8$	84
297			
298			
299	Figure 46	The fraction of tracks as a function (a, b) of momentum, (c, d) of interaction lengths with $E \leq 0$ for tracks with positive (on the left) and negative (on the right) charge.	86
300			
301			
302			
303	Figure 47	$\langle E/p \rangle_{\text{BG}}$ as a function of the track momentum for tracks with (a) $ \eta < 0.6$, (b) $0.6 < \eta < 1.1$, and as a function of the track pseudorapidity for tracks with (c) $1.2 < p/\text{GeV} < 1.8$, (d) $1.8 < p/\text{GeV} < 2.2$	87
304			
305			
306			
307	Figure 48	$\langle E/p \rangle_{\text{COR}}$ as a function of track momentum, for tracks with (a) $ \eta < 0.6$, (b) $0.6 < \eta < 1.1$, (c) $1.8 < \eta < 1.9$, and (d) $1.9 < \eta < 2.3$	88
308			
309			
310	Figure 49	$\langle E/p \rangle_{\text{COR}}$ calculated using LCW-calibrated topological clusters as a function of track momentum for tracks with (a) zero or more associated topological clusters or (b) one or more associated topological clusters.	89
311			
312			
313			
314	Figure 50	Comparison of the $\langle E/p \rangle_{\text{COR}}$ for tracks with (a) less than and (b) greater than 20 hits in the TRT.	90
315			
316	Figure 51	Comparison of the $\langle E/p \rangle_{\text{COR}}$ for (a) positive and (b) negative tracks as a function of track momentum for tracks with $ \eta < 0.6$	90
317			
318			
319	Figure 52	Comparison of the E/p distributions for (a) positive and (b) negative tracks with $0.8 < p/\text{GeV} < 1.2$ and $ \eta < 0.6$, in simulation with the FTFP_BERT and QGSP_BERT physics lists.	91
320			
321			
322			
323	Figure 53	Comparison of the response of the hadronic calorimeter as a function of track momentum (a) at the EM-scale and (b) after the LCW calibration.	91
324			
325			
326	Figure 54	Comparison of the response of the EM calorimeter as a function of track momentum (a) at the EM-scale and (b) with the LCW calibration.	92
327			
328			

329	Figure 55	The reconstructed mass peaks of (a) K_S^0 , (b) Λ , and (c) $\bar{\Lambda}$ candidates.	93
330			
331	Figure 56	The E/p distribution for isolated (a) π^+ , (b) π^- , (c) proton, and (d) anti-proton tracks.	94
332			
333	Figure 57	The fraction of tracks with $E \leq 0$ for identified (a) π^+ and π^- , and (b) proton and anti-proton tracks	94
334			
335	Figure 58	The difference in $\langle E/p \rangle$ between (a) π^+ and π^- (b) p and π^+ , and (c) \bar{p} and π^-	95
336			
337	Figure 59	$\langle E/p \rangle_{\text{COR}}$ as a function of track momentum for (a) π^+ tracks and (b) π^- tracks.	96
338			
339	Figure 60	The ratio of the calorimeter response to single parti- cles of various species to the calorimeter response to π^+ with the physics list FTFP_BERT.	96
340			
341			
342	Figure 61	The spectra of true particles inside anti- k_t , $R = 0.4$ jets with (a) $90 < p_T/\text{GeV} < 100$, (b) $400 < p_T/\text{GeV} <$ 500 , and (c) $1800 < p_T/\text{GeV} < 2300$	100
343			
344			
345	Figure 62	The JES uncertainty contributions, as well as the total JES uncertainty, as a function of jet p_T for (a) $ \eta < 0.6$ and (b) $0.6 < \eta < 1.1$	102
346			
347			
348	Figure 63	The JES correlations as a function of jet p_T and $ \eta $ for jets in the central region of the detector.	103
349			
350	Figure 64	A schematic diagram of an R-Hadron event with a life- time around 0.01 ns. The diagram includes one charged R-Hadron (solid blue), one neutral R-Hadron (dashed blue), Lightest Supersymmetric Particles (LSPs) (dashed green) and charged hadrons (solid orange). The pixel detector, calorimeters, and muon system are illustrated but not to scale.	109
351			
352			
353			
354			
355			
356			
357	Figure 65	A schematic diagram of an R-Hadron event with a life- time around 4 ns. The diagram includes one charged R-Hadron (solid blue), one neutral R-Hadron (dashed blue), LSPs (dashed green) and a charged hadron (solid orange). The pixel detector, calorimeters, and muon system are illustrated but not to scale.	110
358			
359			
360			
361			
362			
363	Figure 66	A schematic diagram of an R-Hadron event with a life- time around 5 ns. The diagram includes one charged R-Hadron (solid blue), one neutral R-Hadron (dashed blue), LSPs (dashed green) and charged hadrons (solid orange). The pixel detector, calorimeters, and muon system are illustrated but not to scale.	111
364			
365			
366			
367			
368			
369	Figure 67	A schematic diagram of an R-Hadron event with a life- time around 20 ns. The diagram includes one charged R-Hadron (solid blue), one neutral R-Hadron (dashed blue), LSPs (dashed green) and charged hadrons (solid orange). The pixel detector, calorimeters, and muon system are illustrated but not to scale.	111
370			
371			
372			
373			
374			

375	Figure 68	A schematic diagram of an R-Hadron event with a life-time around 20 ns. The diagram includes one charged R-Hadron (solid blue) and one neutral R-Hadron (dashed blue). The pixel detector, calorimeters, and muon system are illustrated but not to scale.	112
376			
377			
378			
379			
380	Figure 69	The distribution of (a) E_T^{miss} and (b) Calorimeter E_T^{miss} for simulated signal events before the trigger requirement.	116
381			
382			
383	Figure 70	The distribution of E_T^{miss} for data and simulated signal events, after the trigger requirement.	118
384			
385	Figure 71	The trigger efficiency for the HLT_xe70 trigger requirement as a function of (a) E_T^{miss} and (b) Calorimeter E_T^{miss} for simulated signal events.	119
386			
387			
388	Figure 72	The dependence of dE/dx on N_{split} in data after basic track hit requirements have been applied.	120
389			
390	Figure 73	The distribution of dE/dx with various selections applied in data and simulated signal events.	120
391			
392	Figure 74	The distribution of track momentum for data and simulated signal events, after previous selection requirements have been applied.	121
393			
394			
395	Figure 75	The distribution of M_T for data and simulated signal events, after previous selection requirements have been applied.	122
396			
397			
398	Figure 76	The distribution of summed tracked momentum within a cone of $\Delta R < 0.25$ around the candidate track for data and simulated signal events, after previous selection requirements have been applied.	123
399			
400			
401			
402	Figure 77	The normalized, two-dimensional distribution of E/p and f_{EM} for simulated (a) $Z \rightarrow ee$, (b) $Z \rightarrow \tau\tau$, (c) 1200 GeV Stable R-Hadron events, and (d) 1200 GeV, 10 ns R-Hadron events.	124
403			
404			
405			
406	Figure 78	Two-dimensional distribution of dE/dx versus charge signed momentum (qp) for minimum-bias tracks. The fitted distributions of the most probable values for pions, kaons and protons are superimposed.	125
407			
408			
409			
410	Figure 79	The distribution of mass estimated using dE/dx for simulated stable R-Hadrons with masses between 1000 and 1600 GeV.	126
411			
412			
413	Figure 80	The acceptance \times efficiency as a function of R-Hadron (a) mass and (b) lifetime. (a) shows all of the combinations of mass and lifetime considered in this search, and (b) highlights the lifetime dependence for 1000 GeV and 1600 GeV R-Hadrons.	128
414			
415			
416			
417			

418	Figure 81	The distribution of (a) dE/dx and (b) momentum for tracks in data and simulated signal after requiring the event level selection and the track selection on p_T , hits, and N_{split} . Each sub-figure shows the normalized distributions for tracks classified as hadrons, electrons, and muons in data and R-Hadrons in the simulated signal.	130
425	Figure 82	The distribution of $M_{dE/dx}$ (a) before and (b) after the ionization requirement for tracks in simulated W boson decays and for the randomly generated background estimate.	132
429	Figure 83	The distribution of $M_{dE/dx}$ (a) before and (b) after the ionization requirement for tracks in the validation region and for the randomly generated background estimate.	133
433	Figure 84	The trigger efficiency for the HLT_xe70 trigger requirement as a function of Calorimeter E_T^{miss} for simulated data events with a W boson selection. Simulated signal events and simulated W boson events are also included.	138
438	Figure 85	The efficiency of the muon veto for R-hadrons of two different masses, as a function of $\frac{1}{\beta}$ for simulated R-Hadron tracks.	140
441	Figure 86	The average reconstructed MDT β distribution for $Z \rightarrow \mu\mu$ events in which one of the muons is reconstructed as a slow muon, for both data and simulation. A gaussian fit is superimposed.	141
445	Figure 87	The observed mass distribution of events in data and the generated background distribution in (a) the stable and (b) the metastable signal region. A few example simulated signal distributions are superimposed.	142
449	Figure 88	The observed and expected cross section limits as a function of mass for the stable simulated signal. The predicted cross section values for the corresponding signals are included.	145
453	Figure 89	The observed and expected cross section limits as a function of mass for each generated lifetime. The predicted cross section values for the corresponding signals are included.	146
457	Figure 90	The excluded range of masses as a function of gluino lifetime. The expected lower limit (LL), with its experimental $\pm 1\sigma$ band, is given with respect to the nominal theoretical cross-section. The observed 95% LL obtained at $\sqrt{s} = 8$ TeV [79] is also shown for comparison.	148

462 **Figure 91** The constraints on the gluino mass as a function of
463 lifetime for a split-supersymmetry model with the gluino
464 R-Hadrons decaying into a gluon or light quarks and
465 a neutralino with mass of 100 GeV. The solid lines in-
466 dicate the observed limits, while the dashed lines in-
467 dicate the expected limits. The area below the curves
468 is excluded. The dots represent results for which the
469 particle is assumed to be prompt or stable. 149

470 LIST OF TABLES

471	Table 1	The particles in the SM and their corresponding super-partners in the Minimal Supersymmetric Model (MSSM).	22
472			
473	Table 2	The design parameters of the LHC beam that determines the energy of collisions and the luminosity, for both the injection of protons and at the nominal circulation.	34
474			
475			
476			
477	Table 3	The performance goals for each of the subsystems of the ATLAS detector. The $ \eta $ coverage specifies the range where the subsystem needs to be able to provide measurements with the specified resolution. The resolutions include a p_T or E dependence that is added in quadrature with a p_T/E independent piece.	39
478			
479			
480			
481			
482			
483	Table 4	A summary of the parameters of each of the three magnet systems on ATLAS	41
484			
485	Table 5	A summary of the parameters of the inner detector and each of the subdetectors [6].	46
486			
487	Table 6	A summary of the expected performance of the combined inner detector [11]. Included are the reconstruction efficiencies for multiple particle types as well as the momentum and impact parameter (IP) resolution for various momenta.	47
488			
489			
490			
491			
492	Table 7	The trigger menu for the 2015 data collection with $L = 5 \times 10^{33} \text{ cm}^{-2} \text{ s}^{-1}$. Both the L1 and high level trigger (HLT) selection requirements and their trigger rates are shown measured at the specified luminosity are shown. The typical offline selections represent a typical set of offline requirements imposed after the trigger in an analysis.	61
493			
494			
495			
496			
497			
498			
499	Table 8	The dominant sources of corrections and systematic uncertainties in the JES estimation technique, including typical values for the correcting shift (Δ) and the associated uncertainty (σ).	101
500			
501			
502			
503	Table 9	The expected number of events at each level of the selection for metastable 1600 GeV, 10 ns R-Hadrons, along with the number of events observed in data, for 3.2 fb^{-1} . The simulated yields are shown with statistical uncertainties only. The total efficiency \times acceptance is also shown for the signal.	127
504			
505			
506			
507			
508			

509	Table 10	A summary of the sources of systematic uncertainty for the data-driven background in the signal region. If the uncertainty depends on the mass, the maximum values are reported.	135
510			
511			
512			
513	Table 11	A summary of the sources of systematic uncertainty for the simulated signal yield. The uncertainty depends on the mass and lifetime, and the maximum negative and positive values are reported in the table.	137
514			
515			
516			
517	Table 12	Example of the contributing systematic variations to the total systematic for the E_T^{miss} Scale, as measured in a 1200 GeV, Stable R-Hadron signal sample.	139
518			
519			
520	Table 13	The estimated number of background events and the number of observed events in data for the specified selection regions prior to the requirement on mass. The background estimates show statistical and systematic uncertainties.	142
521			
522			
523			
524			
525	Table 14	The left and right extremum of the mass window for each generated mass point with a 10 ns lifetime.	143
526			
527	Table 15	The left and right extremum of the mass window used for each generated stable mass point.	143
528			
529	Table 16	The expected number of signal events, the expected number of background events, and the observed number of events in data with their respective statistical errors within the respective mass window for each generated stable mass point	144
530			
531			
532			
533			
534	Table 17	The expected number of signal events, the expected number of background events, and the observed number of events in data with their respective statistical errors within the respective mass window for each generated mass point with a lifetime of 10 ns.	144
535			
536			
537			
538			
539	Table 18	The observed and expected 95% CL lower limit on mass for gluino R-Hadrons for each considered lifetime.	147
540			
541	Table 19	The left and right extremum of the mass window for each generated mass point with a 50 ns lifetime.	159
542			
543	Table 20	The left and right extremum of the mass window for each generated mass point with a 30 ns lifetime.	159
544			
545	Table 21	The left and right extremum of the mass window for each generated mass point with a 10 ns lifetime.	160
546			
547	Table 22	The left and right extremum of the mass window used for each generated mass point with a lifetime of 3 ns.	160
548			
549	Table 23	The left and right extremum of the mass window used for each mass point with a lifetime of 1 ns.	160
550			
551	Table 24	The left and right extremum of the mass window for each generated mass point with a lifetime of 0.4 ns.	161
552			
553	Table 25	The left and right extremum of the mass window used for each generated stable mass point.	161
554			

555	Table 26	The expected number of signal events, the expected number of background events, and the observed number of events in data with their respective statistical errors within the respective mass window for each generated mass point with a lifetime of 50 ns.	161
556			
557			
558			
559			
560	Table 27	The expected number of signal events, the expected number of background events, and the observed number of events in data with their respective statistical errors within the respective mass window for each generated mass point with a lifetime of 30 ns.	162
561			
562			
563			
564			
565	Table 28	The expected number of signal events, the expected number of background events, and the observed number of events in data with their respective statistical errors within the respective mass window for each generated mass point with a lifetime of 10 ns.	162
566			
567			
568			
569			
570	Table 29	The expected number of signal events, the expected number of background events, and the observed number of events in data with their respective statistical errors within the respective mass window for each generated mass point with a lifetime of 3 ns.	163
571			
572			
573			
574			
575	Table 30	The expected number of signal events, the expected number of background events, and the observed number of events in data with their respective statistical errors within the respective mass window for each generated mass point with a lifetime of 1 ns.	163
576			
577			
578			
579			
580	Table 31	The expected number of signal events, the expected number of background events, and the observed number of events in data with their respective statistical errors within the respective mass window for each generated mass point with a lifetime of p4 ns.	164
581			
582			
583			
584			
585	Table 32	The expected number of signal events, the expected number of background events, and the observed number of events in data with their respective statistical errors within the respective mass window for each generated stable mass point	164
586			
587			
588			
589			

591 ACRONYMS

- 592 SM Standard Model
593 CERN European Organization for Nuclear Research
594 SUSY Supersymmetry
595 LSP Lightest Supersymmetric Particle
596 LHC Large Hadron Collider
597 ATLAS A Toroidal LHC ApparatuS
598 CMS Compact Muon Solenoid
599 ALICE A Large Ion Collider Experiment
600 LHCb Large Hadron Collider beauty experiment
601 LEP the Large Electron Positron collider
602 PS Proton Synchrotron
603 PSB Proton Synchrotron Booster
604 SPS Super Proton Synchrotron
605 SCT silicon microstrip
606 TRT Transition Radiation Tracker
607 LAr liquid argon
608 EM electromagnetic
609 RPC Resistive Plate Chamber
610 TGC Thin Gap Chamber
611 MDT Monitored Drift Tube
612 CSC Cathode Strip Chamber
613 ToT time over threshold
614 RoI Region of Interest
615 LCW local cluster weighted
616 MIP minimally ionizing particle
617 IP impact parameter

- 618 EPJC European Physical Journal C
619 JES jet energy scale
620 LLP Long-Lived Particle
621 CR Control Region
622 NLO next-to-leading order
623 NLL next-to-leading logarithmic
624 PDF parton distribution function
625 ISR initial state radiation
626 RMS root mean square
627 IBL Insertible B-Layer
628 CP Combined Performance
629 MDT Monitored Drift Tube
630 RF radiofrequency
631 HLT high level trigger
632 QCD quantum chromodynamics
633 BSM beyond the Standard Model
634 MSSM Minimal Supersymmetric Model

635

PART I

636

INTRODUCTION

637

You can put some informational part preamble text here.

1

638

639 INTRODUCTION

640

PART II

641

THEORETICAL CONTEXT

642

You can put some informational part preamble text here.

2

643

644 STANDARD MODEL

645 The SM of particle physics seeks to explain the symmetries and interactions of
646 fundamental particles. The SM provides predictions in particle physics for in-
647 teractions up to the Planck scale (10^{15} - 10^{19} GeV). It has been tested by several
648 generations of experiments and has been remarkably successful; no significant
649 deviations from its predictions have been found.

650 The theory itself is a quantum field theory grown from an underlying sym-
651 metry, $SU(3) \times SU(2) \times U(1)$, that generates all of the interactions consistent
652 with experimental observations. These interactions are referred to as the Strong,
653 Weak, and Electromagnetic forces. Each postulated symmetry necessitates the
654 existence of an associated conserved charge, which appear as properties of the
655 observed particles in nature.

656 Although this model has been very predictive, the theory is incomplete; for
657 example, it is not able to describe gravity or astronomically observed dark mat-
658 ter. These limitations suggest a need for an extension or new theory to describe
659 physics at higher energies.

660 2.1 ACTION AND THE LAGRANGIAN

Originally, both action and the Lagrangian were constructed for an integral reformulation of the laws of classical mechanics, which is a purely mathematical step: any differential equation can be re-expressed in terms of an integral equation. The Lagrangian, \mathcal{L} , is classically given by the difference of kinetic energy and potential energy. The Lagrangian is defined this way so that the action, \mathcal{S} , given by

$$\mathcal{S}[\mathbf{q}(t)] = \int_{t_1}^{t_2} \mathcal{L}(\mathbf{q}, \dot{\mathbf{q}}, t) dt \quad (1)$$

661 returns the classical equations of motion when one requires it to be stationary
662 in the path, $\mathbf{q}(t)$. This formulation of classical mechanics is extremely useful in
663 calculations, and generalizes beautifully to cover all types of physics.

664 In particular, with the development of quantum mechanics in the twentieth
665 century, the concepts of action and the Lagrangian were found to generalize to
666 more complicated physics for which the classical laws do not hold. Quantum
667 mechanics and quantum field theory can be constructed from the action, using
668 the path integral formulation, by assuming that a particle undergoes all possible
669 paths $\mathbf{q}(t)$ with an imaginary phase given by $e^{i\mathcal{S}[\mathbf{q}(t)]/\hbar}$. This reduces to classical
670 mechanics in the limit as \hbar goes to zero, as all paths for which the action is not
671 stationary interfere with each other so as to cancel their contributions. Because
672 the wavefunction of a particle can be completely determined through the action

673 and the action depends only on the Lagrangian, the Lagrangian itself is sufficient
 674 to describe the physics governing the particle.

675 So, in both classical and quantum mechanics, the Lagrangian of a system con-
 676 tains everything there is to know about the system, apart from initial conditions.
 677 Thus, the most natural way to express that a system has a certain symmetry is to
 678 require that the Lagrangian is invariant under a corresponding symmetry trans-
 679 formation. This makes the Lagrangian the central piece of the discussion of
 680 gauge invariance; the mathematical representation of gauge invariance is that a
 681 gauge transformation on the appropriate components of the Lagrangian returns
 682 an identical Lagrangian. That is,

$$\mathcal{L}(\psi, D^\mu) = \mathcal{L}(U\psi, D'^\mu) \quad (2)$$

683 where ψ is the wavefunction and D^μ is the covariant derivative, both of which
 684 transform under a symmetry operation. There are a number of immediate and
 685 surprisingly powerful consequences of requiring that the Lagrangian is invariant
 686 under a symmetry operation.

687 2.2 GAUGE INVARIANCE AND FORCES

688 The simplest possible relativistic, quantum Lagrangian is the free Dirac Lagrangian,
 689 which describes a relativistic fermion in a vacuum.

$$\mathcal{L} = i\bar{\psi}\not{d}\psi - m\bar{\psi}\psi \quad (3)$$

690 A fermion denotes a particle with spin-1/2, and the kinematic term is chosen to
 691 correctly describe the free propagation of a fermionic particle with mass m . This
 692 equation is clearly invariant under a global $U(1)$ transformation, that is chang-
 693 ing ψ by a complex phase has no effect. The derivative operator commutes with
 694 a constant phase factor, and wherever ψ appears its complex conjugate also ap-
 695 pears so as to cancel out the change of phase. However, the Lagrangian as written
 696 is not invariant under the local $U(1)$ symmetry postulated for the SM, which can
 697 be written as $U = e^{ia(x)}$. The piece of the Lagrangian involving a derivative will
 698 return an extra term that will break the invariance of the Lagrangian under this
 699 transformation:

$$\begin{aligned} \mathcal{L}' &= i(\bar{\psi}U^\dagger)\not{d}(U\psi) - m(\bar{\psi}U^\dagger)(U\psi) \\ &= i(\bar{\psi}U^\dagger)U(\not{d} - \gamma^\mu\partial_\mu\alpha(x))\psi - m(\bar{\psi}U^\dagger)(U\psi) \\ &= i\bar{\psi}\not{d}\psi - m\bar{\psi}\psi - i\gamma^\mu\partial_\mu\alpha(x)\bar{\psi}\psi \\ &= \mathcal{L} - i\gamma^\mu\partial_\mu\alpha(x)\bar{\psi}\psi \\ &\neq \mathcal{L} \end{aligned}$$

700 So, in order to enforce the required symmetry, the typical approach is to con-
 701 struct a covariant derivative, that is to add a term to the derivative operator

so that the unwanted term in \mathcal{L}' is exactly canceled. A generic form for such a derivative is given by

$$D^\mu = \partial^\mu - iqA^\mu$$

where at this point A^μ is an arbitrary field that transforms under the $U(1)$ operator and q is a scaling factor. Adding this component to the above Lagrangian gives

$$\mathcal{L}' = i(\bar{\psi}U^\dagger)U(\not{d} - \gamma^\mu\partial_\mu\alpha(x) - iq\gamma^\mu A'_\mu)\psi - m(\bar{\psi}U^\dagger)(U\psi) \quad (4)$$

$$\mathcal{L}' = \mathcal{L} + \gamma^\mu(-i\partial_\mu\alpha(x) - iqA'_\mu + iqA_\mu)\bar{\psi}\psi \quad (5)$$

and because the transformation of A^μ is unspecified, $\mathcal{L} = \mathcal{L}'$ whenever

$$A'_\mu = A_\mu - \frac{1}{q}\partial_\mu\alpha(x)$$

The above procedure demonstrated that beginning with the Lagrangian for a free fermion and imposing a local $U(1)$ symmetry required the existence of a vector field A^μ , and specified its transformation under the $U(1)$ gauge group. The additional term in the derivative can be expanded to form a completely separate term in the Lagrangian,

$$\mathcal{L} = i\bar{\psi}\not{d}\psi - m\bar{\psi}\psi - (q\bar{\psi}\gamma^\mu\psi)A^\mu \quad (6)$$

and in this form it is clear that the A^μ term has the exact form of the electromagnetic interaction. That is, this is the Lagrangian which reproduces the relativistic form of Maxwell's equations for a particle interacting with an electromagnetic field. It is natural to also introduce a term to the Lagrangian at this point to describe the free propagation of the vector A field, where the propagation of a vector field has the form of

$$-\frac{1}{16\pi}F^{\mu\nu}F_{\mu\nu} \quad \text{with} \quad F_{\mu\nu} = \partial_\mu A_\nu - \partial_\nu A_\mu \quad (7)$$

This then also describes the electromagnetic interactions in a vacuum and the propagation of a photon. The photon is an example of a gauge boson, a spin-0 particle required to exist by a gauge symmetry of the Lagrangian and one that corresponds to a force. In summary, requiring the $U(1)$ symmetry was enough to recover all of electromagnetism and to predict the existence of a photon in the **SM**.

The interaction term that was placed into the Lagrangian by this procedure can be conveniently summarized with Feynman diagrams, which diagrammatically represent a transition from an initial state to a final state. All diagrams that start with the same initial state and end with the same final state must be considered, but more complicated diagrams can be built by linking together the simplest versions. A diagram that corresponds to the above term, $(q\bar{\psi}\gamma^\mu\psi)A^\mu$, is shown in Figure 1, for an interaction with a generic fermion.

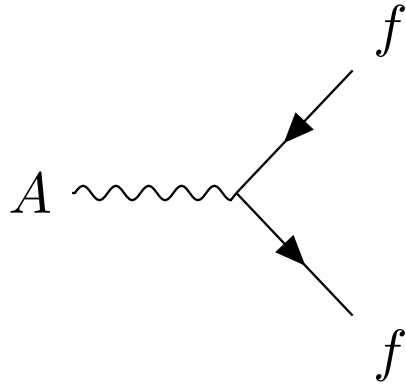


Figure 1: A Feynman diagram representing the interaction of the A field with a generic fermion, f .

732 2.2.1 $SU(2) \times U(1)$ AND THE ELECTROWEAK FORCE

733 The full picture of the electroweak section of the SM is more complicated than the
734 simplified explanation of the electromagnetic piece described above. In practice,
735 it is necessary to consider the entire $SU(2) \times U(1)$ symmetry together, but the
736 procedure is the same. Enforcing the symmetry on the Lagrangian requires the
737 introduction of a covariant derivative, this time with four total distinct terms,
738 one for each of the generators of $SU(2) \times U(1)$. The result is a series of terms
739 in the Lagrangian which describe the interaction of a fermion with four vector
740 fields, the W_1 , W_2 , W_3 , and B fields. These fields can mix in the quantum sense,
741 and linear combinations form the W^+ , W^- , Z , and A fields that are considered
742 actual particles in the SM¹.

743 2.2.2 $SU(3)$ AND THE STRONG FORCE

744 The same procedure can be applied starting with the $SU(3)$ symmetry require-
745 ment, where eight additional fields must be introduced, one for each of the gen-
746 erators of $SU(3)$. The resulting Lagrangian describes quantum chromodynam-
747 ics (QCD) and predicts the existence of eight gauge bosons known collectively as
748 gluons.

749 2.3 NOETHER'S THEOREM, CHARGES, AND MATTER

750 Another direct consequence of the symmetries stipulated in the SM are a series
751 of conserved quantities, Noether charges, named after the mathematician and
752 physicist Emmy Noether. The charges arise as a direct consequence of Noether's
753 theorem, which can be informally stated as

¹ These states are the actual particles because they are mass eigenstates, but the full explanation of this will have to wait for the discussion of the Higgs mechanism.

754 *For every symmetry of the Lagrangian, there exists a corresponding phys-*
 755 *ical quantity whose value is conserved in time.*

756 Or, stated another way, symmetries of the Lagrangian mathematically require
 757 the conservation of specific quantities taken from the Lagrangian. This rela-
 758 tionship can also be thought of as operating in the other direction, the exis-
 759 tence of a conserved charge can be shown to generate the symmetry in the La-
 760 grangian. This theorem is actually quite striking in a somewhat unexpected re-
 761 lation between simple geometric symmetries and physically observable conser-
 762 vation laws. For example, the theorem connects the translation invariance of
 763 the Lagrangian in space to the conservation of momentum and the translation
 764 invariance in time to the conservation of energy.

765 In the context of the SM, the required symmetries of $U(1) \times SU(2) \times SU(3)$
 766 correspond to the charges that are considered properties of all elementary par-
 767 ticles. The most familiar of these properties is the electric charge, Q , which is
 768 one of the conserved quantities of $SU(2) \times U(1)$. The remaining pieces of
 769 $SU(2) \times U(1)$ correspond to weak isospin, T and T_3 , where T has only non-
 770 negative values and T_3 can be positive and negative. The $SU(3)$ symmetry is
 771 generated by the three colors of QCD, red, green, and blue, each with a corre-
 772 sponding opposite color, anti-red, anti-green, and anti-blue.

773 The matter in the observable universe consists of a collection of particles which
 774 carry these charges, in addition to spin and mass. The particles typically thought
 775 of as matter are all fermions: particles with spin-1/2. All of the fermions belong
 776 to one of two groups, quarks and leptons, and one of three generations. Each
 777 of the generations have similar properties but significantly different masses; the
 778 particles in consecutive generations have increasing mass. Quarks are distin-
 779 guished from leptons in that they carry color charge, in addition to electric charge
 780 and weak isospin. The particles in the SM are summarized in Figure 2, and the
 781 matter particles are the twelve types of fermions displayed on the left side of the
 782 graphic.

783 2.3.1 QUARKS

784 The three generations of quarks each have a particle with electric charge +2/3
 785 and one with charge -1/3. They are referred to us up and down, charm and
 786 strange, and top and bottom respectively, and these are referred to as the quark
 787 flavors. Although Figure 2 only shows these six flavors, there is a unique particle
 788 for each combination of the three colors and flavor. And each quark has an anti-
 789 particle with the opposite electric and color charge values.

790 However, individual quarks are never observed in nature, but instead form
 791 color-neutral bound states. One way to form a color neutral combination is a
 792 bound state of three quarks with three different color charges, called a baryon.
 793 Baryons are the most common type of quark configuration in conventional mat-
 794 ter, and include protons and neutrons. The other common configuration is a
 795 bound state of a quark and an anti-quark, called a meson, where the two quarks
 796 have the same type but opposite colors. The conservation of the various charges
 797 carried by quarks, along with the requirement that quarks appear in color-neutral

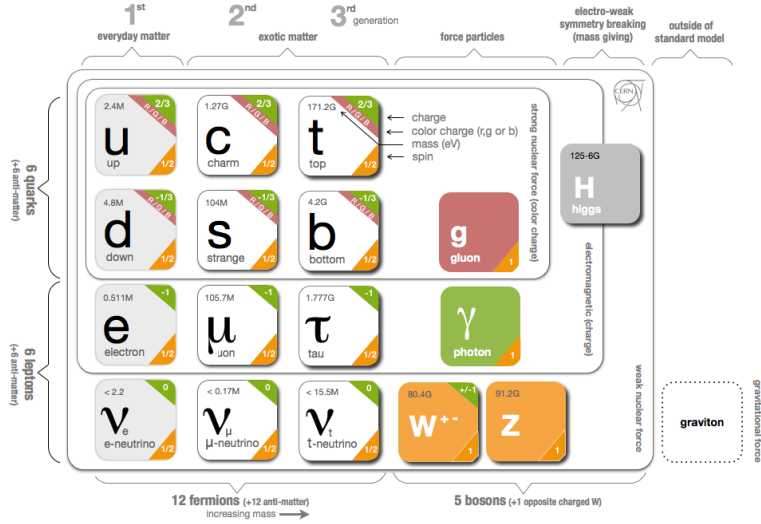


Figure 2: The particle content of the SM.

798 states, result in the observed conservation of baryon number, B , where baryons
 799 have $B = 1$ and mesons have $B = 0$.

800 2.3.2 LEPTONS

801 The remaining fermions, the leptons, do not carry color charge. Each generation
 802 contains an electrically charged lepton, the electron, muon, and tau, and an elec-
 803 trically neutral lepton called a neutrino. For the charged leptons, the flavors are
 804 mass eigenstates, with the masses listed in Figure 2. The flavors of the neutrinos,
 805 on the other hand, are not mass eigenstates: they propagate in mass eigenstates
 806 and so can oscillate between different flavors. The absolute masses of the neu-
 807 trinos are not currently known, but the phenomenon of oscillations shows that
 808 they have three different mass values. Although there is no direct conservation
 809 law resulting from the symmetries of the SM Lagrangian, no interactions have
 810 been observed which alter lepton number, L , the difference in the number of lep-
 811 tons and anti-leptons.

812 2.3.3 CHIRALITY

813 All of the fermions described above have two possible values of the magnitude
 814 of weak isospin, T , either 0 or 1/2. The fermions with $T = 0$ are called right-
 815 handed, while those with $T = 1/2$ are called left-handed. For left-handed fermions,
 816 each of the quark and lepton generations have one particle with $T_3 = -1/2$ and
 817 one with $T_3 = +1/2$. The neutrinos have $T_3 = +1/2$, while the charged leptons
 818 have $T_3 = -1/2$. Similarly, the positively charged quarks have $T_3 = +1/2$ and the
 819 negatively charged quarks have $T_3 = -1/2$. Because the right-handed neutrinos
 820 would have no charge of any type, it is not clear if they exist at all.

821 2.4 HIGGS MECHANISM AND MASS

822 The description of the electroweak forces above left out an important part of the
 823 observed nature of the electroweak force. Many physical experiments observed
 824 phenomena corresponding to the interaction of the weak bosons that were best
 825 explained if they had significant masses. A large mass for the W and Z bosons
 826 would explain the relative weakness of their interactions compared to the elec-
 827 tromagnetic field. The Lagrangian's discussed above did not include a mass term
 828 for the gauge bosons, and in fact such a term would not be allowed by the require-
 829 ment of gauge invariance. This was a significant problem for the SM, and the
 830 symmetry of the electroweak sector would have to be broken in order to allow
 831 for non zero masses for some of the gauge bosons.

832 One mechanism to allow for this spontaneous symmetry breaking is the Higgs
 833 mechanism, which posits the existence of an additional scalar field. It begins
 834 with a $SU(2) \times U(1)$ invariant Lagrangian of the form

$$\mathcal{L} = |D_\mu \phi|^2 - \frac{1}{2}\mu^2\phi^+\phi - \frac{1}{4}\lambda(\phi^+\phi)^2 \quad (8)$$

835 where ϕ is the new scalar field and, importantly, μ^2 is negative. This leads to a
 836 minimum value of the field at a non-zero value of ϕ , specifically where

$$\langle \phi \rangle = \frac{1}{\sqrt{2}} \begin{pmatrix} 0 \\ v \end{pmatrix} \quad \text{with} \quad v = \frac{2\mu^2}{\lambda} \quad (9)$$

837 Expanding the original Lagrangian about its expectation value,

$$\langle \phi \rangle = \frac{1}{\sqrt{2}} \begin{pmatrix} 0 \\ v + H \end{pmatrix} \quad (10)$$

838 gives potential terms in the Lagrangian like

$$\mathcal{L}_H = -\frac{1}{2}m_H^2 H^2 - \sqrt{\frac{\lambda}{2}}m_H H^3 - \frac{1}{4}\lambda H^4 \quad (11)$$

839 where $m_H = \sqrt{2}\mu$. The form of this Lagrangian shows that the non-zero ex-
 840 pectation value of the ϕ field has introduced a massive scalar field H with self
 841 interaction terms. It has an additional important consequence on the description
 842 of the gauge bosons, through the expansion of the term involving the covariant
 843 derivative:

$$|D_\mu \phi|^2 \supset \frac{1}{8} (g^2(W_{1\mu}W_1^\mu + W_{2\mu}W_2^\mu) + (g'B_\mu - gW_3\mu)^2) \quad (12)$$

844 where the W_i and B fields are the original $SU(2) \times U(1)$ gauge fields men-
 845 tioned previously. The above equation can be rearranged using linear combina-
 846 tions of the fields to from mass terms for the gauge bosons, and the mass eigen-
 847 states are exactly the W^\pm , Z , and A fields. Only the A field, corresponding to

848 the photon, results in a zero mass, and the remaining three fields acquire masses.
 849 Because the originally introduced Lagrangian, written in terms of ϕ , was clearly
 850 gauge invariant, this resulting configuration must also be gauge invariant.

851 This is the Higgs mechanism, where the introduction of a gauge invariant
 852 scalar field with a non-zero expectation value can generate masses for the gauge
 853 bosons without violating the underlying symmetries. The particle that is asso-
 854 ciated with the perturbations of this field, H , is called the Higgs boson, and is
 855 said to generate the masses of the remaining bosons. The resulting masses are
 856 listed in Figure 2. Because this mechanism was so successful in describing the
 857 observed properties of the W and Z bosons, it has been considered part of the
 858 SM for decades, although the actual Higgs boson was only recently observed in
 859 2012, confirming the theory.

860 The Higgs mechanism is also responsible for generating the masses of the
 861 fermions. The original mass terms that were listed in the Lagrangian for fermions
 862 are replaced with Yukawa coupling terms, which introduce interactions between
 863 the ϕ field and the fermions. Like with the gauge bosons, the non-zero expec-
 864 tation value of the field yields mass terms, and the expansion about that value
 865 introduces interaction terms between the fermions and the Higgs boson. The
 866 masses are different between each fermion because each has a different Yukawa
 867 coupling, which results in the masses listed in Figure 2.

868 2.5 PHENOMENOLOGY

869 The SM Lagrangian described above contains all of the information necessary
 870 to describe particle physics through the path integral formulation. However, a
 871 tremendous amount of complexity emerges from that description because of the
 872 diverse allowed interactions between the ensemble of particles in the SM. A qual-
 873 itative understanding of the phenomenology produced by those interactions is
 874 immensely helpful in understanding the analysis of particle physics.

875 2.5.1 ELECTROWEAK PHYSICS

876 The masses of the W and Z bosons result in significantly different processes
 877 for the weak fields than the electromagnetic field, despite their interactions be-
 878 ing similar before symmetry breaking. The massless photon is stable, and can
 879 propagate in a vacuum, resulting in the familiar long range interactions of elec-
 880 tromagnetism. The W and Z bosons, however, are unstable, as they have large
 881 enough masses to decay to fermions, such as the decays shown in Figure 3. For
 882 this reason, photons can be observed directly, while the other bosons are suffi-
 883 ciently short-lived that they can only be measured from their decay products.

884 Because the W and Z bosons interact with both quarks and leptons, they are
 885 responsible for the production of leptons in proton-proton collisions. Z bosons
 886 produce pairs of opposite sign, same flavor leptons. W bosons, on the other hand,
 887 produce a single lepton and the corresponding neutrino.

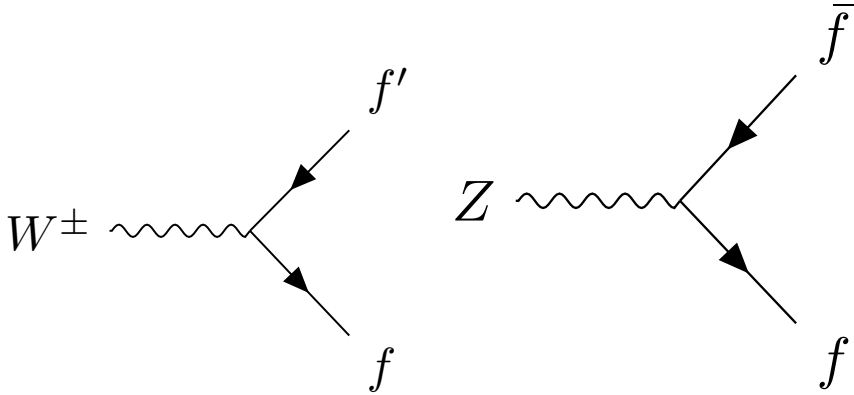


Figure 3: The Feynman diagrams representing the decays of the W and Z bosons to fermions. Here f indicates a generic fermion, \bar{f} its antiparticle, and f' the partner of that fermion in the same generation.

888 2.5.2 STRONG PHYSICS

889 The phenomenology of the strong sector differs significantly from the weak sec-
 890 tor because the gluons are massless but color charged. Because of this, gluons
 891 can interact with each other, and contributions from multiple gluon interactions
 892 lead to a significant growth in the strength of the field at low energies. The depen-
 893 dence of the field strength on the energy scale is described by renormalization,
 894 and in QCD the coupling is only small at high energies. Above around the GeV
 895 scale, the interactions of quarks become perturbative, similar to the electroweak
 896 fields; this phenomenon is known as asymptotic freedom.

897 At lower energies, however, the strength of the strong interaction is so signif-
 898 icant that the interactions of color-charged particles create additional particles
 899 until they form neutral bound-states. This process is known as hadronization,
 900 and explains why no quarks are observed isolated in nature: they all form bound
 901 states of hadrons like protons, neutrons, and pions. The hadronization process
 902 can produce a significant number of particles, so that a single energetic quark
 903 recoiling against another quark can generate a cascade of dozens of hadrons.
 904 Because of the initial boost of such an energetic configuration, the resulting
 905 hadrons are collimated, and conical spray of particles often referred to as a jet.

906 2.5.3 PROTON-PROTON COLLISIONS

907 Proton-proton collisions are a convenient way to generate high energy interac-
 908 tions to probe the SM and to search for new physics. At the energies that will be
 909 discussed in this analysis, the substructure of the protons is very important to the
 910 description of the resulting interactions. At lowest order, protons are composed
 911 of two up quarks and one down quark, but this description is incomplete. The
 912 actual bound state includes a chaotic sea of additional quarks and gluons, each of
 913 which carries a variable fraction of the proton's energy. When a proton-proton

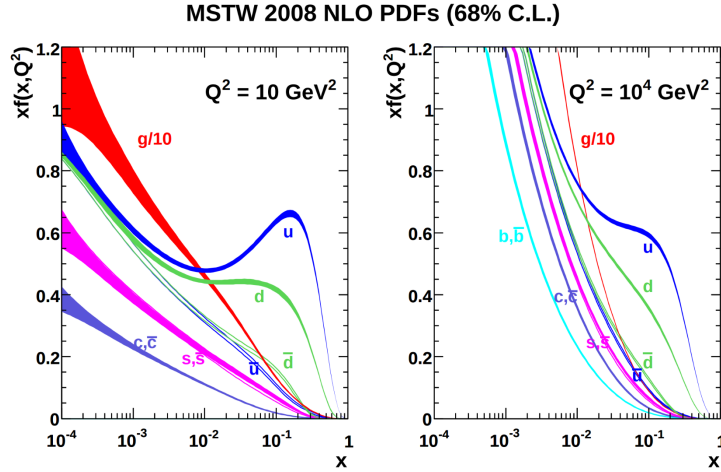


Figure 4: The PDFs for proton-proton collisions at $Q^2 = 10 \text{ GeV}^2$ and $Q^2 = 10^4 \text{ GeV}^2$. Each shows the fraction of particles which carry a fraction x of the total proton energy at the specified scale [1].

914 collision takes place, it is these constituents that interact with each other, resulting
 915 in a highly variable collision energy even when the proton-proton energy is
 916 consistent.

917 The fraction of the energy carried by each constituent varies moment to moment,
 918 but can be modelled probabilistically by PDFs. These are difficult to predict
 919 theoretically, as the QCD calculations are extremely complex, and instead
 920 are measured in hard-scattering experiments. They are usually represented by
 921 how often a given type of particle carries a fraction x of the total proton energy.
 922 Those fraction change significantly with the scale of the interaction; the PDFs of
 923 proton-proton collisions at both $Q^2 = 10 \text{ GeV}^2$ and $Q^2 = 10^4 \text{ GeV}^2$ are shown
 924 in Figure 4.

925 26 LIMITATIONS

926 Despite the great success of the relatively simple SM in describing such a broad
 927 range of emergent phenomena, it is clear that the picture it presents of the interactions
 928 of fundamental particles is incomplete. The SM contains concerning
 929 coincidences that suggest a more ordered underlying substructure that is not ex-
 930 pressed in the current form. It also fails to explain a number of cosmological
 931 measurements of the nature of matter in the universe. These limitations suggest
 932 the need for new, beyond the Standard Model (BSM) physics that would provide
 933 a more complete description at higher energies.

934 2.6.1 THEORETICAL CONCERNS

935 There have been no successful integrations of the SM's description of the elec-
 936 troweak and strong forces with the description of gravity, and it is still unclear
 937 how to account for the effects of gravity at the Plank scale of approximately 10^{19}

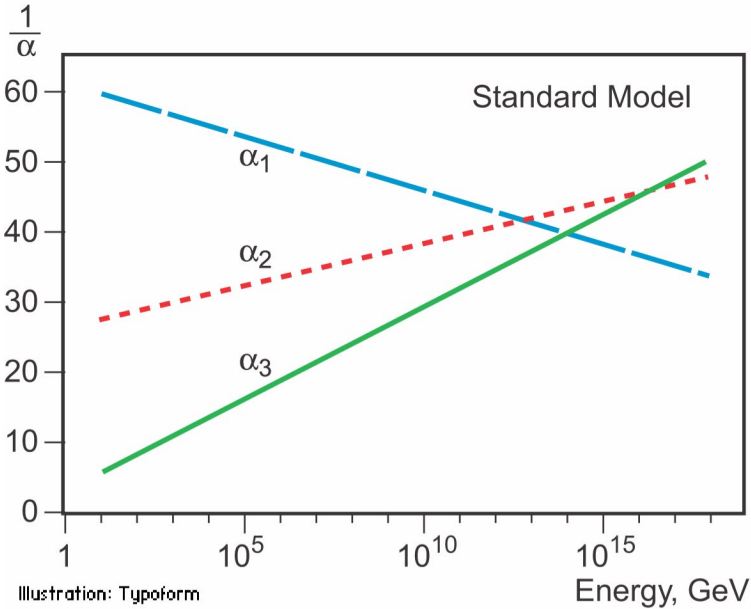


Figure 5: An approximation of the running of the coupling constants in the SM up to the Planck scale [unification_plot].

938 GeV, where it can no longer be ignored. The Plank scale is an important cutoff
 939 for the SM, as it is clear that the SM must break down somewhere between the
 940 current highest energy tests of the SM, around 1 TeV, and the Plank scale.

941 One example of this is the Higgs mass, which is determined in the SM by a
 942 sum of its bare mass and the interactions in the vacuum with all massive parti-
 943 cles. As their must be new physics at the Plank scale to describe gravity, some
 944 of those corrections would include contributions at a scale seventeen orders of
 945 magnitude above the mass of the Higgs. Either the bare mass of the Higgs boson
 946 precisely cancels those contributions to leave a remainder seventeen orders of
 947 magnitudes smaller, or a new theory exists at a lower scale the shields the Higgs
 948 mass from those terms. A theory where such a unlikely cancellation of free pa-
 949 rameters occurs is called fine-tuned, and one that is free from such cancellations
 950 is called natural. Theories where the mass of the Higgs is natural are usually
 951 preferred, as the suggest an underlying coherent structure.

952 There is also a compelling argument that the $SU(3) \times SU(2) \times U(1)$ gauge
 953 structure of the SM might originate from a single, unified gauge theory. For ex-
 954 ample, it is possible to represent that gauge structure as a $SU(5)$ gauge group
 955 with only a few inconsistencies with the current implementation. This unifica-
 956 tion is suggested by the scaling of the coupling constants for each of the forces
 957 under renormalization, they come close to converging to a single value at higher
 958 energies, as seen in Figure 5. An additional correction to the scaling of the cou-
 959 pling constants from new physics above the TeV scale could cause them to merge
 960 into a single value at high energies.

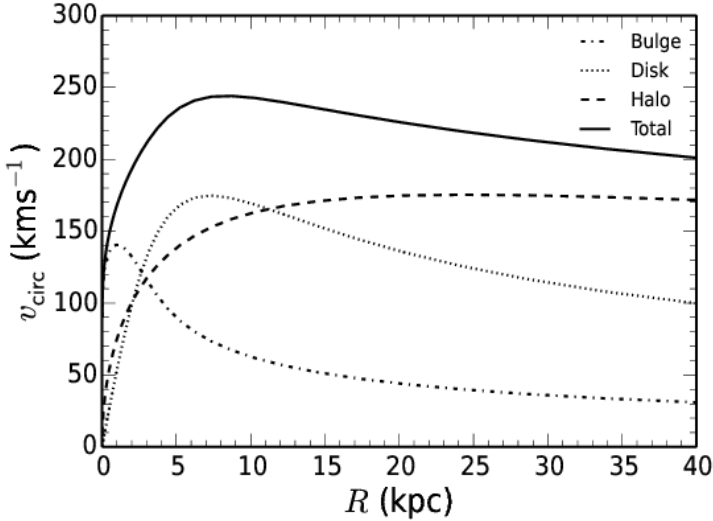


Figure 6: The distribution of velocities of stars as a function of the radius from the center of the galaxy. The contributions to the velocity from the various components of matter in the galaxy are shown [2].

961 2.6.2 COSMOLOGICAL OBSERVATIONS

962 The SM contains a symmetry in the description of matter and antimatter that is
 963 not reflected in cosmological observations. The process of the standard model
 964 create or remove matter and antimatter in equal amounts, so a universe that be-
 965 gins with an equal quantity of each should result in a universe with an approxi-
 966 mate balance of matter and antimatter. However, cosmological observations of
 967 the relative amount of each type clearly show that the directly observable mass
 968 of the universe is overwhelmingly made of matter. As this difference is largely
 969 a difference in the generation of baryons and anti-baryons, this discrepancy is
 970 often referred to as the baryogenesis problem.

971 A number of astrophysical observations of large scale gravitational interac-
 972 tions suggest the presence of a significant amount of non-luminous matter that
 973 interacts with the normal matter only gravitationally. The first evidence of this
 974 came from the observation of galactic rotation curves, the velocities of stars as
 975 a function of the radius from the center of a galaxy. These can be directly pre-
 976 dicted from the amount of matter contained within the sphere up to the radius
 977 of the star. An estimate based only on the luminous matter in the galaxies would
 978 predict a dependence that falls off with the radius, but the observed curves show
 979 a mostly constant distribution of velocities [2], as seen in Figure 6. The higher
 980 velocities than predicted by the luminous matter can be explained by a halo of
 981 dark matter that extends significantly outside the galactic disk.

982 This dark matter accounts for a majority of the matter in the universe, and is
 983 incompatible with the matter particles predicted by the SM. Many observations
 984 support its existence, but there have been no direct detections of a particle which
 985 could account for the large quantity of gravitationally interacting dark matter.
 986 The SM would have to require a significant extension to include the particles

987 needed to explain dark matter and the processes needed to explain the observed
988 matter-antimatter asymmetry.

990 SUPERSYMMETRY

991 The theory of Supersymmetry ([SUSY](#)) presents an extension to the [SM](#) that solves
992 a number of the outstanding issues. It is based on another proposed symmetry,
993 one which introduces an equality between the fermionic particles and proposed
994 bosonic partners. The symmetry is defined by extended spacetime into a super-
995 space, which includes on dimension that describes a particle's spin: a transfor-
996 mation in this spacetime moves a fermion with spin-1/2 to a boson with spin-0 or
997 vice-versa. Requiring the [SM](#) to be symmetrical under these transformations re-
998 quires the existence of a bosonic partner for every current matter fermion in the
999 [SM](#) and a fermionic partner for every boson. The partners are called sparticles,
1000 where quarks partner with squarks and leptons partner with sleptons, and each
1001 boson has a fermionic partner called a gaugino, such as the wino for the W boson.
1002 The superpartners, in the original form of the theory, should be identical to the
1003 original particle in every way except for spin; that is they would have the same
1004 quantum charges and the same mass.

1005 However, the simplest version of the theory, where the symmetry is unbroken,
1006 is incompatible with current observations of physics in a number of systems. For
1007 example, the existence of an electron with spin-0 would introduce a stable, elec-
1008 trically charged constituent of atoms that would not follow the Pauli exclusion
1009 principle and would thus significantly change atomic structure. Various high en-
1010 ergy physics measurements have also confirmed the spin of the W and Z bosons,
1011 for example, and a fermionic gaugino has never been produced at those masses.
1012 The solution to this incompatibility with observation is to conjecture that the
1013 symmetry exists but is broken, where the masses of the supersymmetric parti-
1014 cles are significantly larger than those of the current [SM](#) particles.

1015 3.1 STRUCTURE AND THE MSSM

1016 There are a number of ways to model [SUSY](#), but many of the resulting phenomena
1017 are similar, and a discussion of an example is sufficient to describe the structure
1018 and results of the theory. The [MSSM](#) is one example of a complete description
1019 that includes the necessary symmetry breaking to result in the different masses
1020 between particles and sparticles. It is called minimal because it is designed to
1021 use the simplest possible extension to the [SM](#) that incorporates [SUSY](#) and remains
1022 self-consistent. The theory includes a sparticle partner for every standard model
1023 particle, which are listed in Table 1.

1024 To then provide the different masses for those sparticles, the [MSSM](#) then intro-
1025 duces a second Higgs interaction. The resulting scalar field, along with the origi-
1026 nal Higgs field, generates five total particles, h^0 , the original Higgs boson, A^0 , H^0 ,
1027 and H^\pm , where the last two are electrically charged. These Higgs bosons can mix
1028 with the supersymmetric gauginos to form a series of mass eigenstates. These

Sector	Particles	Sparticles
Baryonic Matter	(u, d)	(\tilde{u}, \tilde{d})
	(c, s)	(\tilde{c}, \tilde{s})
	(t, b)	(\tilde{t}, \tilde{b})
Leptonic Matter	(ν_e, e)	$(\tilde{\nu}_e, \tilde{e})$
	(ν_μ, μ)	$(\tilde{\nu}_\mu, \tilde{\mu})$
	(ν_τ, τ)	$(\tilde{\nu}_\tau, \tilde{\tau})$
Higgs	(H_u^+, H_u^0)	$(\tilde{H}_u^+, \tilde{H}_u^0)$
	(H_d^0, H_d^-)	$(\tilde{H}_d^0, \tilde{H}_d^-)$
Strong	g	\tilde{g}
Electroweak	(W^\pm, W^0)	$(\tilde{W}^\pm, \tilde{W}^0)$
	B^0	\tilde{B}^0

Table 1: The particles in the **SM** and their corresponding superpartners in the **MSSM**.

1029 are usually referred to by the order of their masses, where the neutral gauginos
 1030 (neutralinos) are labelled $\tilde{\chi}_1^0, \tilde{\chi}_2^0, \tilde{\chi}_3^0$, and $\tilde{\chi}_4^0$. The charged gauginos (charginos)
 1031 are similarly labelled $\tilde{\chi}_1^\pm$ and $\tilde{\chi}_2^\pm$.

1032 In addition to the new particle content, the **MSSM** introduces new interactions
 1033 for the gauge bosons and gauginos. All interaction terms are added to the La-
 1034 grangian which describe the interaction of a gauge boson or gaugino with a par-
 1035 ticle or sparticle with the appropriate charge. Such terms include a few interac-
 1036 tions which would violate the observed $B - L$ symmetry that prevents proton
 1037 decay. Either the couplings on these terms must be fine-tuned to match the ex-
 1038 perimental limits on those decays, or an additional symmetry must be imposed
 1039 to exclude the terms. The **MSSM** and several other **SUSY** models choose to intro-
 1040 duce a new symmetry known as R-parity. Sparticles are R-parity odd while **SM**
 1041 particles are R-parity even. And by requiring that each term in the supersymmet-
 1042 ric Lagrangian conserves R-parity, it is enforced that sparticles are produced in
 1043 pairs.

1044 The conservation of R-parity removes the $B - L$ violating terms naturally
 1045 from the Lagrangian. The remaining terms include all of the interactions of the
 1046 **SM** where two of the particles are replaced with their **SUSY** partners, so that R-
 1047 parity is conserved in the interactions. This also has an important significance in
 1048 making the **LSP**, the $\tilde{\chi}_1^0$, stable, as it cannot decay to only **SM** particles without vi-
 1049 olating the conservation of R-parity. The heavier sparticles then decay in chains,
 1050 emitting an **SM** particle in each step, and leaving behind the **LSP** at the end of the
 1051 chain.

1052 3.2 MOTIVATION

4

1053

1054 LONG-LIVED PARTICLES

1055 4.1 MECHANISMS

1056 4.1.1 EXAMPLES IN SUPERSYMMETRY

1057 4.2 PHENOMENOLOGY

1058 4.2.1 DISIMILARITIES TO PROMPT DECAYS

1059 4.2.2 CHARACTERISTIC SIGNATURES

1060

PART III

1061

EXPERIMENTAL STRUCTURE AND RECONSTRUCTION

1062

You can put some informational part preamble text here.

1063

1064 THE LARGE HADRON COLLIDER

1065 The [LHC](#), a two-ring superconducting hadron accelerator, provides high energy
 1066 proton-proton collisions for several large experiments at European Organization
 1067 for Nuclear Research ([CERN](#)) in Geneva, Switzerland [3, 4]. It is the largest,
 1068 highest-luminosity, and highest-energy proton collider ever built, and was con-
 1069 structed by a collaboration of more than 10,000 scientists from the more than
 1070 100 countries that contribute to [CERN](#). The original design of the [LHC](#) focused on
 1071 providing collision energies of up to 14 TeV and generating enough collisions to
 1072 reveal physics beyond the [SM](#) which is predicted to exist at higher energy scales.

1073 The [LHC](#) was installed in an existing 27 km tunnel at [CERN](#) which was orig-
 1074 inally designed to house the Large Electron Positron collider ([LEP](#)) [5]. This al-
 1075 lows the collider to use existing accelerators at the same complex to provide the
 1076 initial acceleration of protons up to 450 GeV before injecting into [LHC](#). The in-
 1077 jected hadrons are accelerated up to as much as 14 TeV while being focused into
 1078 two beams traveling in opposite directions. During this process the protons cir-
 1079 culate around the tunnel millions of times, while the beams are intermittently
 1080 crossed at the four locations of the experiments to provide collisions. These col-
 1081 lision points correspond to the four major [LHC](#) experiments: [ATLAS](#), Compact
 1082 Muon Solenoid ([CMS](#)), Large Hadron Collider beauty experiment ([LHCb](#)), and
 1083 A Large Ion Collider Experiment ([ALICE](#)), and Figure 7 shows the layout of the
 1084 experiments both on the surface and below. [ATLAS](#) and [CMS](#) are both general pur-
 1085 pose, high-luminosity detectors which search for a wide range of new types of
 1086 physics [6, 7]. [LHCb](#) studies the interactions of b-hadrons to explore the asymme-
 1087 try between matter and antimatter [8]. [ALICE](#) focuses on the collisions of lead
 1088 ions, which the [LHC](#) also provides, in order to study the properties of quark-
 1089 gluon plasma [9].

1090 During the first five years of continued operation, after the [LHC](#) turned on in
 1091 2010, the [LHC](#) has provided four major data collecting periods. In 2010 the [LHC](#)
 1092 generated collisions at several energies, starting at 900 GeV. It increased the
 1093 energy from 900 GeV to 2.76 TeV and then subsequently to 7 TeV, with a peak
 1094 luminosity of $2 \times 10^{32} \text{ cm}^{-2}\text{s}^{-1}$, and a total delivered luminosity of 50 pb^{-1} .
 1095 The next run, during 2011, continued the operation at 7 TeV and provided an
 1096 additional 5 fb^{-1} with a peak luminosity of $4 \times 10^{33} \text{ cm}^{-2}\text{s}^{-1}$. The energy was
 1097 then increased to 8 TeV for the data collection during 2012, which provided 23 fb^{-1}
 1098 with a peak luminosity of $7.7 \times 10^{33} \text{ cm}^{-2}\text{s}^{-1}$. After the first long shutdown
 1099 for 2013 and 2014, the [LHC](#) resumed operation and increased the energy to 13
 1100 TeV in 2015, where it delivered 4.2 fb^{-1} with a peak luminosity of $5.5 \times 10^{33} \text{ cm}^{-2}\text{s}^{-1}$.
 1101 The [LHC](#) is currently providing additional 13 TeV collisions in 2016
 1102 with higher luminosities than during any previous data collection periods. These
 1103 running periods are summarized in Figure 8, which shows the total delivered

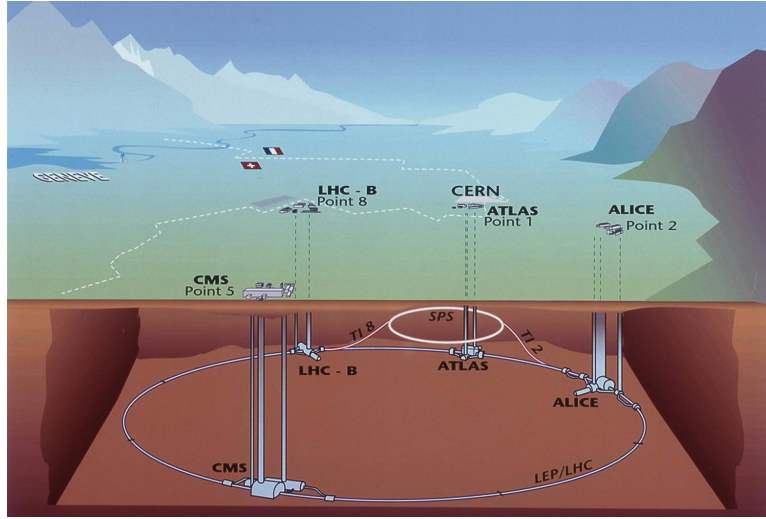


Figure 7: The four collision points and corresponding experiments of the [LHC](#). The image includes the location of the nearby city of Geneva as well as the border of France and Switzerland.

1104 luminosity over time for the [ATLAS](#) experiment during each of the four years of
1105 data collection since 2011.

1106 5.1 INJECTION CHAIN

1107 The [LHC](#) takes advantage of the presence of previously built accelerators at [CERN](#)
1108 to work up to the target energy in consecutive stages. The series of accelerators
1109 that feed into the [LHC](#) are known collectively as the injection chain, and together
1110 with the [LHC](#) form the accelerator complex. The full complex is illustrated in
1111 Figure 9, which details the complex series required to reach collisions of 13 or
1112 14 TeV.

1113 Protons at the [LHC](#) begin as hydrogen atoms in the Linac 2, a linear accelerator
1114 which replaced Linac 1 as the primary proton accelerator at CERN in 1978. In
1115 Linac 2, the hydrogen atoms are stripped of their electrons by a strong magnetic
1116 field, and the resulting protons are accelerated up to 50 MeV by cylindrical con-
1117 ductors charged by radio frequency cavities. The protons are then transferred
1118 to the Proton Synchrotron Booster ([PSB](#)), which uses a stack of four synchrotron
1119 rings to accelerate the protons up to 1.4 GeV. Then the protons are injected
1120 into the Proton Synchrotron ([PS](#)) which again uses synchrotron rings to bring
1121 the energy up to 25 GeV. The intermediate step between Linac 2 and the [PS](#) is
1122 not directly necessary, as the [PS](#) can accelerate protons starting from as low as
1123 50 MeV. The inclusion of the [PSB](#) allows the [PS](#) to accept a higher intensity of
1124 injection and so increases the deliverable luminosity in the [LHC](#). The penulti-
1125 mate stage of acceleration is provided by the Super Proton Synchrotron ([SPS](#)), a
1126 large synchrotron with a 7 km circumference that was commissioned at CERN
1127 in 1976. During this step the protons increase in energy to 450 GeV, after which
1128 they can be directly injected into the [LHC](#).

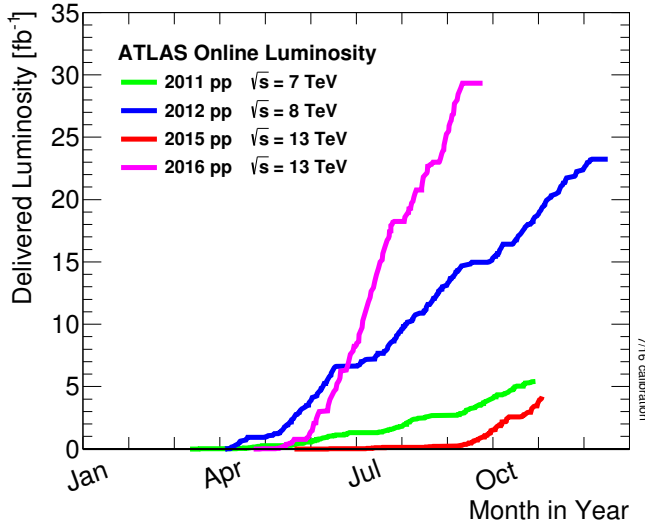


Figure 8: The cumulative luminosity over time delivered to the [ATLAS](#) experiment from high energy proton-proton collisions since 2011. The energies of the collisions are listed for each of the data-taking periods.

1129 The final step is the [LHC](#) itself, which receives protons from the [SPS](#) into two
 1130 separate beam pipes which circulate in opposite directions. The filling process
 1131 at this steps takes approximately 4 minutes, and the subsequent acceleration to
 1132 the final energy (6.5 TeV during 2015 and up to 7 TeV by design) takes approxi-
 1133 mately half an hour. At this point the protons circulate around the circumference
 1134 tens of thousands of times a second and continue for up to two hours.

1135 5.2 DESIGN

1136 5.2.1 LAYOUT

1137 Many of the aspects of the [LHC](#) design are driven by the use of the existing [LEP](#)
 1138 tunnel. This tunnel slopes gradually, with a 1.4% decline, with 90% of its length
 1139 built into molasse rock which is particularly well suited to the application. The
 1140 circumference is composed of eight 2987 meter arcs and eight 528 meter straight
 1141 sections which connect them; this configuration is illustrated in Figure 10. The
 1142 tunnel diameter is 3.7 m throughout its length.

The design energy is directly limited by the size of this tunnel, with its radius of curvature of 2804 m. A significant magnetic field is required to curve the protons around that radius of curvature; the relationship is given by

$$p \simeq 0.3BR \quad (13)$$

1143 where p is the momentum of the particle in GeV, B is the magnetic field in Tesla,
 1144 and R is the radius of curvature in meters. From the target design energy of
 1145 14 TeV, or 7 TeV of momentum for protons in each beam, the required mag-
 1146 netic field is 8.33 Tesla. This is too large a field strength to be practical with
 1147 iron electromagnets, because of the enormous power required and the resulting

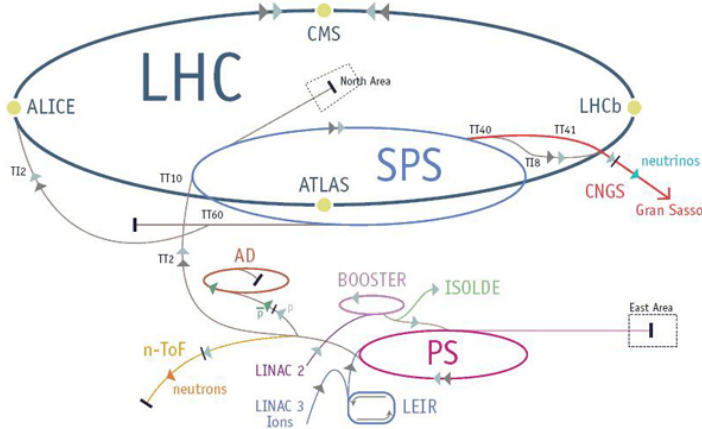


Figure 9: The accelerator complex that builds up to the full design energies at the LHC. The protons are passed in order to Linac 2, the PSB, the PS, the SPS and then the LHC.

1148 requirements for cooling. Because of these constraints, the LHC uses superconducting
 1149 magnets which can maintain that field strength with significantly less
 1150 power consumption.

1151 5.2.2 MAGNETS

1152 The magnets chosen were Niobium and Titanium (NbTi) which allow for field
 1153 strengths as high as 10 Tesla when cooled down to 1.9 K. Reaching the target
 1154 temperature of 1.9 K for all of the magnets requires superfluid helium and a large
 1155 cryogenic system along the entire length of the tunnel. During normal operation,
 1156 the LHC uses 120 tonnes of helium within the magnets, and the entire system is
 1157 cooled by eight cryogenic helium refrigerators. The temperature increase that
 1158 occurs during transit from the refrigerator along the beam necessitates that the
 1159 refrigerators cool the helium down to 1.8 K. Any significant increase above this
 1160 temperature range can remove the superconductive properties of the magnets,
 1161 which in turn generates drastically larger heat losses from the current within the
 1162 magnets and causes a rapid rise in temperature called a quench.

1163 There are approximately 8000 superconducting magnets distributed around
 1164 the LHC. The 1232 bending magnets, which keep the protons curving along the
 1165 length of the beam, are twin bore cryodipoles, which allow both proton beams
 1166 to be accommodated by one magnet and all of the associated cooling structure.
 1167 Figure 11 shows the cross section of the design for these dipoles. The magnets
 1168 are very large, 16.5 m long with a diameter of 0.57 meters and a total weight of 28
 1169 tonnes. They are slightly curved, with an angle of 5.1 mrad, in order to carefully
 1170 match the beam path. The twin bore accommodates both magnets inside the
 1171 two 5 cm diameter holes which are surrounded by the superconducting coils.
 1172 The coils require 12 kA of current in order to produce the required magnetic
 1173 field. These coils are comprised of NbTi cable wound in two layers; the wire in

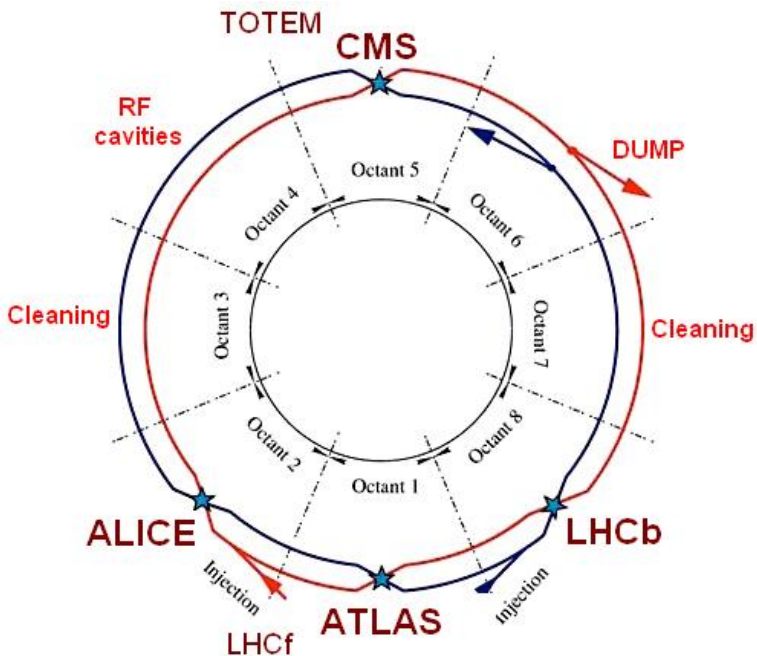


Figure 10: A schematic of the layout of the LHC, not to scale. The arched and straight sections are illustrated at the bottom of the schematic, and all four crossing sites are indicated with their respective experiments.

the inner layer has a diameter of 1.065 mm while the wire in the outer layer has a diameter of 0.825 mm.

The large currents in the wires, along with the magnetic field produced, result in forces on the magnets which would tend to push them apart with over 10,000 Newtons per meter. Constraining the magnets requires a significant amount of structure including non-magnetic stainless steel collars. Both the presence of these electromagnetic forces and the varying thermal contraction coefficient of the pieces of the magnet produce significant forces on the cold mass structure. The cold mass is carefully engineered to so that these stresses do not significantly alter the magnetic field shape, which must be maintained between magnets to a precision of approximately 10^{-4} for successful operation.

The remaining 6800 magnets are a variety of quadrupole, sextapole, octopole, and single bore dipole magnets. These are used to damp oscillations, correct beam trajectories, focus the beams during circulation, and to squeeze the beams before collisions.

5.2.3 RF CAVITIES

Sixteen RF cavities produce the actual acceleration of the proton beam up to the design energy. These RF cavities are tuned to operate at 400 MHz, and are powered by high-powered electron beams modulated at the same frequency, called klystrons. The resonance within the cavity with the oscillating electric field establishes a voltage differential of 2 MV per cavity. The sixteen cavities are split between the two beams, so combined the cavities provide 16 MV per beam,

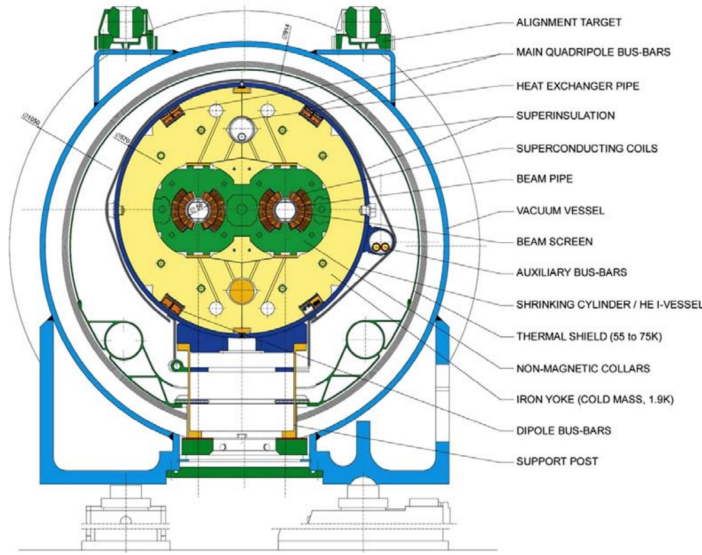


Figure 11: A cross section of the cryodipole magnets which bend the flight path of protons around the circumference of the LHC. The diagram includes both the superconducting coils which produce the magnetic field and the structural elements which keep the magnets precisely aligned.

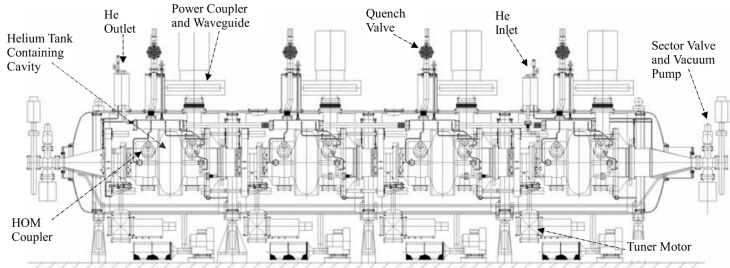


Figure 12: The arrangement of four RF cavities within a cryomodule.

1196 which accelerate the protons on each consecutive pass through the cavity. This
 1197 acceleration is also necessary during circulation even after the target energy has
 1198 been reached in order to compensate for losses from synchrotron radiation.

1199 The cavities are arranged in cryomodules which contain four cavities, with
 1200 two cryomodules per beam; this arrangement is illustrated in Figure 12. These
 1201 cryomodules are necessary to maintain the superconducting state of the cavities,
 1202 which are also constructed from niobium. The RF cavities use niobium along
 1203 with copper to allow for low power losses in the superconductors. The copper
 1204 provides a reduced susceptibility to quenching, as it rapidly conducts away heat
 1205 generated by imperfections in the niobium, as well as natural shielding from the
 1206 earth's magnetic field which can interfere with the RF system.

1207 The nature of the radio frequency oscillations tends to group protons together
 1208 into buckets. A proton traveling exactly in phase with the RF oscillations will not
 1209 be displaced at all during a single circulation, and those slightly ahead or behind
 1210 of that phase will slightly decelerate or accelerate, respectively. This produces

1211 separate clusters of protons which arrive in phase to the cavities every 2.5 ns,
 1212 corresponding to the 400 MHz frequency.

1213 5.2.4 BEAM

1214 The beams of protons circulate within 54 km of 5 cm diameter beam pipe. This
 1215 entire structure is kept under vacuum at 1.9 K to prevent interactions between
 1216 the beam pipe and the magnets as well as to prevent any interactions between the
 1217 circulating protons and gas in the pipe. The vacuum within the pipe establishes
 1218 a pressure as low as 10^{-9} mbar before the protons are introduced.

1219 Because of the very high energies of the circulating protons, synchrotron ra-
 1220 diation is not negligible in the bending regions. The protons are expected to
 1221 radiate 3.9 kW per beam at 14 TeV, with 0.22 W/m, which is enough power to
 1222 heat the liquid helium and cause a quench were it absorbed by the magnets. To
 1223 prevent this, a copper screen is placed within the vacuum tube that absorb the
 1224 emitted photons. This screen is kept between 5 and 20 K by the liquid helium
 1225 cooling system.

1226 5.3 LUMINOSITY PARAMETERS

In addition to the high energy of the collisions, the rate of collisions is extremely important to enabling the discovery of new physics. Many measurements and searches require a large number of events in order to be able to make statistically significant conclusions. The rate of collisions is measured using luminosity, the number of collisions per unit time and unit cross section for the proton-proton collisions. From the beam parameters, luminosity is given by

$$\mathcal{L} = \frac{N_b^2 n_b f_{rev} \gamma}{4\pi\epsilon_n \beta^*} F \quad (14)$$

1227 where N_b is the number of protons per bunch, n_b is the number of bunches per
 1228 beam, f_{rev} is the frequency of revolution, γ is the Lorentz factor for the protons
 1229 at the circulating energy, ϵ_n is the emittance, β^* is the amplitude function at the
 1230 collision point, and F is a geometric factor that accounts for the crossing angle of
 1231 the beams at the collision point. The emittance measures the average spread of
 1232 particles in both position and momentum space, while the amplitude function
 1233 is a beam parameter which measures how much the beam has been squeezed.
 1234 Together ϵ_n and β^* give the size of the beam in the transverse direction, $\sigma = \sqrt{\epsilon\beta^*}$. β
 1235 changes over the length of the beam as the accessory magnets shape the
 1236 distribution of protons, but only the value at the point of collisions, β^* , affects
 1237 the luminosity.

1238 The luminosity is maximized to the extent possible by tuning the parameters
 1239 in Equation 14. A number of these are constrained by the design decisions. The
 1240 revolution frequency is determined entirely by the length of the tunnel, as the
 1241 protons travel at very close to the speed of light. The geometric factor F is de-
 1242 termined by the crossing angle of the beams at the collision points, again a com-

Parameter	Unit	Injection	Nominal
Beam Energy	TeV	0.450	7
Peak Instantaneous Luminosity	$\text{cm}^{-2}\text{s}^{-1}$	-	10^{34}
Bunch Spacing	ns	25	25
Number of Filled Bunches	-	2808	2808
Normalized Transverse Emittance	μm	3.75	3.75
Frequency	MHz	400.789	400.790
RF Voltage/Beam	MV	8	16
Stored Energy	MJ	-	362
Magnetic Field	T	0.54	8.33
Operating Temperature	K	1.9	1.9

Table 2: The design parameters of the [LHC](#) beam that determines the energy of collisions and the luminosity, for both the injection of protons and at the nominal circulation.

ponent of the tunnel design; this angle is already very small at $285 \mu\text{rad}$, which helps to maximize the geometric factor.

The major pieces that can be adjusted are the number of protons per bunch, N_b , the number of bunches in the beam, n_b , and the amplitude function β . Increasing either N_b or n_b increases the amount of energy stored in the beam, which presents a danger if control of the beam is lost. At design specifications, the beam stores 362 MJ, which is enough energy to damage the detectors or accelerator if the beam were to wander out of the beam pipe. So, the luminosity is primarily controlled at the [LHC](#) by adjusting β^* , where lowering β^* increases the luminosity. β^* is tuned to provide the various values of luminosity used at the [LHC](#) which can be raised to as much as 10^{34} .

The nominal bunch structure consists of 3654 bunches, each holding 10^{11} protons, which cross a collision point in 25 ns. These are further subdivided into the buckets mentioned in Section 5.2.3 by the clustering properties of the RF cavities. The bunches are further grouped into trains of 72 bunches which are separated by a gap which would otherwise hold 12 bunches. At nominal operation 2808 of the bunches will actually be filled with protons, while the remainder are left empty to form an abort gap that can be used in case the beam needs to be dumped.

The various beam parameters are summarized in Table 2 for the designed operation. In practice, the beam has operated at lower energies and lower luminosities than the design values for the majority of its lifetime, but the [LHC](#) has begun to operate at full design values during Run 2.

5.4 DELIVERED LUMINOSITY

During the data collection of 2015, the [LHC](#) operated at luminosities as large as $5 \times 10^{33} \text{ cm}^{-2}\text{s}^{-1}$. It is convenient to refer to the integrated luminosity, the inte-

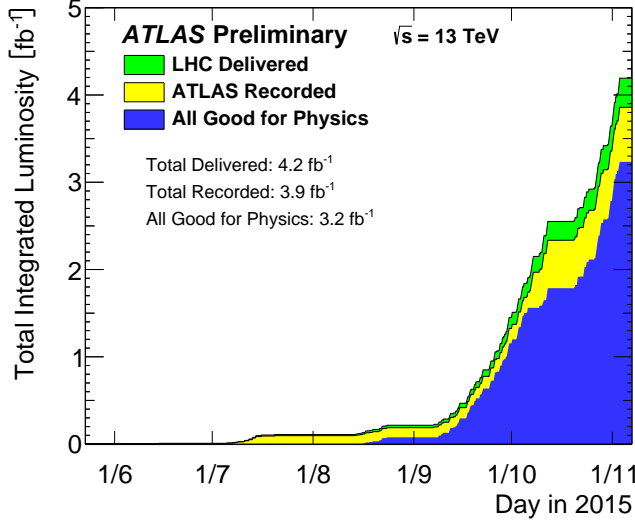


Figure 13: The cumulative luminosity versus time delivered to ATLAS (green), recorded by ATLAS (yellow), and certified to be good quality data (blue) during stable beams for pp collisions at 13 TeV in 2015.

gral of the instantaneous luminosity, which corresponds directly to the number of delivered events for a given process.

$$N = \sigma \times \int \mathcal{L}(t) dt$$

where σ is the cross section for the process of interest. The integrated luminosity over time is shown in Figure 13. This includes the luminosity delivered by the LHC as well as the luminosity that was recorded by ATLAS. ATLAS only records collisions when the LHC reports that the beam conditions are stable, so some of the delivered luminosity is not recorded. The figure also includes the amount of luminosity marked as good for physics, which includes additional requirements on the operation of the detector during data collection that are necessary for precise measurements.

Because the beam circulates and collides bunches of protons, it is possible for a single crossing to produce multiple proton-proton collisions. As the instantaneous luminosity is increased, the average number of collisions generated per bunch crossing increases. An event refers to the entire collection of interactions during a single bunch crossing, while interactions refer to the individual proton-proton collisions. The additional interactions produced during each bunch crossing are referred to as pileup, which can be more precisely defined quantified using the average number of additional proton-proton interactions per crossing, often denoted μ . Figure 14 shows the luminosity-weighted distribution of the mean number of interactions for events collected in 2015. The presence of as many as twenty interactions in a single collision provides a significant challenge in reconstructing events and isolating the targeted physical processes.

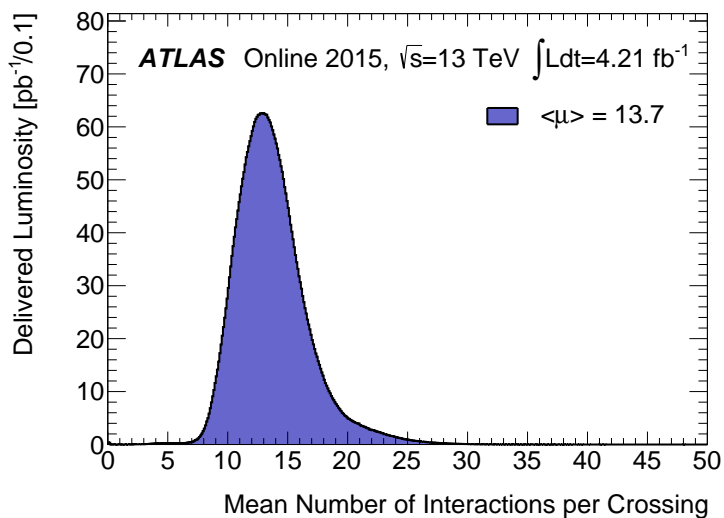


Figure 14: The luminosity-weighted distribution of the mean number of interactions per crossing for the 2015 pp collision data at 13 TeV.

1287

1288 THE ATLAS DETECTOR

1289 The four major LHC experiments at CERN seek to use the never before matched
1290 energies and luminosities of the new collider to explore the boundaries of par-
1291 ticle physics and to gain insight into the fundamental forces of nature. Two of
1292 these experiments, ATLAS and CMS, are general purpose detectors that seek to
1293 measure a variety of processes in the up to 13 TeV proton-proton collisions that
1294 occur as much as 800 million times per second at the LHC at the design lumi-
1295 nosity of $10^{34} \text{ cm}^{-2}\text{s}^{-1}$. ATLAS employs a hermetic detector design, one which
1296 encloses the particle collisions as completely as possible with detecting elements,
1297 that allows it to study a wide range of physics from SM and Higgs measurements
1298 to searches for new physics in models like SUSY [6].

1299 Accommodating this wide variety of goals is a challenge for the design of the
1300 detector. The wide range of energies involved requires high measurement pre-
1301 cision over several orders of magnitude, and the numerous physics processes
1302 require an ability to measure a variety of particle types. At the time of the con-
1303 struction of ATLAS, the Higgs boson had yet to be discovered, but the diphoton
1304 decay mode was (correctly) expected to be important and necessitated a high
1305 resolution photon measurement. The potential for decays of new heavy gauge
1306 bosons, W' and Z', required a similarly high momentum resolution for leptons
1307 with momentum up to several TeV. Hadronic decay modes of several possible
1308 new high energy particles could result in very energetic jets, again up to several
1309 TeV, and reconstructing the decay resonances would again require good energy
1310 resolution. Several models, such as SUSY or Extra Dimensions, predict the exis-
1311 tence of particles which would not interact with traditional detecting elements.
1312 However these particles can still be observed in a hermetic detector by accurately
1313 measuring the remaining event constituents to observe an imbalance in energy
1314 called missing energy or E_T^{miss} . Measuring E_T^{miss} implicitly requires a good res-
1315 olution on all SM particles that can be produced. And at the lower end of the
1316 energy spectrum, precision SM measurements would require good resolution of
1317 a variety of particle types at energies as low as a few GeV, so the design needs to
1318 accommodate roughly three orders of magnitude.

1319 This broad spectrum of measurements requires a variety of detector systems
1320 working together to form a cohesive picture of each collision. Two large mag-
1321 net systems produce magnetic fields that provide a curvature to the propaga-
1322 tion of charged particles and allows for precision momentum measurements by
1323 other systems. The inner detector uses a combination of tracking technologies
1324 to reconstruct particle trajectories and vertices for charged particles. A variety
1325 of calorimeters measure the energies of hadrons, electrons, and photons over a
1326 large solid angle. A large muon spectrometer identifies muons and uses the sec-
1327 ond magnet system to provide an independent measurement of their momentum

1328 from the inner detector and improve the resolution. The layout of all of these
 1329 systems is shown in Figure 15.

1330 The performance goals needed to achieve the various targeted measurements
 1331 and searches discussed above can be summarized as resolution and coverage re-
 1332 quirements on each of these systems. Those requirements are listed in Table 3.

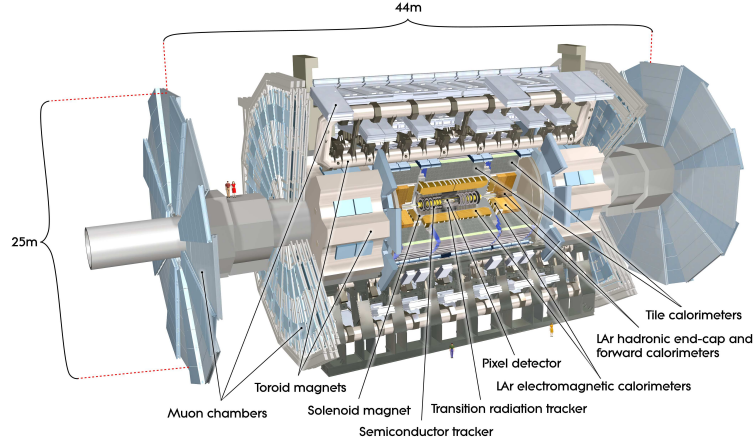


Figure 15: A cut-away schematic of the layout of the [ATLAS](#) detector. Each of the major subsystems is indicated.

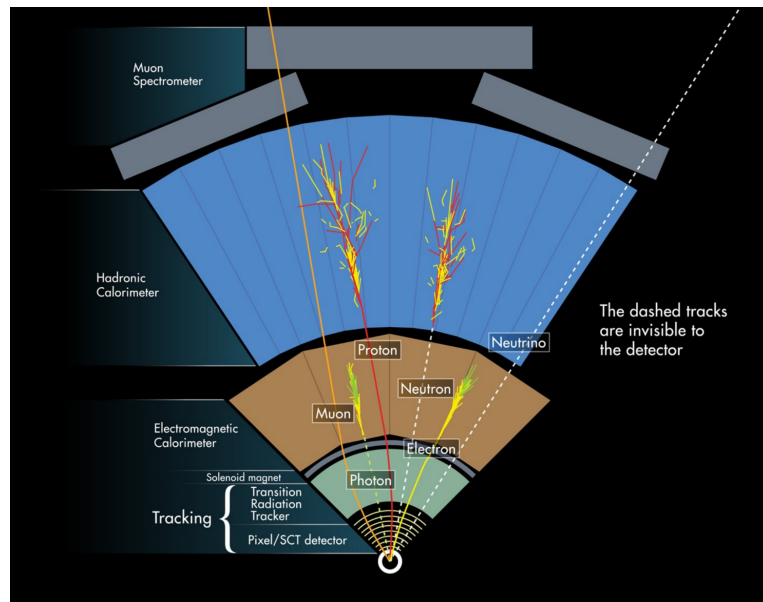


Figure 16: A cross-sectional slice of the [ATLAS](#) experiment which illustrates how the various SM particles interact with the detector systems.

1333 Incorporating these various pieces into a single detector is a significant tech-
 1334 nical challenge. The resulting detector has a diameter of 22 m, is 46 m long,
 1335 and weighs 7,000 tons; it is the largest volume particle detector ever constructed.
 1336 The various detector elements need to be constructed and assembled with pre-
 1337 cision as low as micrometers. These systems all need to function well even after
 1338 exposure to the significant radiation dose from the collisions. Designing, con-

Detector Component	Required Resolution	$ \eta $ Coverage	
		Measurement	Trigger
Tracking	$\sigma_{p_T}/p_T = 0.05\% p_T + 1\%$	2.5	-
EM Calorimetry	$\sigma_E/E = 10\%/\sqrt{E} + 0.7\%$	3.2	2.5
Hadronic Calorimetry			
Barrel and Endcap	$\sigma_E/E = 50\%/\sqrt{E} + 3\%$	3.2	3.2
Forward	$\sigma_E/E = 100\%/\sqrt{E} + 10\%$	3.1 – 4.9	3.1 – 4.9
Muon Spectrometer	$\sigma_{p_T}/p_T = 10\% \text{ at } p_T = 1 \text{ TeV}$	2.7	2.4

Table 3: The performance goals for each of the subsystems of the [ATLAS](#) detector. The $|\eta|$ coverage specifies the range where the subsystem needs to be able to provide measurements with the specified resolution. The resolutions include a p_T or E dependence that is added in quadrature with a p_T/E independent piece.

1339 structing, and installing the detector took the combined effort of more than 3000
 1340 scientists from 38 countries over almost two decades.

1341 6.1 COORDINATE SYSTEM

1342 The coordinate system defined for the [ATLAS](#) detector is used throughout all of
 1343 the sections of this thesis. The system begins with the choice of a z axis along
 1344 the beamline. The positive z side of the detector is commonly referred to
 1345 as the *A*-side, and the negative z side is referred to as the *C*-side. The $x - y$
 1346 plane is then the plane transverse to the beam direction, with the x direction
 1347 defined as pointing from the interaction point to the center of the [LHC](#) ring and
 1348 the y direction defined as pointing upwards. The nominal interaction point is
 1349 the origin of this system.

1350 It is more convenient in practice to use a cylindrical coordinate system; this
 1351 choice of coordinate system reflects the cylindrical symmetry of the [ATLAS](#) de-
 1352 tector. The distance from the beamline is the radius, r' , and the angle from the
 1353 z -axis is θ . The azimuthal angle uses the usual definition, with ϕ running around
 1354 the z -axis and $\phi = 0$ corresponding to the x -axis. Many aspects of the detector
 1355 are independent of the this coordinate to first order. The θ direction is typically
 1356 specified using rapidity or pseudorapidity, where rapidity is defined as

$$y = \frac{1}{2} \ln \frac{E + p_z}{E - p_z} \quad (15)$$

1357 Rapidity is particularly useful to indicate the component along the z direction
 1358 because differences in rapidity are invariant to boosts along the z -direction. A
 1359 similar quantity which depends only the θ is pseudorapidity,

$$\eta = -\ln \tan \frac{\theta}{2} \quad (16)$$

1360 which is the same as rapidity when the particle is massless and in the limit where
 1361 the energy is much larger than the particle's mass. It is often useful to refer to
 1362 differences in solid angle using the pseudorapidity and the azimuthal angle:

$$\Delta R = \sqrt{\Delta\phi^2 + \Delta\eta^2} \quad (17)$$

1363 The pseudorapidity is also invariant to boosts along the z -axis for high mo-
 1364 mentum particles, and is preferable to rapidity because it does not depend on
 1365 the specific choice of particle. Pseudorapidity is also preferable to θ because par-
 1366 ticle production is roughly uniform in equal-width intervals of η up to about
 1367 $\eta = 5.0$. A particle traveling along the beampipe has $\eta = \text{inf}$ and a particle
 1368 traveling perpendicular to the beampipe has $\eta = 0$. The extent of the tracker,
 1369 $|\eta| < 2.5$, corresponds to approximately $0.05\pi < \theta[\text{rad}] < 0.95\pi$ and the
 1370 extent of the calorimeters, $|\eta| < 4.9$ corresponds to approximately $0.005\pi <$
 1371 $\theta[\text{rad}] < 0.995\pi$. Many detector components are broken into multiple subsys-
 1372 tems to provide coverage at greater $|\eta|$. The lower $|\eta|$ region is referred to as the
 1373 barrel, typically with $|\eta| \lesssim 2$, and the greater $|\eta|$ region is often referred to as the
 1374 endcap.

1375 The initial energy and momentum of a proton-proton collision along the z di-
 1376 rection is unknown in hadron colliders because different energies and momenta
 1377 can be carried by the partons. Along the transverse plane, however, the vector
 1378 sum of momentum will be zero. For this reason, many physical quantities are
 1379 quantified in terms of their projection onto the transverse plan, such as p_T or
 1380 E_T . In addition, p_T alone determines the amount of curvature in the magnetic
 1381 field, and can be measured independently by measuring the curvature of a parti-
 1382 cle's propagation.

1383 6.2 MAGNETIC FIELD

1384 The magnet system used in [ATLAS](#) is designed to provide a substantial magnetic
 1385 field in the two regions where the trajectory of particles is measured, the inner
 1386 detector and the muon spectrometer. The magnetic field provides a curvature to
 1387 the trajectory of charged particles and allows the precision tracking elements to
 1388 make high resolutions measurements of p_T . To provide a magnetic field in these
 1389 regions, [ATLAS](#) uses a hybrid system with four separate, superconducting mag-
 1390 nets. A single solenoid provides a 2 T axial, uniform magnetic field for the inner
 1391 detector, while a barrel toroid and two endcap toroids produce a non-uniform
 1392 magnetic field of 0.5 and 1 T, respectively, for the muon detectors. This geom-
 1393 etry is illustrated in Figure 17, and the parameters of the three magnet systems
 1394 are summarized in Table 4.

1395 The central solenoid uses a single-layer coil with a current of 7.730 kA to gen-
 1396 erate the 2 T axial field at the center of the magnet. The single-layer coil design
 1397 enables a minimal amount of material to be used in the solenoid's construction,
 1398 which is important because the solenoid is placed between the inner detector
 1399 and the calorimeters. At normal incidence the magnet has only 0.66 radiation
 1400 lengths worth of material, where one radiation length is the mean distance over

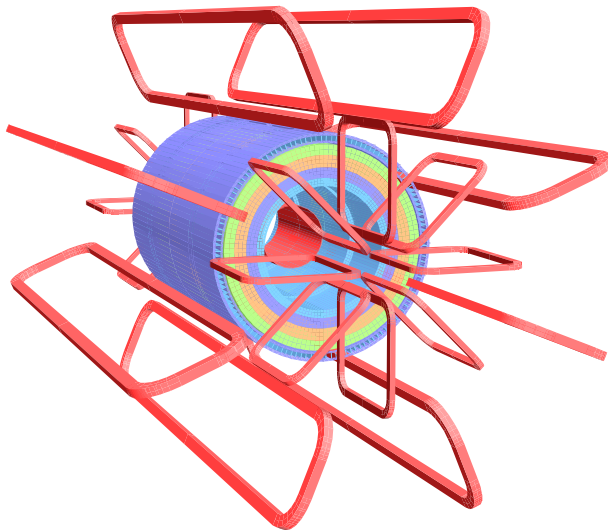


Figure 17: The layout of the four superconducting magnets in the [ATLAS](#) detector.

Parameter	Unit	Solenoid	Barrel Toroid	Endcap Toroids
Inner Diameter	m	2.4	9.4	1.7
Outer Diameter	m	2.6	20.1	10.7
Axial Length	m	5.3	25.3	5.0
Weight	tons	5.7	830	239
Conductor Size	mm ²	30×4.25	57×12	41×4.25
Peak Field	T	2.6	3.9	4.1
Heat Load	W	130	990	330
Current	kA	7.7	20.5	20.0
Stored Energy	MJ	38	1080	206

Table 4: A summary of the parameters of each of the three magnet systems on [ATLAS](#).

1401 which a high-energy electron loses all but $1/e$ of its energy through material in-
 1402 teractions [10]. The coil is made of a high-strength aluminum stabilized NbTi
 1403 superconductor which was optimized to achieve a high field with minimal thick-
 1404 ness. The axial magnetic field produced by the solenoid bends charged particles
 1405 in the ϕ direction, following a circular path with a radius specified by Maxwell's
 1406 equations (see Equation 13).

1407 The barrel toroid consists of eight coils which generate a 0.5 T magnetic field,
 1408 on average, in the cylindrical region around the calorimeters with an approxi-
 1409 mately 20 kA current. The coils are separated only by air to reduce the scatter-
 1410 ing of muons as they propagate through the region. The coils are made of an
 1411 aluminum stabilized NbTiCu superconductor and each is separately housed in a
 1412 vacuum and cold chamber. This magnetic configuration produces a field in the
 1413 ϕ and so curves muons traversing the volume primarily in the η direction.

1414 The endcap toroids follow a similar design to the barrel toroid and produce a
 1415 1.0 T magnetic field, on average. Each has eight separate NbTiCu coils, and in
 1416 this case all eight are housed within a single cold mass. This extra structure is
 1417 necessary to withstand the Lorentz forces exerted by the magnets. These mag-
 1418 nets are rotated 22.5% relative to the barrel toroid to provide a uniform field in
 1419 the transition between the two systems. The endcap toroids also produce a field
 1420 in the ϕ direction and curve muons primarily in the η direction.

1421 6.3 INNER DETECTOR

1422 The [ATLAS](#) inner detector provides excellent momentum resolution as well as
 1423 accurate primary and secondary vertex measurements through robust pattern
 1424 recognition that identifies tracks left by charged particles. These tracks fulfill a
 1425 number of important roles in the [ATLAS](#) measurement system: they measure the
 1426 momentum of charged particles including electrons and muons, they can iden-
 1427 tify electrons or photon conversions, they assign various particles and jets to dif-
 1428 ferent vertices, and they provide a correction to E_T^{miss} measurements from low
 1429 energy particles. The system has to be accurate enough to separate tracks from
 1430 dozens of vertices, to resolve each vertex individually, and to measure the p_T of
 1431 very high momentum tracks which curve very little even in the large magnetic
 1432 field. This is accomplished by several independent layers of tracking systems.
 1433 Closest to the interaction point is the very high granularity Pixel detector, in-
 1434 cluding the newly added Insertible B-Layer, which is followed by the [SCT](#) layers.
 1435 These silicon subdetectors both use discrete space-points to reconstruct track
 1436 patterns. The final layer, the Transition Radiation Tracker ([TRT](#)), uses many lay-
 1437 ers of straw tube elements interleaved with transition radiation material to pro-
 1438 vide continuous tracking. The arrangement of these subdetectors is shown in
 1439 Figure 18. To provide the desired hermetic coverage, the subdetectors are di-
 1440 vided into barrel and endcap geometries. Figure 19 shows the layout of the sub-
 1441 detectors in more detail, and illustrates how tracks at various pseudorapidities
 1442 can traverse the subdetectors; tracks with $\eta > 1.1$ begin to traverse the endcap
 1443 subdetectors rather than those in the barrel, and tracks with $\eta > 1.7$ use primar-

ily endcap elements. The **IBL** was not present during the original commissioning of the inner detector and is not shown in this figure.

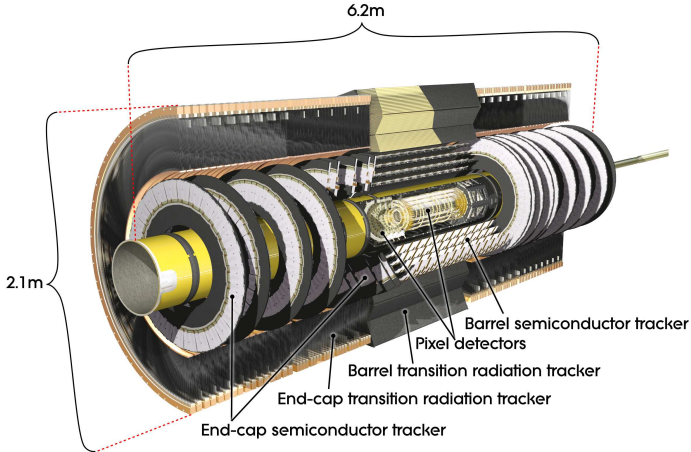


Figure 18: The arrangement of the subdetectors of the **ATLAS** inner detector. Each of the subdetectors is labeled in the cut-away view of the system.

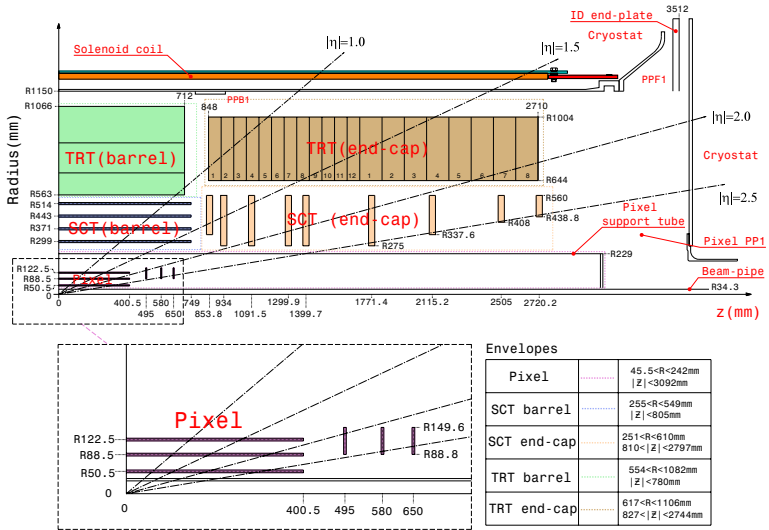


Figure 19: A quarter section of the **ATLAS** inner detector which shows the layout of each of the subdetectors in detail. The lower panel shows an enlarged view of the pixel detector. Example trajectories for a particle with $\eta = 1.0, 1.5, 2.0, 2.5$ are shown. The **IBL**, which was added after the original detector commissioning, is not shown.

Figure 20 shows a computer generated three-dimensional view of the inner detector along the beam axis, which emphasizes the straw tube structure of the **TRT** as well as the overlapping geometry of the **SCT**. This figure also includes the **IBL**, which was added during the long shutdown and provides an additional measurement layer in the Pixel detector as of the beginning of Run 2. Figure 21 shows an alternative computer generated three-dimensional view transverse to the beam axis which emphasizes the endcap structures of the **SCT** and **TRT**.

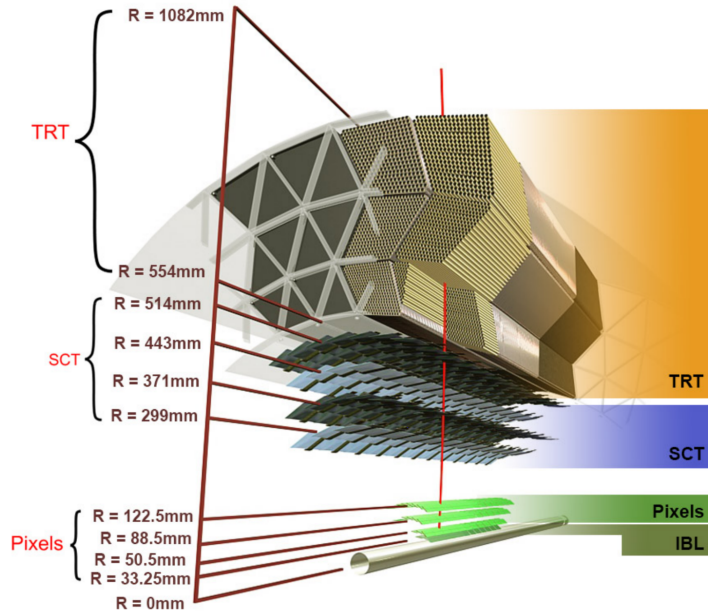


Figure 20: A computer generated three-dimensional view of the inner detector along the line of the beam axis. The subdetectors and their positions are labeled.

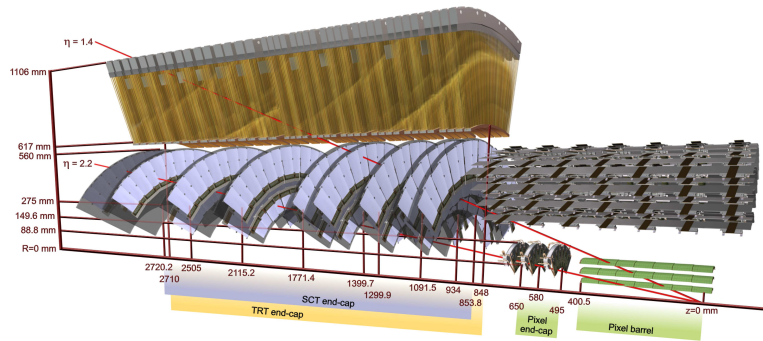


Figure 21: An alternative computer generated three-dimensional view of the inner detector transverse to the beam axis. The subdetectors and their positions are labeled.

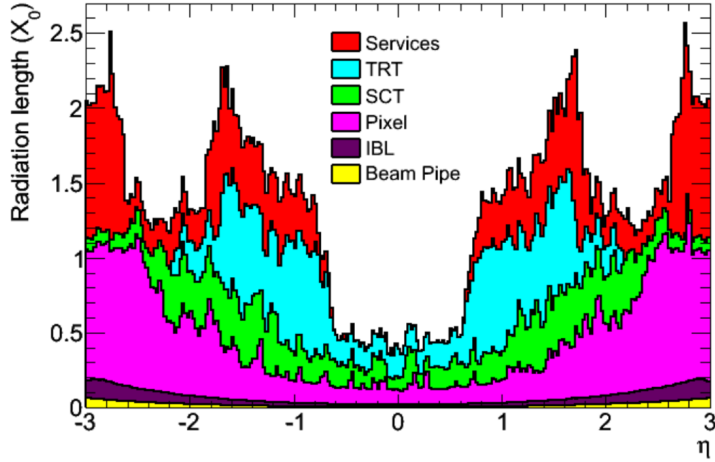


Figure 22: The integrated radiation lengths traversed by a straight track at the exit of the ID envelope, including the services and thermal enclosures. The distribution is shown as a function of $|\eta|$ and averaged over ϕ . The breakdown indicates the contributions of individual sub-detectors, including services in their active volume.

As the closest system to the interaction point, it is crucial for the inner detector to use as little material as possible to avoid scattering of charged particles or photon conversions before they reach the remaining subdetectors. The various components, including the readout electronics, cooling infrastructure, gas volumes, and support structures, were designed to accommodate this need for minimal components. Even with these optimizations, the combination of stringent performance requirements and the harsh radiation environment in the inner detector requires a significant amount of material. This material causes many electrons to lose most of their energy before reaching the electromagnetic calorimeter and approximately 40% of photons convert into an electron-positron pair while traversing the inner detector. Figure 22 shows the integrated radiation lengths traversed by a straight track in the inner detector as a function of η , grouped by subdetector. There is a large increase in the amount of material for support structures around $|\eta| = 1.7$, where the inner detector transitions from barrel to endcap.

The inner detector is designed to work as a cohesive unit to provide complete tracking information for charged particulars, and the subdetectors are complementary. Table 5 summarizes the parameters of each of the subdetectors as well as the parameters of the combined inner detector. Table 6 summarizes the expected performance that can be achieved by the inner detector as a whole.

6.3.1 PIXEL DETECTOR

The Pixel detector is the closest detector to the interaction point and therefore is designed to provide extremely high granularity while simultaneously handling a very large dose of radiation from collisions. It consists of four layers of silicon pixel modules, each of which provides a precision measurement on the trajectory

Parameter	Inner Detector	Pixel	SCT	TRT
Inner Radius	3.1 cm	3.1 cm	30 cm	56 cm
$ \eta $ Coverage	-	2.5	2.5	2.0
Cell Width	-	50 μm	80 μm	4 mm
Cell Length	-	400 μm	12 cm	70 cm
Material at $ \eta = 0.0$	0.3 X/X_0			
Material at $ \eta = 1.7$	1.2 X/X_0			
Material at $ \eta = 2.5$	0.5 X/X_0			
Number of Hits	48	4	8	36
Channels	99 M	92 M	6.3 M	350 k

Table 5: A summary of the parameters of the inner detector and each of the subdetectors [6].

of any charged particle. In the barrel region, the four layers are located at radial distances of 31 mm, 51 mm, 89 mm, and 123 mm. The three outer layers also include endcap elements, illustrated in Figure 19, which are located at 495 mm, 580 mm, and 650 mm away from the interaction point.

The pixel sensor technology uses a p-n junction of n-type bulk that contains both p⁺ and n⁺ impurities. This combination is crucial in maintaining performance after a significant radiation dose, as the n⁺ implants allow the sensor to continue function after the n-type bulk has been converted to a p-type bulk by the accumulation of radiation. In either configuration, when a charged particle passes through the bulk, it ionizes thousands of electron-hole pairs. The electrons and holes are pulled in opposite directions by the electric field established between the anode and cathode of the junction, which then produces a current that can be measured and recorded by readout electronics.

The size of the pixels in the original three layers are 50 μm x 400 μm in the $r - \phi$ and z directions, respectively. Those pixels are bump-bonded to front-end readout chips, the FE-I3, which contains a total of 2880 pixels per chip. In the three original pixel layers, the chips are grouped into modules composed of 16 chips each with 46,080 pixels per module and a total size of 20 mm x 60 mm x 250 μm . The modules are further arranged into long rectangular structures that run parallel to the beamline called staves. By tiling several staves with an offset of 20°, the stave geometry provides full azimuthal coverage in the barrel region while accommodating the readout and cable systems. The endcap regions are instead arranged into petals and then into wheels. This arrangement can be seen in Figure 23 which shows a computer-generated, cut-away image of the outer three layers of the pixel detector. Together these three layers contain 1744 modules between the barrel and two endcap sections.

The innermost layer, the IBL, was added during the long shutdown before Run 2, and provides the fourth track measurement. It was inserted directly into the existing pixel detector by removing the existing beam pipe and replacing it with a significantly smaller version. This insertion can be seen in action in Figure 24,

Parameter	Particle	Value
Reconstruction Efficiency	Muon, $p_T = 1 \text{ GeV}$	96.8%
	Pion, $p_T = 1 \text{ GeV}$	84.0%
	Electron, $p_T = 5 \text{ GeV}$	90.0%
Momentum Resolution	$p_T = 1 \text{ GeV}, \eta \approx 0$	1.3%
	$p_T = 1 \text{ GeV}, \eta \approx 2.5$	2.0%
	$p_T = 100 \text{ GeV}, \eta \approx 0$	3.8%
	$p_T = 100 \text{ GeV}, \eta \approx 2.5$	11%
Transverse IP Resolution	$p_T = 1 \text{ GeV}, \eta \approx 0$	$75 \mu\text{m}$
	$p_T = 1 \text{ GeV}, \eta \approx 2.5$	$200 \mu\text{m}$
	$p_T = 1000 \text{ GeV}, \eta \approx 0$	$11 \mu\text{m}$
	$p_T = 1000 \text{ GeV}, \eta \approx 2.5$	$11 \mu\text{m}$
Longitudinal IP Resolution	$p_T = 1 \text{ GeV}, \eta \approx 0$	$150 \mu\text{m}$
	$p_T = 1 \text{ GeV}, \eta \approx 2.5$	$900 \mu\text{m}$
	$p_T = 1000 \text{ GeV}, \eta \approx 0$	$90 \mu\text{m}$
	$p_T = 1000 \text{ GeV}, \eta \approx 2.5$	$190 \mu\text{m}$

Table 6: A summary of the expected performance of the combined inner detector [11]. Included are the reconstruction efficiencies for multiple particle types as well as the momentum and IP resolution for various momenta.

which emphasizes the extreme precision required to place the the 70 cm long layer with only 2 mm of clearance. The IBL was commissioned to provide continued tracking robustness and high precision in the higher luminosity environment of Run 2 [12]. The proximity of this layer to the collisions necessitated an even higher granularity and better radiation hardness than the other pixel layers. And the strict space requirements to add an active sensing layer so close to the interaction point required a sensor chip with a much higher active area and a larger overall area per chip. These requirements led to the development of a new chip type, the FE-I4 (compared to the FE-I3 chips used in the original pixel detector) with improved radiation hardness and a larger active footprint of 90%. The IBL is comprised of 448 of these individual chips arranged in 14 staves, with 26,880 pixels per chip and a chip size of 18.5 mm x 41.3 mm x 200 μm . The staves, like in the other layers of the pixel detector, are offset by 14° to provide full azimuthal coverage. This arrangement can be seen in Figure 25, which shows two computer-generated images of the IBL geometry and includes the some of the remaining pixel layers.

6.3.2 SEMICONDUCTOR TRACKER

The SCT, the subdetector which immediately surrounds the Pixel detector, provides additional discrete measurements of the trajectory of a charged particle. Because the SCT is further away from the interaction point, the spatial resolution

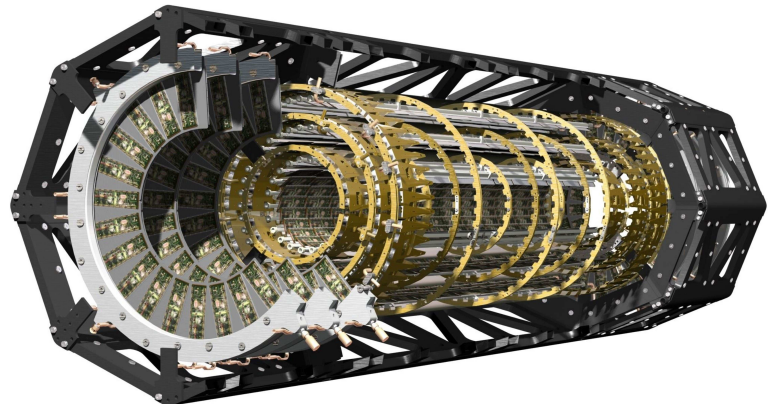


Figure 23: A cut away image of the outer three layers of the pixel detector.



Figure 24: An image of the insertion of the [IBL](#) into the current pixel detector.

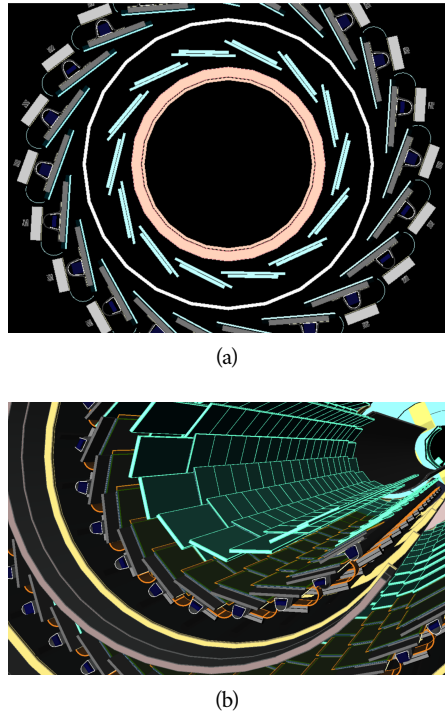


Figure 25: A three-dimensional computer-generated image of the geometry of the [IBL](#) with a view (a) mostly transverse to the beam pipe (b) mostly parallel to the beam pipe.

1528 does not need to be as high as in the pixel detector, and so the [SCT](#) uses micro-
 1529 strips instead of pixels. Although pixels provide a more accurate measurement,
 1530 the number of pixels and readout channels required to cover the cylindrical area
 1531 at the radius of the [SCT](#) layers would be prohibitively complicated and expensive.

1532 Each individual silicon strip sensor contains 768 individual readout strips
 1533 with a total area of $6.36 \text{ cm} \times 6.40 \text{ cm}$ and a pitch of $80 \mu\text{m}$. Pairs of these sen-
 1534 sors are then bonded together to form a combined strip with a length of 12.8 cm.
 1535 Two of these combined strips are then placed back to back with a relative tilt of
 1536 40 mrad. This geometry is illustrated in an expanded view in Figure 26. The pur-
 1537 pose of angular offset of the consecutive layers is to allow the strip sensor areas
 1538 to more accurately measure the position of a particle by comparing the overlap
 1539 of the two strips which were traversed by a track.

1540 Four of these double layers are placed in the barrel region, with radii of 284
 1541 mm, 355 mm, 427 mm, and 498 mm. Together these layers provide eight addi-
 1542 tional measurements for each track that traverses the central $|\eta|$ region. In the
 1543 endcap region, the layers are arranged in wheels, with the double layers simi-
 1544 larly offset to provide improved resolution. With these configurations, the [SCT](#)
 1545 achieves a spatial resolution of $17 \mu\text{m}$ in the $r - \phi$ direction and $580 \mu\text{m}$ in the
 1546 z direction.

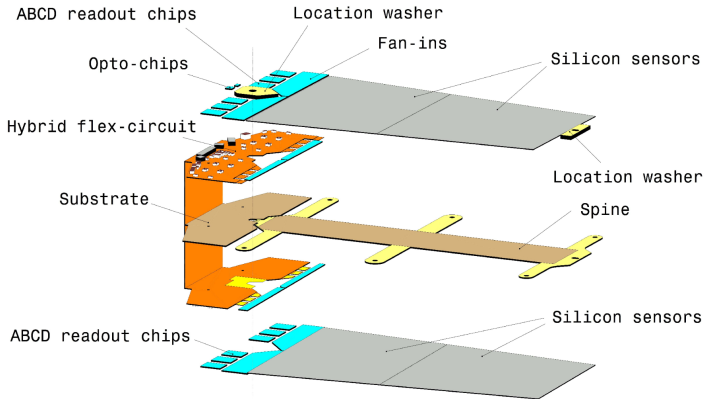


Figure 26: An expanded view of the geometry of the [SCT](#) double layers in the barrel region.

1547 6.3.3 TRANSITION RADIATION TRACKER

1548 The final component of the inner detector, the [TRT](#), provides continuous track-
 1549 ing using straw drift tubes. The tubes are made of Kapton and aluminum with
 1550 a diameter of 4 mm and are filled with a gas mixture of 70% Xe, 27% CO₂, and
 1551 3% O₂. At the center of each tube is a gold-plated anode tungsten wire 30 μm in
 1552 diameter. When a charged particle passes through these tubes, it ionizes the gas
 1553 within. The ions produced drift in the electric field established between the wire
 1554 and the tube wall, and the large electric field near the wire produces avalanche
 1555 multiplication and results in an electric current on the wire that is read out by
 1556 the electronics and provides a track measurement. The time it takes the ioniza-
 1557 tion to drift to the wire can be used to estimate the distance from the wire that
 1558 the particle passed through the tube; this gives a resolution on the distance of ap-
 1559 proximately 130 μm . Combining several such measurements between consecu-
 1560 tive hits in the [TRT](#) tubes allows the trajectory of the particle to be reconstructed
 1561 with much better resolution than is available in each individual tube.

1562 In addition to the continuous tracking, the detector can use transition radia-
 1563 tion produced when a particle passes between the layers to distinguish between
 1564 electrons and heavier charged particles. The space between the tubes is filled
 1565 with CO₂, and so has a different dielectric constant than the gas within the tubes
 1566 which contains Xe. At the transition between those media, a relativistic par-
 1567 ticle emits radiation proportional to γ , so inversely proportional to mass at a
 1568 fixed momentum. The photons produced in this transition then produce an
 1569 ionization cascade which is significantly larger than the signal for the minimally-
 1570 ionizing charged particles. To distinguish between these two cases, the [TRT](#) de-
 1571 fines two signal thresholds, a low threshold for the typical signal produced by a
 1572 minimally ionizing particle ([MIP](#)) and a high threshold for the the signal produced
 1573 by transition radiation. A high momentum electron is expected to produce ap-
 1574 proximately 7 to 10 high threshold hits as it traverses the [TRT](#), and thus these hits
 1575 provide a way to distinguish electrons from other charged particles.

1576 The [TRT](#) contains 351,000 tubes in total, divided between the barrel and end-
 1577 cap regions. In the barrel region, the tubes are 144 cm long and arranged in 73
 1578 layers parallel to the beampipe. In the endcap region, the tubes are 37 cm long
 1579 and arranged in 160 layers transverse to the beampipe. These configurations
 1580 can be seen in Figure 20 and Figure 21. With this geometry the [TRT](#) achieves a
 1581 resolution of $130 \mu\text{m}$ in the $r - \phi$ direction.

1582 6.4 CALORIMETRY

1583 The combination of calorimeter systems used in [ATLAS](#) can measure the energy
 1584 of electrons, photons, hadrons, and hadronic jets with complete coverage up to
 1585 $|\eta| < 4.9$ and across ϕ . Unlike the inner detector, the calorimeters are capable
 1586 of measuring neutral particles. To accomplish precision measurements of these
 1587 particle types, the [ATLAS](#) calorimeter system uses four individual calorimeters,
 1588 a [LAr](#) electromagnetic calorimeter in the barrel region, a tile hadronic calorime-
 1589 ter in the barrel region, a [LAr](#) hadronic endcap calorimeter, and a [LAr](#) forward
 1590 calorimeter. Together these provide hermetic coverage for the [ATLAS](#) detector.
 1591 The configuration of these calorimeters is illustrated in Figure 27. **Note: I could
 1592 make this section much longer. It might be nice to include a more com-
 1593 plete description of showers for example. I will extend this section if there
 1594 is space at the end.**

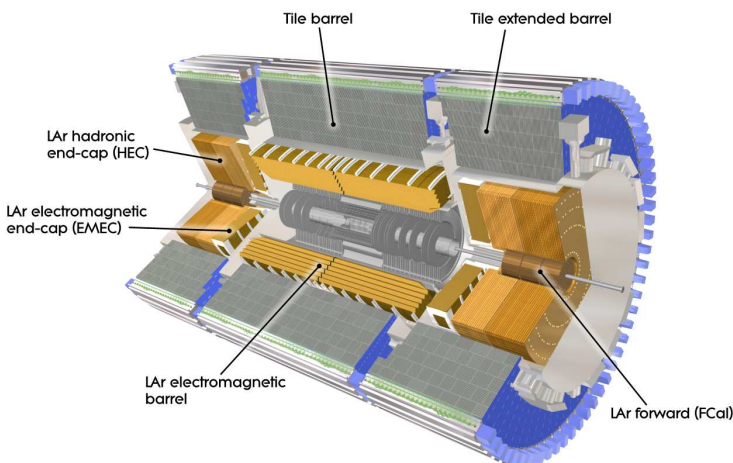


Figure 27

1595 The calorimeters are designed to absorb and measure the energy carried by
 1596 a particle, and completely stop the particle's propagation in the process. This
 1597 requires a significant amount of material to provide interactions. These interac-
 1598 tions then produce secondary particles, which can produce secondary particles
 1599 in turn, and thus form a cascade of particles called an electromagnetic ([EM](#)) or
 1600 hadronic shower, depending on the governing mechanism. Electromagnetic and
 1601 hadronic showers have very different properties and require different technolo-
 1602 gies to measure them accurately. All of the calorimeters in the [ATLAS](#) calorimeter
 1603 system are sampling calorimeters: they use alternating layers of absorbing and

active material. The dense absorbing layers initiate the showers while the active layers measure the energy of the produced particles. A fraction of the energy is lost in the inactive layers, so the energy measurement from the active layers has to be corrected to estimate the actual energy of the particle.

The EM calorimeter provides around 20 radiation lengths (X_0) while the hadronic calorimeter provides around 10 interaction lengths (λ_0). As mentioned previously, radiation lengths measure the distance over which an electromagnetically interacting particle loses a characteristic fraction of its energy. Interaction lengths, on the other hand, measure the mean distance traveled by a hadronic particle before undergoing a nuclear interaction [10]. Figure 28 show the radiation lengths in the layers of the EM calorimeter in the barrel region as well as the interaction lengths for all calorimeters.

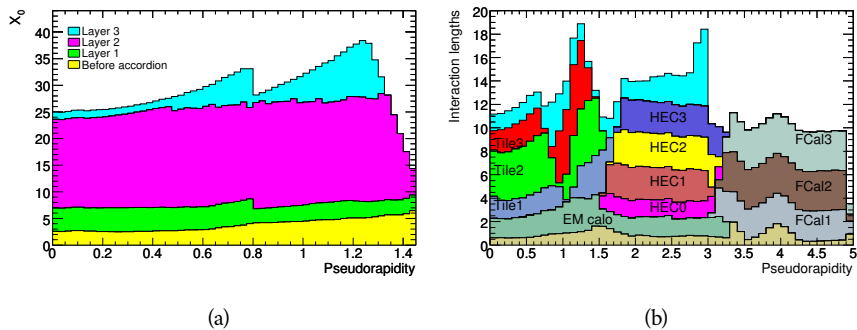


Figure 28: The depth of (a) the electromagnetic barrel calorimeter in radiation lengths and (b) all calorimeters in interaction lengths as a function of pseudorapidity.

6.4.1 ELECTROMAGNETIC CALORIMETER

The electromagnetic calorimeters use alternating layers of liquid argon and lead in an accordion shape. The accordion shape provides complete coverage in the ϕ direction while also providing many alternating layers for the a particle to pass through. The configuration is detailed in Figure 29. When an electron or photon passes through the lead, it produces an electromagnetic shower. The particles produced in those showers then pass into and ionize the liquid argon; the ions produced can then be collected by an electrode in the liquid argon layer to provide the actual energy measurement.

The barrel region is covered by a presampler and three separate sampling layers with decreasing segmentation. The presampler is a thin layer of liquid argon which measures the energy of any electromagnetic showers which are initiated before the particle reaches the calorimeter due to interactions with the detector material. The first layer is the strip layer, which has fine segmentation in η to enhance the identification of shower shapes and to provide a precise η measurement for reconstructing photons and electrons. The strip layer has only 4 radiation lengths worth of material, and has a segmentation of $\Delta\eta = 0.003$ and $\Delta\phi = 0.1$. The second layer is also finely segmented, with a segmentation of $\Delta\eta = 0.025$ and $\Delta\phi = 0.025$, and a thickness of 16 X_0 . This layer is designed

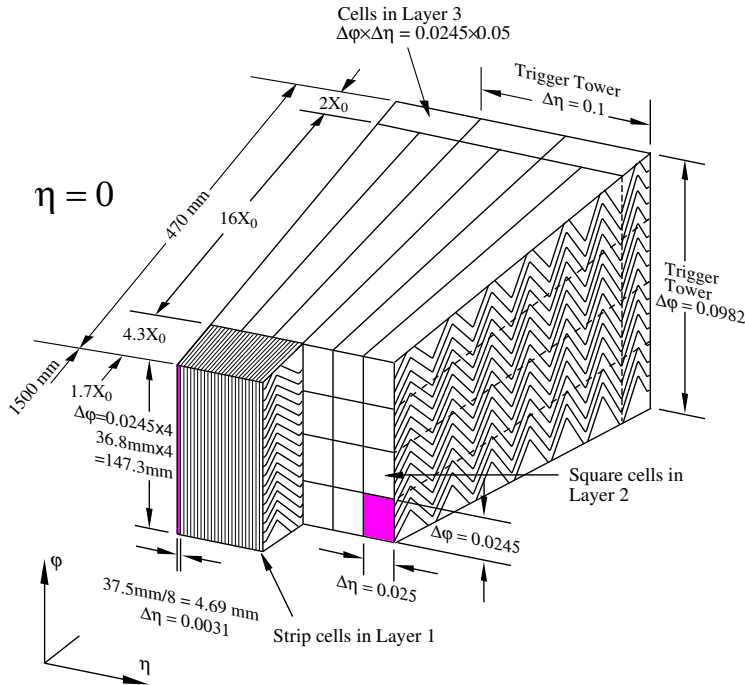


Figure 29: A schematic of the LAr calorimeter in the barrel region, highlighting the accordion structure.

1635 to contain an electromagnetic shower and to measure the majority of the energy
 1636 for photons and electrons. The third layer is only $2 X_0$ thick and measures the
 1637 energy of electromagnetic showers which leak out of the second layer, and helps
 1638 to separate electromagnetic showers from hadronic showers. The structure of
 1639 the LAr endcap calorimeter is similar except that the layers are arranged parallel
 1640 to the beampipe to measure energy deposits from high η particles.

1641 6.4.2 HADRONIC CALORIMETERS

1642 The hadronic calorimeters use a few different technologies to satisfy the resolu-
 1643 tion demands in the different areas of the detector, and together they cover the
 1644 region $|\eta| < 2.7$. In the barrel region, for $|\eta| < 1.7$, the hadronic calorimeters
 1645 are constructed of alternating tiles of steel and plastic scintillator. Like in the
 1646 electromagnetic calorimeter, the dense layer initiates a shower (in this case the
 1647 dense layer is the steel and the shower is hadronic) of particles which pass into
 1648 and ionize the following layer. The ionization in the plastic scintillator instead
 1649 produces a light signal proportional to the amount of ionization produced by the
 1650 shower, and this signal is measured using photomultipliers and provides the ac-
 1651 tual energy measurement. The construction of a tile in the calorimeter is shown
 1652 Figure 30, which highlights the alternating layers of steel and scintillator.

1653 This tile calorimeter, as well as the remaining hadronic calorimeters, have a
 1654 much coarser granularity than the electromagnetic calorimeters. The high gran-
 1655 ularity is not needed for an accurate energy measurement, and the hadronic
 1656 calorimeters are not designed to distinguish particle types like the electromag-

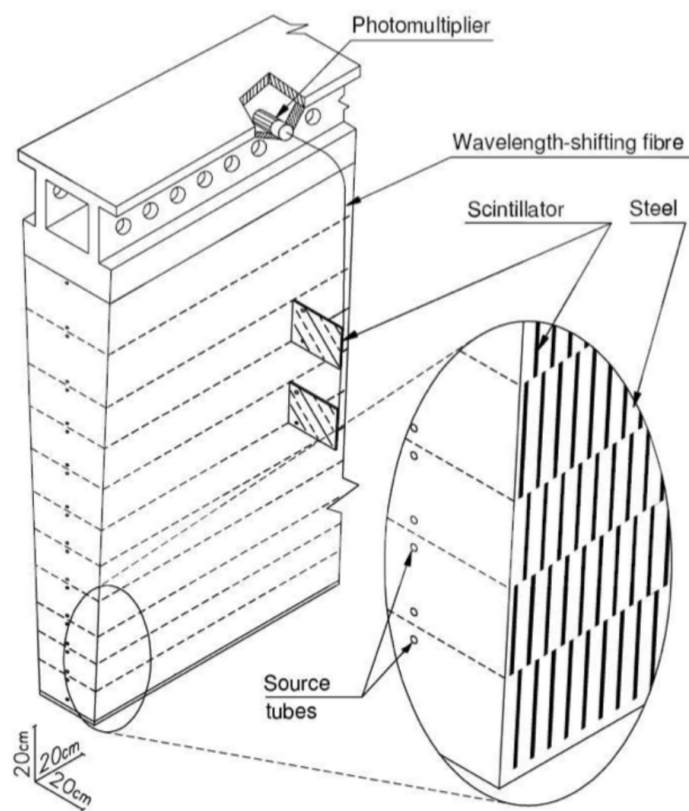


Figure 30: A schematic of a hadronic tile module which shows the alternating layers of steel and plastic scintillator.

netic calorimeters. The tile granularity is approximately $\Delta\eta = 0.1$ and $\Delta\phi = 0.1$, and the segmentation in depth and η is shown in Figure 31.

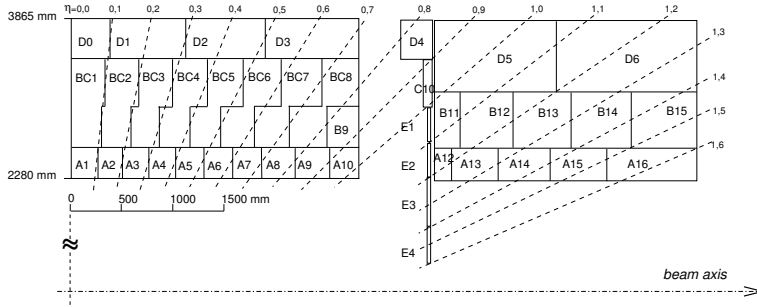


Figure 31: The segmentation in depth and η of the tile-calorimeter modules in the central (left) and extended (right) barrels.

The remaining hadronic calorimeters all use the same alternating, sampling structure but with different active and inactive materials. The hadronic endcap calorimeter covers the range of $1.5 < |\eta| < 3.2$ and uses an inactive layer of copper and an active layer of liquid argon. The forward calorimeter covers the range of $3.1 < |\eta| < 4.9$ and uses a dense matrix of copper and tungsten filled with liquid argon.

6.5 MUON SPECTROMETER

Among SM particles, only muons and neutrinos consistently pass through the calorimeters. Because the neutrinos are also electrically neutral, there is no feasible option to measure them directly in ATLAS. The muons, on the other hand, are charged and are thus already measured as a track in the inner detector. The muon spectrometer provides a way to consistently identify muon tracks and also a way to provide an additional measurement of their momentum.

The muon spectrometer contains four subdetectors that cover the barrel and endcap regions. In the barrel region, the muon spectrometer uses a combination of Resistive Plate Chambers (RPCs) and MDTs to provide both a coarse, fast measurement for triggering and a precise momentum measurement for offline event reconstruction. Similarly, in the endcap region, the TGCs, MDTs, and CSCs allow for both triggering and precise measurements. The CSCs are used only in the innermost layer of the endcap region between $2.0 < |\eta| < 2.7$ where the particle flux is too large for the MDTs to provide accurate measurements. The overall layout of the muon systems are shown in the cut-away diagram in Figure 32, and Figure 33 shows a precise schematic of the layout of each of the detecting elements. The geometric arrangement shown provides consistent coverage for muons produced up to $|\eta| < 2.7$, and takes full advantage of the bending of the muons in the toroidal magnetic field, described in Section 6.2, to measure their momentum. Figure 34 shows a cross-section of the arrangement of the muon spectrometer in the barrel; the layers are divided into eight small and eight large chambers that are overlapped to provide complete coverage in ϕ .

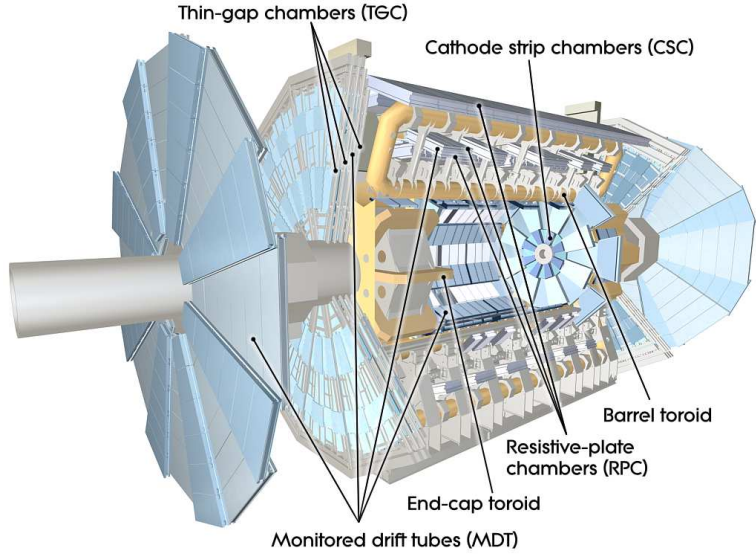


Figure 32: A cut-away diagram of the muon systems on [ATLAS](#).

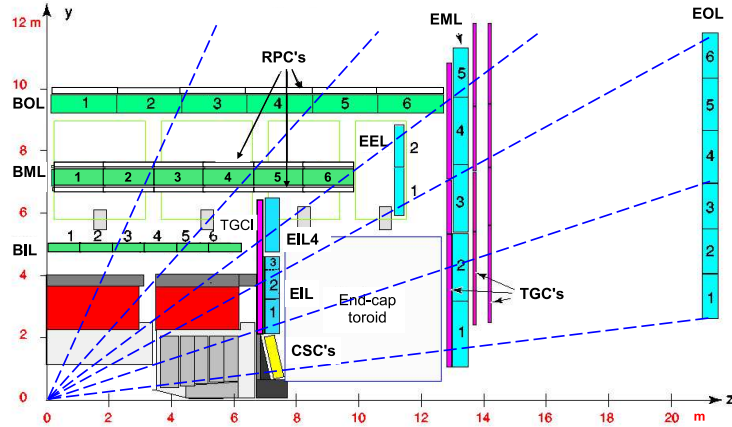


Figure 33: A quarter view of the muon spectrometer which highlights the layout of each of the detecting elements. The BOL, BML, BIL, EOL, EML, and EIL are all [MDT](#) elements, where the acronyms encode their positions.

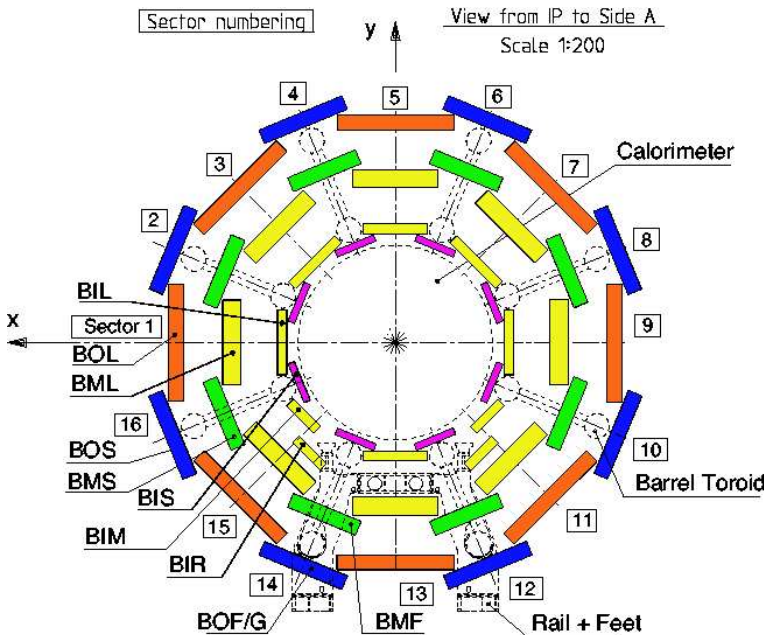


Figure 34: A schematic of the cross-section of the muon spectrometer in the barrel region.

1688 6.5.1 MONITORED DRIFT TUBE

1689 The momentum measurements in the barrel region are provided by three con-
 1690 secutive layers of MDT elements, located at approximately 5 m, 7 m, and 9 m from
 1691 the interaction point. Each of these layers is a composite of two multilayers of
 1692 drift tubes: two layers of three to four layers of tubes, as shown in Figure 35.
 1693 These aluminum tubes are 3 cm in diameter, with lengths between 0.9 and 6.2 m,
 1694 and are filled with a mixture of ArCO₂ kept at 3 bar absolute pressure. A central
 1695 tungsten-rhenium wire with a diameter of 50 μm runs along the length of the
 1696 tube, and is kept at a potential of 3080 V.

1697 A muon traversing these tubes ionizes the gas, and the ionization electrons
 1698 then drift in the electric field toward the central wire. Close to the wire, the
 1699 electric field is strong enough to cause the original ionization electrons to ionize
 1700 additional electrons, producing an avalanche that can be measured as a current
 1701 along the wire. The time of arrival of that current depends on how far the muon
 1702 entered from the wire, and can be used to achieve a position resolution of 80 μm
 1703 in an individual tube. The combination of the measurements in the consecutive
 1704 layers of tubes improves this position resolution to 35 μm transverse to the tubes,
 1705 with a resolution of 1 m along the tube direction.

1706 To achieve a good resolution over the entire length of a muon track, the rel-
 1707 ative positions of the tubes of the muon spectrometer must be known to an ac-
 1708 curacy of 30 μm . This is achieved by an optical laser alignment system placed in
 1709 each of the individual chambers and throughout the cavern. These monitor any
 1710 changes in position or alignment due to effects like gravitational sag, tempera-
 1711 ture shifts, and the magnetic field. The configuration of the alignment system
 1712 within an individual chamber is also shown in Figure 34.

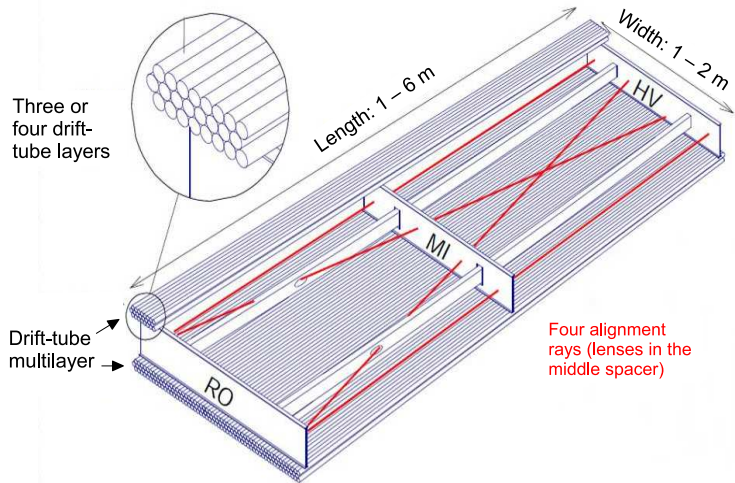


Figure 35: A schematic of a single [MDT](#) chamber, which shows the multilayers of drift tubes as well as the alignment system.

[1713](#) 6.5.2 RESISTIVE PLATE CHAMBER

[1714](#) The [RPC](#) is the outermost detecting layer in the muon spectrometer in the barrel
[1715](#) region, and provides a fast measurement of the ϕ position of muons for trigger-
[1716](#) ing. The speed of the measurement, with a time resolution of just a few tens of
[1717](#) nanoseconds, requires a poor spatial resolution of approximately 1 cm. There
[1718](#) are three [RPCs](#) layers in the muon spectrometer, two located on either side of
[1719](#) the central [MDT](#) layer and one located outside the final [MDT](#) layer, as shown in
[1720](#) Figure 33. The [RPCs](#) consist of two layers of parallel plates filled with a gas mix-
[1721](#) ture of $C_2H_2F_4$. A muon passing through these systems ionizes the gas, like in
[1722](#) the [MDT](#), which causes an avalanche of ionization electrons in the electric field
[1723](#) maintained between the plates. Metal strips on the outside of the chamber ca-
[1724](#) pacitively couple to the accumulated charge, and are read out to measure the η
[1725](#) and ϕ positions of the muon track.

[1726](#) 6.5.3 CATHODE STRIP CHAMBER

[1727](#) The majority of the momentum measurements in the endcap region are provided
[1728](#) by the [MDTs](#). In the most forward region of the muon spectrometer, between
[1729](#) $2.0 < \eta < 2.7$, the particle flux is very high due to contributions from low energy
[1730](#) photons and neutrons. The [MDT](#) can only sustain a hit rate of approximately 150
[1731](#) Hz/cm² because of limitations in the drift times of the gas and the capacity of
[1732](#) the readout electronics. The [CSCs](#) were designed to handle higher hit rates, up to
[1733](#) 1000 Hz/cm², and provide the necessary coverage in that high flux region.

[1734](#) The [CSC](#) consists of several multiwire proportional chambers, where the wires
[1735](#) are oriented in the radial direction out from the beampipe. There are eight large
[1736](#) and eight small chambers, arranged to partially overlap in the ϕ direction, as
[1737](#) shown in Figure 36. Like in the [MDT](#), a muon traversing the system produces
[1738](#) ionization in the gas; here, however, the ionization is collected on a number of

1739 wires. These wires couple to cathodes on the chambers which are segmented
 1740 into strips in two directions. The relative amount of charge on each of the neigh-
 1741 boring strips can be used to interpolate to the position of the muon in both η
 1742 and ϕ .

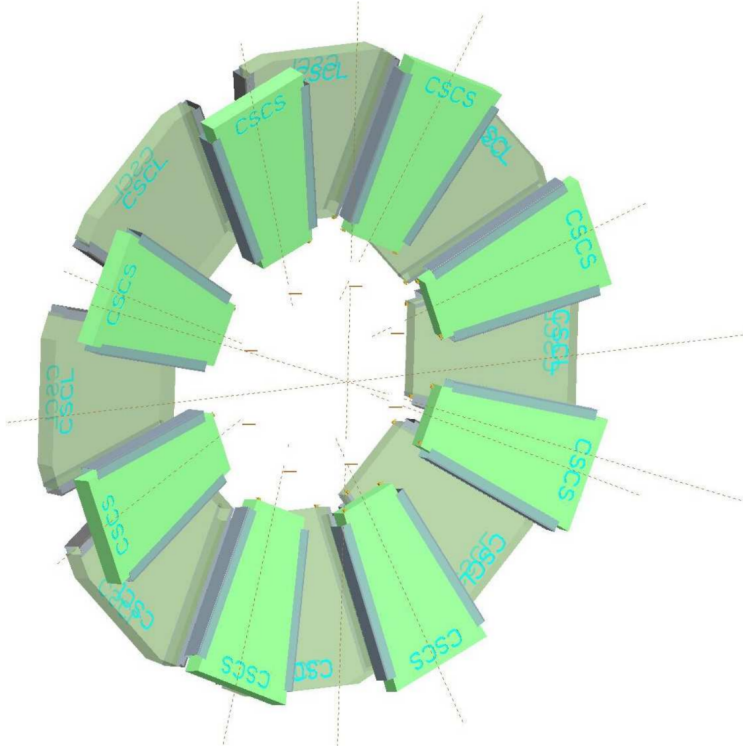


Figure 36: A schematic of the [CSC](#) endcap, showing the overlapping arrangement of the eight large and eight small chambers.

1743 6.5.4 THIN GAP CHAMBER

1744 Like in the barrel region, a separate, fast detector is required to provide position
 1745 measurements of muons for trigger in the endcap region. This is provided by
 1746 the [TGC](#) which consists of seven layers in the middle station of the endcap, two
 1747 doublet layers and one triplet layer, and a single doublet layer in the inner endcap
 1748 station. Figure 37 shows the arrangement of the triple and doublet layers of the
 1749 [TGCs](#).

1750 Like the [CSCss](#), the [TGCs](#) are multiwire proportional chambers with a wire-to-
 1751 cathode distance of 1.4 mm and a wire-to-wire distance of 1.8 mm. Readout
 1752 strips on the outside of the chambers run perpendicular to the wires, and couple
 1753 to the charge collected on the wires to provide a position measurement in the η
 1754 direction. The current induced on the wires is also readout to provide a position
 1755 measurement in the ϕ direction. The high electric field and small wire-to-wire
 1756 distance give it the required good time resolution to be used for triggering events.

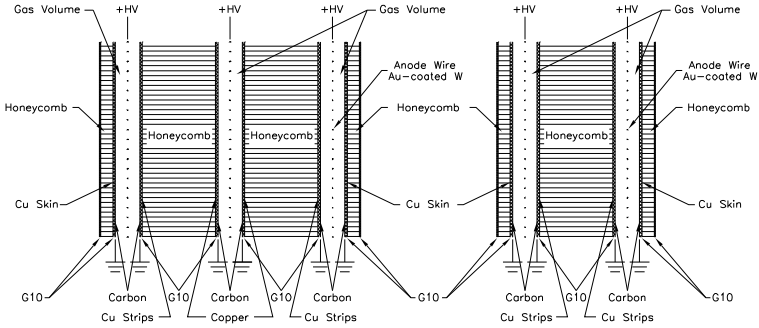


Figure 37: A schematic of the TGC doublet and triplet layers.

1757 6.6 TRIGGER

1758 It is not possible for the detector and the associated computing systems to record
 1759 the terabytes of data that the 40 MHz event rate produces every second. Instead,
 1760 a small fraction of these events are selected by the trigger system to be recorded
 1761 and later analyzed. Selecting interesting events at such a high rate poses a sig-
 1762 nificant challenge for the both the detector design and the implementation of a
 1763 trigger decision and data acquisition system. The trigger must balance the time
 1764 needed to decide to keep an event, to avoid losing information, with the filtering
 1765 accuracy to consistently select a full menu of physics events that can be used for
 1766 the wide array of searches and measurements targeted by [ATLAS](#).

1767 The [ATLAS](#) trigger system, as of Run 2, consists of two levels of decision mak-
 1768 ing. The first level, referred to as L1, is hardware based and uses inputs from
 1769 a subset of the detector elements to narrow the considered event rate from the
 1770 original 40 MHz down to 100 kHz. The 100 kHz rate is the maximal rate that the
 1771 event information can be transferred from the detector. The second, software-
 1772 based level, referred to as the [HLT](#), makes the final decisions on which events to
 1773 keep for analysis and selects a rate of around 1 kHz. The collection of selection
 1774 criteria used to make the L1 decisions feed into subsequent selection criteria in
 1775 the [HLT](#), and the set of these combinations of L1 and [HLT](#) criteria from the trig-
 1776 ger menu which defines exactly what events are recorded on [ATLAS](#). The trigger
 1777 menu used for 2015 data collection is shown in Table 7, which summarizes the
 1778 selection requirements at both levels and additionally shows the peak measured
 1779 rates contributed by each.

1780 At L1, the trigger system uses information primarily from the calorimeters
 1781 and muon spectrometer to select high p_T jets, electrons, photons, and muons.
 1782 The electromagnetic calorimeter uses reduced granularity energy measure-
 1783 ments as well as isolation requirements to select electrons and photons. The hadronic
 1784 calorimeter also uses a combination of reduced granularity energy measure-
 1785 ments and isolation to select high momentum jets and hadronically decaying tau lep-
 1786 tons.

1787 The calorimeters are also used to provide triggers based on missing energy:
 1788 the coarse granularity energy measurements are used to calculate a directional
 1789 sum of energies and to trigger on a significant imbalance. Only the [RPCs](#) and

Trigger	Typical offline selection	Trigger Selection		Level-1 Peak Rate (kHz)	HLT Peak Rate (Hz)
		Level-1 (GeV)	HLT (GeV)		
		$L = 5 \times 10^{33} \text{ cm}^{-2}\text{s}^{-1}$			
Single leptons	Single iso μ , $p_T > 21$ GeV	15	20	7	130
	Single e , $p_T > 25$ GeV	20	24	18	139
	Single μ , $p_T > 42$ GeV	20	40	5	33
	Single τ , $p_T > 90$ GeV	60	80	2	41
Two leptons	Two μ 's, each $p_T > 11$ GeV	2×10	2×10	0.8	19
	Two μ 's, $p_T > 19, 10$ GeV	15	18, 8	7	18
	Two loose e 's, each $p_T > 15$ GeV	2×10	2×12	10	5
	One e & one μ , $p_T > 10, 26$ GeV	$20 (\mu)$	7, 24	5	1
	One loose e & one μ , $p_T > 19, 15$ GeV	15, 10	17, 14	0.4	2
	Two τ 's, $p_T > 40, 30$ GeV	20, 12	35, 25	2	22
	One τ , one μ , $p_T > 30, 15$ GeV	12, 10 (+jets)	25, 14	0.5	10
Three leptons	One τ , one e , $p_T > 30, 19$ GeV	12, 15 (+jets)	25, 17	1	3.9
	Three loose e 's, $p_T > 19, 11, 11$ GeV	15, 2×7	17, 2×9	3	< 0.1
	Three μ 's, each $p_T > 8$ GeV	3×6	3×6	< 0.1	4
	Three μ 's, $p_T > 19, 2 \times 6$ GeV	15	18, 2×4	7	2
	Two μ 's & one e , $p_T > 2 \times 11, 14$ GeV	$2 \times 10 (\mu\text{'s})$	$2 \times 10, 12$	0.8	0.2
One photon	Two loose e 's & one μ , $p_T > 2 \times 11, 11$ GeV	$2 \times 8, 10$	$2 \times 12, 10$	0.3	< 0.1
	one γ , $p_T > 125$ GeV	22	120	8	20
Two photons	Two loose γ 's, $p_T > 40, 30$ GeV	2×15	35, 25	1.5	12
	Two tight γ 's, $p_T > 25, 25$ GeV	2×15	2×20	1.5	7
Single jet	Jet ($R = 0.4$), $p_T > 400$ GeV	100	360	0.9	18
	Jet ($R = 1.0$), $p_T > 400$ GeV	100	360	0.9	23
E_T^{miss}	$E_T^{\text{miss}} > 180$ GeV	50	70	0.7	55
Multi-jets	Four jets, each $p_T > 95$ GeV	3×40	4×85	0.3	20
	Five jets, each $p_T > 70$ GeV	4×20	5×60	0.4	15
	Six jets, each $p_T > 55$ GeV	4×15	6×45	1.0	12
b -jets	One loose b , $p_T > 235$ GeV	100	225	0.9	35
	Two medium b 's, $p_T > 160, 60$ GeV	100	150, 50	0.9	9
	One b & three jets, each $p_T > 75$ GeV	3×25	4×65	0.9	11
	Two b & two jets, each $p_T > 45$ GeV	3×25	4×35	0.9	9
b -physics	Two μ 's, $p_T > 6, 4$ GeV plus dedicated b -physics selections	6, 4	6, 4	8	52
Total				70	1400

Table 7: The trigger menu for the 2015 data collection with $L = 5 \times 10^{33} \text{ cm}^{-2}\text{s}^{-1}$. Both the L1 and HLT selection requirements and their trigger rates are shown measured at the specified luminosity are shown. The typical offline selections represent a typical set of offline requirements imposed after the trigger in an analysis.

1790 TGCs muon subdetectors contribute to the decision at L1, and are used to identify
 1791 high momentum muons. The contributions to the triggering rate of the various
 1792 types of L1 triggers are shown in Figure 38. The total rate is indicated in black
 1793 and is lower than the sum of individual rates because their is significant overlap
 1794 between different trigger channels. The majority of the rate comes from lepton
 1795 and photon triggers.

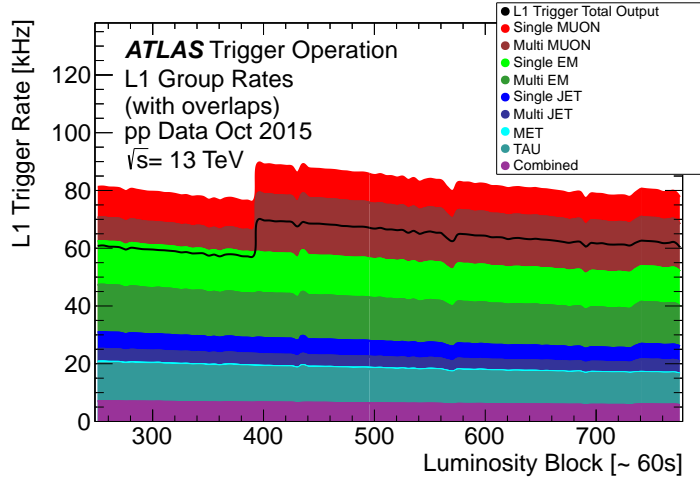


Figure 38: The L1 Trigger rate broken down into the types of triggers as a function of the luminosity block for the 2015 data collection period.

1796 After an event is chosen by the L1 trigger, the detector measurements from the
 1797 bunch crossing which fired the trigger is read out from the front-end electronics
 1798 and stored on read-out boards. This inclusive information is necessary to make
 1799 more the more precise event selections than is possible with the reduced infor-
 1800 mation at L1. The HLT then uses this information with software algorithms to
 1801 decide whether or not to permanently record the event. The L1 trigger also for-
 1802 wards which decision was made and Region of Interests (RoIs) to the HLT, which
 1803 allows the HLT to focus on particular algorithms and particular sections of the
 1804 detector to greatly improve the algorithmic selection speed. The additional in-
 1805 formation available to the HLT allows it to implement additional trigger targets,
 1806 such as identified jets from the decays of b-hadrons. The contributions to the
 1807 triggering rate of the various types of HLT triggers are shown in Figure 39.

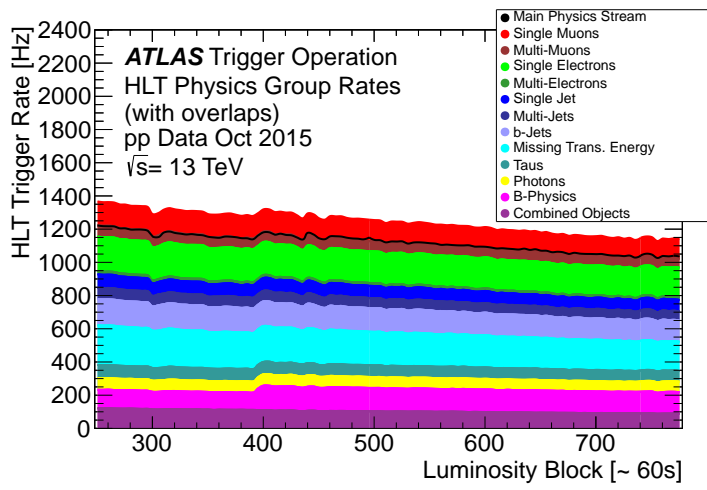


Figure 39: The HLT Trigger rate broken down into the types of triggers as a function of the luminosity block for the 2015 data collection period.

1808

1809 EVENT RECONSTRUCTION

1810 The ATLAS experiment combines measurements in the subdetectors to form a
 1811 cohesive picture of each physics event. The majority of particles that traverse
 1812 the detector leave behind some combination of ionization hits in the tracking
 1813 detectors or energy deposits in the calorimeters, and these measurements can
 1814 be used to reconstruct physical quantities like the particle's energy, momentum,
 1815 or trajectory. Even the type of the particle can be distinguished by comparing
 1816 the various ways that different species of stable particles interact with the sub-
 1817 detectors. Reconstruction is the series of algorithms which take the electronic
 1818 outputs of the detector and assigns them into individual physics objects. The
 1819 physics objects summarize the properties of particles produced by the collision
 1820 or subsequent decays, either for individual isolated particles like leptons, or for
 1821 a collection of the cascade of products produced in the decay of an energetic
 1822 hadron, called a jet. These are the objects and quantities most often used in anal-
 1823 ysis to make measurements of SM processes or to search for new physics.

1824 7.1 CHARGED PARTICLES

1825 As described in Section 6.3, charged particles that traverse the inner detector
 1826 leave behind hits in the subdetectors. Each of these hits translates into a position
 1827 measurement along the trajectory of that particle, with position resolutions de-
 1828 pending on the subdetector that provided the measurement. Track reconstruc-
 1829 tion uses these position measurements to collect hits in consecutive layers of
 1830 the detector into a trajectory consistent with a particle curving in a magnetic
 1831 field [13, 14]. This reconstructed trajectory is called a track. The number of hits
 1832 in the inner detector for each event makes a combinatorial method completely
 1833 infeasible: the algorithms that form tracks must be significantly more intelligent
 1834 so that event reconstruction does not exhaust computing resources.

1835 The first and primary algorithm employed in track reconstruction is called
 1836 the inside-out method, which begins with the assumption that the track orig-
 1837 inated from the interaction point. Its purpose is to identify primary particles,
 1838 those which originate in the proton-proton collisions and with a lifetime long
 1839 enough to reach the inner detector. Combinations of three hits are considered
 1840 from measurements in the Pixel detector and the SCT, and form the seed for a
 1841 track. Specifically, the seeding algorithm looks for a seed using three pixel hits,
 1842 two pixel hits and one SCT hit, or three SCT hits. The seed is then extrapolated
 1843 forwards and backwards into the Pixel and SCT detectors depending on the seed
 1844 location, and hits in each layer are considered to be added to the track using a
 1845 combinatorial Kalman filter [14]. After all of the silicon layers have been consid-
 1846 ered, tracks are filtered to reduce ambiguities from other nearby tracks or from
 1847 combinatorial coincidences. Then the tracks are extended outwards into the TRT

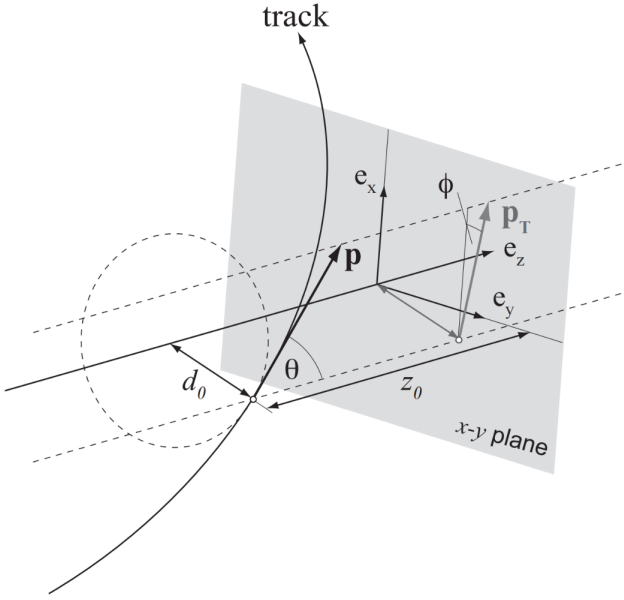


Figure 40: An illustration of the perigee representation of track parameters for an example track. The charge is not directly shown, but is indicated by the direction of curvature of the track [15].

in the same way. This algorithm is how the hits are chosen to be incorporated into a single track. Once the hits are collected, a fitting algorithm calculates the track parameters which best model the locations of the hits and their resolutions. The fitting uses five parameters, $(d_0, z_0, \phi, \theta, q/p)$, to specify a track in a perigee representation: d_0 and z_0 are the transverse and longitudinal impact parameters at the closest approach to the nominal beam axis, ϕ and θ are the usual angular coordinates, and q/p is the charge divided by the momentum. These parameters are illustrated in Figure 40. Those parameters directly determine the direction and momentum of the particle which produced the track.

This inside-out algorithm is complemented by an outside-in algorithm, which is used to find tracks from secondary particles, those produced in the decays or interactions of the primary particles inside the detector. As the name indicates, the outside-in algorithm begins by seeding tracks in the outermost layers of the inner detector, in the TRT. The seed in this case is formed by a segment in the TRT, and the track is propagated backwards into the SCT before being refitted to use all the included points. Some tracks are found with TRT segments only, which can result from interactions with the detector following the SCT. Figure 41 shows an example of the geometry of tracks formed by both algorithms, where the hits belonging to tracks found using the inside-out algorithm are highlighted in red, and the hits belonging to the tracks found using the outside-in algorithm are circled in black. The figure highlights the presence of a large number of both primary and secondary tracks in a single event, as well as the overall large number of hits present in the inner detector.

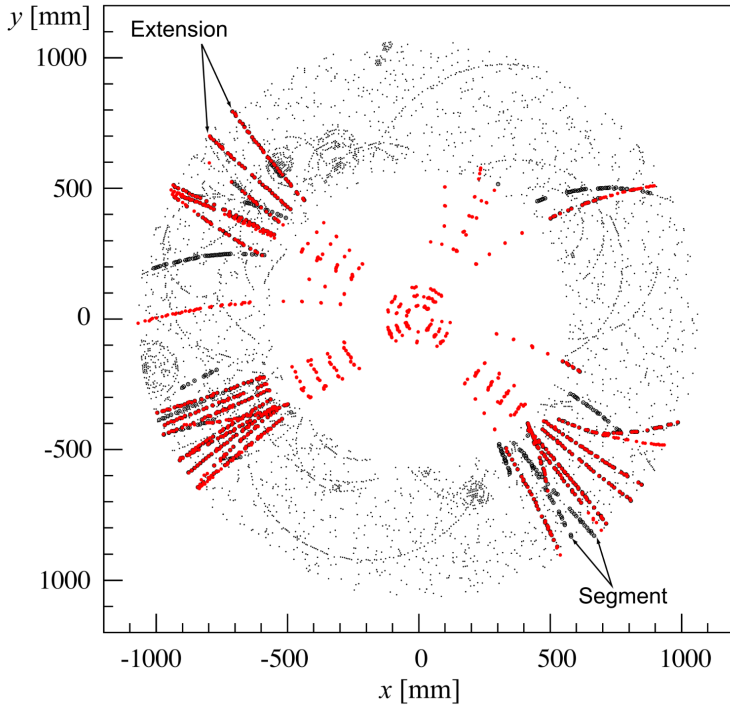


Figure 41: The x and y locations of the hits generated in a simulated $t\bar{t}$ event in the inner detector. The hits which belong to tracks formed using the inside-out algorithm are highlighted in red, while the hits which belong to tracks formed using the outside-in algorithm are circled in black.

1871 The tracks resulting from these algorithms can be contaminated by nearby
 1872 particles confusing the tracking algorithm in a high luminosity environment.
 1873 For example, enough hits present in the inner detector can lead to fake tracks
 1874 from combinations of hits from multiple individual tracks. Therefore, after the
 1875 tracks are formed and fitted, additional quality requirements are imposed in
 1876 order to reduce such backgrounds. Most tracking applications require at least
 1877 seven silicon hits, that is, seven hits between the Pixel detector and SCT. Then the
 1878 tracks are required to have at most two holes in the Pixel detector, where holes
 1879 are non-existing but expected measurements in a layer of the subdetector. If the
 1880 missing hit corresponds to an inactive module, however, it is not counted as a
 1881 hole but instead as a hit for tracking as the lack of a measurement is expected in
 1882 that case.

1883 7.1.1 PIXEL NEURAL NETWORK

1884 The hits in the Pixel detector are not typically confined to a single pixel, but
 1885 rather the charge is spread over several pixels per layer which are grouped to-
 1886 gether into clusters. The clustering of these pixels for isolated tracks is relatively
 1887 straightforward, but complications can arise in the high occupancy environment
 1888 where hits from multiple particles can overlap in a single cluster. Figure 42
 1889 shows examples of clusters generated by a single isolated particle, two nearly
 1890 overlapping particles, and a particle which emits a δ -ray. A δ -ray is a secondary

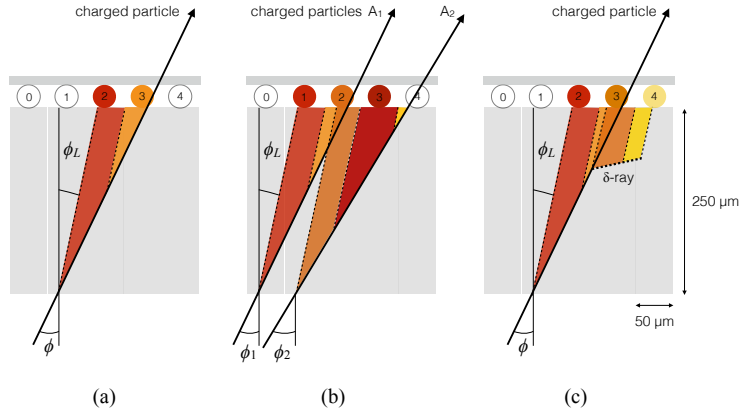


Figure 42: Examples of the clusters formed in a single layer of the pixel detector for (a) a single isolated particle, (b) two nearly-overlapping particles, and (c) a particle which emits a δ -ray [16].

1891 electron which is generated with enough energy to escape a significant distance
 1892 away from the original particle and to generate additional ionization.

1893 A series of neural-networks analyzes the shape of the clusters to determine
 1894 how many particles produced the cluster and to estimate the positions of each
 1895 of the particles within the cluster. These allow for an identification of clusters
 1896 caused by more than one particle or by a particle that emits a δ -ray. In a high-
 1897 density tracking environment, the multiple position outputs can be used as the
 1898 locations of individual hits to allow reconstruction of tracks which almost over-
 1899 lap and with a much better separation than is possible without the splitting of
 1900 individual clusters.

1901 7.1.2 PIXEL DE/DX

1902 A hit in the Pixel detector corresponds to the voltage generated from ionization
 1903 current rising above a threshold value that is tuned to consistently record the
 1904 passing of MIPs. A larger amount of charge deposited results in a larger voltage,
 1905 and a larger signal remains above the threshold for a longer period of time. The
 1906 time over threshold (**ToT**) is read out of the Pixel detector, and can be used to
 1907 provide a measurement of the charge deposited in each pixel. The charge mea-
 1908 surements from each of the pixels included in a pixel cluster are summed to form
 1909 one charge measurement per layer of the pixel detector. That charge measure-
 1910 ment, combined with the angle of incidence of the track and the known sizes of
 1911 each detector element, can be converted into a measurement of dE/dx , the ion-
 1912 ization energy deposited per unit distance, measured in $\text{MeVg}^{-1}\text{cm}^2$. The **IBL**
 1913 only has sixteen available values (4 bits) of **ToT** to readout, compared to the 256
 1914 available values (8 bits) in the remaining pixel layers. To help alleviate this lack
 1915 of range, the **IBL** also records if is in overflow: when the ionization is sufficient
 1916 to generate a **ToT** above the largest value that can be recorded in the 4 bits.

1917 The measurements across multiple layers are combined to form an average
 1918 value of dE/dx for the track as a whole. Depending on where a charge particle
 1919 is produced, it will traverse four Pixel layers and create four clusters on average.
 1920 It can produce as few as two clusters in the Pixel detector if it passes through in-
 1921 active modules, and as many as five if it is in a region of the detector where multiple
 1922 modules overlap. To reduce the influence of the typical long Landau tails of the
 1923 distribution of dE/dx deposits [10], the average is calculated as a truncated mean
 1924 of these clusters. The value measured in the IBL is removed if it is in overflow, as
 1925 the measured value is not reliable in that case. If a track has five measurements
 1926 in the pixel detector, the two highest cluster values are removed. If a track has
 1927 two, three, or four measurements in the pixel detector, only the single highest
 1928 cluster value is removed. The remaining values are averaged to form the pixel
 1929 dE/dx .

1930 7.1.3 VERTEX RECONSTRUCTION

1931 A vertex represents the intersection of multiple tracks and corresponds to the
 1932 location of an interaction. If at least two charged particles result from the in-
 1933 teraction, the intersection of their resulting tracks reveals its position with high
 1934 precision. Vertices are divided into two groups, primary vertices which corre-
 1935 spond to the actual proton-proton collisions, and secondary vertices which cor-
 1936 respond to decays of short-lived particles or interactions with the detector. Pri-
 1937 mary vertices are particularly important, as they can provide a precise location
 1938 for the interaction which generated the observed particles. Understanding that
 1939 location is crucial in understanding the geometry of the event.

1940 Primary vertices are reconstructed by iteratively identifying seeds from recon-
 1941 structed tracks [17]. Each track's extrapolated z position at the beamline forms a
 1942 seed, and nearby tracks are fitted using that position as a point along their trajec-
 1943 tory. The goodness of fit with that vertex is considered for each track, measured
 1944 in χ^2 . The final position of the vertex is determined by a fit to all of the con-
 1945 sidered tracks, where the contribution from each track is weighted according to
 1946 the χ^2 compatibility with that vertex. Any tracks from this procedure that are
 1947 displaced by more than 7σ from that vertex are removed from the fit and used
 1948 to seed a new vertex. This procedure is iterated until no additional vertices can
 1949 be found.

1950 This procedure is typically performed twice. The first set of vertices is used
 1951 to fit a profile for the beamspot, which indicates the position of the intersection
 1952 of beams in that particular bunch crossing. The fitted beamspot then provides
 1953 a constraint for the second attempt to locate primary vertices, where both the
 1954 track fitting and seeding of vertices are required to be consistent with interac-
 1955 tions occurring within the beamspot.

1956 7.2 ELECTRONS AND PHOTONS

1957 Electrons are measured as both a charged particle track and energy deposits in
 1958 the electromagnetic calorimeter. Photons, on the other hand, leave energy de-

1959 posits in the electromagnetic calorimeter but do not produce a corresponding
 1960 track. Because the electromagnetic interactions with the calorimeter of both
 1961 photons and electrons produces more photons and electrons, the behavior in the
 1962 calorimeter is very similar and there is significant overlap in the reconstruction
 1963 techniques for each.

1964 The reconstruction of a photon or an electron in the calorimeter is based on
 1965 clustering algorithms which identify groups of energy deposits [18–20]. For this
 1966 purpose, the entire electromagnetic calorimeter is subdivided into a grid of 200
 1967 by 256 towers in the η and ϕ directions, respectively, where the individual grid
 1968 units have a size of $\Delta\eta = 0.025$ and $\Delta\phi = 0.025$. These towers correspond to
 1969 individual cells in the middle, coarsest layer of the EM calorimeter, and in the re-
 1970 maining layers the cells are grouped together cover the same area in $\eta - \phi$ space.
 1971 The clustering begins by finding seeds with a sliding-window algorithm based
 1972 on the towers: a window of 3 by 5 towers is formed and translated until the sum
 1973 of the energy within the window is maximized. If that energy is above 2.5 GeV,
 1974 then that region becomes a seed. The choice of 2.5 GeV was chosen to com-
 1975 promise between maximizing reconstruction efficiency while minimizing fake
 1976 electron seeds from electronic noise or soft hadrons from additional interactions.
 1977 The seeds are rejected if the energy measured in the hadronic calorimeter behind
 1978 the seed is large, as this typically indicates a hadron rather than an electron or
 1979 photon.

1980 Next, the inner detector tracks within a cone of $\Delta R = 0.3$ are compared to
 1981 the location and energy of the seed. Tracks are matched to the cluster if the ex-
 1982 trapolation of the track to the energy-weighted center in the middle layer of the
 1983 EM calorimeter falls within $\Delta\phi < 0.2$ in the direction of the curvature of the
 1984 track or $\Delta\phi < 0.05$ in the direction opposite of the curvature of the track. If the
 1985 seed matches with a track that originated from a primary vertex, the combina-
 1986 tion of track and electromagnetic cluster is reconstructed as an electron. If the
 1987 seed matches with a track that did not originate from a primary vertex, then the
 1988 electromagnetic cluster is reconstructed as a converted photon. And if there is
 1989 no corresponding track in the inner detector, than the cluster is reconstructed
 1990 as a photon.

1991 After classification, the final clustering of the energy in the EM calorimeter
 1992 calorimeter is performed. The classification must be done first, as the expected
 1993 size of the energy deposits in the calorimeter are different for electrons and pho-
 1994 tons. In the barrel region, the final clusters for electrons are formed in rectangles
 1995 of 3 towers in the η -direction and 7 towers in the ϕ -direction. This asymmetric
 1996 window accounts for the curving of the produced charged particles only in the
 1997 ϕ direction. For photons, the size of the rectangle is 3 towers by 5 towers. In the
 1998 endcap region, all object types are clustered in rectangles of 5 towers by 5 tow-
 1999 ers, as the effect of the magnetic field curvature is less pronounced in this region.
 2000 The sum of the energies in these clusters provide the final energy measurement
 2001 for the electron or photon.

2002 7.2.1 PHOTON IDENTIFICATION

2003 The original requirement for constructing a photon cluster, a significant energy
 2004 deposit in the electromagnetic calorimeter without a corresponding track or en-
 2005 ergy deposits in the hadronic calorimeter, is already effective in identifying pho-
 2006 tons. However, there is a significant background for prompt photon production
 2007 from the decays of pions, $\pi^0 \rightarrow \gamma\gamma$. These can be identified using the shape of
 2008 the cluster in the narrow η granularity in the first layer of the EM calorimeter.

2009 7.2.2 ELECTRON IDENTIFICATION

2010 Prompt electrons have a number of backgrounds, such as secondary electrons
 2011 from hadron decays or misidentified hadronic jets, that can be rejected using ad-
 2012 dditional information from the EM calorimeter and the inner detector. The most
 2013 basic level of electron identification, referred to as Loose, makes requirements
 2014 on the shower shapes in the high granularity first layer of the EM calorimeter
 2015 as well as the quality of the inner detector track. It also requires a good match
 2016 between the track and the calorimeter energy deposits and a small fraction of
 2017 energy in the hadronic calorimeter behind the electromagnetic cluster. ATLAS
 2018 defines several additional working points, including Medium and Tight, which
 2019 provide progressively lower background rates for electrons by imposing addi-
 2020 tionally strict requirements on the above variables as well as new requirements
 2021 like the impact parameter of the inner detector track or the comparison of the
 2022 cluster energy to the momentum in the inner detector.

2023 7.3 MUONS

2024 Muons produced in ATLAS first traverse the inner detector and leave behind a
 2025 track as described in Section 7.1. The muon then passes through the calorimeter,
 2026 leaving behind a small, characteristic amount of energy, and then passes through
 2027 the muon spectrometer where it produces hits in the MDTs or CSCs. Muon tracks
 2028 are formed from local segments of hits in each layer of the MDTs or CSCs, and
 2029 then the final muon spectrometer track is formed by combining the two local
 2030 segments [21]. When a track is reconstructed in both the inner detector and
 2031 the muon spectrometer, the track is refitted to include the hits in both the inner
 2032 detector and the muon spectrometer, and forms a combined muon.

2033 In a few regions of the detector, a muon may fail to leave behind both a com-
 2034 plete inner detector and muon system track. For a very small fraction of the
 2035 acceptance of the muon system, there is only one layer of muon chambers and a
 2036 global muon system track is not formed. In this case, as long as the track in the
 2037 inner detector exists and geometrically matches to a segment, a segment-tagged
 2038 muon is formed using momentum measurements from the inner detector. In
 2039 the region where the muon system has coverage but the inner detector does not,
 2040 $2.5 < |\eta| < 2.7$, a stand-alone muon is formed which uses only information
 2041 from the muon system. And for muons produced within one of the few holes in
 2042 the muon system, including $|\eta| < 0.1$, the characteristic energy deposits in the

2043 calorimeter can be used to tag an inner detector track as a calo-tag muon. These
 2044 additional categories are used to achieve high efficiency over a larger range of
 2045 acceptance, but the combined muons are the most reliable.

2046 7.3.1 MUON IDENTIFICATION

2047 The various types of muons are incorporated into three working points: Loose,
 2048 Medium, and Tight, which reflect the increasing muon purity for each of the
 2049 selections definitions. Tight muons include only combined muons with a good
 2050 track fit quality and momentum resolution and at least two hits in a precision
 2051 muon system layer. Medium muons include those in tight as well as combined
 2052 muons with one precision hit and one precision hole, where hole is defined in
 2053 the same way as in Section 7.1. The medium working point also includes stand-
 2054 alone muons with $|\eta| > 2.5$ and at least two hits in precision layers. And finally
 2055 the loose working point includes both medium and tight muons, but additional
 2056 includes segment-tagged and calo-tagged muons in the region $|\eta| < 0.1$.

2057 7.4 JETS

2058 A jet does not directly correspond to a physical particle, unlike all of the recon-
 2059 structed objects described above, but instead tries to capture the conical cascade
 2060 of particles produced in the hadronization of a quark or gluon from the proton-
 2061 proton collision. The hadronization process creates a very large number of col-
 2062 limated particles, with a high enough density that individually reconstructing all
 2063 of the produced particles in the calorimeter is not possible within ATLAS. How-
 2064 ever most analyses are interested only in the kinematics of the particle which
 2065 produced the cascade, rather than the individual products. Therefore, jets are
 2066 a useful tool to measure the combined energy and direction of the ensemble of
 2067 products and thus represents the kinematics of the original. Jet algorithms are
 2068 very generic and can be used to group together a number of types of objects to
 2069 form aggregate representations. For example, truth particles in simulation can
 2070 be grouped in truth jets, or tracks from the inner detector can be grouped to-
 2071 gether to form track jets. This section, however, will focus on calorimeter jets
 2072 which take topoclusters of energy deposits in the calorimeter as inputs and pro-
 2073 duce a combined object which represents the energy measured by the calorime-
 2074 ter and the location where it was deposited.

2075 7.4.1 TOPOLOGICAL CLUSTERING

2076 Hadrons often deposit their energy into multiple individual cells in both the elec-
 2077 tromagnetic and hadronic calorimeters. The purpose of topological clustering is
 2078 to group cells in all three dimensions into clusters that represent a single energy
 2079 deposit. The procedure must be robust enough to reject noise fluctuations in
 2080 the cell energy measurements that can come from both electronic noise and ad-
 2081 dditional low energy particles produced in pileup activity. The background level

of calorimeter noise is called σ_{noise} , and is an important component of the topological clustering.

The topological clusters are formed in a three step process called the 4-2-0 threshold scheme, which uses three energy thresholds to build up a cluster from cells [22]. First, any cells with a measured energy above $4\sigma_{\text{noise}}$ are identified as seed cells. The cells adjacent to the seed cells with a measured energy above $2\sigma_{\text{noise}}$ are called secondary cells. All of the cells which are adjacent to a secondary cell with $E_{\text{cell}} > 2\sigma_{\text{noise}}$ are also labeled secondary cells. Tertiary cells are those immediately adjacent to a seed or secondary cell with a measured energy above zero. Adjacency in this sense is defined in three dimensions, cells are adjacent if they are neighbors within a layer but also if they have the same $\eta - \phi$ coordinates but are in adjacent layers or even in an adjacent layer in another calorimeter.

From these definitions, clusters are built by resolving the seeds in order of significance, the ratio $E_{\text{cell}}/\sigma_{\text{noise}}$. All adjacent secondary cells to the highest significance seed are added to that seed's topocluster, and any of those cells which would also have qualified as seeds are removed from the list of seeds. Once all of the secondary cells have been added, the tertiary cells are then added to that cluster as well. This procedure is then iterated until no seeds remain, forming the first round of topoclusters.

It is also useful to split topoclusters into multiples if local maxima are present within the topocluster, as clusters produced by multiple nearby particles can merge. The splitting process begins by finding local maxima cells in the middle layer of the calorimeters with a minimum energy of 500 MeV and at least four neighboring secondary cells. These requirements reduce the likelihood to split a cluster due to random fluctuations, as the middle layers provide the most reliable energy measurements. Cells between two local maxima can then be shared between two clusters to account for overlapping contributions from two particles. The energy sharing is weighted by the energy of each cluster as well as the distance of the cell to the centroid of that cluster.

The energies of all the cells in the cluster are then summed together to form the energy of that cluster. The energy needs to be corrected for the various losses expected in the calorimeter, as described in Section 6.4. The simplest correction, scaling the measured energy by the sampling fraction, brings the cluster energies to the EM scale. It is called the EM scale because it accurately describes the energy of electromagnetic showers.

Another scale is defined to improve accuracy for hadronic processes, the local cluster weighted (LCW) scale, that helps to correct for the expected variations in hadronic energy deposits. The LCW correction first determines if the shower is hadronic or electromagnetic, based on the depth of the shower and the cluster energy density. For hadronic showers, the energy is corrected for calorimeter non-compensation, an effect which reduces the measured energy of hadronic showers because some of the energy goes into invisible processes like the break up of nuclei. All clusters are then corrected for energy that may be deposited in uninstrumented regions in that cluster's location in the calorimeter, and they are

2127 also corrected with an estimate of how much energy falls outside the extent of
 2128 the cluster based on its shape and the deposit type.

2129 7.4.2 JET ALGORITHMS

2130 Using the topological clusters as inputs, a jet algorithm groups them together
 2131 into a collection of adjacent energy deposits that is intended to correspond to
 2132 a single process [23]. Jet algorithms need a few key characteristics to be usable
 2133 for physics analysis. First, the jets produced by the algorithm should have little
 2134 dependence on the addition of soft particles to the event (infrared safety), as a
 2135 negligible addition of energy should not significantly modify the event topology.
 2136 Similarly, the jets produced by the algorithm should also not significantly depend
 2137 on mostly collinear splitting of an input particle (collinear safety); that is, a single
 2138 quark replaced by two, parallel quarks with half the original's momentum should
 2139 not change the resulting jets, which are intended to capture only the properties
 2140 of the aggregate and not those of individual particles. And finally the algorithm
 2141 needs to be sufficiently simple and fast to be used for the large rate of collected
 2142 proton-proton collisions on [ATLAS](#).

2143 The most commonly used algorithm on [ATLAS](#) that satisfies these requirements
 2144 is called the anti- k_t algorithm, and is discussed in further detail in Reference [24].
 2145 The anti- k_t , in brief, relies on iteratively combining the input objects that are
 2146 closest together, where closest is defined by a particular distance metric, $d_{i,j}$,
 2147 where the index i represents the combination constructed so far and j is an ad-
 2148 ditional object being considered. The combinations stop when the closest re-
 2149 maining object is the beam itself, where the distance to the beam is called $d_{i,B}$.
 2150 An entire class of algorithms follows this procedure with the following distance
 2151 metrics

$$d_{i,j} = \min(k_{ti}^{2p}, k_{tj}^{2p}) \frac{\Delta_{ij}^2}{R^2} \quad (18)$$

$$d_{i,B} = k_{ti}^{2p} \quad (19)$$

2152 where $\Delta_{ij} = (y_i - y_j)^2 + (\phi_i - \phi_j)^2$, k_{ti} is the transverse momentum of the
 2153 object, y is the rapidity, and p is a parameter of the algorithm. Anti- k_t is the
 2154 particular case where $p = -1$, and is a choice that results in an algorithm that is
 2155 both infrared and collinear safe.

2156 The algorithm is repeated until there are no input objects remaining, which
 2157 results in a series of jets. Each jet has a complete four momentum from the com-
 2158 bination of its input clusters, where the combinations assume a mass of zero.
 2159 The jet energies then need to be calibrated to attempt to match the energy of the
 2160 object which produced the jet.

2161 7.4.3 JET ENERGY SCALE

2162 Though the [LCW](#) scheme attempts to correct the topoclusters to reflect the true
 2163 deposited energy, the correction does not fully account for energy lost within

2164 the calorimeters. Because of these effects, the original reconstructed jet energy
 2165 does not reflect the true energy of the particle which initiated the jet. Therefore
 2166 it is necessary to additionally correct the reconstructed jet itself, in addition to
 2167 the corrections on the inputs. This correction is referred to as the **JES**, which
 2168 combines several individual steps of calibration [25].

2169 The first calibration step corrections the direction of the jet to ensure that it
 2170 points back to the primary vertex. Next, the energy of the jet is corrected for
 2171 pileup by subtracting the expected contribution from pileup based on the mo-
 2172 mentum, η , and area of the jet as well as the number of reconstructed vertices
 2173 and expected number of interactions per crossing. The largest single correction
 2174 is the absolute η and scale correction, where the jet energy and pseudorapidity
 2175 is corrected to attempt to match the energy and pseudorapidity of the parton
 2176 which produced it. This correction is measured in simulation by comparing the
 2177 reconstructed jet energies to the energy of the truth particle which produced it.
 2178 However the simulation is not relied on alone to estimate this correction, and an
 2179 additional step applies an additional energy correction based on in-situ measure-
 2180 ments in data. These corrections come from various techniques which measure
 2181 jet energies indirectly by balancing them with other, well-measured objects. In
 2182 the central region ($|\eta| < 1.2$), jets are balanced against photons and the leptonic
 2183 decays of Z bosons and high momentum jets ($p_T > 210$ GeV) are also balanced
 2184 against multiple smaller jets in multijet events. Jets at larger pseudorapidities,
 2185 above $|\eta| = 1.2$, are calibrated by balancing with lower pseudorapidity jets.

2186 These steps introduce a number of systematic uncertainties, referred to as
 2187 the **JES** uncertainty. The largest of these comes from the in-situ measurements,
 2188 which are statistically limited in measuring high momentum and high pseudora-
 2189 pidity jets. The total, fractional **JES** uncertainty is shown as a function of p_T in
 2190 Figure 43. The uncertainty falls to a minimum value of just over 1.0% around a
 2191 few hundred GeV, and rises again at high momentum because of the difficulty of
 2192 measuring jet balance in data above 2-3 TeV. The uncertainty is also minimized
 2193 at low $|\eta|$, and grows at large $|\eta|$ again where making in-situ measurements is
 2194 difficult. This technique does not actually provide a measurement of the uncer-
 2195 tainty for the highest energy jets, above 3 TeV, because there are not enough
 2196 measured data events to provide them. An alternative method for deriving the
 2197 **JES** and **JES** uncertainty that can be used even for very high p_T jets will be dis-
 2198 cussed in Chapter 9.

2199 7.5 MISSING TRANSVERSE ENERGY

2200 Among stable **SM** particles, only the neutrino cannot be directly measured in the
 2201 **ATLAS** detector. Because the neutrino carries neither electric nor color charge, it
 2202 is very unlikely to interact with the tracking detectors or the calorimeters, and in-
 2203 stead passes through the detector completely unobserved. Some particles which
 2204 have been conjectured to exist, like the **LSP** in many **SUSY** models, would also
 2205 have the same behavior. Therefore, it is important for **ATLAS** to provide some
 2206 way to assess the momentum carried away by a neutral, colorless particle. This
 2207 can be accomplished through a measurement of missing energy in the transverse

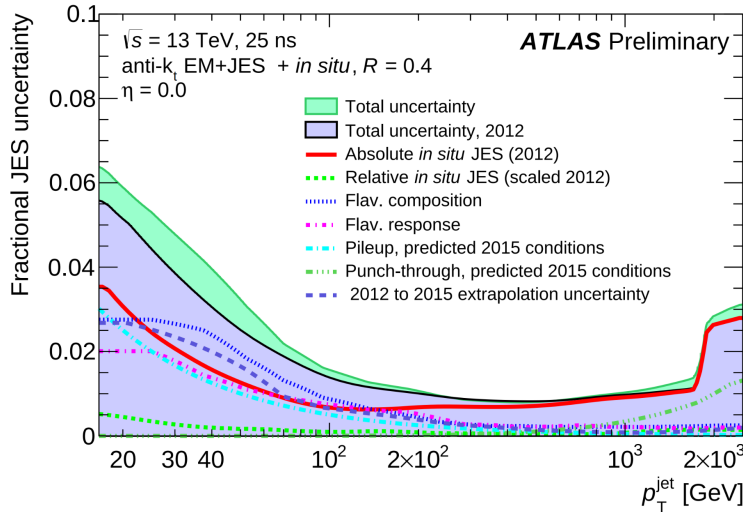


Figure 43: The total, fractional JES uncertainties estimated for 2015 data as a function of jet p_T .

2208 direction, or E_T^{miss} , which quantifies the momentum imbalance of the observed
 2209 particles. From the conservation of momentum and the lack of the initial mo-
 2210 mentum in the transverse plane in the proton-proton collisions, any imbal-
 2211 ance of momentum can be inferred to be carried away by an unmeasured particle.

2212 E_T^{miss} is more precisely defined as the magnitude of the vector sum of the
 2213 (p_x, p_y) components of each observed object's momentum. The definition is
 2214 simple, but there can be significant complexity in defining the inputs. As of Run
 2215 2, ATLAS uses a common algorithmic approach to carefully calculate missing en-
 2216 ergy, but each analysis is free to define its own inputs. For the analysis discussed
 2217 throughout this thesis, the missing energy inputs consist of the electrons, pho-
 2218 tons, muons, and jets discussed in the previous sections, in addition to a track-
 2219 based soft term.

2220 To produce the most precise measurement of E_T^{miss} , it is important to use the
 2221 best representation of the momentum of each of the input objects, which can
 2222 often be reconstructed as multiple different types in a single event. For example,
 2223 an electron can be reconstructed separately as an electron (Section 7.2) and a
 2224 jet (Section 7.4), but the electron representation has the highest precision for
 2225 reconstructing the true electron momentum. To ensure no duplications in the
 2226 E_T^{miss} definition, the inputs are collectively considered for overlap removal. Only
 2227 the most precise object type is kept for objects that fall within a cone of $\Delta R < 0.2$
 2228 for pairs of electrons and jets and a cone of $\Delta R < 0.4$ for other pair types.

2229 The fully reconstructed objects do not include all of the energy within the
 2230 events, as some clusters do not enter into a jet and some tracks are not classified
 2231 as electrons or muons. These momentum carried by these objects is accounted
 2232 for in a soft-term, which tallies all of the energy carried by the particles too soft
 2233 to form separate objects. The track soft term uses only tracking information to
 2234 estimate the contribution of soft objects, and does so by vectorially summing the
 2235 momentum of all well-reconstructed tracks with momentum above 400 MeV.

2236 All of these contributions together give a single E_T^{miss} value for a given event.
2237 The direction of that missing energy is taken as opposite the vector sum of all the
2238 constituents, to correspond to the momentum an invisible particle would have to
2239 have to make the event balanced. Depending on the context, this missing energy
2240 can be considered the energy of a neutrino or an LSP, with a large missing energy
2241 being a common signal criteria for searches for new physics.

2242

PART IV

2243

CALORIMETER RESPONSE

2244

You can put some informational part preamble text here.

2245

2246 RESPONSE MEASUREMENT WITH SINGLE HADRONS

2247 As discussed in Section 7.4, colored particles produced in collisions hadronize
2248 into jets of multiple hadrons. One approach to understanding jet energy mea-
2249 surements in the ATLAS calorimeters is to evaluate the calorimeter response to
2250 those individual hadrons; measurements of individual hadrons can be used to
2251 build up an understanding of the jets that they form. The redundancy of the
2252 momentum provided by the tracking system and the energy provided by the
2253 calorimeter provides an opportunity to study calorimeter response using real
2254 collisions, as described further in Section 8.2.

2255 Calorimeter response includes a number of physical effects that can be ex-
2256 tracted to provide insight into many aspects of jet modeling. First, many charged
2257 hadrons interact with the material of the detector prior to reaching the calorime-
2258 ters and thus do not deposit any energy. Comparing this effect in data and simu-
2259 lation is a powerful tool in validating the interactions of particles with the mate-
2260 rial of the detector and the model of the detector geometry in simulation, see Sec-
2261 tion 8.2.2. The particles which do reach the calorimeter deposit their energy into
2262 several adjacent cells, which are then clustered together. The energy of the clus-
2263 ter is then the total energy deposited by that particle. Comparing the response of
2264 hadrons in data to that of simulated hadrons provides a direct evaluation of the
2265 showering of hadronic particles and the energy deposited by particles in matter
2266 (Section 8.2.4).

2267 The above studies all use an inclusive selection of charged particles, which are
2268 comprised predominantly of pions, kaons, and (anti)protons. It is also possible to
2269 measure the response to various identified particle types separately to evaluate
2270 the simulated interactions of each particle, particularly at low energies where
2271 differences between species are very relevant. Pions and (anti)protons can be
2272 identified through decays of long-lived particles, in particular Λ , $\bar{\Lambda}$, and K_S^0 , and
2273 then used to measure response as described above. This is discussed in detail in
2274 Section 8.3.

2275 The results in this chapter use data collected at 7 and 8 TeV collected in 2010
2276 and 2012, respectively. Both are included as the calorimeter was repaired and
2277 recalibrated between those two data-taking periods. Both sets of data are com-
2278 pared to an updated simulation that includes new physics models provided by
2279 Geant4 [26] and improvements in the detector description [27, 28]. The present
2280 results are published in European Physical Journal C (EPJC) [29] and can be com-
2281 pared to a similar measurement performed in 2009 and 2010 [30], which used
2282 the previous version of the simulation framework [31].

2283 8.1 DATASET AND SIMULATION

2284 8.1.1 DATA SAMPLES

2285 The two datasets used in this chapter are taken from dedicated low-pileup runs
 2286 where the fraction of events with multiple interactions was negligible. These
 2287 datasets are used rather than those containing full-pileup events to facilitate mea-
 2288 surement of isolated hadrons. The 2012 dataset at $\sqrt{s} = 8$ TeV contains 8 mil-
 2289 lion events and corresponds to an integrated luminosity of 0.1 nb^{-1} . The 2010
 2290 dataset at $\sqrt{s} = 7$ TeV contains 3 million events and corresponds to an inte-
 2291 grated luminosity of 3.2 nb^{-1} . The latter dataset was also used for the 2010 re-
 2292 sults [30], but it has since been reanalyzed with an updated reconstruction in-
 2293 cluding the final, best understanding of the detector description for the material
 2294 and alignment from Run 1.

2295 8.1.2 SIMULATED SAMPLES

2296 The two datasets above are compared to simulated single-, double-, and non-
 2297 diffractive events generated with Pythia8 [32] using the A2 configuration of
 2298 hadronization [33] and the MSTW 2008 parton-distribution function set [34,
 2299 35]. The admixture of the single-, double-, and non-diffractive events uses the
 2300 default relative contributions from Pythia8. The conditions and energies for
 2301 the two simulations are chosen so that they match those of the corresponding
 2302 dataset.

2303 To evaluate the interaction of hadrons with detector material, the simulation
 2304 uses two different collections of hadronic physics models, called physics lists, in
 2305 Geant4 9.4 [36]. The first, QGSP_BERT, combines the Bertini intra-nuclear
 2306 cascade [37–39] below 9.9 GeV, a parametrized proton inelastic model from 9.5
 2307 to 25 GeV [40], and a quark-gluon string model above 12 GeV [41–45]. The
 2308 second, FTFP_BERT, combines the Bertini intra-nuclear cascade [37–39] below
 2309 5 GeV and the Fritiof model [46–49] above 4 GeV. In either list, Geant4 en-
 2310 forces a smooth transition between models where multiple models overlap.

2311 8.1.3 EVENT SELECTION

2312 The event selection for this study is minimal, as the only requirement is selecting
 2313 good-quality events with an isolated track. Such events are triggered by requir-
 2314 ing at least two hits in the minimum-bias trigger scintillators. After trigger, each
 2315 event is required to have exactly one reconstructed vertex, and that vertex is re-
 2316 quired to have four or more associated tracks.

2317 The particles which are selected for the response measurements are first iden-
 2318 tified as tracks in the inner detector. The tracks are required to have at least 500
 2319 MeV of transverse momentum. To ensure a reliable momentum measurement,
 2320 these tracks are required to have at least one hit in the pixel detector, six hits in
 2321 the SCT, and small longitudinal and transverse impact parameters with respect
 2322 to the primary vertex [30]. For the majority of the measurements in this chapter,

2323 the track is additionally required to have 20 hits in the TRT, which significantly
 2324 reduces the contribution from tracks which undergo nuclear interactions. This
 2325 requirement and its effect is discussed in more detail in Section 8.2.5. In addition,
 2326 tracks are rejected if there is any other reconstructed track which extrapolates
 2327 to the calorimeter within a cone of $\Delta R = \sqrt{(\Delta\phi)^2 + (\Delta\eta)^2} < 0.4$. This require-
 2328 ment guarantees that the contamination of energy from nearby charged particles
 2329 is negligible [30].

2330 8.2 INCLUSIVE HADRON RESPONSE

2331 The calorimeter response is more precisely defined as the ratio of the measured
 2332 calorimeter energy to the true energy carried by the particle, although this true
 2333 energy is unknown. For charged particles, however, the inner detector provides
 2334 a very precise measurement of momentum (with uncertainty less than 1%) that
 2335 can be used as a proxy for true energy. The ratio of the energy deposited by
 2336 the charged particle in the calorimeter, E , to its momentum measured in the
 2337 inner detector p , forms the calorimeter response measure called E/p . Though
 2338 the distribution of E/p contains a number of physical features, this study focuses
 2339 on the trends in two aggregated quantities: $\langle E/p \rangle$, the average of E/p for the
 2340 selected tracks, and the zero fraction, the fraction of tracks with no associated
 2341 energy in the calorimeter for those tracks.

2342 The calorimeter energy assigned to a track is defined using clusters. The clus-
 2343 ters are formed using a 4–2–0 algorithm [50] that begins with seeds requiring
 2344 at least 4 times the average calorimeter cell noise. The neighboring cells with
 2345 at least twice that noise threshold are then added to the cluster, and all bound-
 2346 ing cells are then added with no requirement. This algorithm minimizes noise
 2347 contributions through its seeding process, and including the bounding cells im-
 2348 proves the energy resolution [51]. The clusters are associated to a given track
 2349 if they fall within a cone of $\Delta R = 0.2$ of the extrapolated position of the track,
 2350 which includes about 90% of the energy on average [30]. This construction is
 2351 illustrated in Figure 44.

2352 8.2.1 E/P DISTRIBUTION

2353 The E/p distributions measured in both data and simulation are shown in Fig-
 2354 ure 45 for two example bins of track momentum and for tracks in the central
 2355 region of the detector. These distributions show several important features of
 2356 the E/p observable. The large content in the bin at $E = 0$ comes from tracks that
 2357 have no associated cluster, which occurs due to interactions with detector mate-
 2358 rial prior to reaching the calorimeter or the energy deposit being insufficiently
 2359 large to generate a seed, and are discussed in Section 8.2.2. The small negative
 2360 tail also comes from tracks that do not deposit any energy in the calorimeter but
 2361 are randomly associated to a cluster with an energy below the noise threshold.
 2362 The long positive tail above 1.0 comes from the contribution of neutral parti-
 2363 cles. Nearby neutral particles deposit (sometimes large) additional energy in the
 2364 calorimeter but do not produce tracks in the inner detector, so they cannot be

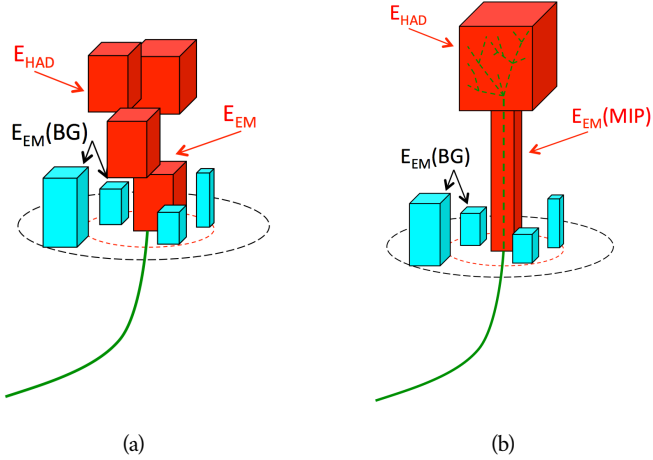


Figure 44: An illustration (a) of the E/p variable used throughout this paper. The red energy deposits come from the charged particle targeted for measurement, while the blue energy deposits are from nearby neutral particles and must be subtracted. The same diagram (b) for the neutral-background selection, described in Section 8.2.3.

2365 rejected by the track isolation requirement. Additionally the peak and mean of
2366 the distribution falls below 1.0 because of the loss of energy not found within
2367 the cone as well as the non-compensation of the calorimeter.

The data and simulation share the same features, but the high and low tails are significantly different. The simulated events tend to overestimate the contribution of neutral particles to the long tail, an effect which can be isolated and removed as discussed in Section 8.2.3. Additionally, the simulated clusters have less noise on average, although this is a small effect on the overall response.

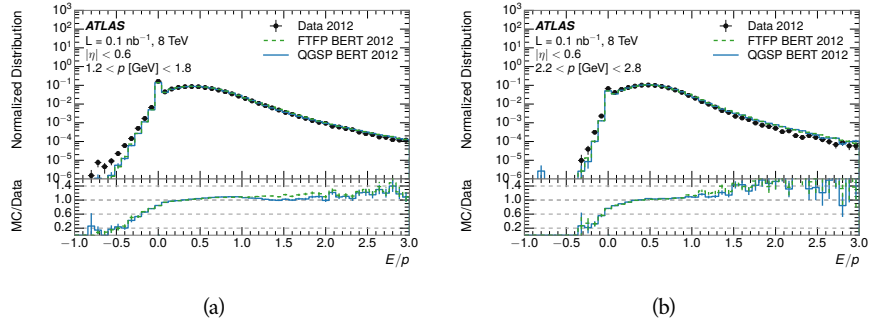


Figure 45: The E/p distribution and ratio of simulation to data for isolated tracks with (a) $|\eta| < 0.6$ and $1.2 < p/\text{GeV} < 1.8$ and (b) $|\eta| < 0.6$ and $2.2 < p/\text{GeV} < 2.8$.

2373 8.2.2 ZERO FRACTION

2374 The fraction of particles with no associated clusters, or similarly those with $E \leq$
 2375 0, reflects the modeling of both the detector geometry and hadronic interactions.

2376 The zero fraction is expected to rise as the amount of material a particle traverses
 2377 increases, while it is expected to decrease as the particle energy increases. This
 2378 dependence can be seen in Figure 46, where the zero fraction in data and simulation
 2379 is shown as a function of momentum and the amount of material measured
 2380 in interaction lengths. The trends are similar between 2010 and 2012 and for
 2381 positively and negatively charged particles. The zero fraction decreases with
 2382 energy as expected. The absolute discrepancy in zero fraction decreases with
 2383 momentum from 5% to less than 1%, but this becomes more pronounced in the
 2384 ratio as the zero fraction shrinks quickly with increasing momentum. There is
 2385 a small constant difference between the data and simulation in both interaction
 2386 models that becomes more pronounced. The amount of material in the detector
 2387 increases with η , which is used to obtain results for interaction lengths ranging
 2388 between 0.1 and 0.65 λ . As the data and simulation have significant disagree-
 2389 ment in the zero fraction over a number of interaction lengths, the difference
 2390 must be primarily from the modeling of hadronic interactions with detector ma-
 2391 terial and not just the detector geometry. Although two different hadronic in-
 2392 teraction models are shown in the figure, they have very similar discrepancies to
 2393 data because both use the same description (the BERT model) at low momentum.

2394 8.2.3 NEUTRAL BACKGROUND SUBTRACTION

2395 The isolation requirement on hadrons is only effective in removing an energy
 2396 contribution from nearby charged particles. Nearby neutral particles, predomi-
 2397 nantly photons from π^0 decays, also add their energy to the calorimeter clusters,
 2398 but mostly in the electromagnetic calorimeter. It is possible to measure this con-
 2399 tribution, on average, using late-showering hadrons that minimally ionize in the
 2400 electromagnetic calorimeter. Such particles are selected by requiring that they
 2401 deposit less than 1.1 GeV in the EM calorimeter within a cone of $\Delta R < 0.1$
 2402 around the track. To ensure that these particles are well measured, they are addi-
 2403 tionally required to deposit between 40% and 90% of their energy in the hadronic
 2404 calorimeter within the same cone.

2405 These particles provide a clean sample to measure the nearby neutral back-
 2406 ground because they do not deposit energy in the area immediately surrounding
 2407 them in the EM calorimeter, as shown in Figure 44. So, the energy deposits in the
 2408 region $0.1 < \Delta R < 0.2$ can be attributed to neutral particles alone. To estimate
 2409 the contribution to the whole cone considered for the response measurement,
 2410 that energy is scaled by a geometric factor of $4/3$. This quantity, $\langle E/p \rangle_{BG}$, mea-
 2411 sured in aggregate over a number of particles, gives the contribution to $\langle E/p \rangle$
 2412 from neutral particles in the EM calorimeter. Similar techniques were used in
 2413 the individual layers of the hadronic calorimeters to show that the background
 2414 from neutrals is negligible in those layers [30].

2415 The distribution of this background estimate is shown in Figure 47 for data
 2416 and simulation with the two different physics lists. The contribution from neu-
 2417 tral particles falls from 0.1 at low momentum to around 0.03 for particles above
 2418 7 GeV. Although the simulation captures the overall trend, it significantly over-
 2419 estimates the neutral contribution for tracks with momentum between 2 and 8

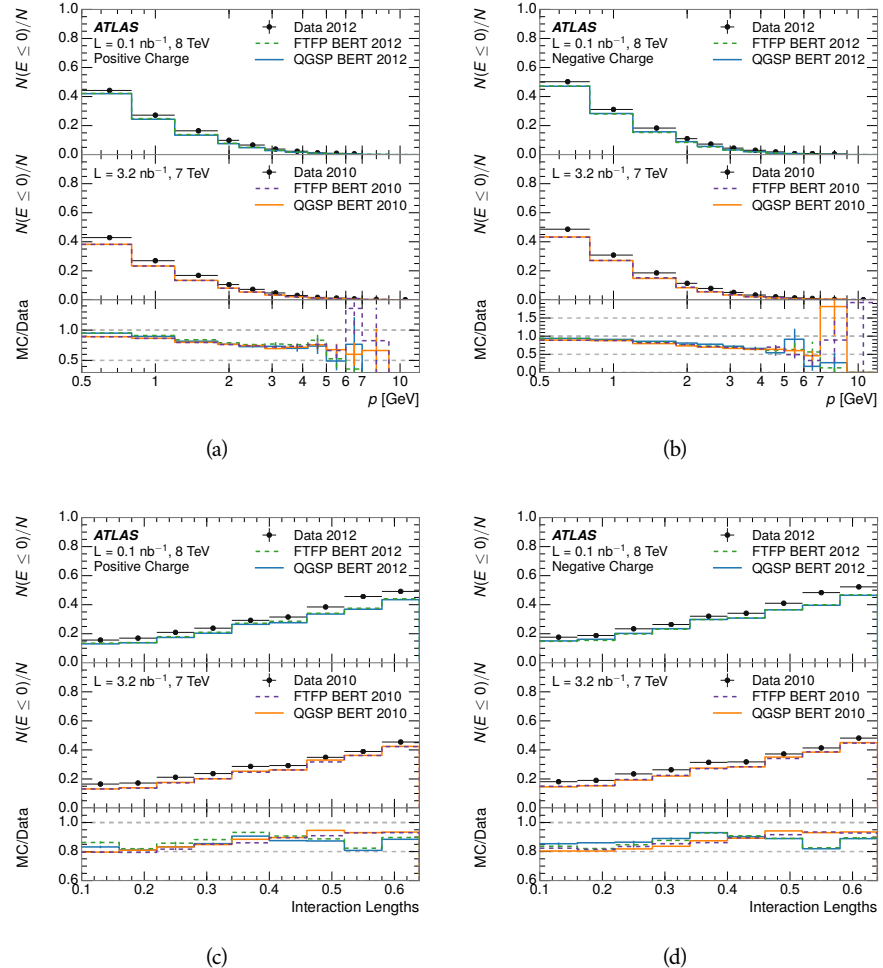


Figure 46: The fraction of tracks as a function (a, b) of momentum, (c, d) of interaction lengths with $E \leq 0$ for tracks with positive (on the left) and negative (on the right) charge.

2420 GeV. This effect was also seen in the tails of the E/p distributions in Figure 45.
 2421 This difference is likely due to modeling of coherent neutral particle radiation
 2422 in Pythia8 that overestimates the production of π^0 near the production of the
 2423 charged particles. The discrepancy does not depend on η and thus is unlikely to
 2424 be a mismodeling of the detector. This difference can be subtracted to form a
 2425 corrected average E/p , as in Section 8.2.4.

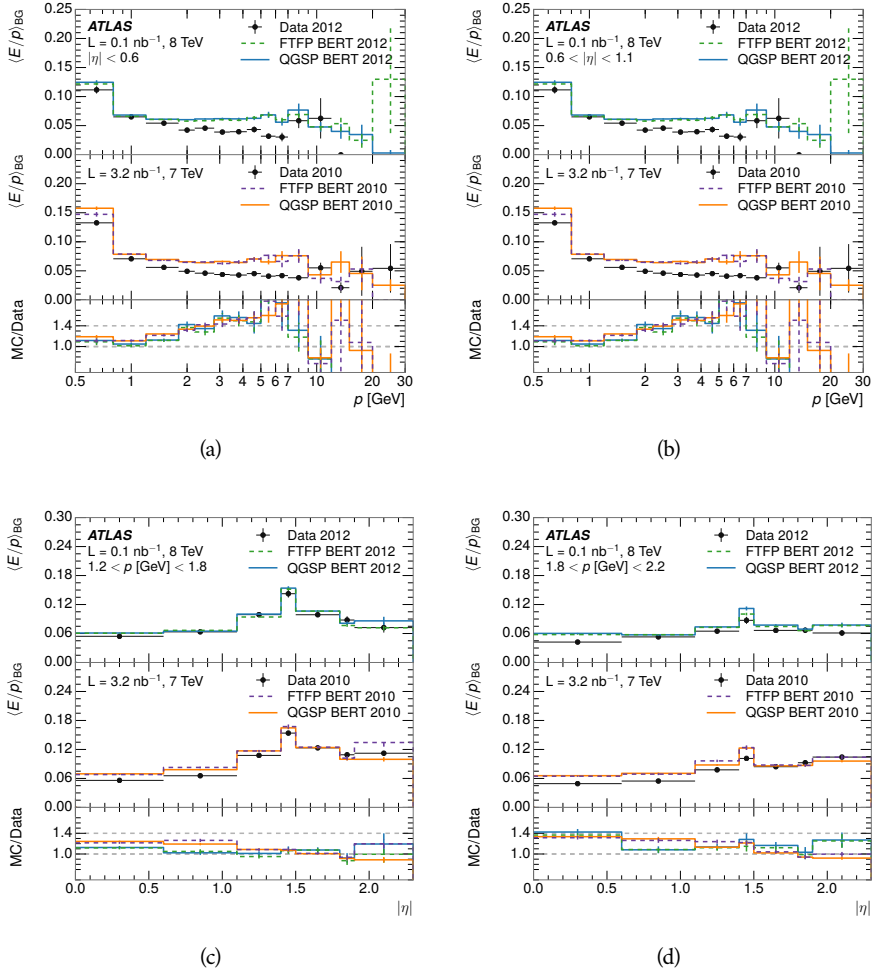


Figure 47: $\langle E/p \rangle_{BG}$ as a function of the track momentum for tracks with (a) $|\eta| < 0.6$,
 (b) $0.6 < |\eta| < 1.1$, and as a function of the track pseudorapidity for tracks
 with (c) $1.2 < p/\text{GeV} < 1.8$, (d) $1.8 < p/\text{GeV} < 2.2$.

2426 8.2.4 CORRECTED RESPONSE

2427 Figure 48 shows $\langle E/p \rangle_{COR}$ as a function of momentum for several bins of pseudo-
 2428 rapidity. This corrected $\langle E/p \rangle_{COR} \equiv \langle E/p \rangle - \langle E/p \rangle_{BG}$ measures the average
 2429 calorimeter response without the contamination of neutral particles. It is the
 2430 most direct measurement of calorimeter response in that it is the energy mea-
 2431 sured for fully isolated hadrons. The correction is performed separately in data
 2432 and simulation, so that the mismodeling of the neutral background in simulation

is removed from the comparison of response. The simulation overestimates the response at low momentum by about 5%, an effect that can be mostly attributed to the underestimation of the zero fraction mentioned previously. For $|\eta| < 0.6$, the data-simulation agreement has a larger discrepancy by about 5% for 2010 than 2012, although this is not reproduced in at higher pseudorapidity.

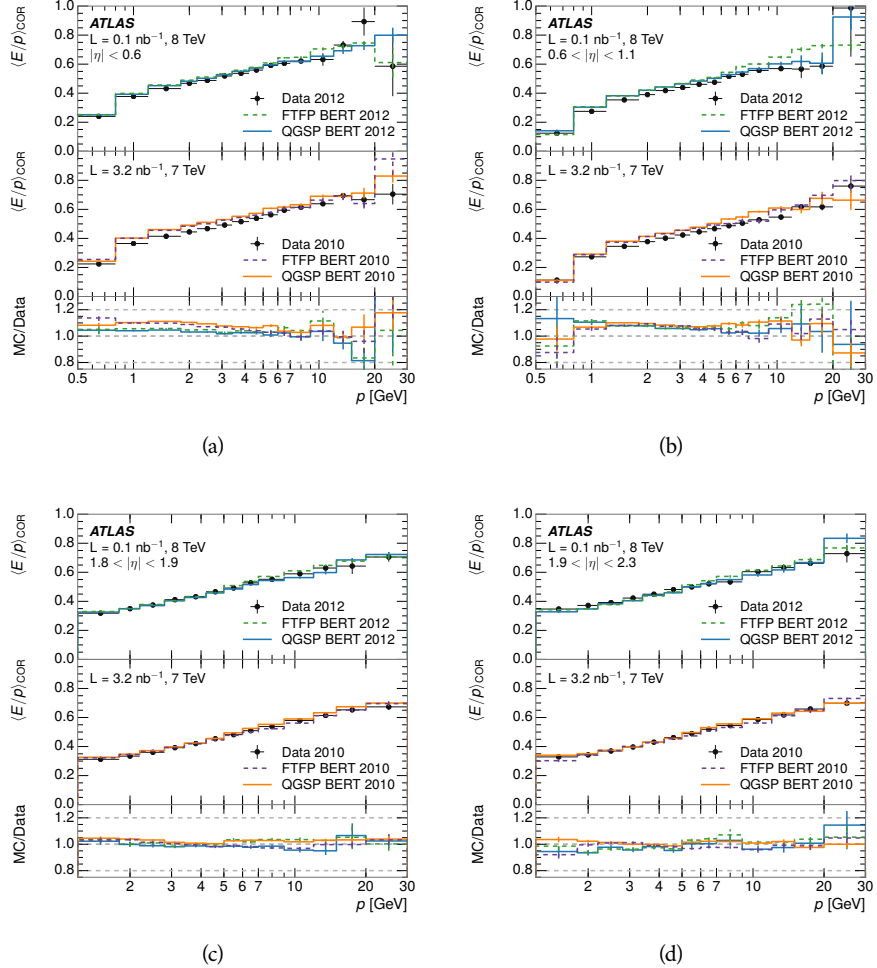


Figure 48: $\langle E/p \rangle_{\text{COR}}$ as a function of track momentum, for tracks with (a) $|\eta| < 0.6$, (b) $0.6 < |\eta| < 1.1$, (c) $1.8 < |\eta| < 1.9$, and (d) $1.9 < |\eta| < 2.3$.

The response measurement above used topological clustering at the EM scale, that is clusters were formed to measure energy but no corrections were applied to correct for expected effects like energy lost outside of the cluster or in uninstrumented material. It is also interesting to measure $\langle E/p \rangle_{\text{COR}}$ using LCW energies, which accounts for those effects by calibrating the energy based on the properties of the cluster such as energy density and depth in the calorimeter. Figure 49 shows these distributions for tracks with zero or more clusters and separately for tracks with one or more clusters. The calibration moves the mean value of $\langle E/p \rangle_{\text{COR}}$ significantly closer to 1.0 as desired. The agreement between data and simulation improves noticeably when at least one cluster is required, as this removes the contribution from the mismodeling of the zero fraction. The

good agreement in that case again demonstrates that the difference in $\langle E/p \rangle_{\text{COR}}$ between data and simulation is caused predominantly by the difference in zero fraction.

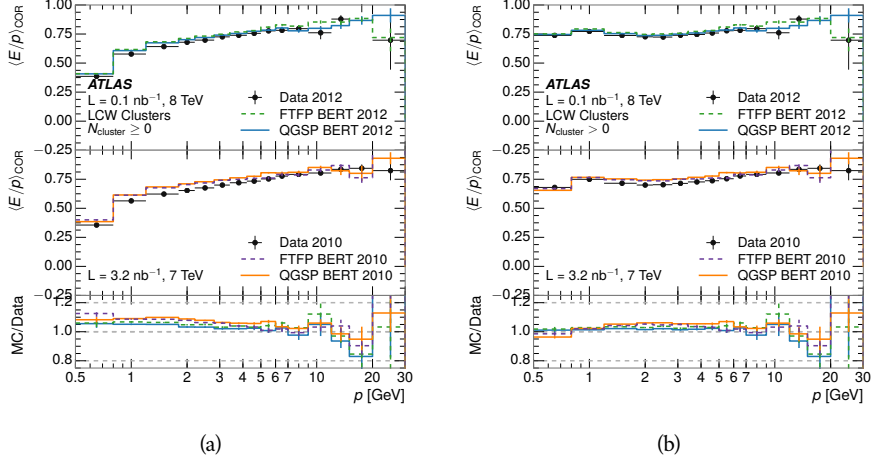


Figure 49: $\langle E/p \rangle_{\text{COR}}$ calculated using LCW-calibrated topological clusters as a function of track momentum for tracks with (a) zero or more associated topological clusters or (b) one or more associated topological clusters.

8.2.5 ADDITIONAL STUDIES

As has been seen in several measurements in previous sections, the simulation does not correctly model the chance of a low momentum hadron to reach the calorimeter. Because of the consistent discrepancy across pseudorapidity and interaction lengths, this can be best explained by incomplete understanding of hadronic interactions with the detector [29]. For example, a hadron that scatters off of a nucleus in the inner detector can be deflected through a significant angle and not reach the expected location in the calorimeter. In addition, these interactions can produce secondary particles that are difficult to model.

The requirement used throughout the previous sections on the number of hits in the TRT reduces these effects by preferentially selecting tracks that do not undergo nuclear interactions. It is interesting to check how well the simulation models tracks with low numbers of TRT hits, which selects tracks that are more likely to have undergone a hadronic interaction. Figure 50 compares the distributions with $N_{\text{TRT}} < 20$ to $N_{\text{TRT}} > 20$ for real and simulated particles. As expected, the tracks with fewer hits are poorly modeled in the simulation as $\langle E/p \rangle_{\text{COR}}$ differs by as much as 25% at low momentum.

Another interesting aspect of the simulation is the description of antiprotons at low momentum, where QGSP_BERT and FTFP_BERT have significant differences. This can be seen to have an effect in the inclusive response measurement when separated into positive and negative charge. The $\langle E/p \rangle_{\text{COR}}$ distributions for positive and negative particles are shown in Figure 51, where a small difference between QGSP_BERT and FTFP_BERT can be seen in the distribution for

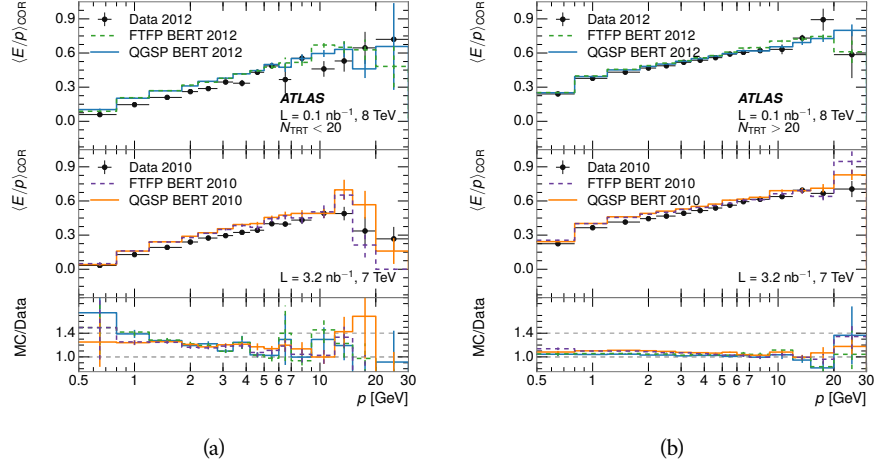


Figure 50: Comparison of the $\langle E/p \rangle_{\text{COR}}$ for tracks with (a) less than and (b) greater than 20 hits in the TRT.

negative tracks. This is demonstrated more clearly in Figure 52, which shows the E/p distribution in the two simulations separated by charge. There is a clear difference around $E/p > 1.0$, which can be explained by the additional energy deposited by the annihilation of the antiproton in the calorimeter that is modeled well only in FTFP_BERT. This is also explored with data using identified antiprotons in Section 8.3.

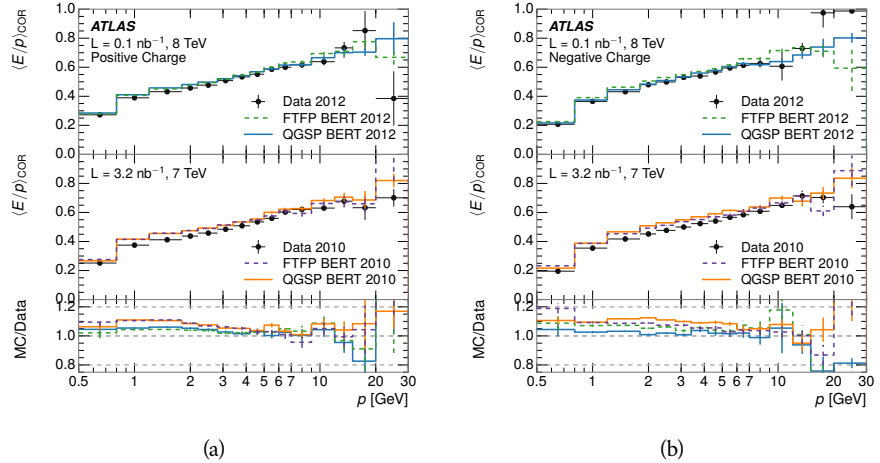


Figure 51: Comparison of the $\langle E/p \rangle_{\text{COR}}$ for (a) positive and (b) negative tracks as a function of track momentum for tracks with $|\eta| < 0.6$.

The $\langle E/p \rangle$ results in previous sections have considered the electromagnetic and hadronic calorimeters together as a single energy measurement, to emphasize the total energy deposited for a given particle. However, the deposits in each calorimeter are available separately and $\langle E/p \rangle$ can be constructed for each layer. As the layers are composed of different materials and are modeled separately in the detector geometry, confirmation that the simulation matches the data well

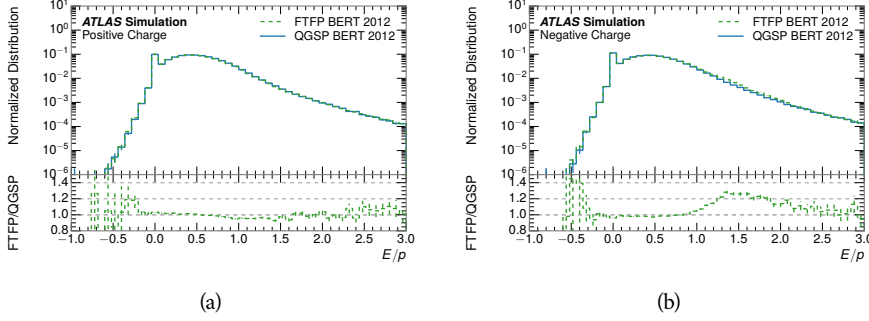


Figure 52: Comparison of the E/p distributions for (a) positive and (b) negative tracks with $0.8 < p/\text{GeV} < 1.2$ and $|\eta| < 0.6$, in simulation with the FTFP_BERT and QGSP_BERT physics lists.

in each layer adds confidence in both the description of hadronic interactions with the two different materials and also the geometric description of each.

The technique discussed in Section 8.2.3 for selecting MIPs in the electromagnetic calorimeter is also useful in studying deposits in the hadronic calorimeter. Those MIPs deposit almost all of their energy exclusively in the hadronic calorimeter. Figure 53 shows $\langle E/p \rangle_{\text{RAW}}^{\text{Had}}$, where RAW indicates that no correction has been applied for neutral backgrounds and Had indicates that only clusters for the hadronic calorimeter are included. The RAW and COR versions of $\langle E/p \rangle$ in this case are the same, as the neutral background is negligible in that calorimeter layer. The distributions are shown both for the original EM scale calibration and after LCW calibration. The data and simulation agree very well in this comparison, except in the lowest momentum bin which has 5% discrepancy that has already been seen in similar measurements.

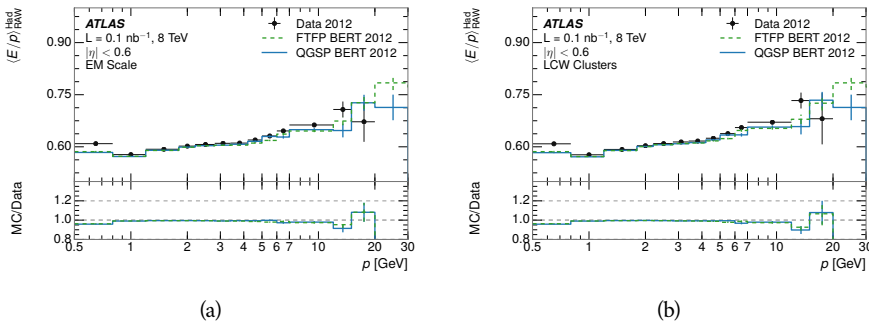


Figure 53: Comparison of the response of the hadronic calorimeter as a function of track momentum (a) at the EM-scale and (b) after the LCW calibration.

A similar comparison can be made in the electromagnetic calorimeter by selecting particles which have no associated energy in the hadronic calorimeter. These results are measured in terms of $\langle E/p \rangle_{\text{COR}}^{\text{EM}}$, where EM designates that only clusters in the electromagnetic calorimeter are included and COR designates that the neutral background is subtracted as the neutral background is present in this case. Figure 54 shows the analogous comparisons to Figure 53 in

2506 the electromagnetic calorimeter. In this case the disagreement between data and
 2507 simulation is more pronounced, with discrepancies as high as 5% over a larger
 2508 range of momenta. This level of discrepancy indicates that the description of
 2509 the electromagnetic calorimeter is actually the dominant source of discrepancy
 2510 in the combined distributions in Section 8.2.4.

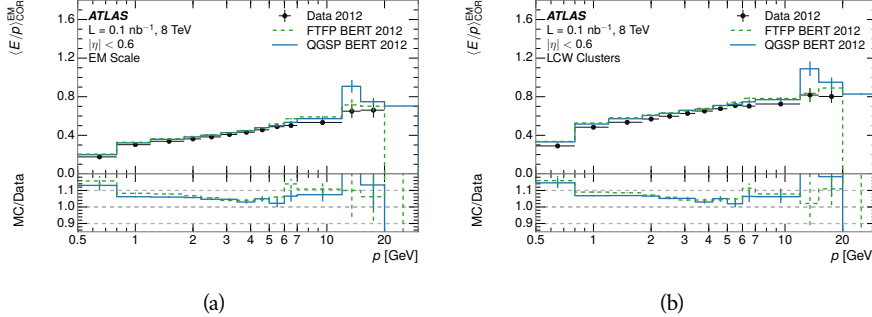


Figure 54: Comparison of the response of the EM calorimeter as a function of track momentum (a) at the EM-scale and (b) with the LCW calibration.

2511 **NOTE: There are more studies that I skipped for brevity that could be in-**
 2512 **cluded if interesting. E/p at different cluster threshold settings, E/p with**
 2513 **pileup, E/p with cells. I also left out a lot of eta bins that appear in the**
 2514 **paper so that this section didn't turn into 20 pages of plots.**

2515 8.3 IDENTIFIED PARTICLE RESPONSE

2516 The inclusive response measurement for hadrons can be augmented by measur-
 2517 ing the response for specific particle species. The simulation models each parti-
 2518 cle type separately, and understanding the properties of each is important in con-
 2519 straining the uncertainty on jets. In order to select and measure specific hadrons,
 2520 this section relies on the displaced decays of long-lived particles. Such decays
 2521 can be identified by reconstructing secondary vertices with a requirement on
 2522 mass. In particular, Λ , $\bar{\Lambda}$, and K_S^0 can be used to select a pure sample of protons,
 2523 antiprotons, and pions, respectively.

2524 8.3.1 DECAY RECONSTRUCTION

2525 The measurement of response for identified particles uses the same selection as
 2526 for inclusive particles (Section 8.1.3) with a few additions. Each event used is
 2527 required to have at least one secondary vertex, and the tracks are required to
 2528 match to that vertex rather than the primary vertex. Pions are selected from
 2529 decays of $K_S^0 \rightarrow \pi^+ \pi^-$, which is the dominant decay for K_S^0 to charged particles.
 2530 Protons are selected from decays of $\Lambda \rightarrow \pi^- p$ and antiprotons from $\bar{\Lambda} \rightarrow \pi^+ \bar{p}$,
 2531 which are similarly the dominant decays of Λ and $\bar{\Lambda}$ to charged particles. The
 2532 species of parent hadron in these decays is determined by reconstructing the
 2533 mass of the tracks associated to the secondary vertex. The sign of the higher

momentum decay particle can distinguish between Λ and $\bar{\Lambda}$, which of course have the same mass, as the proton or antiproton is kinematically favored to have higher momentum. Examples of the reconstructed masses used to select these decays are shown in Figure 55.

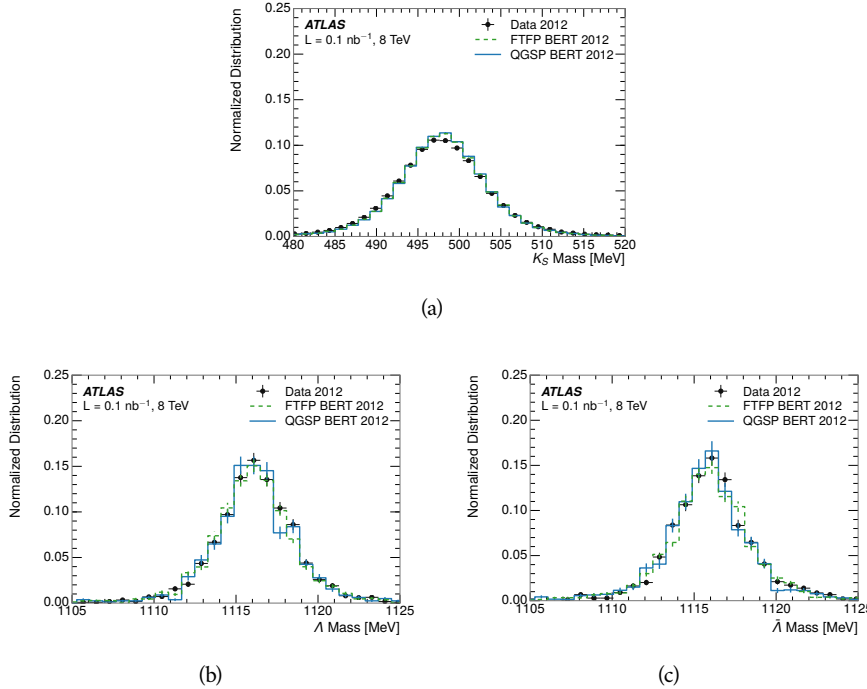


Figure 55: The reconstructed mass peaks of (a) K_S^0 , (b) Λ , and (c) $\bar{\Lambda}$ candidates.

The dominant backgrounds for the identified particle decays are nuclear interactions and combinatoric sources. These are suppressed by the kinematic requirements on the tracks as well as an additional veto which removes candidates that are consistent with both a Λ or $\bar{\Lambda}$ and a K_S^0 hypothesis, which is possible because of the different assumptions on particle mass in each case [30]. After these requirements, the backgrounds are found to be negligible compared to the statistical errors on these measurements.

8.3.2 IDENTIFIED RESPONSE

With these techniques the E/p distributions are extracted in data and simulation for each particle species and shown in Figure 56. These distributions are shown for a particular bin of E_a ($2.2 < E_a/\text{GeV} < 2.8$), rather than p . E_a is the energy available to be deposited in the calorimeter: for pions $E_a = \sqrt{p^2 + m^2}$, for protons $E_a = \sqrt{p^2 + m^2} - m$, and for antiprotons $E_a = \sqrt{p^2 + m^2} + m$. The features of the E/p distributions are similar to the inclusive case. There is a small negative tail from noise and a large fraction of tracks with zero energy from particles which do not reach the calorimeter. The long positive tail is noticeably more pronounced for antiprotons because of the additional energy generated by the annihilation in addition to the neutral background.

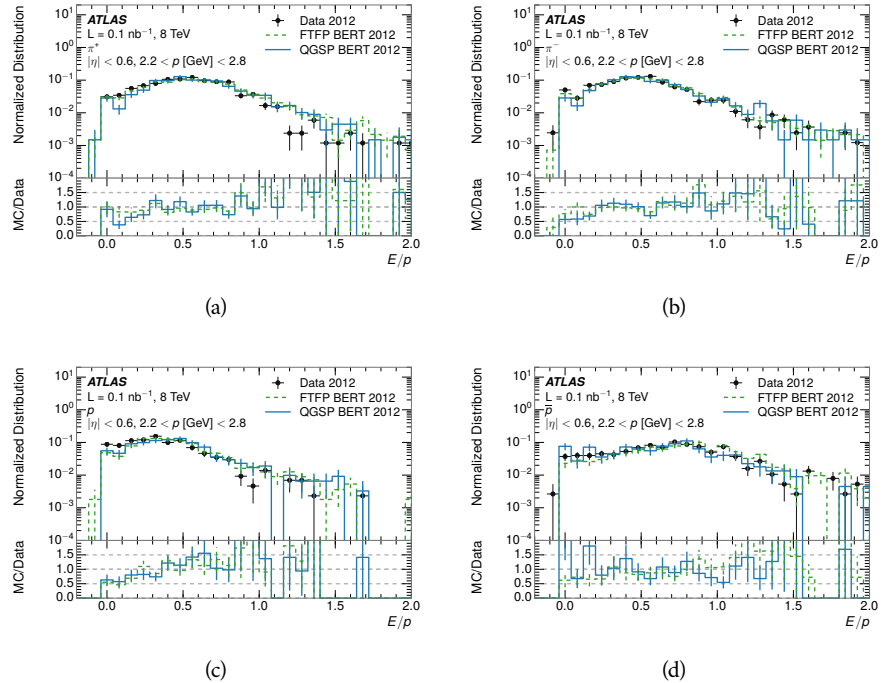


Figure 56: The E/p distribution for isolated (a) π^+ , (b) π^- , (c) proton, and (d) anti-proton tracks.

2556 The zero fraction is further explored in Figure 57 for pions and protons in data
 2557 and simulation. The simulation consistently underestimates the zero fraction
 2558 independent of particle species, which implies that this discrepancy is not caused
 2559 by the model of a particular species but rather a feature common to all.

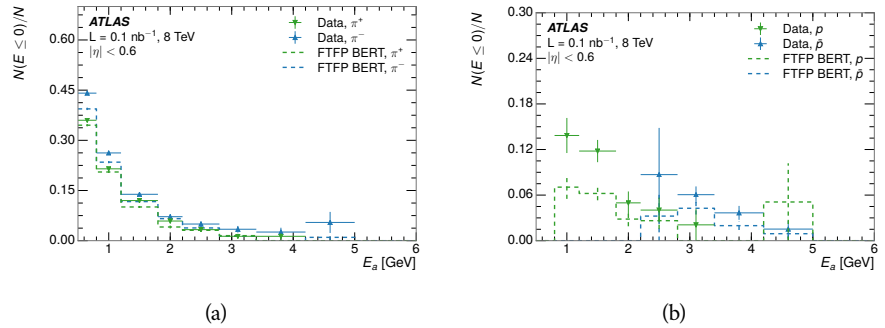


Figure 57: The fraction of tracks with $E \leq 0$ for identified (a) π^+ and π^- , and (b) proton and anti-proton tracks

2560 It is also interesting to compare the response between the different particle
 2561 species. One approach to do this is to measure the difference in $\langle E/p \rangle$ between
 2562 two types, which has the advantage of removing the neutral background. These
 2563 differences are shown in various combinations in Figure 58. The response for
 2564 π^+ is greater on average than the response to π^- because of a charge-exchange
 2565 effect which causes the production of additional neutral pions in the showers of

2566 π^+ [52]. The response for π^+ is also greater on average than the response to p ,
 2567 because a large fraction of the energy of π^+ hadrons is converted to an electro-
 2568 magnetic shower [53, 54]. However, the \bar{p} response is significantly higher than
 2569 the response to π^- because of the annihilation of the antiproton. FTFP_BERT
 2570 does a better job of modeling this effect than QGSP_BERT because of their differ-
 2571 ent descriptions of \bar{p} interactions with material.

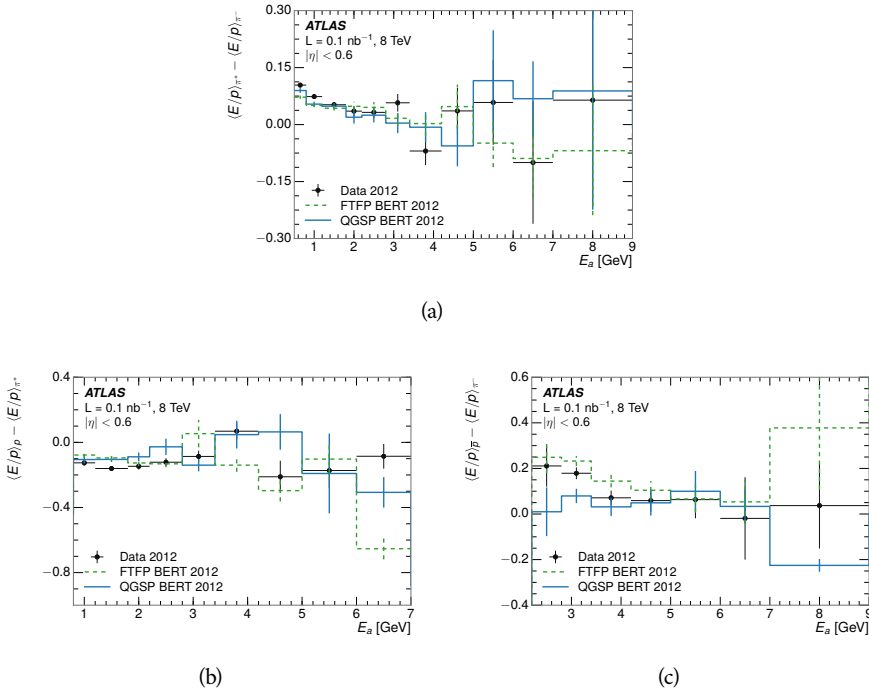


Figure 58: The difference in $\langle E/p \rangle$ between (a) π^+ and π^- (b) p and π^+ , and (c) \bar{p} and π^- .

2572 It is also possible to remove the neutral background from these response dis-
 2573 tributions using the same technique as in Section 8.2.3. The technique is largely
 2574 independent of the particle species and so can be directly applied to $\langle E/p \rangle$ for
 2575 pions. The $\langle E/p \rangle_{\text{COR}}$ distributions for pions are shown in Figure 59, which are
 2576 very similar to the inclusive results. The inclusive hadrons are comprised mostly
 2577 of pions, so this similarity is not surprising. It is also possible to see the small
 2578 differences between π^+ and π^- response here, where $\langle E/p \rangle_{\text{COR}}$ is higher on av-
 2579 erage for π^+ . The agreement between data and simulation is significantly worse
 2580 for the π^- distributions than for the π^+ , with a discrepancy greater than 10%
 2581 below 2-3 GeV.

2582 8.3.3 ADDITIONAL SPECIES IN SIMULATION

2583 The techniques above provide a method to measure the response separately for
 2584 only pions and protons. However the hadrons which forms jets include a num-
 2585 ber of additional species such as kaons and neutrons. The charged kaons are
 2586 an important component of the inclusive charged hadron distribution, which is
 2587 comprised of roughly 60-70% pions, 15-20% kaons, and 5-15% protons. These

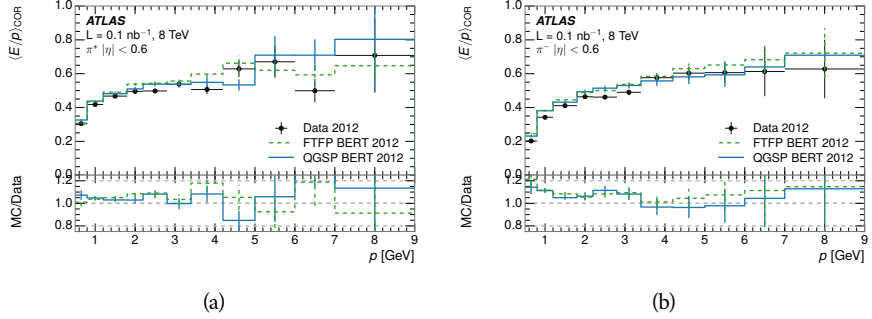


Figure 59: $\langle E/p \rangle_{\text{COR}}$ as a function of track momentum for (a) π^+ tracks and (b) π^- tracks.

2588 are difficult to measure in data at the ATLAS detector, although a template subtraction
 2589 technique has been proposed which may be effective with larger sample sizes [29]. The simulation of these particles includes noticeable differences in
 2590 response at low energies, which are shown in Figure 60 for FTFP_BERT. The
 2591 significant differences in response between low energy protons and antiprotons
 2592 are accounted for above in the definitions of E_a .
 2593

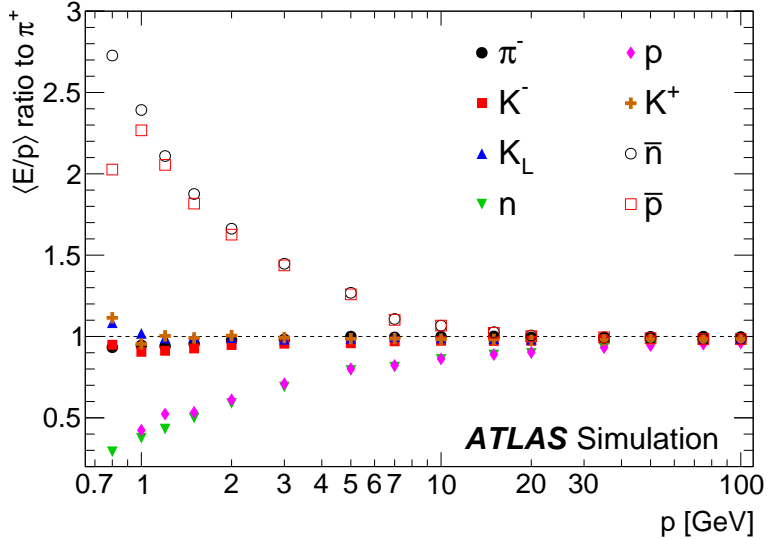


Figure 60: The ratio of the calorimeter response to single particles of various species to the calorimeter response to π^+ with the physics list FTFP_BERT.

2594 8.4 SUMMARY

2595 These various measurements of calorimeter response shown above for data and
 2596 simulation illuminate the accuracy of the simulation of hadronic interactions at
 2597 the ATLAS detector. The results were done using 2010 and 2012 data at 7 and 8
 2598 TeV, but reflect the most current understanding of the detector alignment and
 2599 geometry. A number of measurements focusing on a comparison between pro-

2600 tons and antiprotons suggest that FTFP_BERT models those interaction more
2601 accurately than QGSP_BERT. These measurements, among others, were the moti-
2602 vation to switch the default Geant4 simulation from FTFP_BERT to QGSP_BERT
2603 for all ATLAS samples.

2604 Even with these updates, there are a number of small, approximately 5%, dis-
2605 crepancies in response between the data and simulation at low energies. At
2606 higher energies the simulation of hadronic interactions is very consistent with
2607 data. Chapter 9 discusses how to use these observed differences to constrain the
2608 jet energy scale and its associated uncertainties.

2609

2610 JET ENERGY RESPONSE AND UNCERTAINTY

2611 9.1 MOTIVATION

2612 As jets form a major component of many physics analyses at ATLAS, it is crucial
 2613 to carefully calibrate the measurement of jet energies and to derive an uncer-
 2614 tainty on that measurement. These uncertainties have often been the dominant
 2615 systematic uncertainty in high-energy analyses at the LHC. Dijet and multijet
 2616 balance techniques provide a method to constrain the JES and its uncertainty in
 2617 data, and provide the default values used for ATLAS jet measurements at most
 2618 energies [55]. These techniques are limited by their reliance on measuring jets
 2619 in data, so they are statistically limited in estimating the jet energy scale at the
 2620 highest jet energies. This chapter presents another method for estimating the jet
 2621 energy scale and its uncertainty which builds up a jet from its components and
 2622 thus can be naturally extended to high jet momentum. Throughout this chapter
 2623 the jets studied are simulated using Pythia8 with the CT10 parton distribution
 2624 set [56] and the AU2 tune [33], and corrections are taken from the studies includ-
 2625 ing data and simulation in Chapter 8.

2626 As described in Section 7.4, jets are formed from topological clusters of energy
 2627 in the calorimeters using the anti- k_t algorithm. These clusters originate from a
 2628 diverse spectrum of particles, in terms of both species and momentum, leading to
 2629 significantly varied jet properties and response between jets of similar produced
 2630 momentum. Figure 61 shows the simulated distribution of particles within jets
 2631 at a few examples energies. The E/p measurements provide a thorough under-
 2632 standing of the dominant particle content of jets, the charged hadrons.

2633 9.2 UNCERTAINTY ESTIMATE

2634 Simulated jets are not necessarily expected to correctly model the energy de-
 2635 posits in the calorimeters, because of the various discrepancies discussed in Chap-
 2636 ter 8. To evaluate a jet energy response, the simulated jet energies are compared
 2637 to a corrected jet built up at the particle level. Each cluster in a jet is associated
 2638 to the truth particle which deposited it, and the energy in that cluster is then
 2639 corrected for a number of effects based on measurements in data. The primary
 2640 corrections come from the single hadron response measurements in addition to
 2641 response measured using the combined test beam which covers higher momen-
 2642 tum particles [57]. These corrections include both a shift (Δ), in order to make
 2643 the simulation match the average response in data, and an uncertainty (σ) asso-
 2644 ciated with the ability to constrain the difference between data and simulation.
 2645 Some of the dominant sources of uncertainty are itemized in Table 8 with typi-
 2646 cal values, and the full list considered is described in detail in the associated pa-

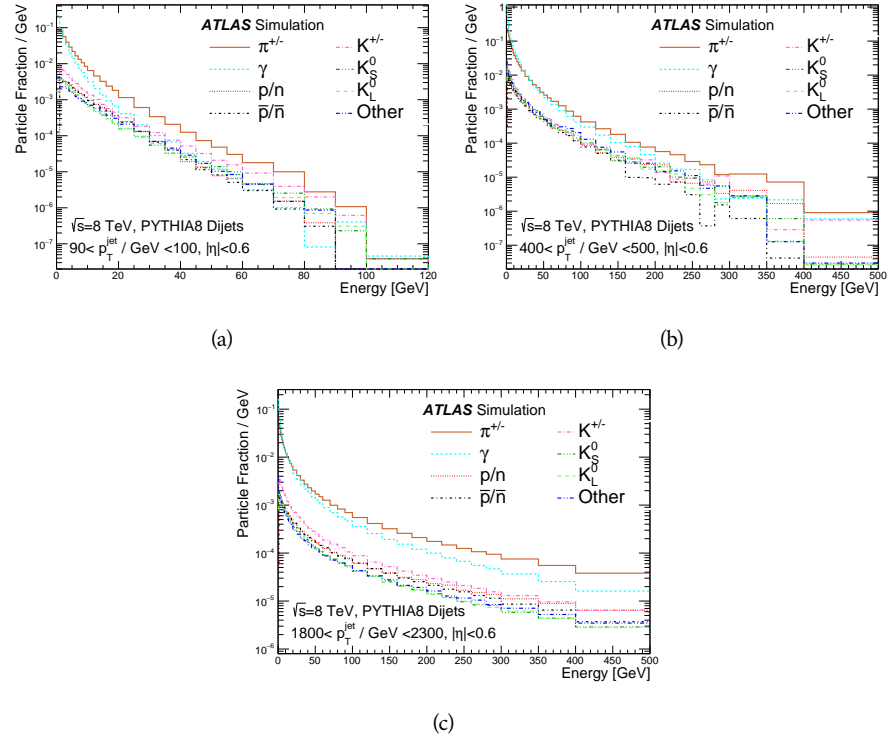


Figure 61: The spectra of true particles inside anti- k_t , $R = 0.4$ jets with (a) $90 < p_T/\text{GeV} < 100$, (b) $400 < p_T/\text{GeV} < 500$, and (c) $1800 < p_T/\text{GeV} < 2300$.

2647 per [29]. These uncertainties cover differences between the data and simulation
 2648 in the modeling of calorimeter response to a given particle. No uncertainties are
 2649 added for the difference between particle composition of jets in data and simu-
 2650 lation.

2651 From these terms, the jet energy scale and uncertainty is built up from indi-
 2652 vidual energy deposits in simulation. Each uncertainty term is treated indepen-
 2653 dently, and are taken to be gaussian distributed. The resulting scale and uncer-
 2654 tainty is shown in Figure 62, where the mean response is measured relative to
 2655 the calibrated energy reported by simulation. The dominant uncertainties come
 2656 from the statistical uncertainties on the E/p measurements at lower energies and
 2657 the additional uncertainty for out of range measurements at higher energies. The
 2658 total uncertainty from this method at intermediate jet energies is comparable to
 2659 other simulation-based methods [58] and is about twice as large as in-situ meth-
 2660 ods using data [55]. This method is the only one which provides an estimation
 2661 above 1.8 TeV, however, and so is still a crucial technique in analyses that search
 2662 for very energetic jets.

2663 These techniques can also be used to measure the correlation between bins of
 2664 average reconstructed jet momentum across a range of p_T and $|\eta|$, where cor-
 2665 relations are expected because of a similarity in particle composition at similar
 2666 energies. Figure 63 shows these correlations, where the uncertainties on jets in
 2667 neighboring bins are typically between 30% and 60% correlated. The uncertainty
 2668 on all jets becomes significantly correlated at high energies and larger pseudora-

Abbrev.	Description	Δ (%)	σ (%)
In situ E/p	The comparison of $\langle E/p \rangle_{\text{COR}}$ as described in Chapter 8 with statistical uncertainties from 500 MeV to 20 GeV.	0-3	1-5
CTB	The main $\langle E/p \rangle$ comparison uncertainties, binned in p and $ \eta $, as derived from the combined test beam results, from 20 to 350 GeV [57].	0-3	1-5
E/p Zero Fraction	The difference in the zero-fraction between data and MC simulation from 500 MeV to 20 GeV.	5-25	1-5
E/p Threshold	The uncertainty in the EM calorimeter response from the potential mismodeling of threshold effects in topological clustering.	0	0-10
Neutral	The uncertainty in the calorimeter response to neutral hadrons based on studies of physics model variations.	0	5-10
K_L	An additional uncertainty in the response to neutral K_L in the calorimeter based on studies of physics model variations.	0	20
E/p Misalignment	The uncertainty in the p measurement from misalignment of the ID.	0	1
Hadrons, $p > 350$ GeV	A flat uncertainty for all particles above the energy range or outside the longitudinal range probed with the combined test beam.	0	10

Table 8: The dominant sources of corrections and systematic uncertainties in the [JES](#) estimation technique, including typical values for the correcting shift (Δ) and the associated uncertainty (σ).

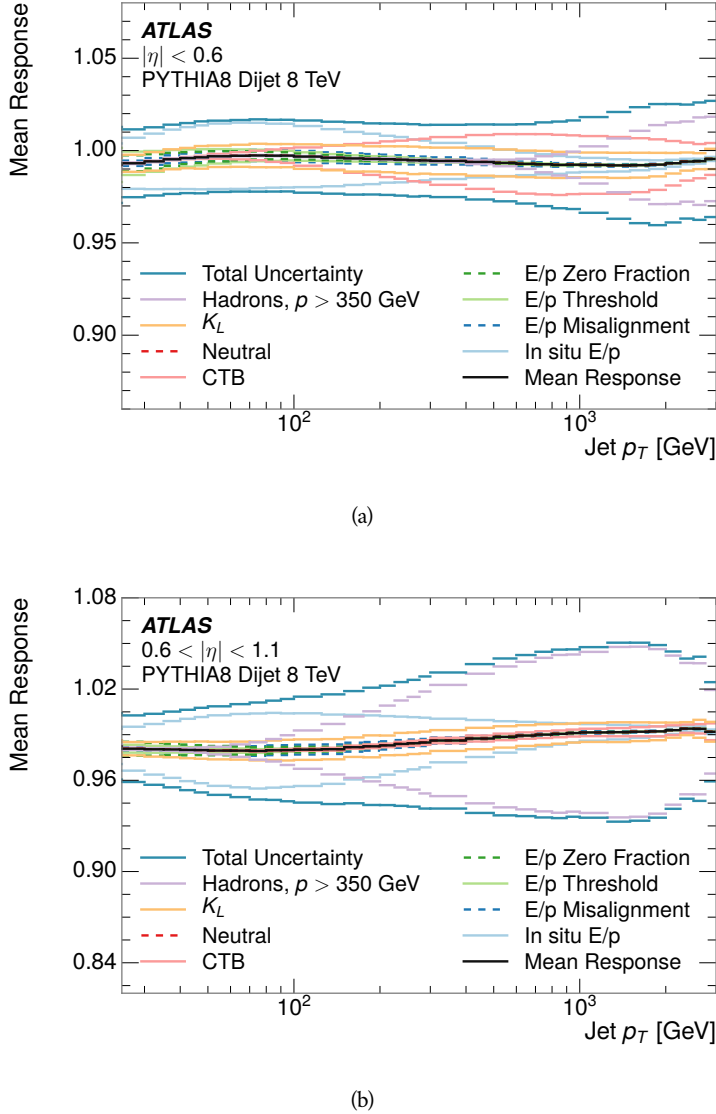


Figure 62: The [JES](#) uncertainty contributions, as well as the total [JES](#) uncertainty, as a function of jet p_T for (a) $|\eta| < 0.6$ and (b) $0.6 < |\eta| < 1.1$.

2669 pidities, when the uncertainty becomes dominated by the single term reflecting
 2670 out of range particles.

2671 9.3 SUMMARY

2672 The technique described above provides a jet energy scale and uncertainty by
 2673 building up jet corrections from the energy deposits of constituent particles. The
 2674 E/p measurements are crucial in providing corrections for the majority of parti-
 2675 cles in the jets. The uncertainty derived this way is between 2 and 5% and is about
 2676 twice as large at corresponding momentum than jet balance methods. However
 2677 this is the only uncertainty available for very energetic jets using 2012 data and
 2678 simulation, and repeating this method with Run 2 data and simulation will be

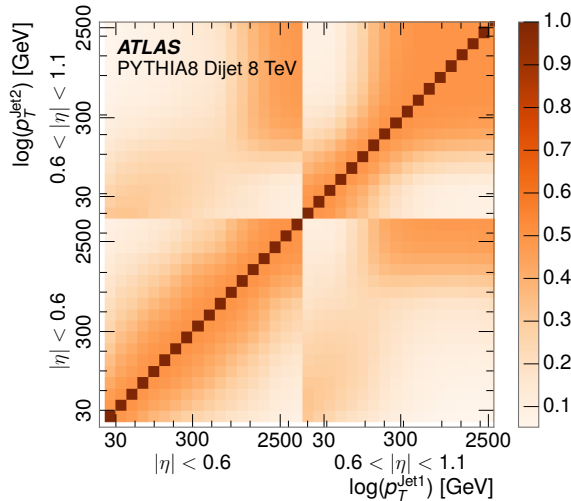


Figure 63: The **JES** correlations as a function of jet p_T and $|\eta|$ for jets in the central region of the detector.

2679 important in providing an uncertainty for the most energetic jets in 13 TeV col-
2680 lisions.

2681

PART V

2682

SEARCH FOR LONG-LIVED PARTICLES

2683

You can put some informational part preamble text here.

2684

2685 LONG-LIVED PARTICLES IN ATLAS

2686 As discussed in Section 2.6, various limitations in the SM suggest a need for new
 2687 particles at the TeV scale. A wide range of extensions to the Standard Model
 2688 predict that these new particles can have lifetimes greater than approximately
 2689 one-hundredth of a nanosecond. These include theories with universal extra-
 2690 dimensions [59, 60], with new fermions [61], and with leptoquarks [62]. Many
 2691 SUSY theories also produce these Long-Lived Particles (LLPs), in both R-Parity
 2692 violating [63–65] and R-Parity conserving [66–69] formulations. Split super-
 2693 symmetry [70, 71], for example, predicts long-lived gluinos with O(TeV) masses.
 2694 This search focuses specifically on the SUSY case, but many of the results are
 2695 generic to any model with LLPs.

2696 Long-lived gluinos or squarks carry color-charge and will thus hadronize into
 2697 color neutral bound states called R-Hadrons. These are composit particles like
 2698 the usual hadrons but with one supersymmetric constituent, for example $\tilde{g}q\bar{q}$
 2699 and $\tilde{q}\bar{q}$. Through this hadronization process, the neutral gluino can acquire a
 2700 charge. Gluino pair production, $pp \rightarrow \tilde{g}\tilde{g}$ has the largest cross sectional increase
 2701 with the increase in energy to 13 TeV, and so this search focuses on gluino R-
 2702 Hadrons. Planned future updates will extend the case to explicitly include squark
 2703 and chargino models, but the method covers any long-lived, charged, massive
 2704 particle.

2705 10.1 EVENT TOPOLOGY

2706 The majority of SUSY models predict that gluinos will be produced in pairs at
 2707 the LHC, through processes like $pp \rightarrow q\bar{q} \rightarrow \tilde{g}\tilde{g}$ and $pp \rightarrow gg \rightarrow \tilde{g}\tilde{g}$, where the
 2708 gluon mode dominates for the collision energy and gluino masses considered
 2709 for this search. During their production, the long-lived gluinos hadronize into
 2710 color singlet bound states including $\tilde{g}q\bar{q}$, $\tilde{g}qqq$, and even $\tilde{g}g$ [72]. The probability
 2711 to form the gluon-only bound states is a free parameter usually taken to be 0.1,
 2712 while the meson states are favored among the R-Hadrons [73]. The charged and
 2713 neutral states are approximately equally likely for mesons, so the R-Hadrons will
 2714 be charged roughly 50% of the time.

2715 These channels produce R-Hadrons with large p_T , comparable to their mass,
 2716 so that they typically propagate with $0.2 < \beta < 0.9$ [73]. The fragmentation that
 2717 produces these hadrons is very hard, so the jet structure around the R-Hadron
 2718 is minimal, with less than 5 GeV of summed particle momentum expected in a
 2719 cone of $\Delta R < 0.25$ around the R-Hadron [73]. After hadronization, depending
 2720 on the gluino lifetime, the R-Hadrons then decay into hadrons and a LSP [72].

2721 In summary, the expected event for pair-produced long-lived gluinos is very
 2722 simple: two isolated, high-momentum R-Hadrons that propagate through the
 2723 detector before decaying into jets. The observable features of such events depend

2724 strongly on the interaction of the R-Hadron with the material of the detector and
 2725 also its lifetime. Section 10.1.1 describes the interactions of R-Hadrons which
 2726 reach the various detector elements in ATLAS and Section 10.1.2 provides a sum-
 2727 mary of the observable event descriptions for R-Hadrons of various lifetimes.

2728 10.11 DETECTOR INTERACTIONS

2729 After approximately 0.2 ns, the R-Hadron reaches the pixel detector. If charged,
 2730 it deposits energy into the material through repeated single collisions that result
 2731 in ionization of the silicon substrate [10]. Because of its comparatively low β ,
 2732 the ionization energy can be significantly greater than expected for SM particles
 2733 because the most-probable energy loss grows significantly as β decreases [10].
 2734 This large ionization can be measured through the ToT read out from the pixel
 2735 detector as described in Section 7.1.2. Large ionization in the inner detector is
 2736 one of the major characteristic features of LLPs.

2737 Throughout the next few nanoseconds, the R-Hadron propagates through the
 2738 remainder of the inner detector. A charged R-Hadron will provide hits in each
 2739 of these systems as would any other charged particle, and can be reconstructed
 2740 as a track. The track reconstruction provides a measurement of its trajectory
 2741 and thus its momentum as described in Section 7.1. The large momentum is
 2742 another characteristic feature of massive particles produced at the LHC. **Note: At**
2743 this point I am failing to mention that the TRT provides a possible dE/dx
2744 measurement, because no one uses it as far as I know.

2745 As of roughly 20 ns, the R-Hadron enters the calorimeter where it interacts
 2746 hadronically with the material. Because of its large mass and momentum, the
 2747 R-Hadron does not typically stop in the calorimeter, but rather deposits a small
 2748 fraction of its energy through repeated interactions with nucleons. The proba-
 2749 bility of interaction between the gluino itself and a nucleon is low because the
 2750 cross section drops off with the inverse square of its mass, so the interactions are
 2751 primarily governed by the light constituents [74]. Each of these interactions can
 2752 potentially change that quark content and thus change the sign of the R-Hadron,
 2753 so that the charge at exit is typically uncorrelated with the charge at entry [73].
 2754 The total energy deposited in the calorimeters during the propagation is small
 2755 compared to the kinetic energy of the R-Hadron, around 20-40 GeV, so that
 2756 E/p is typically less than 0.1 [73].

2757 Then, 30 ns after the collision, it reaches the muon system, where it again
 2758 ionizes in the material if charged and can be reconstructed as a muon track. Be-
 2759 cause of the charge-flipping interactions in the calorimeter, this track may have
 2760 the opposite sign of the track reconstructed in the inner detector, or there may
 2761 be a track present when there was none in the inner detector and vice-versa. The
 2762 propagation time at the typically lower β results in a significant delay compared
 2763 to muons, and that delay can be assessed in terms of a time-of-flight measure-
 2764 ment. Because of the probability of charge-flip and late arrival, there is a signif-
 2765 icant chance that an R-Hadron which was produced with a charge will not be
 2766 identified as a muon. The long time-of-flight is another characteristic feature of
 2767 R-Hadrons which are reconstructed as muons.

2768 10.1.2 LIFETIME DEPENDENCE

2769 The above description assumed a lifetime long enough for the R-Hadron to exit
 2770 the detector, which through this search is referred to as “stable”, even though
 2771 the particle may decay after exiting the detector. There are several unique sig-
 2772 natures at shorter lifetimes where the R-Hadron decays in various parts of the
 2773 inner detector; these lifetimes are referred to as “metastable”.

2774 The shortest case where the R-Hadron is considered metastable is for life-
 2775 times around 0.01 ns, where the particle decays before reaching any of the de-
 2776 tector elements. Although the R-Hadrons are produced opposite each other in
 2777 the transverse plane, each R-Hadron decays to a jet and an LSP. The LSPs are not
 2778 measured, so the produced jets can be significantly imbalanced in the transverse
 2779 plane which results in large missing energy. That missing energy can be used
 2780 to trigger candidate events, and provides the most efficient trigger option for
 2781 shorter lifetimes. Additionally, the precision of the tracking system allows the
 2782 displaced vertex of the R-Hadron decay to be reconstructed from the charged
 2783 particles in the jet. The distance of that vertex from the interaction point can
 2784 be used to distinguish R-Hadron decays from other processes. Figure 64 shows
 2785 a schematic diagram of an example R-Hadron event with such a lifetime. The
 2786 diagram is not to scale, but instead illustrates the detector interactions in the
 2787 pixel detector, calorimeters, and muon system. It includes a representation of
 2788 the charged R-Hadron and the neutral R-Hadron, as well as the LSPs and jets
 2789 (shown as charged hadrons) produced in the decay. Neutral hadrons may also
 2790 be produced in the decay but are not depicted. Previous searches on ATLAS have
 2791 used the displaced vertex to target LLP decays [75].

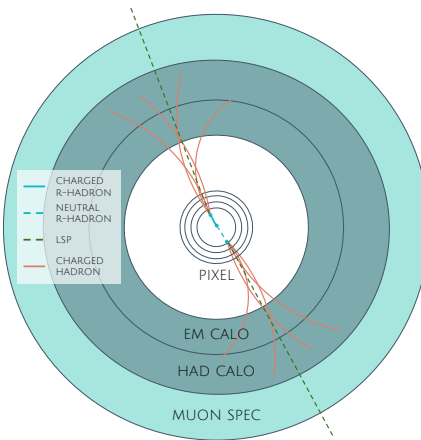


Figure 64: A schematic diagram of an R-Hadron event with a lifetime around 0.01 ns.
 The diagram includes one charged R-Hadron (solid blue), one neutral R-Hadron (dashed blue), LSPs (dashed green) and charged hadrons (solid orange). The pixel detector, calorimeters, and muon system are illustrated but not to scale.

2792 The next distinguishable case occurs at lifetimes greater than 0.1 ns, where
 2793 the R-Hadron forms a partial track in the inner detector. If the decay products
 2794 are sufficiently soft, they may not be reconstructed, and this forms a unique sig-

2795 nature of a disappearing track. An example of such an event is illustrated in
 2796 Figure 65, which shows the short track in the inner detector and the undetected
 2797 soft charged hadron and LSP that are produced. A dedicated search on ATLAS used
 2798 the disappearing track signature to search for LLP in Run 1 [76]. **zNote: might**
 2799 **not be worth mentioning the disappearing track here since it is actually a**
 2800 **chargino search, the soft pion is pretty unique to charginos.**

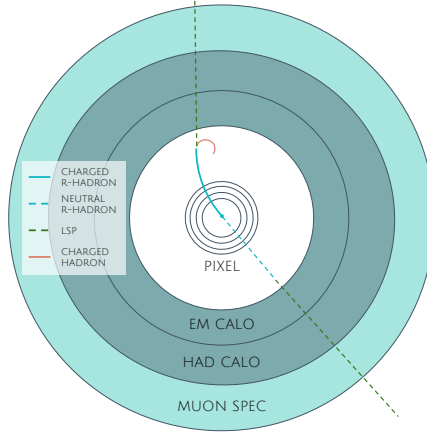


Figure 65: A schematic diagram of an R-Hadron event with a lifetime around 4 ns. The diagram includes one charged R-Hadron (solid blue), one neutral R-Hadron (dashed blue), LSPs (dashed green) and a charged hadron (solid orange). The pixel detector, calorimeters, and muon system are illustrated but not to scale.

2801 If the decay products are not soft, the R-Hadron daughters form jets, resulting
 2802 in an event-level signature of up to two high-momentum tracks, jets, and signif-
 2803 icant missing energy. The missing energy has the same origin as in the case of
 2804 0.01 ns lifetimes, from the decay to unmeasured particles, and again can be large.
 2805 The high-momentum tracks will also have the characteristically high-ionization
 2806 of massive, long-lived particles in the inner detector. Figure 66 illustrates an ex-
 2807 ample event with one charged R-Hadron which decays after approximately 10 ns,
 2808 and shows how the jets from the decay can still be reconstructed in the calorime-
 2809 ter. Several previous searches on ATLAS from Run 1 have used this signature to
 2810 search for R-Hadrons [77, 78], including a dedicated search for metastable parti-
 2811 cles [79].

2812 If the lifetime is longer than several nanoseconds, in the range of 15-30 ns,
 2813 the R-Hadron decay can occur in or after the calorimeters, but prior to reaching
 2814 the muon system. This case is similar to the above, although the jets may not be
 2815 reconstructed, and is covered by many of the same search strategies. The events
 2816 still often have large missing energy, although it is generated through different
 2817 mechanisms. The R-Hadrons do not deposit much energy in the calorimeters, so
 2818 a neutral R-Hadron will not enter into the missing energy calculation. A charged
 2819 R-Hadron opposite a neutral R-Hadron will thus generate significant missing en-
 2820 ergy, and close to 50% of pair-produced R-Hadron events fall into this category.
 2821 If both R-Hadrons are neutral then the missing energy will be low because nei-
 2822 ther is detected. Two charged R-Hadrons will also result in low missing energy
 2823 because both are reconstructed as tracks and will balance each other in the trans-

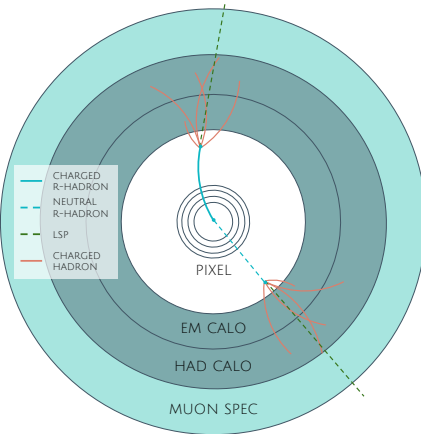


Figure 66: A schematic diagram of an R-Hadron event with a lifetime around 5 ns. The diagram includes one charged R-Hadron (solid blue), one neutral R-Hadron (dashed blue), LSPs (dashed green) and charged hadrons (solid orange). The pixel detector, calorimeters, and muon system are illustrated but not to scale.

verse plane. A small fraction of the time, one of the charged R-Hadron tracks may fail quality requirements and thus be excluded from the missing energy calculation and again result in significant missing energy. Figure 67 illustrates another example event with one charged R-Hadron which decays after approximately 20 ns, and shows how the jets from the decay might not be reconstructed.

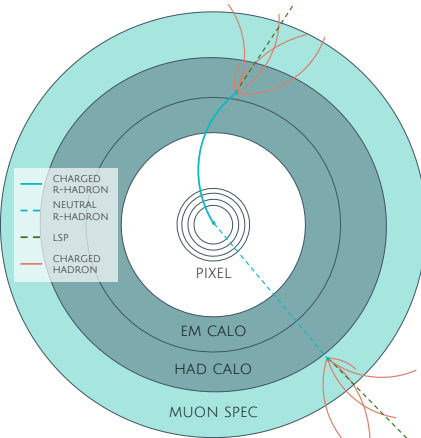


Figure 67: A schematic diagram of an R-Hadron event with a lifetime around 20 ns. The diagram includes one charged R-Hadron (solid blue), one neutral R-Hadron (dashed blue), LSPs (dashed green) and charged hadrons (solid orange). The pixel detector, calorimeters, and muon system are illustrated but not to scale.

The longest lifetimes, the stable case, has all of the features of the 30-50 ns case but with the addition of muon tracks for any R-Hadrons that exit the calorimeter with a charge. That muon track can provide additional information from time-of-flight measurements to help identify LSPs. An example of the event topology for one charged and one neutral stable R-Hadron is shown in Figure 68. Some searches on ATLAS have included this information to improve the search reach for stable particles [78, 80].

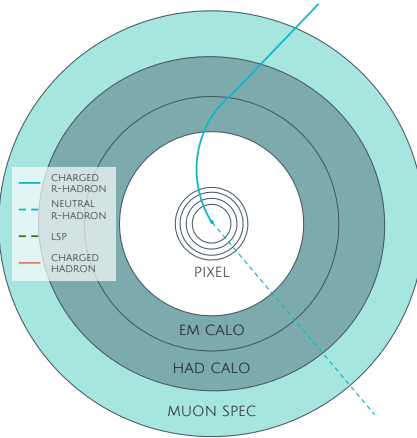


Figure 68: A schematic diagram of an R-Hadron event with a lifetime around 20 ns. The diagram includes one charged R-Hadron (solid blue) and one neutral R-Hadron (dashed blue). The pixel detector, calorimeters, and muon system are illustrated but not to scale.

2836 10.2 SIMULATION

2837 All of the event topologies discussed above are explored by simulations of R-
 2838 Hadron events in the [ATLAS](#) detector. A large number of such samples are gen-
 2839 erated to determine signal efficiencies, to measure expected yields, and to esti-
 2840 mate uncertainties. The primary interaction, pair production of gluinos with
 2841 masses between 400 and 3000 GeV, is simulated using [Pythia 6.4.27](#) [81]
 2842 with the AUET2B [82] set of tuned parameters for the underlying event and the
 2843 CTEQ6L1 [56] PDF set. The simulated interactions include a modeling of pileup
 2844 by adding secondary, minimum bias interactions from both the same (in-time
 2845 pileup) and nearby (out-of-time pileup) bunch crossings. This event generation
 2846 is then augmented with a dedicated hadronization routine to hadronize the long-
 2847 lived gluinos into final states with R-Hadrons [83], with the probability to form
 2848 a gluon-gluino bound set at 10% [84].

2849 The cross sections used for these processes are calculated at next-to-leading
 2850 order ([NLO](#)) in the strong coupling constant with a resummation of soft-gluon
 2851 emmission at next-to-leading logarithmic ([NLL](#)) [85–89]. The nominal predic-
 2852 tions and the uncertainties for each mass point are taken from an envelope of
 2853 cross-section predictions using different PDF sets and factorization and renor-
 2854 malization scales [90].

2855 The R-Hadrons then undergo a full detector simulation [], where the interac-
 2856 tions of the R-Hadrons with the material of the detector are described by dedi-
 2857 cated [Geant4](#) [26] routines. These routines model the interactions described in
 2858 Section 10.1.1, including the ionizing interactions in the silicon modules of the
 2859 inner detector and the R-Hadron-nucleon interactions in the calorimeters [91,
 2860 92]. The specific routine chosen to describe the interactions of the R-Hadrons
 2861 with nucleons, the “generic model”, uses a pragmatic approach where the scatter-
 2862 ing cross section is taken to be a constant 12 mb per light quark. In this model

2863 the gluino itself does not interact at all except through its role as a reservoir of
2864 kinetic energy.

2865 The lifetimes of these R-Hadrons are then simulated at several working points,
2866 $\tau = 0.1, 1.0, 3.0, 10, 30, 50$ and detector stable, where the particle is required to
2867 decay after propagating for a time compatible with its lifetime. Only one decay
2868 mode is simulated for these samples, $\tilde{g} \rightarrow q\bar{q}\tilde{\chi}_1^0$ with the neutralino mass set to
2869 100 GeV, which is chosen because it has the highest sensitivity among all of the
2870 modes studied in previous searches [79]. Heavier neutralinos have similar results
2871 but generate less missing energy which reduces the efficiency of triggering.

2872 All of the simulated events are then reconstructed using the same software
2873 used for collision data. The fully reconstructed events are then reweighted to
2874 match the distribution of initial state radiation in an alternative sample of events,
2875 generated with MG5_aMC@NLO [93], which has a more accurate description of ra-
2876 diate effects than Pythia6. This reweighting provides a more accurate descrip-
2877 tion of the momentum of the gluino-gluino system and is important in modeling
2878 the efficiency of triggering and offline event selection.

2879

2880 EVENT SELECTION

2881 The [LLPs](#) targeted by this search differ in their interactions with the detector from
 2882 [SM](#) particles primarily because of their large mass. When produced at the ener-
 2883 gies available at the [LHC](#), that large mass results in a low β (typically $0.2 < \beta <$
 2884 0.9). Such slow-moving particles heavily ionize in detector material. Each layer
 2885 of the pixel detector provides a measurement of that ionization, through [ToT](#), as
 2886 discussed in Section 7.1.2. The ionization in the pixel detector, quantified in
 2887 terms of dE/dx , provides the major focus for this search technique, along with
 2888 the momentum measured in the entire inner detector. It is effective both for its
 2889 discriminating power and its use in reconstructing a particle’s mass, and it can
 2890 be used for a wide range of masses and lifetimes as discussed in Section 10.1.2.
 2891 However dE/dx needs to be augmented with a few additional selection require-
 2892 ments to provide a mechanism for triggering and to further reduce backgrounds.

2893 Ionization itself is not currently accessible for triggering, so this search in-
 2894 stead relies on E_T^{miss} to trigger signal events. Although triggering on E_T^{miss} can
 2895 be inefficient, E_T^{miss} is often large for many production mechanisms of [LLPs](#), as
 2896 discussed in Section 10.1.

2897 The use of ionization to reject [SM](#) backgrounds relies on well-measured, high-
 2898 momentum tracks, so some basic requirements on quality and kinematics are
 2899 placed on the tracks considered in this search. These quality requirements have
 2900 been significantly enhanced in Run 2 by a newly introduced tracking variable
 2901 that is very effective in removing highly-ionizing backgrounds caused by over-
 2902 lapping tracks. A few additional requirements are placed on the tracks consid-
 2903 ered for [LLP](#) candidates that increase background rejection by targeting specific
 2904 types of [SM](#) particles. These techniques provide a significant analysis improve-
 2905 ment over previous iterations of ionization-based searches on ATLAS by provid-
 2906 ing additional background rejection with minimal loss in signal efficiency.

2907 The ionization measurement with the Pixel detector can be calibrated to pro-
 2908 vide an estimator of $\beta\gamma$. That estimate, together with the momentum measure-
 2909 ment provided by tracking, can be used to reconstruct a mass for each track
 2910 which traverses the pixel detector. That mass variable will be peaked at the [LLP](#)
 2911 mass for any signal, and provides an additional tool to search for an excess. In
 2912 addition to an explicit requirement on ionization, this search constructs a mass-
 2913 window for each targeted signal mass in order to evaluate any excess of events
 2914 and to set limits.

2915 The strategy discussed here is optimized for lifetimes of $O(1) - O(10)$ ns.
 2916 Pixel ionization is especially useful in this regime as particles only need to prop-
 2917 agate through the first seven layers of the inner detector, about 37 cm from the
 2918 beam axis. The search is still competitive with other searches for [LLPs](#) at longer
 2919 lifetimes, because the primary discriminating variables are still applicable even
 2920 for particles that do not decay within the detector [80]. Although the majority of

2921 the requirements will be the same for all lifetimes, two signal regions are defined
 2922 to optimize separately for intermediate and long lifetime particles.

2923 11.1 TRIGGER

2924 Triggering remains a significant difficulty in defining an event selection with
 2925 high signal efficiency in a search for LLPs. There are no triggers available in
 2926 the current ATLAS system that can fire directly from a high momentum track
 2927 with large ionization (Section 6.6). Although in some configurations a charged
 2928 LLP can fire muon triggers, this requirement introduces significant model depen-
 2929 dence on both the allowed lifetimes and the interactions in the calorimeter [73],
 2930 as discussed in Section 10.1.1.

2931 For a search targeting particles which may decay prior to reaching the muon
 2932 system, the most efficient available trigger is based on missing energy [73]. As
 2933 discussed in Section 10.1, signal events can produce significant E_T^{miss} by a few
 2934 mechanisms. At the trigger level however, the missing energy is only calculated
 2935 using the calorimeters (Section 6.6) where the R-Hadrons deposit little energy.
 2936 So, at short lifetimes, E_T^{miss} measured in the calorimeter is generated by an im-
 2937 balance between the jets and undetected LSPs produced in R-Hadron decays. At
 2938 longer lifetimes, without the decay products, missing energy is only produced in
 2939 the calorimeters when the R-Hadrons recoil against an initial state radiation (ISR)
 2940 jet.

2941 These features are highlighted in Figure 69, which shows the E_T^{miss} distribu-
 2942 tions for simulated short lifetime (3 ns) and stable R-Hadron events. The figure
 2943 includes both the offline E_T^{miss} , the missing energy calculated with all available
 2944 information, and Calorimeter E_T^{miss} , the missing energy calculated using only
 2945 information available at the calorimeter which approximates the missing energy
 2946 available at the trigger. The short lifetime sample has significantly greater E_T^{miss}
 2947 and Calorimeter E_T^{miss} than the stable sample as expected. For the stable sam-
 2948 ple, a small fraction of events with very large E_T^{miss} (about 5%) migrate into the
 2949 bin with very small Calorimeter E_T^{miss} because the E_T^{miss} produced by a charged
 2950 R-Hadron track opposite a neutral R-Hadron track does not contribute any miss-
 2951 ing energy in the calorimeters.

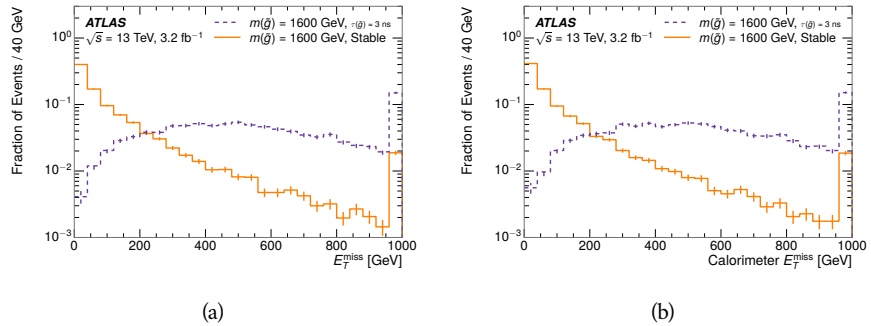


Figure 69: The distribution of (a) E_T^{miss} and (b) Calorimeter E_T^{miss} for simulated signal events before the trigger requirement.

2952 So, either case to some extent relies on kinematic degrees of freedom to pro-
 2953 duce missing energy, as the pair-produced LLPs tend to balance each other in
 2954 the transverse plain. That balance results in a relatively low efficiency for long-
 2955 lifetime particles, roughly 40%, and efficiencies between 65% and 95% for shorter
 2956 lifetimes depending on both the mass and the lifetime. For long lifetimes in par-
 2957 ticular, the presence of ISR is important in providing an imbalance in the trans-
 2958 verse plane, and is an important aspect of modeling the selection efficiency for
 2959 R-Hadron events.

2960 The missing energy trigger with the lowest threshold available is chosen for
 2961 this selection in order to maximize the trigger efficiency. During 2015 data col-
 2962 lection this was the HLT_xe70 trigger, which used a 50 GeV threshold on miss-
 2963 ing energy at LVL1 and a 70 GeV threshold on missing energy at the HLT. These
 2964 formation of the trigger decision for missing energy was discussed in more detail
 2965 in Section 6.6.

2966 11.2 KINEMATICS AND ISOLATION

2967 After the trigger requirement, each event is required to have a primary vertex
 2968 reconstructed from at least two well-measured tracks in the inner detector, each
 2969 with $p_T > 400$ MeV. If more than one such vertex exists, the primary vertex
 2970 is taken to be the one with the largest summed track momentum for all tracks
 2971 associated to that vertex. The offline reconstructed E_T^{miss} is required to be above
 2972 130 GeV to additionally reject SM backgrounds. The transverse missing energy
 2973 is calculated using fully reconstructed and calibrated offline objects, as described
 2974 in Section 7.5. In particular the E_T^{miss} definition in this selection uses jets recon-
 2975 structed with the anti- k_t algorithm with radius $R = 0.4$ from clusters of energy
 2976 in the calorimeter (Section 7.4) and with $p_T > 20$ GeV, as well as reconstructed
 2977 muons, electrons, and tracks not identified as another object type.

2978 The E_T^{miss} distributions are shown for data and a few simulated signals in Fig-
 2979 ure 70, after the trigger requirement. The cut placed at 130 GeV is 95% effi-
 2980 cient for metastable and 90% efficient for stable particles, after the trigger re-
 2981 quirement, because of the missing energy generating mechanisms discussed pre-
 2982 viously. The distribution of data in this figure and subsequent figures in this sec-
 2983 tion can be interpreted as the distribution of backgrounds, as any signal contam-
 2984 ination would be negligible if present at these early stages of the selection (prior
 2985 to the final requirement on ionization). The background falls rapidly with miss-
 2986 ing energy, motivating the direct requirement on E_T^{miss} for the signal region. Al-
 2987 though a tighter requirement than the specified value of 130 GeV would seem to
 2988 increase the search potential from these early distributions, other requirements
 2989 are more optimal when taken as a whole. The specific values for each require-
 2990 ment in signal region were optimized considering the increase in discovery reach
 2991 for tightening the requirement on each discriminating variable. **NOTE: If space**
2992 and time permit, I will add a whole section about signal region optimiza-
2993 tion..

2994 It is typically the practice for searches for new physics on ATLAS to place an
 2995 offline requirement on the triggering variable that is sufficiently tight to guar-

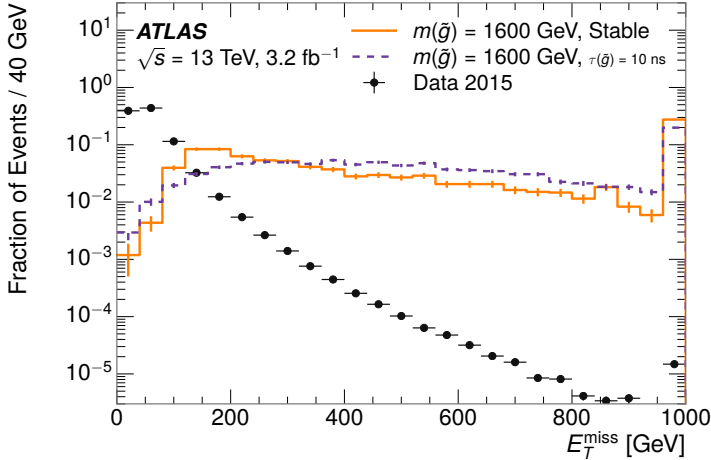


Figure 70: The distribution of E_T^{miss} for data and simulated signal events, after the trigger requirement.

2996 antee that the event would pass the trigger. Such a tight requirement makes the
 2997 uncertainty on the trigger efficiency of the simulation negligible, as modeling the
 2998 regime where the trigger is only partially efficient can be difficult. In this analy-
 2999 sis, however, because of the atypical interactions of R-Hadrons with the tracker
 3000 and the calorimeter, the offline requirement on E_T^{miss} is not sufficient to guar-
 3001 antee a 100% trigger efficiency even at large values, as can be seen in Figure 71.
 3002 This figure shows the efficiency for passing the HLT_xe70 trigger as a function
 3003 of the requirement on E_T^{miss} , which plateaus to roughly 85% even at large values.
 3004 This plateau does not reach 100% because events which have large offline miss-
 3005 ing energy from a neutral R-Hadron produced opposite of a charged R-Hadron
 3006 can have low missing energy in the calorimeters. The Calorimeter E_T^{miss} , on the
 3007 other hand, does not have this effect and reaches 100% efficiency at large values
 3008 because it is the quantity that directly corresponds to the trigger threshold. In
 3009 both cases the efficiency of triggering is greater for the short lifetime sample be-
 3010 cause the late decays to hadrons and LSPs produce an imbalance in the calorime-
 3011 ters even though they may not be reconstructed offline as tracks or jets. For this
 3012 reason, the requirement on E_T^{miss} is determined by optimizing the background
 3013 rejection even though it corresponds to a value of trigger efficiency significantly
 3014 below 1.0.

3015 Potential signal events are then required to have at least one candidate LLP
 3016 track. Although the LLPs are produced in pairs, many models do not consistently
 3017 yield two charged particles. For example, in the R-Hadron model highlighted
 3018 here, only 20% of events have two charged R-Hadrons while 47% of events have
 3019 just one. A signal region requiring two charged candidates could be a powerful
 3020 improvement in background rejection for a larger dataset, but it is not consid-
 3021 ered in this version of the analysis as it was found to be unnecessary to reject the
 3022 majority of backgrounds.

3023 For a track to be selected as a candidate, it must have $p_T > 50 \text{ GeV}$ and pass
 3024 basic quality requirements. The track must be associated to the primary vertex.

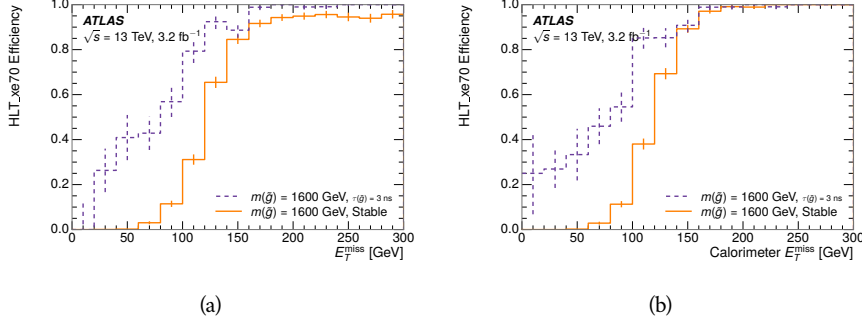


Figure 71: The trigger efficiency for the HLT_xe70 trigger requirement as a function of (a) E_T^{miss} and (b) Calorimeter E_T^{miss} for simulated signal events.

It must also have at least seven clusters in the silicon layers in the inner detector to ensure an accurate measurement of momentum. Those clusters must include one in the innermost layer if the extrapolated track is expected to pass through that layer. And to ensure a reliable measurement of ionization, the track is required to have at least two clusters in the pixel detector that provide a measurement of dE/dx .

At this point in the selection, there is a significant high-ionization background from multiple tracks that significantly overlap in the inner detector. Previous version of this analysis have rejected these overlaps by an explicit overlap rejection between pairs of fully reconstructed tracks, typically by requiring no additional tracks within a cone around the candidate. This technique, however, fails to remove the background from tracks that overlap so precisely that the tracks cannot be separately resolved, which can be produced in very collimated photon conversions or decays of pions.

A new method, added in Run 2, identifies cluster shapes that are likely formed by multiple particles based on a neural network classification algorithm. The number of clusters that are classified this way in the pixel detector for a given track is called N_{split} . As the shape of clusters requires significantly less spatial separation to identify overlaps than it does to reconstruct two fully resolved tracks, this variable is more effective at rejecting backgrounds from overlaps. Figure 72 shows the dependence of ionization on N_{split} ; as N_{split} increases the most probable value of dE/dx grows significantly up to twice the expected value when $N_{\text{split}} = 4$.

This requirement is very successful in reducing the long positive tail of the dE/dx distributions, as can be seen in Figure 73. Comparing the distribution for “baseline tracks”, tracks with only the above requirements on clusters applied and before the requirement on N_{split} , to the distribution with $N_{\text{split}} = 0$, it is clear that the fraction of tracks with large dE/dx is reduced be several orders of magnitude. The tracks without split hits are very close to the dE/dx distribution of identified muons, which are extremely well isolated on average. Figure 73 also includes the distribution of dE/dx in an example signal simulation to demonstrate how effective dE/dx is as a discriminating variable with this isolation applied. The background falls rapidly for $dE/dx > 1.8 \text{ MeVg}^{-1}\text{cm}^2$

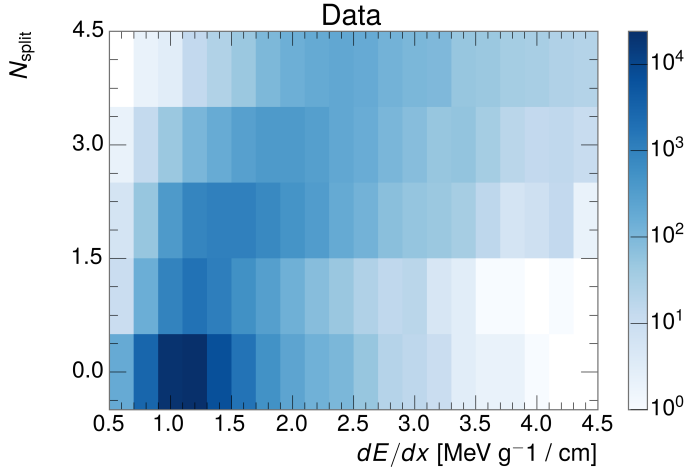


Figure 72: The dependence of dE/dx on N_{split} in data after basic track hit requirements have been applied.

3058 while the majority of the signal, approximately 90% depending on the mass, falls
 3059 above that threshold. Over 90% of [LLP](#) tracks in simulated signal events pass the
 3060 N_{split} -based isolation requirement.

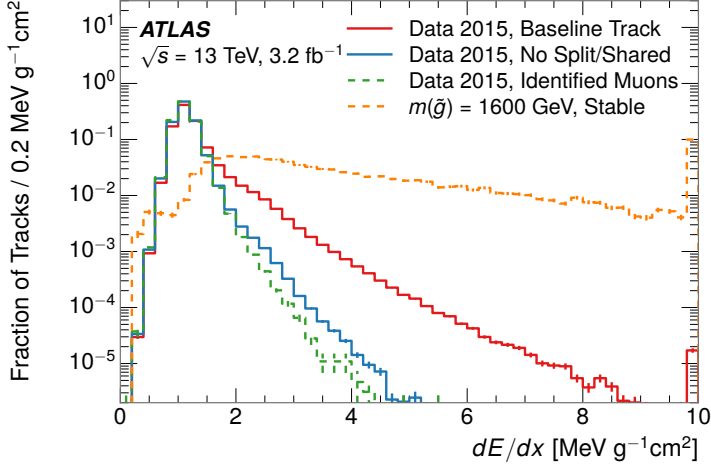


Figure 73: The distribution of dE/dx with various selections applied in data and simulated signal events.

3061 A few additional kinematic requirements are imposed to help reduce [SM](#) back-
 3062 grounds. The momentum of the candidate track must be at least 150 GeV, and
 3063 the uncertainty on that measurement must be less than 50%. The distribution of
 3064 momentum is shown in Figure 74 for tracks in data and simulated signal events
 3065 after the previously discussed requirements on clusters, transverse momentum,
 3066 and isolation have been imposed. The signal particles are much harder on aver-

age than their backgrounds because of the high energy interactions required to produce them. The transverse mass, M_T , defined as

$$M_T = \sqrt{2p_T E_T^{\text{miss}}(1 - \cos(\Delta\phi(E_T^{\text{miss}}, \text{track})))} \quad (20)$$

estimates the mass of a decay of to a single charged particle and an undetected particle and is required to be greater than 130 GeV to reject contributions from the decay of W bosons. Figure 75 shows the distribution of M_T for data and simulated signal events. The signal is distributed over a wide range of M_T , with about 90% above the threshold value of 130 GeV. The data shows a dual-peaked structure, where the first peak comes from W boson decays and the second peak is a kinematic shaping from the requirements on E_T^{miss} and the track p_T in dijet events.

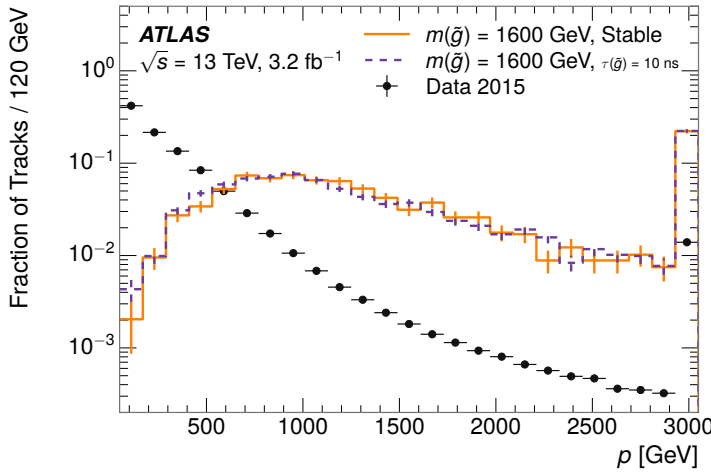


Figure 74: The distribution of track momentum for data and simulated signal events, after previous selection requirements have been applied.

11.3 PARTICLE SPECIES REJECTION

The amount of ionization deposited by particles with low mass and high momentum has a large positive tail [10], so backgrounds can be formed by a wide variety of SM processes when various charged particles have a few randomly large deposits of energy in the pixel detector. Those backgrounds can be additionally reduced by targeting other interactions with the detector where they are expected to have different behavior than R-Hadrons. The interactions with the detector depend on the types of particles produced rather than the processes which produce them, so this search forms a series of rejections to remove backgrounds from individual particle species. These rejections focus on using additional features of the event, other than the kinematics of the candidate track, as they can provide a powerful source of background rejection with very high signal efficiency. However, the lifetime of an R-Hadron can significantly change its

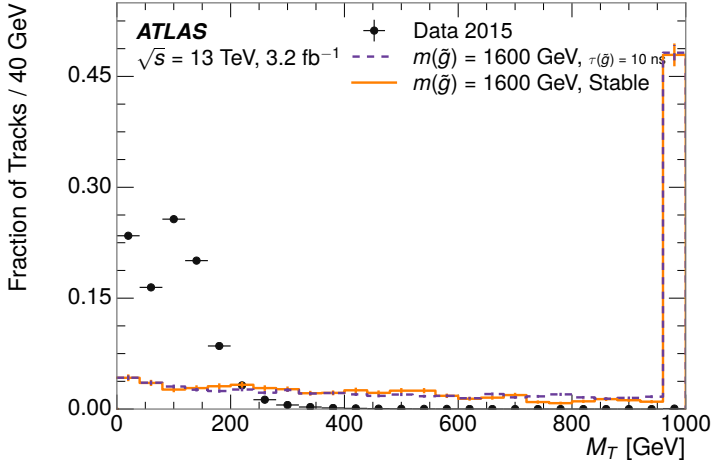


Figure 75: The distribution of M_T for data and simulated signal events, after previous selection requirements have been applied.

3090 detector characteristics, as discussed in Section 10.1.2. To accommodate these
 3091 differences, the SM rejections defined in this section are split to form two signal
 3092 regions, one for long-lifetimes particles, the stable region ($50 \leq \tau[\text{ns}] < \infty \text{ ns}$),
 3093 and one for intermediate lifetime particles, the metastable region ($0.4 < \tau[\text{ns}] <$
 3094 50).

3095 Jets can be very effectively rejected by considering the larger-scale isolation of
 3096 the candidate track. In this case the isolation focuses on the production of nearby
 3097 particles as a jet-veto, rather than the isolation from overlapping tracks based on
 3098 N_{split} that was used to reduce high-ionization backgrounds. As explained in Sec-
 3099 tion 10.1, the fragmentation process which produces an R-Hadron is very hard
 3100 and thus is not expected to produce additional particles with a summed momen-
 3101 tum of more than 5 GeV. The jet-veto uses the summed momentum of tracks
 3102 with a cone of $\Delta R < 0.25$, referred to as p_T^{Cone} , which is shown in Figure 76 for
 3103 data and simulated signal events. In the data this value has a peak at zero from
 3104 isolated tracks such as leptons, and a long tail from jets which contains as much
 3105 as 80% of the background above 20 GeV at this stage of the selection. In signal
 3106 events p_T^{Cone} is strongly peaked at zero and significantly less than 1% of signal
 3107 events have p_T^{Cone} above 20 GeV. This makes a requirement of $p_T^{\text{Cone}} < 20 \text{ GeV}$
 3108 a very effective method to reject background without losing signal efficiency.
 3109 For the stable signal region, this cut is further tightened to $p_T^{\text{Cone}} < 5 \text{ GeV}$ as
 3110 it is the most effective variable remaining to extend the search reach for long
 3111 lifetimes.

3112 Even for fully isolated particles, there are additional methods to reject each
 3113 type of particle using information in the muon system and calorimeters. Muons
 3114 can be identified very reliably using the tracks in the muon system, as described
 3115 in Section 7.3. For intermediate lifetimes the LLPs do not survive long enough
 3116 to reach the muon system, and so muons are vetoed by rejecting tracks that as-
 3117 sociate to a muon with medium muon identification requirements (Section 7.3).
 3118 For longer lifetimes, this rejection is not applied because LLPs which reach the

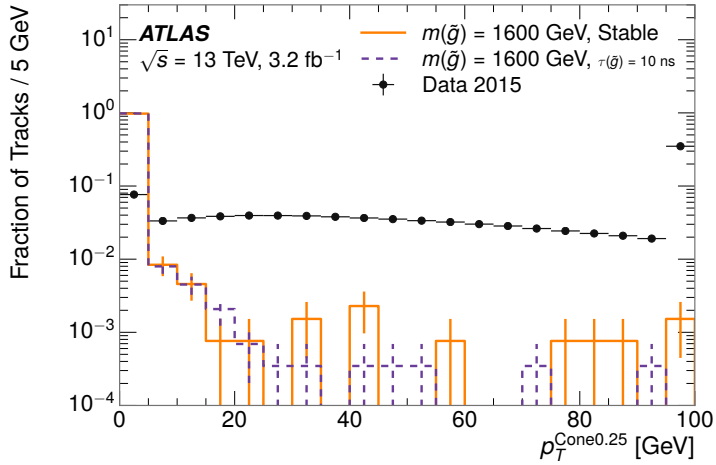


Figure 76: The distribution of summed tracked momentum within a cone of $\Delta R < 0.25$ around the candidate track for data and simulated signal events, after previous selection requirements have been applied.

muon system can be identified as muons as often as 30% of the time in simulated samples.

Calorimeter-based particle rejection relies on the expected small deposits of energy from LLPs. When the lifetime is long enough to reach the calorimeter, a LLP deposits little of its energy as it traverses the material, as discussed in Section 10.1. Even when the particle does decay before the calorimeter, the majority of its energy is carried away by the LSP and not deposited in the calorimeter. In both cases the energy is expected to be distributed across the layers of the calorimeters and not peaked in just one layer. This can be quantified in terms of E/p , the ratio of calorimeter energy of a nearby jet to the track momentum, and f_{EM} , the fraction of energy in that jet within the electromagnetic calorimeter. When no jets fall within a cone of 0.05 of the particle, E/p and f_{EM} are both defined as zero. E/p is expected to be above 1.0 for typical SM particles because of calibration and the contributions from other nearby particles, as discussed in Chapter 8. At these momenta there is no significant zero fraction due to interactions with the detector or insufficient energy deposits (see Section 8.2.2). f_{EM} is peaked close to 1.0 for electrons, and distributed between 10% and 90% for hadrons.

These trends can be seen in the two dimensional distribution for signal in Figure 77 for stable and metastable (10 ns) events. The majority of R-Hadrons in both samples fall into the bin for $E/p = 0$ and $f_{\text{EM}} = 0$ because the majority of the time there is no associated jet. In the stable sample, when there often is an associated jet, E/p is typically still below 0.1, and the f_{EM} is predominantly under 0.8. In the metastable sample, on the other hand, E/p is larger but still typically below 0.1 because of actual jets produced during the decay. The f_{EM} is much lower on average in this case, below 0.1, because the 10 ns lifetime particles rarely decay before passing through the electromagnetic calorimeter. Figure 77 also includes simulated Z decays to electrons or tau leptons. From the decays

3147 to electrons it is clear that the majority of electrons have f_{EM} above 0.9. The
 3148 tau decays include a variety of products. Muons can be seen in the bin where
 3149 $E/p = 0$ and $f_{\text{EM}} = 0$ because they do not have an associated jet. Electrons fall
 3150 into the range where $E/p > 1$ and $f_{\text{EM}} > 0.9$. Hadronic tau decays are the most
 3151 common, and fall in the range of $0.1 < f_{\text{EM}} < 0.9$ and $E/p > 1.0$.

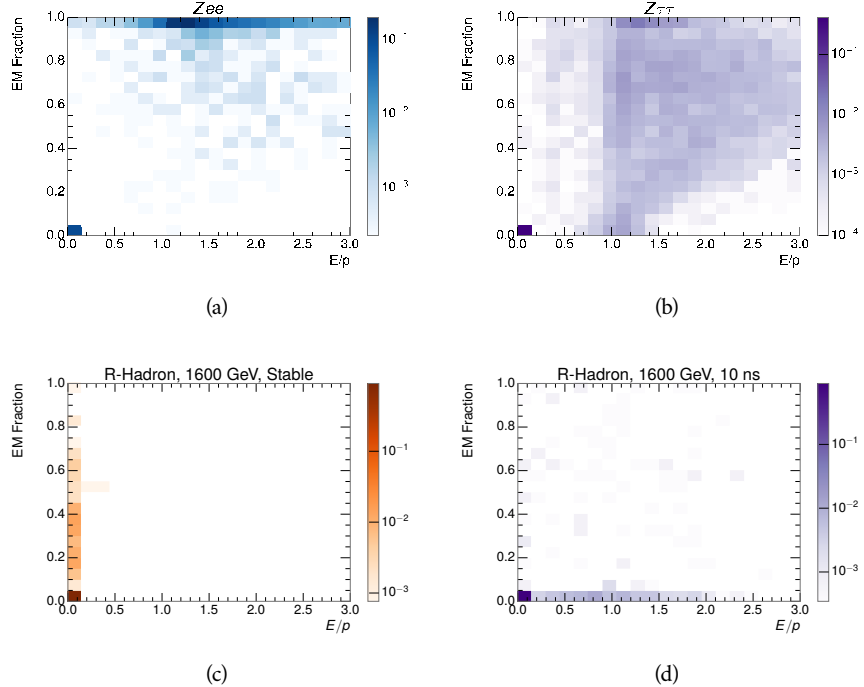


Figure 77: The normalized, two-dimensional distribution of E/p and f_{EM} for simulated
 (a) $Z \rightarrow ee$, (b) $Z \rightarrow \tau\tau$, (c) 1200 GeV Stable R-Hadron events, and (d) 1200
 GeV, 10 ns R-Hadron events.

3152 These differences motivate an electron rejection by requiring an f_{EM} below
 3153 0.9. Similarly, isolated hadrons are rejected by requiring $E/p < 1.0$. These re-
 3154 quirements combine to remove the majority of isolated electrons and hadrons
 3155 but retain over 95% of the simulated signal across a range of masses and lifetimes.

3156 11.4 IONIZATION

3157 The final requirement on the candidate track is the primary discriminating vari-
 3158 able, the ionization in the pixel detector. That ionization is measured in terms
 3159 of dE/dx , which was shown for data and simulated signal events in Figure 73.
 3160 dE/dx is dramatically greater for the high mass signal particles than the back-
 3161 grounds, which start to fall immediately after the minimally ionizing peak at 1.1
 3162 $\text{MeV g}^{-1} \text{cm}^2$. The dE/dx for candidate tracks must be greater than a pseudorapidity-
 3163 dependent threshold, specifically $1.80 - 0.11|\eta| + 0.17\eta^2 - 0.05\eta^3 \text{ MeV g}^{-1} \text{ cm}^{-2}$,
 3164 in order to correct for an approximately 5% dependence of the MIP peak on η .
 3165 The requirement was chosen as part of the signal region optimization, and man-

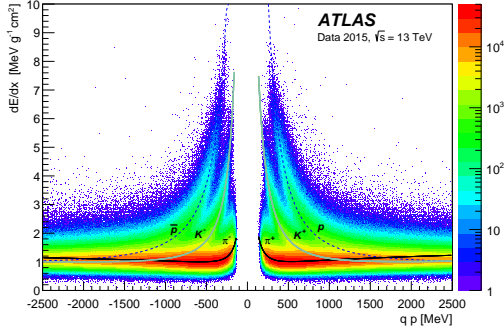


Figure 78: Two-dimensional distribution of dE/dx versus charge signed momentum (qp) for minimum-bias tracks. The fitted distributions of the most probable values for pions, kaons and protons are superimposed.

ages to reduce the backgrounds by a factor of 100 while remaining 70-90% efficient for simulated signal events depending on the mass.

11.4.1 MASS ESTIMATION

The mean value of ionization in silicon is governed by the Bethe equation and the most probable value follows a Landau-Vavilov distribution [10]. Those forms inspire a parametric description of dE/dx in terms of $\beta\gamma$,

$$(dE/dx)_{MPV}(\beta\gamma) = \frac{p_1}{\beta^{p_3}} \ln(1 + [p_2 \beta\gamma]^{p_5}) - p_4 \quad (21)$$

which performs well in the range $0.3 < \beta\gamma < 1.5$. This range includes the expected range of $\beta\gamma$ for the particles targeted for this search, with $\beta\gamma \approx 2.0$ for lower mass particles ($O(100 \text{ GeV})$) and up to $\beta\gamma \approx 0.5$ for higher mass particles ($O(1000 \text{ GeV})$). The parameters, p_i , are fit using a 2015 data sample of low-momentum pions, kaons, and protons as described in Ref. [94]. Figure 78 shows the two-dimensional distribution of dE/dx and momentum along with the above fitted values for $(dE/dx)_{MPV}$.

The above equation (21) is then numerically inverted to estimate $\beta\gamma$ and the mass for each candidate track. In simulated signal events, the mean of this mass value reproduces the generated mass up to around 1800 GeV to within 3%, and 3% shift is applied to correct for this difference. The mass distributions prior to this correction are shown for a few stable mass points in Figure 79. The large widths of these distributions come from the high variability in energy deposits in the pixel detector as well as the uncertainty on momentum measurements at high momentum, but the means converge to the expected values.

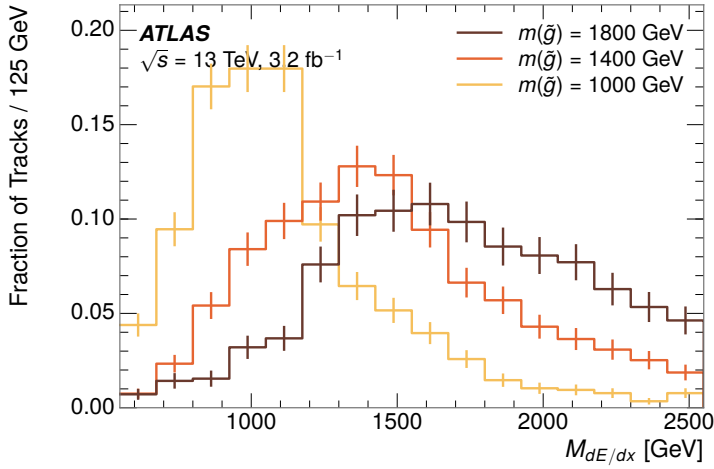


Figure 79: The distribution of mass estimated using dE/dx for simulated stable R-Hadrons with masses between 1000 and 1600 GeV.

3187 This analysis evaluates expected yields and the resulting cross sectional limits
 3188 using windows in this mass variable. The windows are formed by fitting mass
 3189 distributions in simulated signal events like those in Figure 79 to Gaussian distri-
 3190 butions and taking all events that fall within $\pm 1.4\sigma$ of the mean. As can be seen
 3191 in Figure 79, typical values for this width are $\sigma \approx 300 - 500$ GeV depending on
 3192 the generated mass.

3193 11.5 EFFICIENCY

3194 The numbers of events passing each requirement through ionization are shown
 3195 in Table 9 for the full 2015 dataset and a simulated 1600 GeV, 10 ns lifetime R-
 3196 Hadron sample. The table highlights the overall acceptance \times efficiency for sig-
 3197 nal events, which for this example is 19%. Between SM rejection and ionization,
 3198 this signal region reduces the background of tracks which pass the kinematic
 3199 requirements down by an additional factor of almost 2000.

3200 There is a strong dependence of this efficiency on lifetime and mass, with effi-
 3201 ciencies dropping to under 1% at low lifetimes. Figure 80 shows the dependence
 3202 on both mass and lifetime for all signal samples considered in this search. The
 3203 dependence on mass is relatively slight and comes predominantly from the in-
 3204 creasing fraction of R-Hadrons which pass the ionization cut with increasing
 3205 mass. The trigger and E_T^{miss} requirements are most efficient for particles that
 3206 decay before reaching the calorimeters. However, the chance of a particle to be
 3207 reconstructed as a high-quality track decreases significantly at low lifetimes as
 3208 the particle does not propagate sufficiently through the inner detector. These
 3209 effects lead to a maximum in the selection efficiency for lifetimes around 10-30
 3210 ns.

3211 The inefficiency of this signal region at short lifetimes comes almost exclu-
 3212 sively from an acceptance effect, in that the particles do not reach the necessary

Selection	Exp. Signal Events	Observed Events in 3.2 fb^{-1}
Generated	26.0 ± 0.3	
E_T^{miss} Trigger	24.8 ± 0.3 (95%)	
$E_T^{\text{miss}} > 130 \text{ GeV}$	23.9 ± 0.3 (92%)	
Track Quality and $p_T > 50$	10.7 ± 0.2 (41%)	368324
Isolation Requirement	9.0 ± 0.2 (35%)	108079
Track $p > 150 \text{ GeV}$	6.6 ± 0.2 (25%)	47463
$M_T > 130 \text{ GeV}$	5.8 ± 0.2 (22%)	18746
Electron and Hadron Veto	5.5 ± 0.2 (21%)	3612
Muon Veto	5.5 ± 0.2 (21%)	1668
Ionization Requirement	5.0 ± 0.1 (19%)	11

Table 9: The expected number of events at each level of the selection for metastable $1600 \text{ GeV}, 10 \text{ ns}$ R-Hadrons, along with the number of events observed in data, for 3.2 fb^{-1} . The simulated yields are shown with statistical uncertainties only. The total efficiency \times acceptance is also shown for the signal.

3213 layers of the SCT. This can be seen more clearly by defining a fiducial region
 3214 which includes events with at least one R-Hadron that is produced with non-
 3215 zero charge, $p_T > 50 \text{ GeV}$, $p > 150 \text{ GeV}$, $|\eta| < 2.5$, and a decay distance greater
 3216 than 37 cm in the transverse plane. At short (1 ns) lifetimes, the acceptance into
 3217 this region is as low as 4%. Once this acceptance is accounted for, the selection
 3218 efficiency ranges from 25% at lifetimes of 1 ns up to 45% at lifetimes of 10 ns.

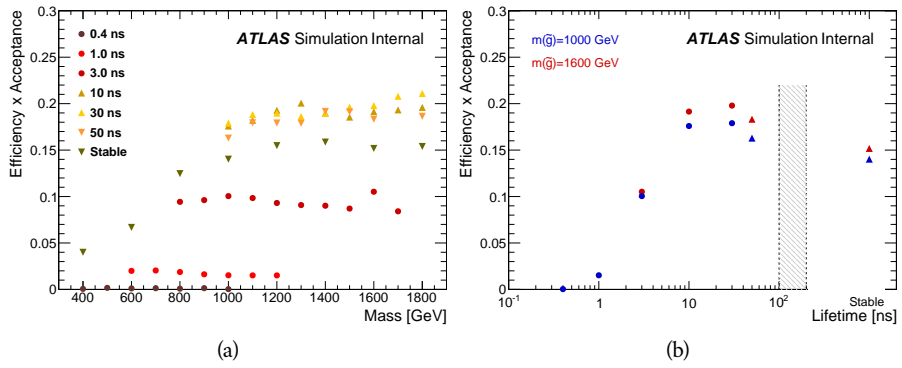


Figure 80: The acceptance \times efficiency as a function of R-Hadron (a) mass and (b) lifetime. (a) shows all of the combinations of mass and lifetime considered in this search, and (b) highlights the lifetime dependence for 1000 GeV and 1600 GeV R-Hadrons.

3219

3220 BACKGROUND ESTIMATION

3221 The event selection discussed in the previous section focuses on detector sig-
 3222 natures, emphasizing a single high-momentum, highly-ionizing track. That track
 3223 is then required to be in some way inconsistent with the expected properties
 3224 of SM particles, with various requirements designed to reject jets, hadrons,
 3225 electrons, and muons (Section 11.3). Therefore the background for this search comes
 3226 entirely from reducible backgrounds that are outliers of various distributions in-
 3227 cluding dE/dx , f_{EM} , and p_T^{Cone} . The simulation can be tuned in various ways to
 3228 do an excellent job of modeling the average properties of each particle type [95],
 3229 but it is not necessarily expected to accurately reproduce outliers. For this rea-
 3230 sons, the background estimation used for this search is estimated entirely using
 3231 data.

3232 12.1 BACKGROUND SOURCES

3233 SM charged particles with lifetimes long enough to form tracks in the inner de-
 3234 tector can be grouped into three major categories based on their detector inter-
 3235 actions: hadrons, electrons, and muons. Every particle that enters into the back-
 3236 ground for this search belongs to one of these types. Relatively pure samples of
 3237 tracks from each of these types can be formed in data by inverting the various
 3238 rejection techniques in Section 11.3. Specifically, muons are selected requiring
 3239 medium muon identification, electrons requiring $E/p > 1.0$ and $f_{\text{EM}} > 0.95$,
 3240 and hadrons requiring $E/p > 1.0$ and $f_{\text{EM}} < 0.95$.

3241 Figure 81 shows the distributions of momentum and dE/dx for these cate-
 3242 gories in data, after requiring the event level selection as well as the track re-
 3243 quirements on p_T , hits, and N_{split} , as discussed in Section 11.2. Simulated signal
 3244 events are included for reference. These distribution are only illustrative of the
 3245 differences between types, as the rejection requirements could alter their shape.
 3246 This is especially significant for momentum which enters directly into E/p and
 3247 can indirectly affect muon identification. However the various types show clear
 3248 differences in both distributions. The distributions of momentum are not nec-
 3249 cessarily expected to match between the various types because the production
 3250 mechanisms for each type result in different kinematic distributions. dE/dx is
 3251 also different between types because of incomplete isolation; although the re-
 3252 quirement on N_{split} helps to reduce the contribution of nearby particles it does
 3253 not completely remove the effect of overlaps. Muons are better isolated because
 3254 they do not have the additional particle from hadronization present for hadrons
 3255 and they are significantly less likely do interact with the detector and produce
 3256 secondary particles compared to hadrons and electrons. Thus muons have the
 3257 smallest fraction of dE/dx above the threshold of $1.8 \text{ MeVg}^{-1}\text{cm}^2$; hadrons and
 3258 electrons have a larger fraction above this threshold.

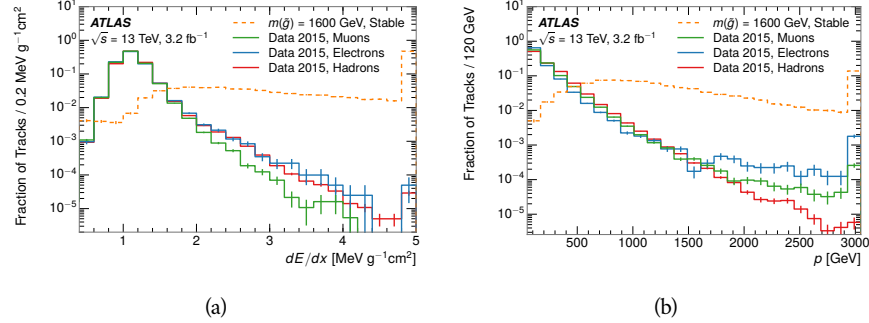


Figure 81: The distribution of (a) dE/dx and (b) momentum for tracks in data and simulated signal after requiring the event level selection and the track selection on p_T , hits, and N_{split} . Each sub-figure shows the normalized distributions for tracks classified as hadrons, electrons, and muons in data and R-Hadrons in the simulated signal.

3259 It is difficult to determine what fraction of each particle type enters into the fi-
 3260 nal signal region. The background method will not have significant dependence
 3261 on the relative contributions of each species, but it is useful to understand the
 3262 differences between each when considering the various tests of the method.

3263 12.2 PREDICTION METHOD

3264 The data-driven background estimation relies on the independence between ion-
 3265 ization and other kinematic variables in the event. For standard model particles
 3266 with momenta above 50 GeV, dE/dx is not correlated with momentum; though
 3267 there is a slight relativistic rise as momentum increases, the effect is small com-
 3268 pared to the width of the distribution of ionization energy deposits.. So, the
 3269 proposed method to estimate the mass distribution of the signal region is to use
 3270 momentum from a track with low dE/dx (below the threshold value) and to com-
 3271 bine it with a random dE/dx value from a dE/dx template. The resulting track is
 3272 just as likely as the original, so a number of such random generations provide the
 3273 expected distributions of momentum and ionization. These are then combined
 3274 using the parametrization described in Section 11.4.1 to form a distribution of
 3275 mass for the signal region.

3276 Algorithmically this method is implemented by forming two distinct Control
 3277 Regions (**CR**s). The first **CR**, CR1, is formed by applying the entire event selec-
 3278 tion from Chapter 11 up to the dE/dx and mass requirements. The dE/dx re-
 3279 quirement is instead inverted for this region. Because of the independence of
 3280 dE/dx , the tracks in this control region have the same kinematic distribution
 3281 as the tracks in the signal region, and are used to measure a two-dimensional
 3282 template of p and η . The second **CR**, CR2, is formed from the event selection
 3283 through the dE/dx requirement, but with an inverted E_T^{miss} requirement. The
 3284 tracks in this control region are expected to have similar dE/dx distributions to
 3285 the signal region before the ionization requirement, and so this region is used to
 3286 measure a two-dimensional template of dE/dx and η .

3287 The contribution of any signal to the control regions is minimized by the in-
 3288 verted selection requirements. Only less than 10% of simulated signal events
 3289 have either dE/dx or E_T^{miss} below the threshold values in the original signal re-
 3290 gion, while the backgrounds are significantly enhanced by inverting those re-
 3291 quirements. The signal contamination is less than 1% in both control regions
 3292 for all of the simulated masses and lifetimes considered in this analysis.

3293 With those measured templates, the shape of the mass estimation is generated
 3294 by first selecting a random (p, η) combination from CR1. This momentum
 3295 value is combined with a dE/dx value taken from the appropriate distribution
 3296 of dE/dx for the selected η from CR2. The use of η in both random samplings
 3297 controls for any correlation between p , dE/dx , and η . Those values are then
 3298 used to calculate a mass in the same way that is done for regular tracks in data,
 3299 see Section 11.4.1. As this procedure includes all dE/dx values, the cut at 1.8
 3300 MeVg $^{-1}$ cm 2 is then enforced to fully model the signal region. The generated
 3301 mass distribution is then normalized by scaling the background estimate to the
 3302 data in the region $M < 160$ GeV, where signals of this type have already been
 3303 excluded [79]. This normalization uses the distributions of mass generated with-
 3304 out the ionization requirement.

3305 The statistical uncertainties on these background distributions are calculated
 3306 by independently fluctuating each bin of the input templates according to their
 3307 Poisson uncertainties. These fluctuations are repeated a large number of times,
 3308 and the uncertainty on the resulting distribution is taken as the root mean square
 3309 (RMS) deviation of the fluctuations from the average. As the procedure uses one
 3310 million random combinations to generate the distributions, The statistical un-
 3311 certainty from the actual random generations is negligible compared to the un-
 3312 certainty from measuring the templates.

3313 12.3 VALIDATION

3314 The validity of the background estimation technique can be evaluated in both
 3315 data and simulation. The underlying assumption that random combinations of
 3316 dE/dx and momentum can predict a mass distribution in an orthogonal region
 3317 can be tested using simulated samples where concerns like multiple particle types
 3318 can be controlled. Using the same technique in another set of signal-depleted
 3319 regions in data then extends this confidence to the more complicated case where
 3320 several particle species are inherently included.

3321 12.3.1 CLOSURE IN SIMULATION

3322 The first test of the procedure is done using a simulated sample of $W \rightarrow \mu\nu$
 3323 decays. These types of events provide the ingredients required to test the back-
 3324 ground estimate, E_T^{miss} and isolated tracks, with high statistics. In this example
 3325 there is no signal, so simulated events in the orthogonal CRs are used to estimate
 3326 the shape of the mass distribution of the simulated events in the signal region. To
 3327 reflect the different topology for W boson decays, the CRs use slightly modified
 3328 definitions. In all CRs, the requirement of $p > 150$ GeV and the SM rejection

3329 requirements are removed. Additionally, for the signal region the requirement
 3330 on E_T^{miss} is relaxed to 30 GeV and the corresponding inverted requirement on
 3331 CR2 is also set at 30 GeV.

3332 With these modified selections, the simulated and randomly generated distri-
 3333 butions of $M_{dE/dx}$ are shown in Figure 82. This figure includes the mass distri-
 3334 butions before and after the requirement on dE/dx , which significantly shapes
 3335 the distributions. In both cases the background estimation technique repro-
 3336 duces the shape of $M_{dE/dx}$ in the signal region. There is a small difference in the pos-
 3337 itive tail of the mass distribution prior to the ionization cut, where the random
 3338 events underestimate the fraction of tracks with mass above 150 GeV by about
 3339 20%. After the ionization requirement, however, this discrepancy is not present
 3340 and the two distributions agree to within statistical uncertainties.

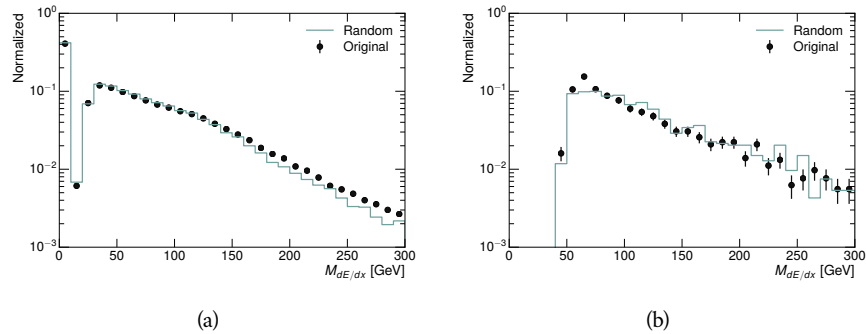


Figure 82: The distribution of $M_{dE/dx}$ (a) before and (b) after the ionization requirement for tracks in simulated W boson decays and for the randomly generated background estimate.

3341 This ability to reproduce the shape of the mass distribution in simulated events
 3342 shows that the technique works as expected. No significant biases are acquired
 3343 in using low dE/dx events to select kinematic templates or in using low E_T^{miss}
 3344 events to select ionization templates, as either would result in a mismodeling of
 3345 the shape of the mass distribution. The simulated events contain only one par-
 3346 ticle type, however, so this test only establishes that the technique works well
 3347 when the the CRs are populated by exactly the same species.

3348 12.3.2 VALIDATION REGION IN DATA

3349 The second test of the background estimate is performed using data in an or-
 3350 thogonal validation region. The validation region, and the corresponding CRs,
 3351 are formed using the same selection requirements as in the nominal method but
 3352 with a modified requirement on momentum, $50 < p[\text{GeV}] < 150$. This allows
 3353 the technique to be checked in a region with very similar properties but where
 3354 the signal is depleted, as the majority of the signal has momentum above 150
 3355 GeV while the backgrounds are enhanced below that threshold. Any biases on
 3356 the particle composition of the CRs for the signal region will be reflected in the
 3357 CRs used to estimate the mass distribution in the validation region.

3358 Figure 83 shows the measured and randomly generated mass distributions for
 3359 data before and after the ionization requirement. The background estimate does
 3360 an excellent job of modeling the actual background before the ionization require-
 3361 ment, with good agreement to within the statistical uncertainties out to the limit
 3362 of the mass distribution. There are very few events in the validation region after
 3363 the ionization requirement, but the few observed events are consistent with the
 3364 background prediction. The good agreement in this validation region provides
 3365 a confirmation that the technique works even in the full-complexity case with
 3366 multiple particle types entering the distributions. Any bias from changes in par-
 3367 ticle composition between regions is small compared to statistical uncertainties.

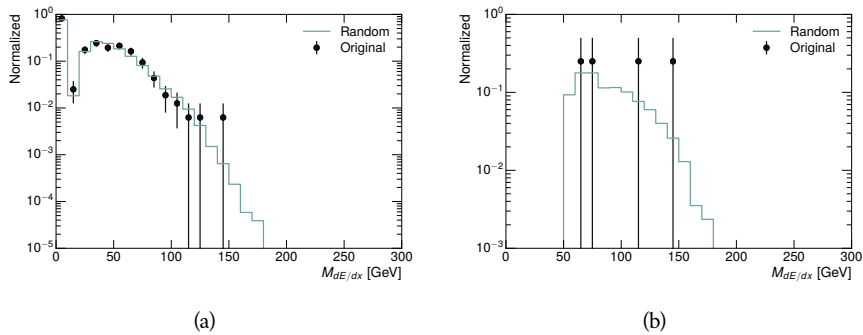


Figure 83: The distribution of $M_{dE/dx}$ (a) before and (b) after the ionization require-
 ment for tracks in the validation region and for the randomly generated back-
 ground estimate.

3368

3369 SYSTEMATIC UNCERTAINTIES AND RESULTS

3370 13.1 SYSTEMATIC UNCERTAINTIES

3371 A number of systematic uncertainties affect the interpretation of the results of
 3372 the search. These uncertainties can broken down into two major categories,
 3373 those which affect the estimate of the background using data and those which
 3374 affect the measurement of the signal yield estimated with simulated events. The
 3375 total measured systematic uncertainties are 7% for the background estimation
 3376 and approximately 32% for the signal yield depending on lifetime. These system-
 3377atic uncertainties are expected to be small compared to the statistical fluctuations
 3378 of the measured yields so that measured cross-sectional limits will be dominated
 3379 by statistical uncertainties. The following sections describe each source of sys-
 3380 tematic uncertainty for each of the two types.

3381 13.1.1 BACKGROUND ESTIMATE

3382 The systematic uncertainties on the background estimate come primarily from
 3383 considering alternative methods for generating the background distributions.
 3384 These uncertainties are small compared to the statistical uncertainties on the
 3385 background estimate which come from the limited statistics in measuring the
 3386 template distributions, as described in Section 12.2. They are summarized in
 3387 Table 10.

Source of Uncertainty:	Value [%]
Analytic Description of dE/dx	4.0
Muon Fraction (Stable Region only)	3.0
IBL Ionization Correction	3.8
Normalization	3.0
Total (Metastable Region):	6.3
Total (Stable Region):	7.0

Table 10: A summary of the sources of systematic uncertainty for the data-driven background in the signal region. If the uncertainty depends on the mass, the maximum values are reported.

3388 13.1.1.1 ANALYTIC DESCRIPTION OF DE/DX

3389 The background estimate uses a binned template distribution to estimate the
 3390 dE/dx of tracks in the signal region, as described in Section 12.2. It is also possi-

ble to fit that measured distribution to a functional form to help smooth the distribution in the tails of dE/dx where the template is driven by a small number of tracks. Both Landau convolved with a Gaussian and Crystal Ball functions are considered as the functional form and used to re-estimate the background distribution. The deviations compared to the nominal method are found to be 4%, and this is taken as a systematic uncertainty to cover the inability carefully predict the contribution from the long tail of dE/dx where there are few measurements available in data.

3399 13.11.2 MUON FRACTION

3400 The stable region of the analysis explicitly includes tracks identified as muons,
 3401 which have a known difference in their dE/dx distributions compared to non-
 3402 muon tracks (Section 12.1). To account for a difference in muon fraction be-
 3403 tween the background region and the signal region for this selection, the dE/dx
 3404 templates for muons and non-muons are measured separately and then the rel-
 3405 ative fraction of each is varied in the random generation. The muon fraction
 3406 is varied by its statistical uncertainty and the resulting difference of 3% in back-
 3407 ground yield is taken as the systematic uncertainty.

3408 13.11.3 IBL CORRECTIONS

3409 The IBL, described in Section 6.3.1, received a significant dose of radiation during
 3410 the data collection in 2015. The irradiation can cause a drift in the frontend
 3411 electronics and thus alter the dE/dx measurement which includes the ToT output
 3412 by the IBL. These effects are corrected for in the nominal analysis by scaling the
 3413 dE/dx measurements by a constant factor derived for each run to match the
 3414 average dE/dx value to a reference run where the IBL was known to be stable
 3415 to this effect. However, this corrective factor does not account for inter-run
 3416 variations. To account for this potential drift of dE/dx , the correction procedure
 3417 is repeated by varying the corrections up and down by the maximal run-to-run
 3418 variation from the full data-taking period, which results in an uncertainty of
 3419 3.8%.

3420 13.11.4 NORMALIZATION

3421 As described in Section 12.2, the generated distribution of masses is normalized
 3422 in a shoulder region ($M < 160$ GeV) where signals have been excluded by pre-
 3423 vious analyses. That normalization factor is varied by its statistical uncertainty
 3424 and the resulting fluctuation in the mass distribution of 3% is taken as a system-
 3425 atic uncertainty on the background estimate.

3426 13.1.2 SIGNAL YIELD

3427 The systematic uncertainties on the signal yield can be divided into three cate-
 3428 gories; those on the simulation process, those on the modeling of the detector
 3429 efficiency or calibration, and those affecting the overall signal yield. They are
 3430 summarized in Table 10. The largest uncertainty comes from the uncertainty

3431 on the production cross section for gluinos, which is the dominant systematic
3432 uncertainty in this analysis.

Source of Uncertainty	-[%]	+[%]
ISR Modeling (Metastable Region)	1.5	1.5
ISR Modeling (Stable Region)	14	14
Pile-up Reweighting	1.1	1.1
Trigger Efficiency Reweighting	0.9	0.9
E_T^{miss} Scale	1.1	2.2
Ionization Parametrization	7.1	0
Momentum Parametrization	0.3	0.0
Electron Rejection	0.0	0.0
Hadron Rejection	0.0	0.0
μ Identification	4.3	4.3
Luminosity	5	5
Signal size uncertainty	28	28
Total (Metastable Region)	30	29
Total (Stable Region)	33	32

Table 11: A summary of the sources of systematic uncertainty for the simulated signal yield. The uncertainty depends on the mass and lifetime, and the maximum negative and positive values are reported in the table.

3433 13.1.2.1 ISR MODELING

3434 As discussed in Section 10.2, MadGraph is expected to reproduce the distribution
3435 of ISR in signal events more accurately than the nominal Pythia samples. The
3436 analysis reweights the distribution of ISR in the simulated signal events to match
3437 the distribution found in generated MadGraph samples. This has an effect on the
3438 selection efficiency in the signal samples, where ISR contributes to the generation
3439 of E_T^{miss} . To account for the potential inaccuracy on the simulation of ISR at high
3440 energies, half of the difference between the signal efficiency with the reweighted
3441 distribution and the original distribution is taken as a systematic uncertainty.

3442 13.1.2.2 PILEUP REWEIGHTING

3443 The simulated events were generated prior to data collection with an estimate of
3444 the average number of interactions per bunch crossing. This estimate does not
3445 match the value of pileup during actual data collection, but a large fraction of the
3446 simulated events would be discarded in order to match the distribution in data.
3447 Therefore the simulated signal events are not reweighted for pileup by default
3448 in the analysis. The effect of the pileup on signal efficiency is not expected to
3449 depend on the mass or lifetime of the generated signal events, which allows all

3450 of the generated signal events to be used together to assess the pileup dependence.
 3451 To account for the potential effect of the difference in the number of interactions
 3452 per bunch crossing between data and simulation, the difference in yield between
 3453 the nominal signal events and the reweighted events averaged over all masses
 3454 and lifetimes is taken as a systematic uncertainty on the yield for each mass and
 3455 lifetime (1.1%).

3456 13.1.2.3 TRIGGER EFFICIENCY REWEIGHTING

3457 As described in Section 11.2, the selection for this analysis does not require a suf-
 3458 ficiently large value of E_T^{miss} to be above the plateau of trigger efficiency. There-
 3459 fore, some signal events which would otherwise pass the event selection can be
 3460 excluded because of the trigger requirement. These effects can be difficult to es-
 3461 timate in simulation, and thus are constrained by comparing data and simulated
 3462 events in an alternative W boson region which uses decays to muons to find a rel-
 3463 atively pure sample of events with missing energy. The trigger efficiency for data
 3464 and simulated W events are shown in Figure 84. The comparison between data
 3465 and MC in this region constrains the simulation of the trigger efficiency. The
 3466 simulated signal events are reweighted by the ratio of data to simulation in the
 3467 W boson decays, while the difference between the data and simulation in those
 3468 decays is taken as a systematic uncertainty. This results in an uncertainty of only
 3469 0.9% as the majority of events are well above the plateau and the disagreement
 3470 between data and simulation is small even below that plateau.

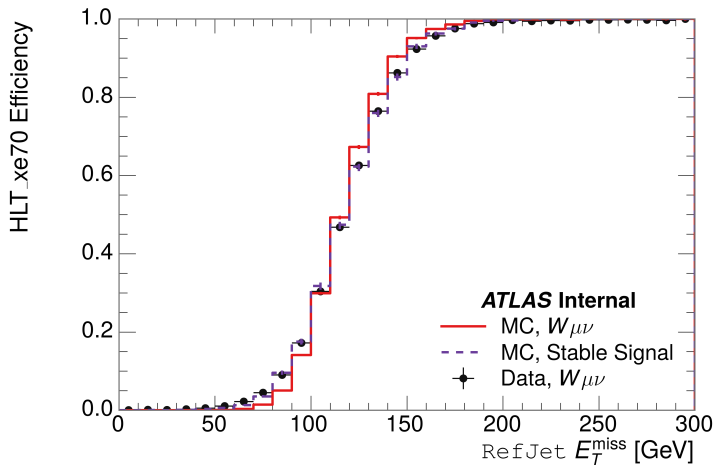


Figure 84: The trigger efficiency for the HLT_xe70 trigger requirement as a function of Calorimeter E_T^{miss} for simulated data events with a W boson selection. Simulated signal events and simulated W boson events are also included.

3471 13.1.2.4 MISSING TRANSVERSE MOMENTUM SCALE

3472 The ATLAS Combined Performance (CP) group provides a default recommenda-
 3473 tion for systematic variations of jets and missing energy (**note: I'm not quite**
 3474 **sure what to cite for this - I don't see any papers from the jet/met group**

Systematic Variation	-[%]	+[%]
JET_GroupedNP_1	-0.7	1.3
JET_GroupedNP_2	-0.7	1.2
JET_GroupedNP_3	-0.5	1.3

Table 12: Example of the contributing systematic variations to the total systematic for the E_T^{miss} Scale, as measured in a 1200 GeV, Stable R-Hadron signal sample.

3475 **after this was implemented).** These variations enter into this analysis only in
 3476 the requirement on E_T^{miss} . The effect of the measured scale of E_T^{miss} is evaluated
 3477 by varying the E_T^{miss} scale according to the one sigma variations provided by all
 3478 **CP** recommendations on objects affecting event kinematics in simulated signal
 3479 events. Missing energy is reconstructed from fully reconstructed objects so any
 3480 systematic uncertainties affecting jets, muons, electrons, or the E_T^{miss} soft terms
 3481 are included. The only non-negligible contributions found using this method are
 3482 itemized in Table 12 for an example signal sample (1200 GeV, Stable R-Hadron),
 3483 where the systematic is measured as the relative difference in the final signal ef-
 3484 ficiency after applying the associated variation through the CP tools. The only
 3485 variations that are significant are the grouped jet systematic variations, which
 3486 combine recommended jet systematic uncertainties into linearly independent
 3487 variations.

3488 As the peak of the reconstructed E_T^{miss} distribution in the signal is significantly
 3489 above the current threshold for events which pass the trigger requirement, the
 3490 effect of scale variation is expected to be small, which is consistent with the mea-
 3491 sured systematic of approximately 2%. Events which do not pass the trigger re-
 3492 quirement usually fail because there are no ISR jets in the event to balance the
 3493 R -hadrons' transverse momentum, so the reconstructed E_T^{miss} is low and there-
 3494 fore also expected to be not very sensitive to scale changes.

3495 13.1.2.5 MOMENTUM PARAMETRIZATION

3496 The uncertainty on the signal efficiency from track momentum is calculated us-
 3497 ing the **CP** group recommendations for tracks. In particular, only one recom-
 3498 mended systematic variation affects track momentum, the sagitta bias for q/P .
 3499 This uncertainty is propagated to the final selection efficiency by varying the
 3500 track momentum by the recommended one sigma variation, and the associated
 3501 uncertainty is found to be negligible (0.3%).

3502 13.1.2.6 IONIZATION REQUIREMENT

3503 The dE/dx distributions in data and simulated events have different most prob-
 3504 able values, which is due in part to radiation effects in the detector that are not
 3505 fully accounted for in the simulation. The difference does not affect the mass
 3506 measurement used in this analysis, as independent calibrations are done in sim-
 3507 ulation and in data. However, it does affect the efficiency of the high dE/dx
 3508 selection requirement. To calculate the size of the effect on the signal efficiency,

3509 the dE/dx distribution in signal simulation is scaled by a scale factor obtained
 3510 from comparing the dE/dx distribution of inclusive tracks in data and in sim-
 3511 ulation. The difference in efficiency for this sample with a scaled dE/dx dis-
 3512 tribution, relative to the nominal case, is taken as a systematic uncertainty on
 3513 signal efficiency. The uncertainty is as large as 7% for low masses and falls to a
 3514 negligible effect for large masses.

3515 13.1.2.7 ELECTRON AND JET REJECTION

3516 The systematic uncertainty on the electron rejection is measured by varying the
 3517 EM fraction requirement significantly, from 0.95 to 0.9. This is found to have
 3518 a less than 0.04% effect on signal acceptance, on average, and so is completely
 3519 negligible. Similarly, the uncertainty on jet rejection is measured by tightening
 3520 the E/p requirement from 0.5 to 0.4. This is found to have no effect on signal
 3521 acceptance, so again the systematic is again negligible.

3522 13.1.2.8 MUON VETO

3523 The metastable signal region requires that the candidate tracks are not identi-
 3524 fied as medium muons because the majority of R-Hadrons in the lifetime range
 3525 included in that region do not reach the muon spectrometers before they de-
 3526 cay. However, the exponential tail of the R-Hadron lifetime distribution results
 3527 in some R-Hadrons traversing the muon spectrometer. These can still fail the
 3528 muon medium identification because they can fail on the requirement on the
 3529 number of precision hits required to pass the loose selection because they ar-
 3530 rive late to the muon spectrometer. This can be seen in Figure 85, which shows
 3531 the efficiency of the muon veto as a function of $1/\beta$, for two simulated stable
 3532 R-Hadron samples.

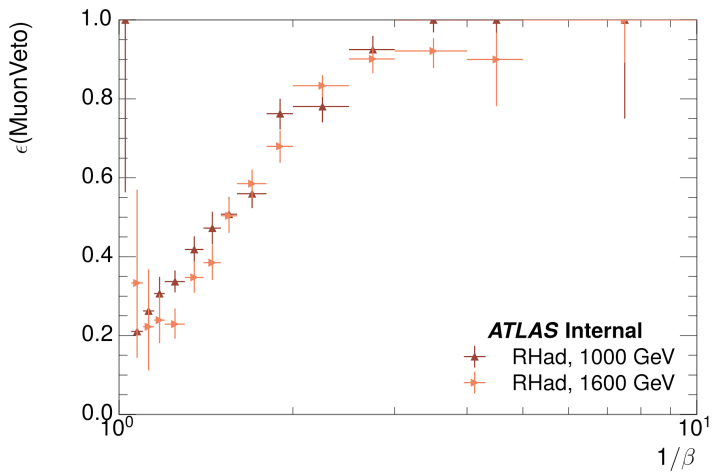


Figure 85: The efficiency of the muon veto for R -hadrons of two different masses, as a function of $\frac{1}{\beta}$ for simulated R-Hadron tracks.

3533 Thus, the efficiency of the muon veto depends on the timing resolution of
 3534 the spectrometer, so an uncertainty is applied to the signal efficiency to cover

3535 differences in timing resolution between data and simulation. First, a sample of
 3536 $Z \rightarrow \mu\mu$ events is selected in data in which one of the muons has a late arrival
 3537 time measured in the MDT. Then the reconstructed β distribution is compared
 3538 to the distribution in simulated $Z \rightarrow \mu\mu$ events; the difference between these
 3539 two distributions reflects the difference in timing resolution between data and
 3540 simulation. To emulate this difference in simulated signal events, the magnitude
 3541 of the difference is used to scale and shift the true β distribution of R-Hadrons in
 3542 simulation. Signal events are then reweighted based on this varied β distribution,
 3543 and the difference in the efficiency of the muon veto selection is compared with
 3544 the nominal and reweighted true β distributions. The difference in muon veto
 3545 efficiency is taken as a systematic uncertainty of the muon veto.

3546 The comparison of reconstructed β between data and simulation is performed
 3547 separately in the barrel, transition, and endcap regions of the spectrometer, and
 3548 the reweighting of the true β distribution in signal is done per region. The com-
 3549 parison of average reconstructed MDT β between data and simulation for the
 3550 barrel region is shown in Figure 86 for $Z \rightarrow \mu\mu$ events. As expected, The uncer-
 3551 tainty is found to be negligible for R-hadrons with short lifetimes, and is only
 3552 significant for lifetimes above 30 ns.

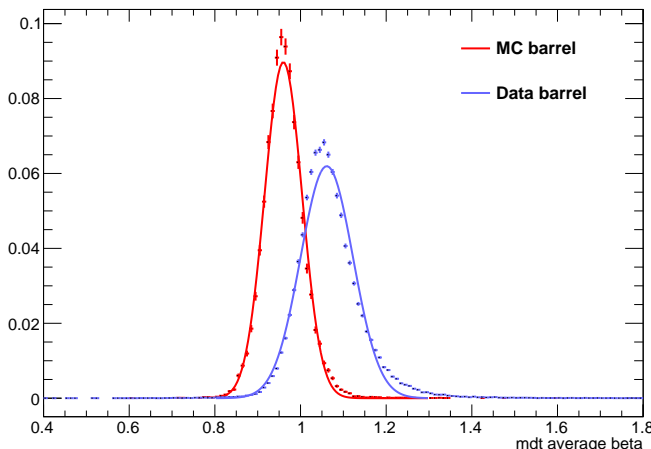


Figure 86: The average reconstructed MDT β distribution for $Z \rightarrow \mu\mu$ events in which
 one of the muons is reconstructed as a slow muon, for both data and simula-
 tion. A gaussian fit is superimposed.

3553 13.1.2.9 LUMINOSITY

3554 The luminosity uncertainty is provided by a luminosity measurement on ATLAS
 3555 and was measured to be 5% at the time of the publication of this analysis.

3556 13.1.2.10 SIGNAL SIZE

3557 As discussed in Section 10.2, the signal cross sections are calculated at NLO in the
 3558 strong coupling constant with a resummation of soft-gluon emission at NLL. The
 3559 uncertainties on those cross sections are between 14% to 28% for the R-Hadrons

Selection Region	Expected Background	Data
Stable	$17.2 \pm 2.6 \pm 1.2$	16
Metastable	$11.1 \pm 1.7 \pm 0.7$	11

Table 13: The estimated number of background events and the number of observed events in data for the specified selection regions prior to the requirement on mass. The background estimates show statistical and systematic uncertainties.

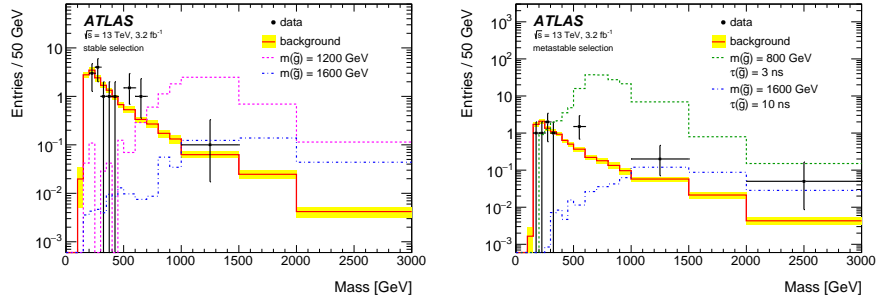


Figure 87: The observed mass distribution of events in data and the generated background distribution in (a) the stable and (b) the metastable signal region. A few example simulated signal distributions are superimposed.

3560 in the range of 400 to 1800 GeV [91, 92], where the uncertainty increases with
3561 the mass.

3562 13.2 FINAL YIELDS

3563 This full analysis was performed using the 3.2 fb^{-1} from the 2015 data-taking.
3564 Using the selections discussed in Chapter 11, sixteen events were observed in
3565 the stable signal region and eleven events were observed in the metastable signal
3566 region, prior to requirements on the candidate track mass. The background esti-
3567 mate discussed in Chapter 12 predicts $17 \pm 2.6(\text{stat}) \pm 1.2(\text{syst})$ events for the
3568 stable region and $11.1 \pm 1.7(\text{stat}) \pm 0.7(\text{syst})$ events for the metastable region.
3569 These counts are summarized in Table 13.

3570 The mass estimated using dE/dx (Section 11.4.1) provides the final discrimi-
3571 nating variable, where the signal would be expected as an excess in the falling ex-
3572 ponential tail of the expected background. The observed distribution of masses
3573 is shown in Figure 87, along with the predicted distribution from the background
3574 estimate for each signal region. Both include a few example simulated signal dis-
3575 tributions, which show the scale of an excess were the R-Hadron signals present.
3576 Their is no statistically significant evidence of an excess in the data over the back-
3577 ground estimation. From this distribution it is clearly possible to rule out signals
3578 with lower masses, around 1200 GeV, which have larger cross sections.

3579 13.3 CROSS SECTIONAL LIMITS

3580 Because there is no observed significant excess of events in the signal region, this
 3581 analysis sets upper limits on the allowed cross section for R-Hadron production.
 3582 These limits are set for each mass point by counting the observed events in data,
 3583 along with the expected background and simulated signal events, in windows of
 3584 mass. The mass windows are formed by fitting the distribution of signal events to
 3585 a Gaussian distribution, and the window is then $\pm 1.4\sigma$ around the center of that
 3586 Gaussian. Two examples of the windows formed by this procedure are shown
 3587 in Tables 14-15, for the stable and 10 ns working points. The corresponding
 3588 counts of observed data, expected background, and simulated signal for those
 3589 same working points are shown in Tables 16-17. Appendix B includes the mass
 3590 windows and counts for all of the considered signal points.

$m(\tilde{g})$ [GeV]	Left Extremum [GeV]	Right Extremum [GeV]
1000	655	1349
1100	734	1455
1200	712	1631
1300	792	1737
1400	717	1926
1500	815	2117
1600	824	2122
1700	900	2274
1800	919	2344

Table 14: The left and right extremum of the mass window for each generated mass point with a 10 ns lifetime.

$m(\tilde{g})$ [GeV]	Left Extremum [GeV]	Right Extremum [GeV]
800	627	1053
1000	726	1277
1200	857	1584
1400	924	1937
1600	993	2308
1800	1004	2554

Table 15: The left and right extremum of the mass window used for each generated stable mass point.

3591 The 95% confidence level upper limits on the cross sections for a large grid of
 3592 masses (between 800 and 1800 GeV) and lifetimes (between 0.4 and stable) are
 3593 extracted from these counts with the CL_S method using the profile likelihood

$m(\tilde{g})$ [GeV]	Expected Signal	Expected Background	Observed Data
800	462.83 ± 14.86	1.764 ± 0.080	2.0
1000	108.73 ± 3.38	1.458 ± 0.070	1.0
1200	31.74 ± 0.95	1.137 ± 0.060	1.0
1400	10.22 ± 0.29	1.058 ± 0.058	1.0
1600	3.07 ± 0.09	0.947 ± 0.054	1.0
1800	1.08 ± 0.05	0.940 ± 0.054	1.0

Table 16: The expected number of signal events, the expected number of background events, and the observed number of events in data with their respective statistical errors within the respective mass window for each generated stable mass point

$m(\tilde{g})$ [GeV]	Expected Signal	Expected Background	Observed Data
1000	144.48 ± 5.14	1.499 ± 0.069	2.0
1100	73.19 ± 2.61	1.260 ± 0.060	2.0
1200	41.54 ± 1.41	1.456 ± 0.067	2.0
1300	22.58 ± 0.77	1.201 ± 0.058	2.0
1400	12.70 ± 0.42	1.558 ± 0.071	2.0
1500	6.73 ± 0.24	1.237 ± 0.060	2.0
1600	3.90 ± 0.13	1.201 ± 0.058	2.0
1700	2.27 ± 0.07	1.027 ± 0.052	2.0
1800	1.34 ± 0.04	1.019 ± 0.052	2.0

Table 17: The expected number of signal events, the expected number of background events, and the observed number of events in data with their respective statistical errors within the respective mass window for each generated mass point with a lifetime of 10 ns.

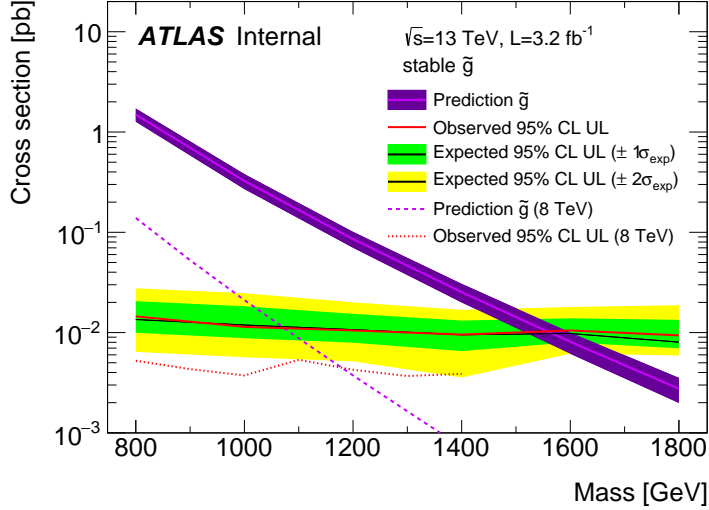


Figure 88: The observed and expected cross section limits as a function of mass for the stable simulated signal. The predicted cross section values for the corresponding signals are included.

ratio as a test statistic [96]. For this procedure, the systematic uncertainties estimated for the signal and background yields are treated as Gaussian-distributed nuisance parameters. The uncertainty on the normalization of the expected background distribution is included in the expected background events. At this point the expected cross section limit is calculated for both the metastable and stable signal region for each lifetime point, and the region with the best expected limit is selected for each lifetime. Using that procedure, the metastable region is used for lifetimes up to and including 30 ns, and the stable region for lifetimes above it.

The resulting cross-sectional upper limits are shown as a function of mass in Figure 88 and Figure 89 for each lifetime considered. The limits are interpolated linearly between each mass point, and the dependence of the limit on the mass is small as the efficiency is relatively constant for large R-Hadron masses. There is however a strong dependence on lifetime, as discussed in Section 11.5, where the probability to form a fully reconstructed track and the kinematic freedom to produce E_T^{miss} result in a local maximum in the limit at 10–30 ns. The figures also include the expected cross section for pair-produced gluino R-Hadrons for reference. For the 10 ns and stable cross section limits, both the observed limit and expected cross section for the Run 1, 8 TeV version of this analysis are included. There the cross sectional limits are lower because of the increased available luminosity, while the signal cross sections were also much lower because of the lower collision energy.

13.4 MASS LIMITS

The cross-sectional limits can then be used to derive a lower mass limit for gluino R-Hadrons by comparing them to the theoretically predicted production cross

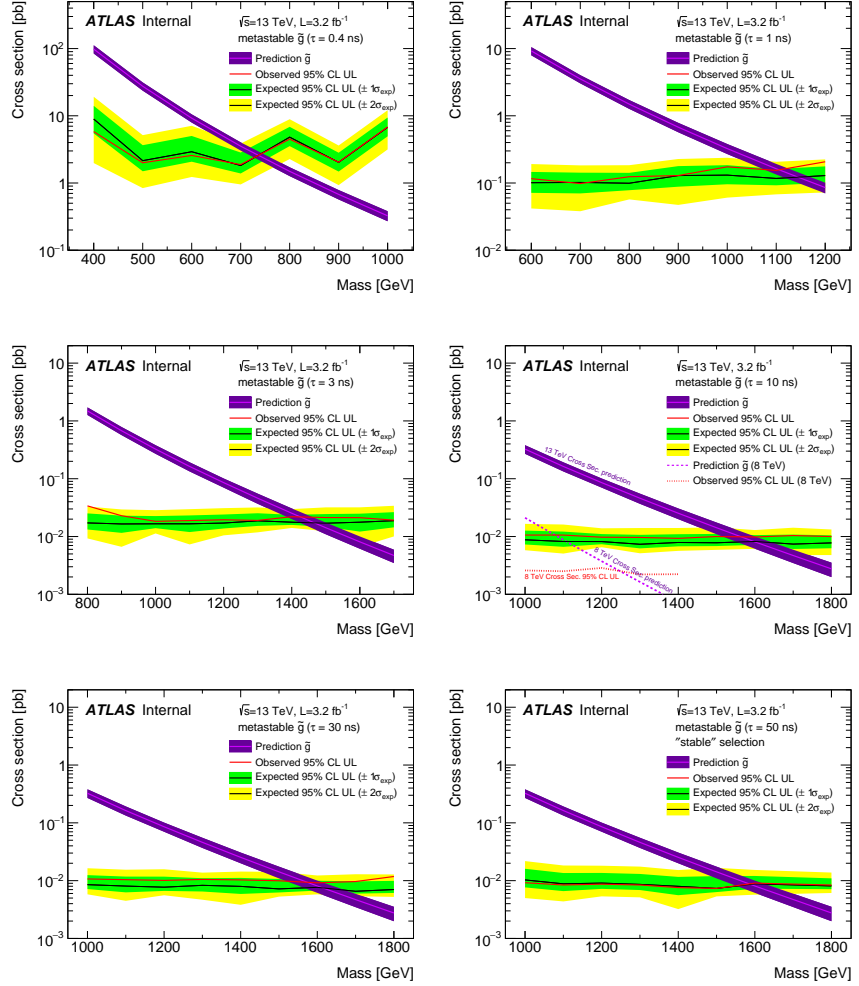


Figure 89: The observed and expected cross section limits as a function of mass for each generated lifetime. The predicted cross section values for the corresponding signals are included.

3619 sections. These mass limits range from only 740 GeV at the lowest lifetimes con-
 3620 sidered, where the selection efficiency is very low, to up to 1580 GeV at 30 ns
 3621 where the selection efficiency is maximized. The observed and expected mass
 3622 limits for each lifetime point are detailed in Table 18, which also lists which se-
 3623 lection region was used for each lifetime. These excluded range of masses as a
 3624 function of lifetime is also shown in Figure 90. The Run 1 limits are included for
 3625 comparison; the limits have increased by about 200 GeV on average. The search
 3626 has also improved since the previous incarnation from Run 1 in optimizing the
 3627 region between 30 GeV and detector-stable lifetimes by introducing the second
 3628 signal region. The definition of the stable region prevents the significant drop
 3629 in mass limit that occurred above 30 GeV in the Run 1 analysis.

Selection	τ [ns]	$M_{\text{obs}} > [\text{GeV}]$	$M_{\text{exp}} > [\text{GeV}]$
Metastable	0.4	740	730
"	1.0	1110	1150
"	3.0	1430	1470
"	10	1570	1600
"	30	1580	1620
Stable	50	1590	1590
"	stable	1570	1580

Table 18: The observed and expected 95% CL lower limit on mass for gluino R-Hadrons for each considered lifetime.

3630 13.5 CONTEXT FOR LONG-LIVED SEARCHES

3631 This search plays an important role in the current, combined [ATLAS](#) search for
 3632 long lived particles. The mass limits provided by various [ATLAS](#) searches for
 3633 long-lived gluino R-Hadrons can be seen in Figure 91. This search provides the
 3634 most competitive limit for lifetimes between 3 ns up through very long lifetimes,
 3635 where it is still competitive with dedicated searches for stable particles. The lim-
 3636 its placed on gluino production are very similar to the limits on promptly decay-
 3637 ing models.

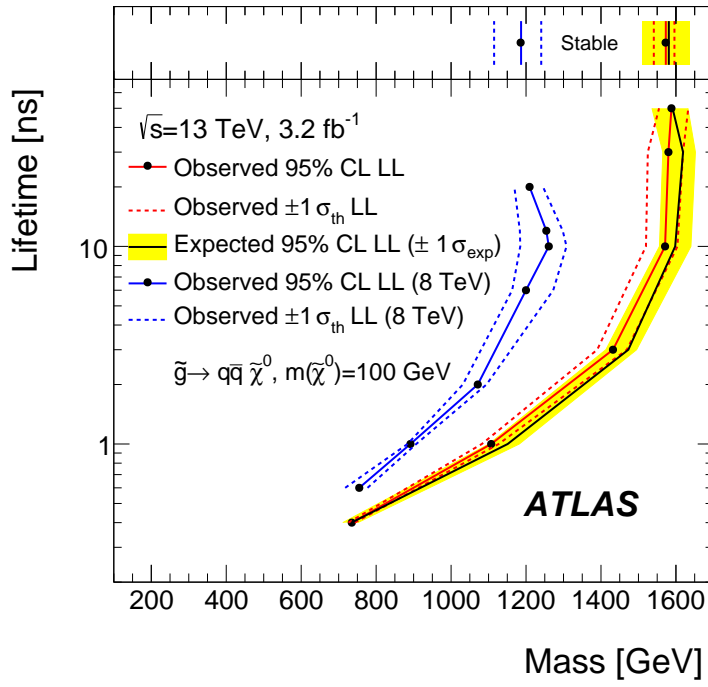


Figure 90: The excluded range of masses as a function of gluino lifetime. The expected lower limit (LL), with its experimental $\pm 1\sigma$ band, is given with respect to the nominal theoretical cross-section. The observed 95% LL obtained at $\sqrt{s} = 8 \text{ TeV}$ [79] is also shown for comparison.

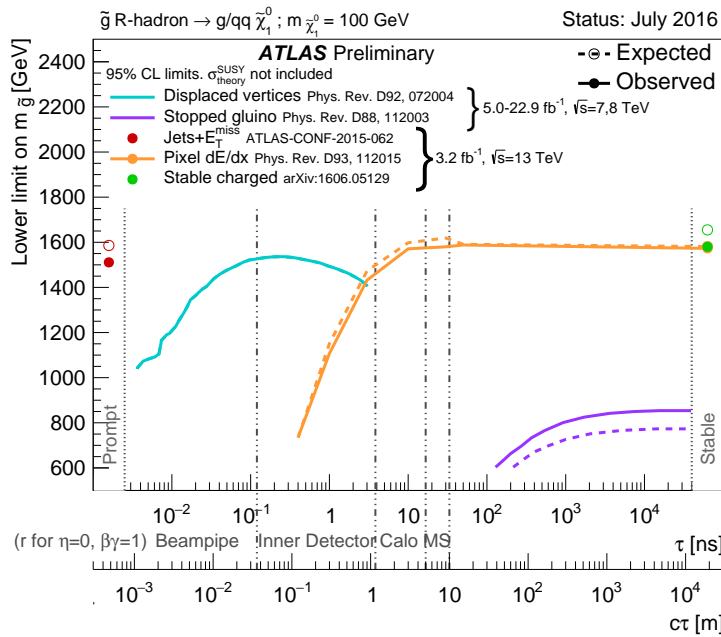


Figure 91: The constraints on the gluino mass as a function of lifetime for a split-supersymmetry model with the gluino R-Hadrons decaying into a gluon or light quarks and a neutralino with mass of 100 GeV. The solid lines indicate the observed limits, while the dashed lines indicate the expected limits. The area below the curves is excluded. The dots represent results for which the particle is assumed to be prompt or stable.

3638

PART VI

3639

CONCLUSIONS

3640

You can put some informational part preamble text here.

14

3641

3642 SUMMARY AND OUTLOOK

3643 14.1 SUMMARY

3644 14.2 OUTLOOK

3645

PART VII

3646

APPENDIX

3647

A

3648

3649 INELASTIC CROSS SECTION

B

3650

3651 EXPANDED R-HADRON YIELDS AND LIMITS

$m(\tilde{g})$ [GeV]	Left Extremum [GeV]	Right Extremum [GeV]
1000	682	1387
1100	763	1478
1200	801	1606
1300	809	1841
1400	861	2011
1500	920	2032
1600	952	2173
1800	1017	2422

Table 19: The left and right extremum of the mass window for each generated mass point with a 50 ns lifetime.

$m(\tilde{g})$ [GeV]	Left Extremum [GeV]	Right Extremum [GeV]
1000	689	1321
1100	746	1513
1200	788	1670
1300	860	1734
1400	833	1925
1500	852	2048
1600	833	2283
1700	946	2379
1800	869	2505

Table 20: The left and right extremum of the mass window for each generated mass point with a 30 ns lifetime.

$m(\tilde{g})$ [GeV]	Left Extremum [GeV]	Right Extremum [GeV]
1000	655	1349
1100	734	1455
1200	712	1631
1300	792	1737
1400	717	1926
1500	815	2117
1600	824	2122
1700	900	2274
1800	919	2344

Table 21: The left and right extremum of the mass window for each generated mass point with a 10 ns lifetime.

$m(\tilde{g})$ [GeV]	Left Extremum [GeV]	Right Extremum [GeV]
800	531	1065
900	576	1165
1000	610	1345
1100	635	1432
1200	663	1563
1300	620	1667
1400	742	1727
1500	761	1937
1600	573	2000
1700	621	2182

Table 22: The left and right extremum of the mass window used for each generated mass point with a lifetime of 3 ns.

$m(\tilde{g})$ [GeV]	Left Extremum [GeV]	Right Extremum [GeV]
600	411	758
700	385	876
800	486	970
900	406	987
1000	408	1136
1100	555	1196
1200	516	1378

Table 23: The left and right extremum of the mass window used for each mass point with a lifetime of 1 ns.

$m(\tilde{g})$ [GeV]	Left Extremum [GeV]	Right Extremum [GeV]
400	204	510
500	295	639
600	288	702
700	323	701
800	190	771
900	277	677
1000	249	688

Table 24: The left and right extremum of the mass window for each generated mass point with a lifetime of 0.4 ns.

$m(\tilde{g})$ [GeV]	Left Extremum [GeV]	Right Extremum [GeV]
800	627	1053
1000	726	1277
1200	857	1584
1400	924	1937
1600	993	2308
1800	1004	2554

Table 25: The left and right extremum of the mass window used for each generated stable mass point.

$m(\tilde{g})$ [GeV]	Expected Signal	Expected Background	Observed Data
1000	131.18 ± 6.35	1.803 ± 0.081	1.0 ± 1.0
1100	71.11 ± 3.35	1.409 ± 0.069	1.0 ± 1.0
1200	37.18 ± 1.75	1.310 ± 0.066	1.0 ± 1.0
1300	20.76 ± 0.95	1.431 ± 0.069	1.0 ± 1.0
1400	12.63 ± 0.57	1.273 ± 0.065	1.0 ± 1.0
1500	6.57 ± 0.29	1.115 ± 0.059	1.0 ± 1.0
1600	3.56 ± 0.16	1.041 ± 0.057	1.0 ± 1.0
1800	1.27 ± 0.05	0.918 ± 0.053	1.0 ± 1.0

Table 26: The expected number of signal events, the expected number of background events, and the observed number of events in data with their respective statistical errors within the respective mass window for each generated mass point with a lifetime of 50 ns.

$m(\tilde{g})$ [GeV]	Expected Signal	Expected Background	Observed Data
1000	144.65 ± 6.34	1.328 ± 0.063	2.0 ± 1.4
1100	75.28 ± 3.27	1.255 ± 0.060	2.0 ± 1.4
1200	40.51 ± 1.75	1.193 ± 0.058	2.0 ± 1.4
1300	20.91 ± 0.93	0.997 ± 0.051	2.0 ± 1.4
1400	11.97 ± 0.51	1.131 ± 0.056	2.0 ± 1.4
1500	6.81 ± 0.28	1.111 ± 0.055	2.0 ± 1.4
1600	4.19 ± 0.16	1.193 ± 0.058	2.0 ± 1.4
1700	2.42 ± 0.09	0.963 ± 0.050	2.0 ± 1.4
1800	1.46 ± 0.05	1.138 ± 0.056	3.0 ± 1.7

Table 27: The expected number of signal events, the expected number of background events, and the observed number of events in data with their respective statistical errors within the respective mass window for each generated mass point with a lifetime of 30 ns.

$m(\tilde{g})$ [GeV]	Expected Signal	Expected Background	Observed Data
1000	144.48 ± 5.14	1.499 ± 0.069	2.0 ± 1.4
1100	73.19 ± 2.61	1.260 ± 0.060	2.0 ± 1.4
1200	41.54 ± 1.41	1.456 ± 0.067	2.0 ± 1.4
1300	22.58 ± 0.77	1.201 ± 0.058	2.0 ± 1.4
1400	12.70 ± 0.42	1.558 ± 0.071	2.0 ± 1.4
1500	6.73 ± 0.24	1.237 ± 0.060	2.0 ± 1.4
1600	3.90 ± 0.13	1.201 ± 0.058	2.0 ± 1.4
1700	2.27 ± 0.07	1.027 ± 0.052	2.0 ± 1.4
1800	1.34 ± 0.04	1.019 ± 0.052	2.0 ± 1.4

Table 28: The expected number of signal events, the expected number of background events, and the observed number of events in data with their respective statistical errors within the respective mass window for each generated mass point with a lifetime of 10 ns.

$m(\tilde{g})$ [GeV]	Expected Signal	Expected Background	Observed Data
800	362.97 ± 14.68	1.841 ± 0.080	5.0 ± 2.2
900	169.20 ± 6.69	1.710 ± 0.076	3.0 ± 1.7
1000	84.78 ± 3.23	1.727 ± 0.076	2.0 ± 1.4
1100	40.06 ± 1.60	1.679 ± 0.075	2.0 ± 1.4
1200	20.06 ± 0.81	1.598 ± 0.072	2.0 ± 1.4
1300	10.76 ± 0.43	1.851 ± 0.080	2.0 ± 1.4
1400	5.52 ± 0.22	1.374 ± 0.064	2.0 ± 1.4
1500	3.16 ± 0.13	1.355 ± 0.064	2.0 ± 1.4
1600	2.13 ± 0.11	2.235 ± 0.093	3.0 ± 1.7
1700	1.10 ± 0.06	1.995 ± 0.085	2.0 ± 1.4

Table 29: The expected number of signal events, the expected number of background events, and the observed number of events in data with their respective statistical errors within the respective mass window for each generated mass point with a lifetime of 3 ns.

$m(\tilde{g})$ [GeV]	Expected Signal	Expected Background	Observed Data
600	431.80 ± 36.60	2.418 ± 0.099	3.0 ± 1.7
700	192.77 ± 15.28	3.267 ± 0.126	3.0 ± 1.7
800	69.63 ± 5.90	2.125 ± 0.089	3.0 ± 1.7
900	28.91 ± 2.59	3.114 ± 0.121	3.0 ± 1.7
1000	13.64 ± 1.22	3.359 ± 0.129	5.0 ± 2.2
1100	6.13 ± 0.57	1.879 ± 0.081	3.0 ± 1.7
1200	3.24 ± 0.30	2.387 ± 0.098	5.0 ± 2.2

Table 30: The expected number of signal events, the expected number of background events, and the observed number of events in data with their respective statistical errors within the respective mass window for each generated mass point with a lifetime of 1 ns.

$m(\tilde{g})$ [GeV]	Expected Signal	Expected Background	Observed Data
400	181.71 ± 75.59	6.780 ± 0.238	4.0 ± 2.0
500	103.88 ± 30.05	4.310 ± 0.160	4.0 ± 2.0
600	28.34 ± 9.34	4.868 ± 0.177	4.0 ± 2.0
700	13.62 ± 4.00	3.908 ± 0.147	4.0 ± 2.0
800	2.75 ± 1.15	9.001 ± 0.308	8.0 ± 2.8
900	2.25 ± 0.71	5.045 ± 0.183	5.0 ± 2.2
1000	0.34 ± 0.19	6.026 ± 0.214	6.0 ± 2.4

Table 31: The expected number of signal events, the expected number of background events, and the observed number of events in data with their respective statistical errors within the respective mass window for each generated mass point with a lifetime of p4 ns.

$m(\tilde{g})$ [GeV]	Expected Signal	Expected Background	Observed Data
800	462.83 ± 14.86	1.764 ± 0.080	2.0 ± 1.4
1000	108.73 ± 3.38	1.458 ± 0.070	1.0 ± 1.0
1200	31.74 ± 0.95	1.137 ± 0.060	1.0 ± 1.0
1400	10.22 ± 0.29	1.058 ± 0.058	1.0 ± 1.0
1600	3.07 ± 0.09	0.947 ± 0.054	1.0 ± 1.0
1800	1.08 ± 0.05	0.940 ± 0.054	1.0 ± 1.0

Table 32: The expected number of signal events, the expected number of background events, and the observed number of events in data with their respective statistical errors within the respective mass window for each generated stable mass point

- 3653 [1] A. D. Martin, W. J. Stirling, R. S. Thorne, and G. Watt. “Parton distributions
3654 for the LHC”. In: *Eur. Phys. J.* C63 (2009), pp. 189–285. doi: [10.1140/epjc/s10052-009-1072-5](https://doi.org/10.1140/epjc/s10052-009-1072-5). arXiv: [0901.0002 \[hep-ph\]](https://arxiv.org/abs/0901.0002).
- 3655 [2] Prajwal Raj Kafle, Sanjib Sharma, Geraint F. Lewis, and Joss Bland-Hawthorn.
3656 “On the Shoulders of Giants: Properties of the Stellar Halo and the Milky
3657 Way Mass Distribution”. In: *Astrophys. J.* 794.1 (2014), p. 59. doi: [10.1088/0004-637X/794/1/59](https://doi.org/10.1088/0004-637X/794/1/59). arXiv: [1408.1787 \[astro-ph.GA\]](https://arxiv.org/abs/1408.1787).
- 3658 [3] Lyndon Evans and Philip Bryant. “LHC Machine”. In: *JINST* 3 (2008), S08001.
3659 doi: [10.1088/1748-0221/3/08/S08001](https://doi.org/10.1088/1748-0221/3/08/S08001).
- 3660 [4] C Lefevre. “LHC: the guide (English version). Guide du LHC (version anglaise)”.
3661 2009. URL: <https://cds.cern.ch/record/1165534>.
- 3662 [5] “LEP Design Report Vol.1”. In: (1983).
- 3663 [6] ATLAS Collaboration. “The ATLAS Experiment at the CERN Large Hadron
3664 Collider”. In: *JINST* 3 (2008), S08003. doi: [10.1088/1748-0221/3/08/S08003](https://doi.org/10.1088/1748-0221/3/08/S08003).
- 3665 [7] S. Chatrchyan et al. “The CMS experiment at the CERN LHC”. In: *JINST*
3666 3 (2008), S08004. doi: [10.1088/1748-0221/3/08/S08004](https://doi.org/10.1088/1748-0221/3/08/S08004).
- 3667 [8] A. Augusto Alves Jr. et al. “The LHCb Detector at the LHC”. In: *JINST* 3
3668 (2008), S08005. doi: [10.1088/1748-0221/3/08/S08005](https://doi.org/10.1088/1748-0221/3/08/S08005).
- 3669 [9] K. Aamodt et al. “The ALICE experiment at the CERN LHC”. In: *JINST* 3
3670 (2008), S08002. doi: [10.1088/1748-0221/3/08/S08002](https://doi.org/10.1088/1748-0221/3/08/S08002).
- 3671 [10] K. A. Olive et al. “Review of Particle Physics”. In: *Chin. Phys. C38* (2014),
3672 p. 090001. doi: [10.1088/1674-1137/38/9/090001](https://doi.org/10.1088/1674-1137/38/9/090001).
- 3673 [11] Daniel Froidevaux and Paris Sphicas. “General-Purpose Detectors for the
3674 Large Hadron Collider”. In: *Annual Review of Nuclear and Particle Science*
3675 56.1 (2006), pp. 375–440. doi: [10.1146/annurev.nucl.54.070103.181209](https://doi.org/10.1146/annurev.nucl.54.070103.181209). URL: <http://dx.doi.org/10.1146/annurev.nucl.54.070103.181209>.
- 3676 [12] M Capeans, G Darbo, K Einsweiller, M Elsing, T Flick, M Garcia-Sciveres,
3677 C Gemme, H Pernegger, O Rohne, and R Vuillermet. *ATLAS Insertable B-*
3678 *Layer Technical Design Report*. Tech. rep. CERN-LHCC-2010-013. ATLAS-
3679 TDR-19. 2010. URL: <https://cds.cern.ch/record/1291633>.
- 3680 [13] T. Cornelissen, M. Elsing, S. Fleischmann, W. Liebig, and E. Moyse. “Con-
3681 cepts, Design and Implementation of the ATLAS New Tracking (NEWT)”.
3682 In: (2007). Ed. by A. Salzburger.
- 3683 [14] “Performance of the ATLAS Inner Detector Track and Vertex Reconstruc-
3684 tion in the High Pile-Up LHC Environment”. In: (2012).
- 3685
- 3686
- 3687
- 3688
- 3689

- 3690 [15] A. Salzburger. “The ATLAS Track Extrapolation Package”. In: (2007).
- 3691 [16] ATLAS Collaboration. “A neural network clustering algorithm for the AT-
3692 LAS silicon pixel detector”. In: *JINST* 9 (2014), P09009. doi: [10.1088/1748-0221/9/09/P09009](https://doi.org/10.1088/1748-0221/9/09/P09009). arXiv: [1406.7690 \[hep-ex\]](https://arxiv.org/abs/1406.7690).
- 3693 [17] ATLAS Collaboration. *Performance of primary vertex reconstruction in proton-
3694 proton collisions at $\sqrt{s} = 7$ TeV in the ATLAS experiment*. ATLAS-CONF-
3695 2010-069. 2010. URL: <https://cds.cern.ch/record/1281344>.
- 3696 [18] ATLAS Collaboration. “Electron reconstruction and identification efficiency
3697 measurements with the ATLAS detector using the 2011 LHC proton–proton
3698 collision data”. In: *Eur. Phys. J. C* 74 (2014), p. 2941. doi: [10.1140/epjc/s10052-014-2941-0](https://doi.org/10.1140/epjc/s10052-014-2941-0). arXiv: [1404.2240 \[hep-ex\]](https://arxiv.org/abs/1404.2240). PERF-2013-03.
- 3699 [19] ATLAS Collaboration. *Electron efficiency measurements with the ATLAS de-
3700 tector using the 2012 LHC proton–proton collision data*. ATLAS-CONF-2014-
3701 032. 2014. URL: <https://cds.cern.ch/record/1706245>.
- 3702 [20] ATLAS Collaboration. *Measurements of the photon identification efficiency
3703 with the ATLAS detector using 4.9 fb^{-1} of pp collision data collected in 2011*.
3704 ATLAS-CONF-2012-123. 2012. URL: <https://cds.cern.ch/record/1473426>.
- 3705 [21] ATLAS Collaboration. “Muon reconstruction performance of the ATLAS
3706 detector in proton–proton collision data at $\sqrt{s} = 13$ TeV”. In: (2016).
3707 arXiv: [1603.05598 \[hep-ex\]](https://arxiv.org/abs/1603.05598). PERF-2015-10.
- 3708 [22] ATLAS Collaboration. “Topological cell clustering in the ATLAS calorime-
3709 ters and its performance in LHC Run 1”. In: (2016). arXiv: [1603.02934](https://arxiv.org/abs/1603.02934)
3710 [hep-ex]. PERF-2014-07.
- 3711 [23] ATLAS Collaboration. *Properties of jets and inputs to jet reconstruction and
3712 calibration with the ATLAS detector using proton–proton collisions at $\sqrt{s} =$
3713 13 TeV*. ATL-PHYS-PUB-2015-036. 2015. URL: <https://cds.cern.ch/record/2044564>.
- 3714 [24] Matteo Cacciari, Gavin P. Salam, and Gregory Soyez. “The anti- k_t jet clus-
3715 tering algorithm”. In: *JHEP* 04 (2008), p. 063. doi: [10.1088/1126-6708/2008/04/063](https://doi.org/10.1088/1126-6708/2008/04/063). arXiv: [0802.1189 \[hep-ph\]](https://arxiv.org/abs/0802.1189).
- 3716 [25] ATLAS Collaboration. *Jet global sequential corrections with the ATLAS detec-
3717 tor in proton–proton collisions at $\sqrt{s} = 8$ TeV*. ATLAS-CONF-2015-002.
3718 2015. URL: <https://cds.cern.ch/record/2001682>.
- 3719 [26] S. Agostinelli et al. “GEANT4: A simulation toolkit”. In: *Nucl. Instrum. Meth.*
3720 A 506 (2003), pp. 250–303. doi: [10.1016/S0168-9002\(03\)01368-8](https://doi.org/10.1016/S0168-9002(03)01368-8).
- 3721 [27] ATLAS Collaboration. “A study of the material in the ATLAS inner de-
3722 tector using secondary hadronic interactions”. In: *JINST* 7 (2012), P01013.
3723 doi: [10.1088/1748-0221/7/01/P01013](https://doi.org/10.1088/1748-0221/7/01/P01013). arXiv: [1110.6191 \[hep-ex\]](https://arxiv.org/abs/1110.6191).
3724 PERF-2011-08.
- 3725 [3726] 3727 [3728] 3729

- 3730 [28] ATLAS Collaboration. “Electron and photon energy calibration with the
 3731 ATLAS detector using LHC Run 1 data”. In: *Eur. Phys. J. C* 74 (2014), p. 3071.
 3732 doi: [10.1140/epjc/s10052-014-3071-4](https://doi.org/10.1140/epjc/s10052-014-3071-4). arXiv: [1407.5063](https://arxiv.org/abs/1407.5063)
 3733 [[hep-ex](#)]. PERF-2013-05.
- 3734 [29] ATLAS Collaboration. “A measurement of the calorimeter response to sin-
 3735 gle hadrons and determination of the jet energy scale uncertainty using
 3736 LHC Run-1 pp -collision data with the ATLAS detector”. In: (2016). arXiv:
 3737 [1607.08842](https://arxiv.org/abs/1607.08842) [[hep-ex](#)]. PERF-2015-05.
- 3738 [30] ATLAS Collaboration. “Single hadron response measurement and calorime-
 3739 ter jet energy scale uncertainty with the ATLAS detector at the LHC”. In:
 3740 *Eur. Phys. J. C* 73 (2013), p. 2305. doi: [10.1140/epjc/s10052-013-2305-1](https://doi.org/10.1140/epjc/s10052-013-2305-1). arXiv: [1203.1302](https://arxiv.org/abs/1203.1302) [[hep-ex](#)]. PERF-2011-05.
- 3742 [31] ATLAS Collaboration. “The ATLAS Simulation Infrastructure”. In: *Eur.*
 3743 *Phys. J. C* 70 (2010), p. 823. doi: [10.1140/epjc/s10052-010-1429-9](https://doi.org/10.1140/epjc/s10052-010-1429-9).
 3744 arXiv: [1005.4568](https://arxiv.org/abs/1005.4568) [[hep-ex](#)]. SOFT-2010-01.
- 3745 [32] T. Sjöstrand, S. Mrenna, and P. Skands. “A Brief Introduction to PYTHIA
 3746 8.1”. In: *Comput. Phys. Commun.* 178 (2008), pp. 852–867. doi: [10.1016/j.cpc.2008.01.036](https://doi.org/10.1016/j.cpc.2008.01.036). arXiv: [0710.3820](https://arxiv.org/abs/0710.3820).
- 3748 [33] ATLAS Collaboration. *Summary of ATLAS Pythia 8 tunes*. ATL-PHYS-PUB-
 3749 2012-003. 2012. URL: <http://cds.cern.ch/record/1474107>.
- 3750 [34] A.D. Martin, W.J. Stirling, R.S. Thorne, and G. Watt. “Parton distributions
 3751 for the LHC”. In: *Eur. Phys. J. C* 63 (2009). Figures from the [MSTW Website](#),
 3752 pp. 189–285. doi: [10.1140/epjc/s10052-009-1072-5](https://doi.org/10.1140/epjc/s10052-009-1072-5). arXiv: [0901.0002](https://arxiv.org/abs/0901.0002).
- 3754 [35] A. Sherstnev and R.S. Thorne. “Parton Distributions for LO Generators”.
 3755 In: *Eur. Phys. J. C* 55 (2008), pp. 553–575. doi: [10.1140/epjc/s10052-008-0610-x](https://doi.org/10.1140/epjc/s10052-008-0610-x). arXiv: [0711.2473](https://arxiv.org/abs/0711.2473).
- 3757 [36] A. Ribon et al. *Status of Geant4 hadronic physics for the simulation of LHC*
 3758 *experiments at the start of LHC physics program*. CERN-LCGAPP-2010-02.
 3759 2010. URL: <http://lcgapp.cern.ch/project/docs/noteStatusHadronic2010.pdf>.
- 3761 [37] M. P. Guthrie, R. G. Alsmiller, and H. W. Bertini. “Calculation of the cap-
 3762 ture of negative pions in light elements and comparison with experiments
 3763 pertaining to cancer radiotherapy”. In: *Nucl. Instrum. Meth.* 66 (1968), pp. 29–
 3764 36. doi: [10.1016/0029-554X\(68\)90054-2](https://doi.org/10.1016/0029-554X(68)90054-2).
- 3765 [38] H. W. Bertini and P. Guthrie. “News item results from medium-energy
 3766 intranuclear-cascade calculation”. In: *Nucl. Instr. and Meth. A* 169 (1971),
 3767 p. 670. doi: [10.1016/0375-9474\(71\)90710-X](https://doi.org/10.1016/0375-9474(71)90710-X).
- 3768 [39] V.A. Karmanov. “Light Front Wave Function of Relativistic Composite
 3769 System in Explicitly Solvable Model”. In: *Nucl. Phys. B* 166 (1980), p. 378.
 3770 doi: [10.1016/0550-3213\(80\)90204-7](https://doi.org/10.1016/0550-3213(80)90204-7).
- 3771 [40] H. S. Fesefeldt. *GHEISHA program*. Pitha-85-02, Aachen. 1985.

- 3772 [41] G. Folger and J.P. Wellisch. “String parton models in Geant4”. In: (2003).
 3773 arXiv: [nucl-th/0306007](#).
- 3774 [42] N. S. Amelin et al. “Transverse flow and collectivity in ultrarelativistic
 3775 heavy-ion collisions”. In: *Phys. Rev. Lett.* 67 (1991), p. 1523. doi: [10.1103/PhysRevLett.67.1523](#).
- 3776 [43] N. S. Amelin et al. “Collectivity in ultrarelativistic heavy ion collisions”. In:
 3777 *Nucl. Phys. A* 544 (1992), p. 463. doi: [10.1016/0375-9474\(92\)90598-E](#).
- 3779 [44] L. V. Bravina et al. “Fluid dynamics and Quark Gluon string model - What
 3780 we can expect for Au+Au collisions at 11.6 AGeV/c”. In: *Nucl. Phys. A* 566
 3781 (1994), p. 461. doi: [10.1016/0375-9474\(94\)90669-6](#).
- 3783 [45] L. V. Bravin et al. “Scaling violation of transverse flow in heavy ion colli-
 3784 sions at AGS energies”. In: *Phys. Lett. B* 344 (1995), p. 49. doi: [10.1016/0370-2693\(94\)01560-Y](#).
- 3786 [46] B. Andersson et al. “A model for low-pT hadronic reactions with general-
 3787 izations to hadron-nucleus and nucleus-nucleus collisions”. In: *Nucl. Phys.*
 3788 *B* 281 (1987), p. 289. doi: [10.1016/0550-3213\(87\)90257-4](#).
- 3789 [47] B. Andersson, A. Tai, and B.-H. Sa. “Final state interactions in the (nuclear)
 3790 FRITIOF string interaction scenario”. In: *Z. Phys. C* 70 (1996), pp. 499–
 3791 506. doi: [10.1007/s002880050127](#).
- 3792 [48] B. Nilsson-Almqvist and E. Stenlund. “Interactions Between Hadrons and
 3793 Nuclei: The Lund Monte Carlo, Fritiof Version 1.6”. In: *Comput. Phys. Com-*
 3794 *mun.* 43 (1987), p. 387. doi: [10.1016/0010-4655\(87\)90056-7](#).
- 3795 [49] B. Ganhuyag and V. Uzhinsky. “Modified FRITIOF code: Negative charged
 3796 particle production in high energy nucleus nucleus interactions”. In: *Czech.*
 3797 *J. Phys.* 47 (1997), pp. 913–918. doi: [10.1023/A:1021296114786](#).
- 3798 [50] ATLAS Collaboration. “Topological cell clustering in the ATLAS calorime-
 3799 ters and its performance in LHC Run 1”. In: (2016). arXiv: [1603.02934](#)
 3800 [[hep-ex](#)].
- 3801 [51] Peter Speckmayer. “Energy Measurement of Hadrons with the CERN AT-
 3802 LAS Calorimeter”. Presented on 18 Jun 2008. PhD thesis. Vienna: Vienna,
 3803 Tech. U., 2008. URL: <http://cds.cern.ch/record/1112036>.
- 3804 [52] CMS Collaboration. “The CMS barrel calorimeter response to particle
 3805 beams from 2 to 350 GeV/c”. In: *Eur. Phys. J. C* 60.3 (2009). doi: [10.1140/epjc/s10052-009-0959-5](#).
- 3807 [53] J. Beringer et al. (Particle Data Group). “Review of Particle Physics”. In:
 3808 *Chin. Phys. C* 38 (2014), p. 090001. URL: <http://pdg.lbl.gov>.
- 3809 [54] P. Adragna et al. “Measurement of Pion and Proton Response and Lon-
 3810 gitudinal Shower Profiles up to 20 Nuclear Interaction Lengths with the
 3811 ATLAS Tile Calorimeter”. In: *Nucl. Instrum. Meth. A* 615 (2010), pp. 158–
 3812 181. doi: [10.1016/j.nima.2010.01.037](#).

- 3813 [55] ATLAS Collaboration. “Jet energy measurement and its systematic uncer-
 3814 tainty in proton–proton collisions at $\sqrt{s} = 7$ TeV with the ATLAS detec-
 3815 tor”. In: *Eur. Phys. J. C* 75 (2015), p. 17. doi: [10.1140/epjc/s10052-014-3190-y](https://doi.org/10.1140/epjc/s10052-014-3190-y). arXiv: [1406.0076 \[hep-ex\]](https://arxiv.org/abs/1406.0076). PERF-2012-01.
- 3817 [56] Hung-Liang Lai, Marco Guzzi, Joey Huston, Zhao Li, Pavel M. Nadolsky,
 3818 et al. “New parton distributions for collider physics”. In: *Phys. Rev. D* 82
 3819 (2010), p. 074024. doi: [10.1103/PhysRevD.82.074024](https://doi.org/10.1103/PhysRevD.82.074024). arXiv: [1007.2241 \[hep-ph\]](https://arxiv.org/abs/1007.2241).
- 3821 [57] E. Abat et al. “Study of energy response and resolution of the ATLAS barrel
 3822 calorimeter to hadrons of energies from 20 to 350 GeV”. In: *Nucl. Instrum.
 3823 Meth. A* 621.1-3 (2010), pp. 134 – 150. doi: <http://dx.doi.org/10.1016/j.nima.2010.04.054>.
- 3825 [58] ATLAS Collaboration. “Jet energy measurement with the ATLAS detector
 3826 in proton–proton collisions at $\sqrt{s} = 7$ TeV”. In: *Eur. Phys. J. C* 73 (2013),
 3827 p. 2304. doi: [10.1140/epjc/s10052-013-2304-2](https://doi.org/10.1140/epjc/s10052-013-2304-2). arXiv: [1112.6426 \[hep-ex\]](https://arxiv.org/abs/1112.6426). PERF-2011-03.
- 3829 [59] Nausheen R. Shah and Carlos E. M. Wagner. “Gravitons and dark matter in
 3830 universal extra dimensions”. In: *Phys. Rev. D* 74 (2006), p. 104008. doi: [10.1103/PhysRevD.74.104008](https://doi.org/10.1103/PhysRevD.74.104008). arXiv: [hep-ph/0608140 \[hep-ph\]](https://arxiv.org/abs/hep-ph/0608140).
- 3832 [60] Jonathan L. Feng, Arvind Rajaraman, and Fumihiro Takayama. “Graviton
 3833 cosmology in universal extra dimensions”. In: *Phys. Rev. D* 68 (2003), p. 085018.
 3834 doi: [10.1103/PhysRevD.68.085018](https://doi.org/10.1103/PhysRevD.68.085018). arXiv: [hep-ph/0307375 \[hep-ph\]](https://arxiv.org/abs/hep-ph/0307375).
- 3836 [61] Paul H. Frampton and Pham Quang Hung. “Long-lived quarks?” In: *Phys.
 3837 Rev. D* 58 (5 1998), p. 057704. doi: [10.1103/PhysRevD.58.057704](https://doi.org/10.1103/PhysRevD.58.057704).
 3838 URL: <http://link.aps.org/doi/10.1103/PhysRevD.58.057704>.
- 3840 [62] C. Friberg, E. Norrbin, and T. Sjostrand. “QCD aspects of leptoquark pro-
 3841 duction at HERA”. In: *Phys. Lett. B* 403 (1997), pp. 329–334. doi: [10.1016/S0370-2693\(97\)00543-1](https://doi.org/10.1016/S0370-2693(97)00543-1). arXiv: [hep-ph/9704214 \[hep-ph\]](https://arxiv.org/abs/hep-ph/9704214).
- 3843 [63] Herbert K. Dreiner. “An introduction to explicit R-parity violation”. In:
 3844 (1997). arXiv: [hep-ph/9707435](https://arxiv.org/abs/hep-ph/9707435).
- 3845 [64] Edmond L. Berger and Zack Sullivan. “Lower limits on R-parity-violating
 3846 couplings in supersymmetry”. In: *Phys. Rev. Lett.* 92 (2004), p. 201801. doi:
 3847 [10.1103/PhysRevLett.92.201801](https://doi.org/10.1103/PhysRevLett.92.201801). arXiv: [hep-ph/0310001](https://arxiv.org/abs/hep-ph/0310001).
- 3848 [65] R. Barbieri, C. Berat, M. Besancon, M. Chemtob, A. Deandrea, et al. “R-
 3849 parity violating supersymmetry”. In: *Phys. Rept.* 420 (2005), p. 1. doi: [10.1016/j.physrep.2005.08.006](https://doi.org/10.1016/j.physrep.2005.08.006). arXiv: [hep-ph/0406039](https://arxiv.org/abs/hep-ph/0406039).
- 3851 [66] M. Fairbairn et al. “Stable massive particles at colliders”. In: *Phys. Rept.* 438
 3852 (2007), p. 1. doi: [10.1016/j.physrep.2006.10.002](https://doi.org/10.1016/j.physrep.2006.10.002). arXiv: [hep-ph/0611040](https://arxiv.org/abs/hep-ph/0611040).

- 3854 [67] Christopher F. Kolda. “Gauge-mediated supersymmetry breaking: Intro-
 3855 duction, review and update”. In: *Nucl. Phys. Proc. Suppl.* 62 (1998), p. 266.
 3856 doi: [10.1016/S0920-5632\(97\)00667-1](https://doi.org/10.1016/S0920-5632(97)00667-1). arXiv: [hep-ph/9707450](https://arxiv.org/abs/hep-ph/9707450).
- 3857 [68] Howard Baer, Kingman Cheung, and John F. Gunion. “A Heavy gluino as
 3858 the lightest supersymmetric particle”. In: *Phys. Rev. D* 59 (1999), p. 075002.
 3859 doi: [10.1103/PhysRevD.59.075002](https://doi.org/10.1103/PhysRevD.59.075002). arXiv: [hep-ph/9806361](https://arxiv.org/abs/hep-ph/9806361).
- 3860 [69] S. James Gates Jr. and Oleg Lebedev. “Searching for supersymmetry in
 3861 hadrons”. In: *Phys. Lett. B* 477 (2000), p. 216. doi: [10.1016/S0370-2693\(00\)00172-6](https://doi.org/10.1016/S0370-2693(00)00172-6). arXiv: [hep-ph/9912362](https://arxiv.org/abs/hep-ph/9912362).
- 3863 [70] G. F. Giudice and A. Romanino. “Split supersymmetry”. In: *Nucl. Phys. B*
 3864 699 (2004), p. 65. doi: [10.1016/j.nuclphysb.2004.11.048](https://doi.org/10.1016/j.nuclphysb.2004.11.048). arXiv:
 3865 [hep-ph/0406088](https://arxiv.org/abs/hep-ph/0406088).
- 3866 [71] N. Arkani-Hamed, S. Dimopoulos, G. F. Giudice, and A. Romanino. “As-
 3867 pects of split supersymmetry”. In: *Nucl. Phys. B* 709 (2005), p. 3. doi: [10.1016/j.nuclphysb.2004.12.026](https://doi.org/10.1016/j.nuclphysb.2004.12.026). arXiv: [hep-ph/0409232](https://arxiv.org/abs/hep-ph/0409232).
- 3869 [72] Glennys R. Farrar and Pierre Fayet. “Phenomenology of the Production,
 3870 Decay, and Detection of New Hadronic States Associated with Supersym-
 3871 metry”. In: *Phys. Lett. B* 76 (1978), pp. 575–579. doi: [10.1016/0370-2693\(78\)90858-4](https://doi.org/10.1016/0370-2693(78)90858-4).
- 3873 [73] A. C. Kraan, J. B. Hansen, and P. Nevski. “Discovery potential of R-hadrons
 3874 with the ATLAS detector”. In: *Eur. Phys. J. C* 49 (2007), pp. 623–640. doi:
 3875 [10.1140/epjc/s10052-006-0162-x](https://doi.org/10.1140/epjc/s10052-006-0162-x). arXiv: [hep-ex/0511014](https://arxiv.org/abs/hep-ex/0511014)
 3876 [[hep-ex](#)].
- 3877 [74] Rasmus Mackeprang and David Milstead. “An Updated Description of
 3878 Heavy-Hadron Interactions in GEANT-4”. In: *Eur. Phys. J. C* 66 (2010), pp. 493–
 3879 501. doi: [10.1140/epjc/s10052-010-1262-1](https://doi.org/10.1140/epjc/s10052-010-1262-1). arXiv: [0908.1868](https://arxiv.org/abs/0908.1868)
 3880 [[hep-ph](#)].
- 3881 [75] ATLAS Collaboration. “Search for massive, long-lived particles using mul-
 3882 titrack displaced vertices or displaced lepton pairs in pp collisions at $\sqrt{s} =$
 3883 8 TeV with the ATLAS detector”. In: *Phys. Rev. D* 92 (2015), p. 072004.
 3884 doi: [10.1103/PhysRevD.92.072004](https://doi.org/10.1103/PhysRevD.92.072004). arXiv: [1504.05162](https://arxiv.org/abs/1504.05162) [[hep-ex](#)].
 3885 SUSY-2014-02.
- 3886 [76] ATLAS Collaboration. “Search for charginos nearly mass degenerate with
 3887 the lightest neutralino based on a disappearing-track signature in pp col-
 3888 lisions at $\sqrt{s} = 8$ TeV with the ATLAS detector”. In: *Phys. Rev. D* 88 (2013),
 3889 p. 112006. doi: [10.1103/PhysRevD.88.112006](https://doi.org/10.1103/PhysRevD.88.112006). arXiv: [1310.3675](https://arxiv.org/abs/1310.3675)
 3890 [[hep-ex](#)]. SUSY-2013-01.
- 3891 [77] ATLAS Collaboration. “Searches for heavy long-lived sleptons and R-Hadrons
 3892 with the ATLAS detector in pp collisions at $\sqrt{s} = 7$ TeV”. In: *Phys. Lett. B*
 3893 720 (2013), p. 277. doi: [10.1016/j.physletb.2013.02.015](https://doi.org/10.1016/j.physletb.2013.02.015). arXiv:
 3894 [1211.1597](https://arxiv.org/abs/1211.1597) [[hep-ex](#)]. SUSY-2012-01.

- 3895 [78] ATLAS Collaboration. “Searches for heavy long-lived charged particles
 3896 with the ATLAS detector in proton–proton collisions at $\sqrt{s} = 8$ TeV”. In: *JHEP* 01 (2015), p. 068. doi: [10.1007/JHEP01\(2015\)068](https://doi.org/10.1007/JHEP01(2015)068). arXiv:
 3897 [1411.6795 \[hep-ex\]](https://arxiv.org/abs/1411.6795). SUSY-2013-22.
- 3898 [79] ATLAS Collaboration. “Search for metastable heavy charged particles with
 3899 large ionisation energy loss in pp collisions at $\sqrt{s} = 8$ TeV using the AT-
 3900 LAS experiment”. In: *Eur. Phys. J. C* 75 (2015), p. 407. doi: [10.1140/epjc/s10052-015-3609-0](https://doi.org/10.1140/epjc/s10052-015-3609-0). arXiv: [1506.05332 \[hep-ex\]](https://arxiv.org/abs/1506.05332). SUSY-
 3901 2014-09.
- 3902 [80] ATLAS Collaboration. “Search for heavy long-lived charged R -hadrons
 3903 with the ATLAS detector in 3.2 fb^{-1} of proton–proton collision data at
 3904 $\sqrt{s} = 13$ TeV”. In: *Phys. Lett. B* 760 (2016), pp. 647–665. doi: [10.1016/j.physletb.2016.07.042](https://doi.org/10.1016/j.physletb.2016.07.042). arXiv: [1606.05129 \[hep-ex\]](https://arxiv.org/abs/1606.05129).
- 3905 [81] Torbjorn Sjöstrand, Stephen Mrenna, and Peter Skands. “PYTHIA 6.4 Physics
 3906 and Manual”. In: *JHEP* 0605 (2006), p. 026. doi: [10.1088/1126-6708/2006/05/026](https://doi.org/10.1088/1126-6708/2006/05/026). arXiv: [hep-ph/0603175](https://arxiv.org/abs/hep-ph/0603175).
- 3907 [82] ATLAS Collaboration. *Further ATLAS tunes of PYTHIA 6 and Pythia 8*. ATL-
 3908 PHYS-PUB-2011-014. 2011. URL: <https://cds.cern.ch/record/1400677>.
- 3909 [83] Aafke Christine Kraan. “Interactions of heavy stable hadronizing parti-
 3910 cles”. In: *Eur. Phys. J. C* 37 (2004), pp. 91–104. doi: [10.1140/epjc/s2004-01946-6](https://doi.org/10.1140/epjc/s2004-01946-6). arXiv: [hep-ex/0404001 \[hep-ex\]](https://arxiv.org/abs/hep-ex/0404001).
- 3911 [84] M. Fairbairn et al. “Stable massive particles at colliders”. In: *Phys. Rept.* 438
 3912 (2007), p. 1. doi: [10.1016/j.physrep.2006.10.002](https://doi.org/10.1016/j.physrep.2006.10.002). arXiv: [hep-ph/0611040](https://arxiv.org/abs/hep-ph/0611040).
- 3913 [85] W. Beenakker, R. Hopker, M. Spira, and P. M. Zerwas. “Squark and gluino
 3914 production at hadron colliders”. In: *Nucl. Phys. B* 492 (1997), p. 51. doi:
 3915 [10.1016/S0550-3213\(97\)00084-9](https://doi.org/10.1016/S0550-3213(97)00084-9). arXiv: [hep-ph/9610490](https://arxiv.org/abs/hep-ph/9610490).
- 3916 [86] A. Kulesza and L. Motyka. “Threshold resummation for squark-antisquark
 3917 and gluino-pair production at the LHC”. In: *Phys. Rev. Lett.* 102 (2009),
 3918 p. 111802. doi: [10.1103/PhysRevLett.102.111802](https://doi.org/10.1103/PhysRevLett.102.111802). arXiv: [0807.2405 \[hep-ph\]](https://arxiv.org/abs/0807.2405).
- 3919 [87] A. Kulesza and L. Motyka. “Soft gluon resummation for the production
 3920 of gluino-gluino and squark-antisquark pairs at the LHC”. In: *Phys. Rev.*
 3921 *D* 80 (2009), p. 095004. doi: [10.1103/PhysRevD.80.095004](https://doi.org/10.1103/PhysRevD.80.095004). arXiv:
 3922 [0905.4749 \[hep-ph\]](https://arxiv.org/abs/0905.4749).
- 3923 [88] Wim Beenakker, Silja Brening, Michael Kramer, Anna Kulesza, Eric Lae-
 3924 nen, et al. “Soft-gluon resummation for squark and gluino hadroprodu-
 3925 ction”. In: *JHEP* 0912 (2009), p. 041. doi: [10.1088/1126-6708/2009/12/041](https://doi.org/10.1088/1126-6708/2009/12/041). arXiv: [0909.4418 \[hep-ph\]](https://arxiv.org/abs/0909.4418).
- 3926 [89] W. Beenakker, S. Brening, M.n Kramer, A. Kulesza, E. Laenen, et al. “Squark
 3927 and Gluino Hadroproduction”. In: *Int. J. Mod. Phys. A* 26 (2011), p. 2637.
 3928 doi: [10.1142/S0217751X11053560](https://doi.org/10.1142/S0217751X11053560). arXiv: [1105.1110 \[hep-ph\]](https://arxiv.org/abs/1105.1110).

- 3938 [90] Michael Krämer et al. *Supersymmetry production cross sections in pp collisions*
 3939 *at $\sqrt{s} = 7 \text{ TeV}$* . 2012. arXiv: [1206.2892 \[hep-ph\]](#).
- 3940 [91] Rasmus Mackeprang and Andrea Rizzi. “Interactions of Coloured Heavy
 3941 Stable Particles in Matter”. In: *Eur. Phys. J.* C50 (2007), pp. 353–362. doi:
 3942 [10.1140/epjc/s10052-007-0252-4](#). arXiv: [hep-ph/0612161 \[hep-ph\]](#).
- 3944 [92] Rasmus Mackeprang and David Milstead. “An Updated Description of
 3945 Heavy-Hadron Interactions in GEANT-4”. In: *Eur. Phys. J.* C66 (2010), pp. 493–
 3946 501. doi: [10.1140/epjc/s10052-010-1262-1](#). arXiv: [0908.1868 \[hep-ph\]](#).
- 3948 [93] J. Alwall, R. Frederix, S. Frixione, V. Hirschi, F. Maltoni, O. Mattelaer, H. S.
 3949 Shao, T. Stelzer, P. Torrielli, and M. Zaro. “The automated computation of
 3950 tree-level and next-to-leading order differential cross sections, and their
 3951 matching to parton shower simulations”. In: *JHEP* 07 (2014), p. 079. doi:
 3952 [10.1007/JHEP07\(2014\)079](#). arXiv: [1405.0301 \[hep-ph\]](#).
- 3953 [94] “dE/dx measurement in the ATLAS Pixel Detector and its use for particle
 3954 identification”. In: (2011).
- 3955 [95] ATLAS Collaboration. “The ATLAS Simulation Infrastructure”. In: *Eur.
 3956 Phys. J.* C70 (2010), pp. 823–874. doi: [10.1140/epjc/s10052-010-
 3957 1429-9](#). arXiv: [1005.4568 \[physics.ins-det\]](#).
- 3958 [96] Alexander L. Read. “Presentation of search results: The CL(s) technique”.
 3959 In: *J. Phys.* G28 (2002). [,11(2002)], pp. 2693–2704. doi: [10.1088/0954-
 3960 3899/28/10/313](#).

3961 DECLARATION

3962 Put your declaration here.

3963 *Berkeley, CA, September 2016*

3964

Bradley Axen

3965

3966 COLOPHON

3967

Not sure that this is necessary.